

INFORMATION TO USERS

This manuscript has been reproduced from the microfilm master. UMI films the text directly from the original or copy submitted. Thus, some thesis and dissertation copies are in typewriter face, while others may be from any type of computer printer.

The quality of this reproduction is dependent upon the quality of the copy submitted. Broken or indistinct print, colored or poor quality illustrations and photographs, print bleedthrough, substandard margins, and improper alignment can adversely affect reproduction.

In the unlikely event that the author did not send UMI a complete manuscript and there are missing pages, these will be noted. Also, if unauthorized copyright material had to be removed, a note will indicate the deletion.

Oversize materials (e.g., maps, drawings, charts) are reproduced by sectioning the original, beginning at the upper left-hand corner and continuing from left to right in equal sections with small overlaps.

Photographs included in the original manuscript have been reproduced xerographically in this copy. Higher quality 6" x 9" black and white photographic prints are available for any photographs or illustrations appearing in this copy for an additional charge. Contact UMI directly to order.

ProQuest Information and Learning
300 North Zeeb Road, Ann Arbor, MI 48106-1346 USA
800-521-0600



TYPE II SUPERNOVAE AS DISTANCE INDICATORS

by

Mario Andrés Hamuy

A Dissertation Submitted to the Faculty of the

DEPARTMENT OF ASTRONOMY

In Partial Fulfillment of the Requirements
For the Degree of

DOCTOR OF PHILOSOPHY

In the Graduate College

THE UNIVERSITY OF ARIZONA

2001

UMI Number: 3031358



UMI Microform 3031358

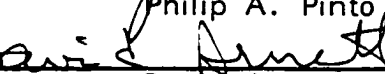
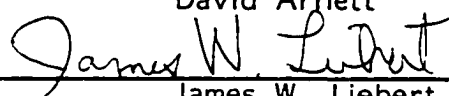
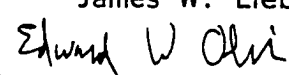
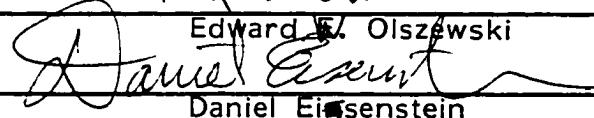
Copyright 2002 by Bell & Howell Information and Learning Company.
All rights reserved. This microform edition is protected against
unauthorized copying under Title 17, United States Code.

Bell & Howell Information and Learning Company
300 North Zeeb Road
P.O. Box 1346
Ann Arbor, MI 48106-1346

THE UNIVERSITY OF ARIZONA ©
GRADUATE COLLEGE

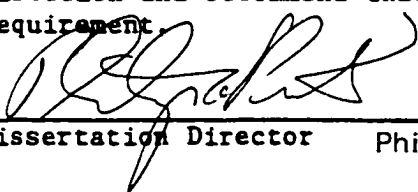
As members of the Final Examination Committee, we certify that we have
read the dissertation prepared by Mario Andrés Hamuy
entitled TYPE II SUPERNOVAE AS DISTANCE INDICATORS

and recommend that it be accepted as fulfilling the dissertation
requirement for the Degree of Doctor of Philosophy

<u></u>	<u>Philip A. Pinto</u>	<u>9/21/01</u>
<u></u>	<u>David Arnett</u>	<u>9/21/01</u>
<u></u>	<u>James W. Liebert</u>	<u>9/21/01</u>
<u></u>	<u>Edward W. Olszewski</u>	<u>9/21/01</u>
<u></u>	<u>Daniel Eisenstein</u>	<u>9/21/01</u>

Final approval and acceptance of this dissertation is contingent upon
the candidate's submission of the final copy of the dissertation to the
Graduate College.

I hereby certify that I have read this dissertation prepared under my
direction and recommend that it be accepted as fulfilling the dissertation
requirement.


Dissertation Director Philip A. Pinto

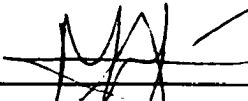
9/21/01
Date

STATEMENT BY AUTHOR

This dissertation has been submitted in partial fulfillment of requirements for an advanced degree at The University of Arizona and is deposited in the University Library to be made available to borrowers under rules of the Library.

Brief quotations from this dissertation are allowable without special permission, provided that accurate acknowledgment of source is made. Requests for permission for extended quotation from or reproduction of this manuscript in whole or in part may be granted by the head of the major department or the Dean of the Graduate College when in his or her judgment the proposed use of the material is in the interests of scholarship. In all other instances, however, permission must be obtained from the author.

SIGNED: _____



ACKNOWLEDGMENTS

I am very grateful to my advisor Phil Pinto for his invaluable support, friendship, and wisdom, to Dave Arnett and Adam Burrows for their input during the preparation of this dissertation, to the astronomers of Steward Observatory for the first-class education they provided me, and to its employees for making the atmosphere so relaxed and helping me to bring my feet to Earth. My enrollment in the Ph.D. program at The University of Arizona would not have been possible without the encouragement of José Maza, Mark Phillips, Nick Suntzeff, and Bob Williams, to whom I feel deeply grateful.

This dissertation would not have been possible without the data obtained through the Calán/Tololo and SOIRS collaborations. I acknowledge the generous work and invaluable help of Roberto Antezana, Roberto Avilés, Pablo Candia, Ricardo Covarrubias, Luis González, Valentin Ivanov, José Maza, Amaya Moro-Martin, César Muena, Mauricio Navarrete, Isabel Pérez, Mark Phillips, Aimee Hungerford, Bob Schommer, Chris Smith, Lou Strolger, Nick Suntzeff, Geraldo Valladares, Lisa Wells, and Marina Wischnjewsky.

A significant fraction of the data included in this dissertation comes from unpublished observations obtained by several colleagues. I thank them for their great generosity, a rare virtue in the competitive world of modern astronomy. In particular, I would like to acknowledge the help and collaboration from Massimo Della Valle, Andrea Pastorello, Enrico Capallaro, and Massimo Turatto, for allowing me to use their spectra and photometry obtained in the course of the ESO Supernova Key Project, and from Mark Phillips and Sofia Kirhakos for making available their extensive dataset of SN 1986L.

A special thank must go to Ron Eastman for providing his model spectra, to Riccardo Giovanelli for his unpublished Tully-Fisher distances, J. G. Cuby for his IR atmospheric transmission spectrum, R. Maiolino for his solar spectrum, and to many astronomers who contributed with their telescope times to obtain valuable observations for this project.

I am very grateful to Las Campanas and Cerro Calán observatories for allocating an office and providing generous operational support to the SOIRS program during 1999-2000. Likewise, I am grateful to the ESO, CTIO, and Las Campanas visitor support staffs for their assistance in the course of our observing runs. Also, I would like to thank the IRAF team for their prompt response to all of my software questions.

My first three years of Ph.D. studies were funded by the Gemini fellowship of the National Science Foundation and Fundación Andes (grants GF-1002-95, GF-1002-96, GF-1002-97). Also, I thank the generous financial support from Phil Pinto and Dave Arnett that permitted me to complete my Ph.D.

This research has made use of the NASA/IPAC Extragalactic Database (NED), which is operated by the Jet Propulsion Laboratory, California Institute of Technology, under contract with the National Aeronautics and Space Administration. This research has made use of and the SIMBAD database, operated at CDS, Strasbourg, France.

.

DEDICATION

A mi familia, especialmente a mis padres. A mis amigos, especialmente a Gonzalo.

TABLE OF CONTENTS

LIST OF FIGURES	8
LIST OF TABLES	11
ABSTRACT	13
Chapter 1 INTRODUCTION	15
1.1 Historical background	15
1.2 Supernova models	16
1.3 Supernovae as distance indicators	18
1.4 Goals of this dissertation	21
Chapter 2 OBSERVATIONS AND REDUCTIONS	23
2.1 Introduction	23
2.2 Sample of supernovae	23
2.2.1 The Calán/Tololo survey	24
2.2.2 The SOIRS survey	25
2.2.3 Other supernovae	26
2.3 Data reductions	26
2.3.1 Optical photometry	26
2.3.2 Additional optical photometry	36
2.3.3 Infrared photometry	39
2.3.4 Spectroscopy	41
2.4 Summary	45
Chapter 3 THE EXPANDING PHOTOSPHERE METHOD	83
3.1 Introduction	83
3.2 The physics of SN II light curves	83
3.3 Basic ideas of EPM	86
3.4 The measurement of angular radii	89
3.5 The determination of dust extinction in the host galaxies	95
3.6 The measurement of physical radii	101
3.7 The determination of errors	107
3.8 Results	109
3.8.1 SN 1986L	109
3.8.2 SN 1987A	114
3.8.3 SN 1988A	119
3.8.4 SN 1990E	122
3.8.5 SN 1990K	126
3.8.6 SN 1991al	129
3.8.7 SN 1992af	132

3.8.8 SN 1992am	134
3.8.9 SN 1992ba	138
3.8.10 SN 1993A	142
3.8.11 SN 1993S	145
3.8.12 SN 1999br	148
3.8.13 SN 1999ca	152
3.8.14 SN 1999cr	155
3.8.15 SN 1999eg	159
3.8.16 SN 1999em	162
3.8.17 SN 2000cb	168
3.9 Summary	172
Chapter 4 THE PERFORMANCE OF THE EXPANDING PHOTOSPHERE METHOD	231
4.1 Introduction	231
4.2 Internal precision	231
4.3 The sensitivity to dust	234
4.4 Error estimates for EPM distances	238
4.5 External comparisons	238
4.5.1 Comparison with other EPM distances	238
4.5.2 Comparison with the cosmic distance ladder	239
4.6 Future applications of the expanding photosphere method	247
4.7 Summary	250
Chapter 5 ON THE INTRINSIC PROPERTIES OF TYPE II SUPERNOVAE	256
5.1 Introduction	256
5.2 Absolute magnitudes	256
5.3 Bolometric corrections	260
5.4 Effective temperature-color relation	263
5.5 Physical analysis of the plateau phase	266
5.6 Physical analysis of the radioactive phase	273
5.7 Type II supernovae as standard candles	279
5.8 Summary	285
Chapter 6 CONCLUSIONS	290
Appendix A THE COMPUTATION OF SYNTHETIC MAGNITUDES	295
Appendix B THE Z BAND PHOTOMETRIC SYSTEM	302
REFERENCES	304

LIST OF FIGURES

Figure 2.1	V band CCD images of the 12 SNe II (part 1)	29
Figure 2.2	V band CCD images of the 12 SNe II (part 2)	30
Figure 2.3	V band CCD images of the 12 SNe II (part 3)	31
Figure 2.4	B band light curves for the 12 CT/SOIRS SNe II (part 1)	32
Figure 2.5	B band light curves for the 12 CT/SOIRS SNe II (part 2)	33
Figure 2.6	B band light curves for 5 SNe II	37
Figure 2.7	$UBVRIZJHK$ light curves of SN 1999em	40
Figure 2.8	Early-time spectra of seven SNe II	43
Figure 2.9	Spectra of 15 SNe II at day ~ 35	44
Figure 2.10	Optical/IR spectra of SN 1999em	46
Figure 3.1	$b_{\lambda}(T)$ relation for B filter	91
Figure 3.2	Color-Temperature relations	92
Figure 3.3	Dilution factors	94
Figure 3.4	$(B - V)_0$ color curve of SNe II (part 1)	96
Figure 3.5	$(B - V)_0$ color curve of SNe II (part 2)	97
Figure 3.6	$(V - I)_0$ color curve of SNe II (part 1)	99
Figure 3.7	$(V - I)_0$ color curve of SNe II (part 2)	100
Figure 3.8	Cross-correlation test	103
Figure 3.9	Example of cross-correlation	106
Figure 3.10	Expansion velocities for SN 1999em	108
Figure 3.11	Photometry and velocities for SN 1986L	111
Figure 3.12	EPM solution for SN 1986L	112
Figure 3.13	Photometry and velocities for SN 1987A	115
Figure 3.14	EPM solution for SN 1987A	116
Figure 3.15	Photometry and velocities for SN 1988A	120
Figure 3.16	EPM solution for SN 1988A	121
Figure 3.17	Photometry and velocities for SN 1990E	123
Figure 3.18	EPM solution for SN 1990E	124
Figure 3.19	Photometry and velocities for SN 1990K	127
Figure 3.20	EPM solution for SN 1990K	128
Figure 3.21	Photometry and velocities for SN 1991al	130
Figure 3.22	EPM solution for SN 1991al	131
Figure 3.23	Photometry and velocities for SN 1992af	133
Figure 3.24	Photometry and velocities for SN 1992am	135
Figure 3.25	EPM solution for SN 1992am	136
Figure 3.26	Photometry and velocities for SN 1992ba	139
Figure 3.27	EPM solution for SN 1992ba	140

Figure 3.28	Photometry and velocities for SN 1993A	143
Figure 3.29	EPM solution for SN 1993A	144
Figure 3.30	Photometry and velocities for SN 1993S	146
Figure 3.31	EPM solution for SN 1993S	147
Figure 3.32	Photometry and velocities for SN 1999br	149
Figure 3.33	EPM solution for SN 1999br	150
Figure 3.34	Photometry and velocities for SN 1999ca	153
Figure 3.35	EPM solution for SN 1999ca	154
Figure 3.36	Photometry and velocities for SN 1999cr	156
Figure 3.37	EPM solution for SN 1999cr	157
Figure 3.38	Photometry and velocities for SN 1999eg	160
Figure 3.39	EPM solution for SN 1999eg	161
Figure 3.40	Photometry and velocities for SN 1999em	163
Figure 3.41	EPM solution for SN 1999em (part 1)	164
Figure 3.42	EPM solution for SN 1999em (part 2)	165
Figure 3.43	Photometry and velocities for SN 2000cb	169
Figure 3.44	EPM solution for SN 2000cb	170
Figure 4.1	Comparison between $D(CC)$ and $D(Fe)$	235
Figure 4.2	Sensitivity of EPM to dust	237
Figure 4.3	Comparison with S94 distances	240
Figure 4.4	Hubble diagrams for six filter/velocity combinations	243
Figure 4.5	Comparison of EPM and Tully-Fisher distances	248
Figure 5.1	Absolute V light curves of SNe II (part 1)	258
Figure 5.2	Absolute V light curves of SNe II (part 2)	259
Figure 5.3	Bolometric corrections for SNe II	261
Figure 5.4	Bolometric luminosity of SN 1987A	264
Figure 5.5	Bolometric luminosity of SN 1999em	265
Figure 5.6	T_{eff} -Color relation for SNe II	267
Figure 5.7	Bolometric luminosities and effective temperatures for SNe II (part 1)	268
Figure 5.8	Bolometric luminosities and effective temperatures for SNe II (part 2)	269
Figure 5.9	Bolometric luminosities and effective temperatures for SNe II (part 3)	270
Figure 5.10	Bolometric luminosities and effective temperatures for SNe II (part 4)	271
Figure 5.11	Expansion velocities for SNe II (part 1)	274
Figure 5.12	Expansion velocities for SNe II (part 2)	275
Figure 5.13	Plateau velocities vs. plateau luminosities for SNe II	276
Figure 5.14	Distribution of ^{56}Co masses for SNe II	278
Figure 5.15	Plateau luminosity vs. M_{Co} for SNe II	280
Figure 5.16	Plateau velocities vs. M_{Co} for SNe II	281
Figure 5.17	Hubble diagram for SNe II as standard candles (V band)	283

Figure 5.18 Hubble diagram for SNe II as standard candles (<i>I</i> band)	284
Figure A.1 <i>BVRI</i> filters functions	296
Figure A.2 <i>Z, J_S, H, K_S</i> filters functions	298
Figure A.3 Adopted spectrophotometric calibration for Vega	300

LIST OF TABLES

Table 2.1	List of Type II Supernovae	47
Table 2.2	Journal of the Photometric Observations	48
Table 2.3	<i>UBVRIZ</i> Sequences	57
Table 2.4	<i>UBVRIZ</i> Photometry for 12 CT/SOIRS SNe II	63
Table 2.5	Journal of the Spectroscopic Observations	76
Table 3.1	Fits to $b_{\bar{\lambda}}(T, z = 0)^a$	173
Table 3.2	Fits to $\zeta(T_S)^a$	174
Table 3.3	Adopted Host Galaxy Reddenings	175
Table 3.4	Expansion Velocities of SN 1986L	176
Table 3.5	EPM Quantities Derived for SN 1986L	177
Table 3.6	EPM Solutions for SN 1986L	179
Table 3.7	Expansion Velocities of SN 1987A	180
Table 3.8	EPM Quantities Derived for SN 1987A	183
Table 3.9	EPM Solutions for SN 1987A	187
Table 3.10	Expansion Velocities of SN 1988A	188
Table 3.11	EPM Quantities Derived for SN 1988A	189
Table 3.12	EPM Solutions for SN 1988A	190
Table 3.13	Expansion Velocities of SN 1990E	191
Table 3.14	EPM Quantities Derived for SN 1990E	192
Table 3.15	EPM Solutions for SN 1990E	193
Table 3.16	Expansion Velocities of SN 1990K	194
Table 3.17	EPM Quantities Derived for SN 1990K	195
Table 3.18	Expansion Velocities of SN 1991al	196
Table 3.19	EPM Quantities Derived for SN 1991al	197
Table 3.20	Expansion Velocities of SN 1992af	198
Table 3.21	EPM Quantities Derived for SN 1992af	199
Table 3.22	Expansion Velocities of SN 1992am	200
Table 3.23	EPM Quantities Derived for SN 1992am	201
Table 3.24	EPM Solutions for SN 1992am	202
Table 3.25	Expansion Velocities of SN 1992ba	203
Table 3.26	EPM Quantities Derived for SN 1992ba	204
Table 3.27	EPM Solutions for SN 1992ba	205
Table 3.28	Expansion Velocities of SN 1993A	206
Table 3.29	EPM Quantities Derived for SN 1993A	207
Table 3.30	EPM Solutions for SN 1993A	208
Table 3.31	Expansion Velocities of SN 1993S	209
Table 3.32	EPM Quantities Derived for SN 1993S	210

Table 3.33	Expansion Velocities of SN 1999br	211
Table 3.34	EPM Quantities Derived for SN 1999br	212
Table 3.35	EPM Solutions for SN 1999br	214
Table 3.36	Expansion Velocities of SN 1999ca	215
Table 3.37	EPM Quantities Derived for SN 1999ca	216
Table 3.38	Expansion Velocities of SN 1999cr	217
Table 3.39	EPM Quantities Derived for SN 1999cr	218
Table 3.40	EPM Solutions for SN 1999cr	220
Table 3.41	Expansion Velocities of SN 1999eg	221
Table 3.42	EPM Quantities Derived for SN 1999eg	222
Table 3.43	EPM Solutions for SN 1999eg	223
Table 3.44	Expansion Velocities of SN 1999em	224
Table 3.45	EPM Quantities Derived for SN 1999em	225
Table 3.46	EPM Solutions for SN 1999em	227
Table 3.47	Expansion Velocities of SN 2000cb	228
Table 3.48	EPM Quantities Derived for SN 2000cb	229
Table 3.49	EPM Solutions for SN 2000cb	230
Table 4.1	Summary of EPM distances	251
Table 4.2	Distances from Other Sources	255
Table 5.1	Fits to BC(color) ^a	286
Table 5.2	Fits to T_{eff} (color) ^a	287
Table 5.3	Physical Parameters for Type II SNe	288
Table 5.4	Plateau V/I magnitudes for Type II SNe	289
Table A.1	Photometric Zero points and Synthetic Magnitudes for Vega	301
Table B.1	Standard Stars for the Z band	303

ABSTRACT

I report photometry and spectroscopy for 16 Type II supernovae (SNe) observed during the Calán/Tololo, SOIRS, and CTIO SN programs, a valuable resource for astrophysical studies.

I perform a detailed assessment of the performance of the “expanding photosphere method” (EPM) in the determination of extragalactic distances. EPM proves very sensitive to the many steps involved in the analysis which can make it an art instead of an objective measurement tool. To minimize biases I implement objective procedures to compute synthetic magnitudes, measure true photospheric velocities, interpolate velocities, estimate dust extinction and realistic errors. While EPM performs well during the initial phases of SN evolution, I find distance residuals as large as 50% as the photosphere approaches the H recombination temperature. Despite the effort to lend credence to EPM, it proves necessary to exercise great care to avoid biasing the results. The main sources of uncertainties are observational errors (8%), dilution factors (11%), velocity interpolations (12%), and dust extinction (14%). The EPM Hubble diagram suggests the true error in an individual EPM distance is 20%. I find values of 63 ± 8 and 67 ± 7 $\text{km s}^{-1} \text{Mpc}^{-1}$ for the Hubble constant, depending on the redshift sample chosen for the analysis. This result is independent of the extragalactic distance scale which yields 65 ± 5 from Cepheid/SNe Ia distances. From four objects the comparison of EPM and Tully-Fisher yields $D(\text{EPM})/D(\text{TF}) = 0.82 \pm 0.12$.

I derive bolometric corrections for plateau SNe (SNe II-P) that permit me to obtain reliable bolometric luminosities from *BVI* photometry. Despite the great diversity displayed by SNe II-P, the duration of the plateau is approximately the same and the luminosities and expansion velocities measured in the middle of the plateau prove highly correlated. From the luminosity of the exponential tail I obtain ^{56}Co masses ranging between

0.02 and 0.28 M_{\odot} , and some evidence that SNe with brighter plateaus produce more Ni (and its daughter Co). The correlation between expansion velocity and luminosity permits me the use of SNe II-P as standard candles with a magnitude dispersion between 0.39-0.20 mag. Using SN 1987A to calibrate the Hubble diagram I get $H_0=55\pm12$ and $H_0=56\pm9$ from the V and I filters, respectively.

CHAPTER 1 INTRODUCTION

1.1 Historical background

In AD 1054, Chinese astronomers witnessed and recorded the appearance of a new star in the constellation Taurus. With a maximum apparent magnitude of -4 (the brightness of Venus), the “guest star” outshined many of the bright stars for about six months and remained visible for a longer period of time until fading from visibility. In 1572 another “guest star” was discovered by Tycho Brahe in the constellation Cassiopeia. A few years later, in 1604 (only six years before the invention of the telescope) Johannes Kepler reported observations of a new bright star in the sky.

The occurrence of this phenomenon became more familiar to astronomers as of the end of the 19th century, with the beginning of the use of photographic plates in astronomy. The first of such objects was discovered by E. Hartwig in the Andromeda “nebula” in 1885. The object reached 7th magnitude and could be observed only with the help of a telescope. With the beginning of systematic surveys the number of “new” stars increased in rapid succession. Astronomers came up with the generic name “nova” to designate this class of objects. By 1927 ~100 novae had been discovered in the magnitude range 16-18. All of these objects were found to be spatially associated to the nebulae, the extended and diffuse objects whose distance and nature was still unknown.

It was not until the recognition that the nebulae that hosted the novae were enormous stellar systems located at great distances outside the Milky Way, that astronomers realized that the luminosity of novae largely exceeded that of the brightest known stars. With a

rapidly growing body of data, it became evident that the class comprised two types of objects differing by their widely different luminosities and discovery frequencies (Baade, 1938; Zwicky, 1938). The brightest of them were designated “supernovae”, while the fainter and common events kept the original designation.

Minkowski (1941) noted that the spectra of supernovae (SNe, hereafter) indicated at least two radically different types of objects. The Type I class was characterized by broad emission features and no clear signs of H in the spectrum, while the Type II group consisted of spectra dominated by strong broad Balmer emission lines. The notable blueshift displayed by the H lines suggested that the emission arose in material ejected at great speed. Except for the Balmer lines the identification of other spectral features was seriously hampered by their Doppler broadening and the superposition of the different lines. It was not until the early 1980s that definite line identifications could be established from synthetic spectra constructed from a thermal continuum and superimposed P-Cygni profiles (emissions and blueshifted absorptions) of low-excitation ions [see Branch (1990) for a historical review]. As the body of spectroscopic data grew, by the mid 1980s it became obvious that the Type I group could be further differentiated according to the presence of the Si $\lambda 6355$ line. If the spectrum showed a strong Si line near maximum light the SN was assigned to the Ia group; otherwise it was designated as a Ib or Ic depending on the presence or absence of He I $\lambda 5876$ in the spectrum, respectively (Harkness & Wheeler, 1990).

1.2 Supernova models

As early as 1934, Baade and Zwicky suggested that SNe were caused by the transformation of ordinary stars into collapsed neutron stars (Baade, 1934; Zwicky, 1935). Although this idea is remarkably consistent with current models of Type II SNe, observations of Type I SNe resisted interpretation for a long time. Another critical piece of information

about the nature of these objects was provided by the stellar environments where they were discovered. While Type II's, Ib's, and Ic's are only observed near star formation regions in late-type galaxies, Ia's occur both in elliptical and spiral galaxies and are not associated to young stellar environments.

The current belief is that the objects in the first group are due to young massive stars with $M_{ZAMS} > 8M_{\odot}$ that explode after a few million years of evolution (M_{ZAMS} is the mass of the star on the zero age main sequence). At the end of their lives they end up with an iron core which grows to the Chandrasekhar mass near $1.4 M_{\odot}$. At this point the pressure provided by the electrons becomes insufficient to balance gravity and the core becomes condemned to gravitational collapse. This catastrophe is followed by the explosion of the star's envelope, presumably due to heat deposited by the neutrinos created in the center [see Burrows (2000) for a review about the explosion mechanisms]. These objects are thus referred to as "core collapse" SNe. The spectral differences among this family are thought to be due to the relative ability of the SN progenitors to retain their outermost envelopes of unprocessed hydrogen or helium. In this scenario, Type II's are possibly the least massive progenitors which keep a significant fraction of their unprocessed H layers, Type Ib's and Ic's are those massive stars that lose their H due to strong stellar winds or transfer to a binary companion. In all these cases, the outcome of the SN is a neutron star (or a black hole if the central mass exceeds $3 M_{\odot}$) surrounded by a rapidly expanding ($\sim 10^4 \text{ km s}^{-1}$) ejecta that "contaminates" the interstellar medium with the heavy metals (mostly α -nuclei) synthesized by the SN progenitor in its interior over its lifetime. This enriched material then leads to a new generation of stars relatively richer in metals which continue the cycle of chemical enrichment of their host galaxies.

Type Ia SNe, on the other hand, are a very different class of explosions. Their lack of H and their occurrence in older stellar populations are explained as due to stars with $M_{ZAMS} < 8M_{\odot}$ which end up their lives as carbon-oxygen white dwarfs (WDs) with

masses below the Chandrasekhar limit (typically $0.6 M_{\odot}$). Most of these WDs die in isolation, slowly releasing their internal heat for billions of years, without producing a supernova. However, a small fraction of these stars have binary companions that transfer matter to the WDs. As a result of the mass transfer the WD grows in mass and contracts. As it approaches the Chandrasekhar limit the compression and heating quickly increase, eventually reaching the point where the C/O material is ignited. Under the degenerate conditions of the WD material the burning is explosive and quickly encompasses the whole star. In this process the entire star is disrupted and the freshly cooked atoms (mostly iron-peak and intermediate-mass elements) are expelled at great velocities to the interstellar medium leaving no compact object (neutron star or black hole) at its center.

1.3 Supernovae as distance indicators

SNe have long been considered attractive cosmological probes, ever since Baade (1938) recognized their high intrinsic luminosities. In particular, astronomers have devoted significant effort in the past decades to the use of SNe as distance indicators, with the hope to test cosmological models via the distance-redshift relationship. This classical test was first used with Cepheid distances by E. Hubble in 1929 to demonstrate that the Universe is expanding. The first application of SNe to the estimate of extragalactic distances was performed by Kowal (1968) from the blue peak luminosities of a sample of SNe I in the Hubble flow, well before the Ib/Ic subclasses were recognized. This study revealed a moderate scatter of 0.6 mag in the Hubble diagram and the great potential of these objects as standard candles. The Hubble diagram was later re-established using genuine Ia events (Leibundgut, 1990; van den Bergh & Pazder, 1992; Sandage & Tammann, 1993), which yielded a scatter in the SN peak magnitudes of 0.3-0.5 mag.

The last decade witnessed significant progress in and improvements to the precision and accuracy of the methods used to derive distances from SNe Ia. The discovery in 1993

of the correlation between the SN absolute peak luminosity and the width of the light curve showed that the precision of the method could be improved significantly (Phillips, 1993). The systematic survey of SNe carried out by astronomers of the Cerro Tololo Inter-American Observatory (CTIO) and the University of Chile at Cerro Calán between 1990-1993 permitted us to enlarge the sample of SNe Ia, obtain high-quality CCD follow-up photometry, and extend the Hubble diagram to redshifts of 0.1 (Hamuy et al., 1995, 1996). The launch of the Hubble Space Telescope (*HST*) provided a precise calibration of the SN peak magnitudes through the observation of Cepheid variables in nearby ($D \leq 25$ Mpc) galaxies (Saha et al., 1999), thus allowing us to narrow the value of the Hubble constant to between $60\text{-}70 \text{ km s}^{-1} \text{ Mpc}^{-1}$ (Hamuy et al., 1996; Saha et al., 1999; Gibson et al., 2000).

The application of the Phillips relationship to the Calán/Tololo sample of 30 SNe revealed that the scatter of the Hubble diagram was remarkably low (~ 0.15 mag in distance modulus, or 7% in distance) and demonstrated that the precision yielded by this method exceeded that of all other secondary distance indicators. This result laid the foundations that enabled the measurement of the elusive cosmological parameters that determine the global properties of the Universe. Recently, two groups of astronomers applied this method to distant SNe Ia. By comparing the distances to high- z SNe Ia with those in the Calán/Tololo sample, these groups independently reported a remarkable finding: contrary to expectations, the expansion of the Universe is accelerating (Riess et al., 1998; Perlmutter et al., 1999). In the frame of general relativity these observations imply a non-zero cosmological constant that dominates the total energy content of the Universe, a result entirely unanticipated by modern physics.

By contrast to SNe Ia, Type II SNe display a wide range (~ 2 mag) in peak luminosities making them useless as standard candles. Nevertheless, because SNe II possess nearly blackbody atmospheres it is possible to use their observed fluxes and temperatures

to derive their angular sizes which, in combination with the physical radii derived from spectroscopic observations, affords the possibility of estimating distances. This technique is known as the “Baade-Wesselink method” (also “expanding photosphere method”, EPM hereafter). It was initially applied to Cepheid variables by Baade (1926). Following upon a suggestion by L. Searle, Kirshner & Kwan (1974) first applied this method to SNe II, assuming that SNe II emitted like perfect blackbodies. More recently, Schmidt et al. (1992) (SKE92, hereafter) refined the method by incorporating distance correction factors (a.k.a. “dilution factor” and denoted by ζ) that account for the departure of the SN atmosphere from a blackbody. Their approach consisted in deriving empirical temperature-dependent dilution factors from SN 1987A and applying them to nine nearby SNe, from which they derived a value of the Hubble constant of $60 \text{ km s}^{-1} \text{ Mpc}^{-1}$. In a subsequent paper Schmidt et al. (1994b) (S94, hereafter) used theoretical dilution factors computed by Eastman et al. (1996) (see below) and high-quality data obtained at CTIO, in order to extend the Hubble diagram to $z=0.05$. From 16 SNe they found that EPM distances average 12% higher than Tully-Fisher distances. Their Hubble diagram yielded a value of $H_0=73 \text{ km s}^{-1} \text{ Mpc}^{-1}$ and a scatter that implied an average uncertainty of 10% in the EPM distances.

A major step forward in the knowledge of the dilution factors was achieved by Eastman et al. (1996) (E96, hereafter) from detailed NLTE models of SNe II-P encompassing a wide range in luminosity, density structure, velocity, and composition. They found that the most important variable determining ζ was the effective temperature; for a given temperature, ζ changed by only 5-10% over a very large variation in the other parameters. This result implied that EPM has the potential to measure accurate distances without the need for a specially-crafted model for each SN. The relatively small scatter in the Hubble diagram established by S94 provided strong support to the E96 claim, offering thus the possibility to apply EPM to high- z objects and obtain a determination of the cosmological

parameters completely independent from the results yielded by SNe Ia (S94).

1.4 Goals of this dissertation

The accelerating Universe deduced from observations of SNe Ia is very interesting as it provides evidence of new physics in the Universe – a “dark energy” component to the energy density of space. This is a remarkable result which, if confirmed, would constitute a revolution in astrophysics. Although the result derived from SNe Ia is based on dozens of objects that permit the lowering of the statistical errors to significant levels, the reality of this conclusion is threatened by systematic errors. Before we can fully believe in this finding an independent check is required, and SNe II offer the promise of providing such check, as long as we could demonstrate that the precision and accuracy in the distance estimates could be lowered to levels that permit us to discriminate between different cosmological models.

Although the S94 study showed the usefulness of EPM in the determination of extragalactic distances, their conclusions were hampered by: 1) the low-quality photographic photometry; 2) sparse observations for some of the SNe of their sample; and 3) the fact that only four of the 16 SNe were sufficiently distant as to be out in the cosmic flow ($cz > 2000 \text{ km s}^{-1}$). All these problems made it difficult to assess the actual performance of EPM. One of the goals of this dissertation is the study of the performance of EPM from a sample of 17 SNe II well-observed in the course of the Calán/Tololo survey and the recent “Supernova Optical and Infrared Survey” (SOIRS), 11 of which have $cz > 2000 \text{ km s}^{-1}$. This dataset will allow me to quantify the actual uncertainties of EPM from the scatter of the SNe relative to a model Hubble flow. If I can demonstrate that EPM can produce distances with a precision and accuracy of 10% or better, the next logical step is to apply the method to high- z SNe in order to measure cosmological parameters. Otherwise, future studies should focus on nearby SNe and more detailed atmosphere models

in order to refine the method.

Besides their importance as distance indicators, SNe are of great astrophysical interest due to their central role in the evolution of galaxies, not only through the chemical enrichment but also by the heating and shaping of the galaxies themselves. This database of 17 SNe II affords a great opportunity to measure intrinsic properties and extract physical parameters for these objects. The next goal of this dissertation is to examine our photometric/spectroscopic dataset, with the aim to find empirical constraints and gain physical insight about the explosion mechanisms and the properties of the SN progenitors.

This dissertation is organized as follows. In Chapter 2 I present the sample of SNe used in this study, the photometric and spectroscopic follow-up observations gathered for these objects, and the reduction procedures employed in the extraction of useful information from the raw data. In Chapter 3 I explain the basic ideas behind EPM and the methods adopted to estimate photometric angular radii, spectroscopic physical radii, and dust extinction in the SN host galaxies. I include also a detailed report on the EPM results for the 17 SNe of our sample, on a SN-to-SN basis. In Chapter 4 I discuss in detail the performance of EPM, its advantages and limitations, and the prospects of using the method for high-precision cosmology. In Chapter 5 I explain the method used to compute bolometric corrections to SNe II which I then employ to get bolometric light curves and intrinsic parameters for my SN sample. Finally, in Chapter 6 I summarize the main conclusions of this study. In Appendix A I describe the details of computing the synthetic magnitudes required by EPM. In Appendix B I define the Z photometric system and I list magnitudes for the standards that I used in our observations.

CHAPTER 2 OBSERVATIONS AND REDUCTIONS

2.1 Introduction

In this chapter I present the sample of 17 SNe included in this study. I describe their origin and the follow-up observations gathered for them. Then I explain the reduction procedures applied to the data, which involve a careful subtraction of the galaxy from the SN images. I demonstrate that if this correction is ignored, significant biases can occur in the derived colors and magnitudes. Since EPM involves measuring a photometric angular radius this correction can have a significant impact on the derived EPM distances. Although most of the photometry reported in this section is limited to the BVI bands, I report some photometry at longer wavelengths ($ZJHK$) in order to test the EPM method over a broader wavelength region.

2.2 Sample of supernovae

The objects of my sample come from a variety of sources. A complete listing of these SNe II is found in Table 2.1 which gives: the SN and host galaxy names [as given in the NASA/IPAC Extragalactic Database (NED)]; the heliocentric redshift of the host galaxy (either taken from NED or from our own spectroscopic observations); the line-of-sight extinction due to our own Galaxy (Schlegel et al., 1998); the SN equatorial coordinates (taken from NED); the name of the survey and discoverer; and the UT discovery date.

2.2.1 The Calán/Tololo survey

Six objects of my sample come from the Calán/Tololo (CT, hereafter) program that was described in detail by Hamuy et al. (1993). In summary, I initiated the CT project in collaboration with astronomers of CTIO and the University of Chile with the specific goal to study the usefulness of SNe as distance indicators. The search phase consisted of photographic observations of 45 fields taken with the CTIO Curtis Schmidt Camera (60/90 cm), with observations carried out approximately twice a month over the 1990-93 period. The Schmidt telescope had a scale of $96.6 \text{ arcsec mm}^{-1}$, which provided a useful sky coverage of $5^\circ \times 5^\circ$ when used with photographic plates. We employed unfiltered IIa-O plates which, in 20 min exposures, yielded a limiting magnitude of ~ 19 . The search produced 50 new SNe in the redshift range $0.01 \lesssim z \lesssim 0.1$. Of these, 30 proved to be members of the Ia class and the analysis of the data has been extensively discussed in the literature (Hamuy et al., 1996). Of the remaining objects, 15 proved to be Type II SNe, five of which had sufficient data for an EPM analysis, namely, SNe 1991al, 1992af, 1992am, 1993A, 1993S. The redshift range for these objects was $0.015 \lesssim z \lesssim 0.045$. In the course of the CT follow-up program we included the Type II SN 1992ba discovered as part of the Rev. Evans survey, which is also listed in Table 2.1.

The follow-up phase of the CT survey consisted of optical spectroscopy and $BV(RI)_{KC}$ CCD imaging. We obtained spectra with the Cassegrain spectrographs available on the CTIO 1.5-m and 4.0-m telescopes, with a variety of gratings, filters, and CCDs providing different spectral coverages from 3200 to 10000 Å. Typically, we got blue (3000-7000 Å) and/or red (5000-10000 Å) spectra. For the red setup we included a OG530 filter to avoid second-order contamination beyond ~ 6600 Å. The resulting spectra had typical dispersions of 3 \AA pix^{-1} on the 4.0-m and 8 \AA pix^{-1} on the 1.5-m telescope. The observations started with calibrations during day time (bias and dome flat-field exposures). The night began with the observation of a spectrophotometric standard [from

the list of Hamuy et al. (1994a)] through a wide slit of 10-20 arcsec, after which we observed the SN with a narrow slit of 1-3 arcsec. We took two exposures per spectral setup, in order to eliminate cosmic rays. Immediately following this observation we observed a He-Ar lamp, at the same position of the SN. We observed several additional flux standards during the night.

We measured light curves from a large number of CCD images obtained with different telescopes under all kind of weather conditions, thanks to the generous collaboration of many CTIO visiting astronomers and staff members. We took the vast majority of the observations (90%) with the 0.9-m telescope, with the remainder coming from the 1.5-m and 4.0-m telescopes. We employed a variety of (TI, TEK, and Thomson) chips with filter sets designed to match the $BV(RI)_{KC}$ system. We observed photometric standards of the list of Landolt (1992) during clear nights, in order to solve for extinction and transformation coefficients to the standard system.

2.2.2 The SOIRS survey

Given the rapid technological development of infrared (IR) light detection over recent years, in 1999-2000 I carried out a program – in collaboration with astronomers from CTIO, Las Campanas and Cerro Calán, and Steward observatory – to obtain optical and IR photometry and spectroscopy of nearby SNe ($z < 0.08$).

The “Supernova Optical and Infrared Survey” (SOIRS) used the Cerro El Roble Maksutov camera of the University of Chile for a photographic search, very much like the CT search (Maza et al., 1981). Also, we coordinated the photographic search with the Nearby Galaxies Supernova Survey (NGSS) carried out with the Kitt Peak 0.9-m telescope and the wide field mosaic CCD array, which discovers SNe down to a limiting magnitude of $R \sim 21$ ($z < 0.15$) (Ströger et al., 1999).

The follow-up observations comprised $UBVRIZJHK$ photometry and spectroscopy involving telescopes at CTIO, the Carnegie Institution of Washington at Las Campanas

Observatory (LCO), the European Southern Observatory (ESO) at La Silla and Cerro Paranal, and the Steward Observatory (SO) of The University of Arizona. Besides the objects discovered by the SOIRS program, we also included in the list of follow-up targets SNe found at other observatories and reported to the IAU Circulars. We obtained optical photometry and spectroscopy with the same procedure described above for the CT survey. The observing/reductions techniques in the IR observations were more involved than in the optical due to the high sky brightness at these wavelengths. Detailed descriptions of the procedures can be found in Hamuy et al. (2001) and Suntzeff et al. (2001).

In the course of 1999-2000 the SOIRS program gathered high-quality observations for \sim 20 SNe, six of which proved to belong to the Type II class (SNe 1999br, 1999ca, 1999cr, 1999eg, 1999em, and 2000cb), which are listed in Table 2.1.

2.2.3 Other supernovae

Besides the 12 CT and SOIRS SNe mentioned above, I include five Type II SNe in Table 2.1 for which I have spectra available for the EPM analysis. SN 1986L was extensively observed at CTIO by M. Phillips and S. Kirhakos, who have generously made me available their unpublished BV photometry and large spectroscopic database. SN 1987A is the best observed SN II, with large amounts of optical/IR photometry available in the literature. The catalogue of optical spectra established at CTIO (Phillips et al., 1988) is readily available in electronic form in the CTIO/KPNO web site. SNe 1988A, 1990E, and 1990K have published photometry, and several unpublished spectra that the CTIO group obtained with the 1.5-m and 4.0-m telescopes, which are also available to me.

2.3 Data reductions

2.3.1 Optical photometry

We obtained optical photometry for the 12 CT/SOIRS SNe on a total of 205 nights between 1991 July 18 and 2000 September 8. A complete journal of the observations is

given in Table 2.2 which contains the following information: the UT date, the telescope employed, the observatory, the list of SNe observed, and the name of the observer(s). This table shows that, while the CT survey produced only $BV(RI)_{KC}$ photometry, the SOIRS program expanded this wavelength range and yielded data through the U filter for four SNe, and the Z band for three objects, thus offering the possibility to test EPM over a broader wavelength range. I performed all of the data reductions using IRAF¹ according to the following procedure:

1. Galaxy subtraction: The extraction of a SN magnitude is generally hampered by the uneven background upon which the object is projected. To get around this problem deep CCD images (in each color) of the SN field were obtained after the SN had faded from detection. I performed a geometric transformation of these host galaxy “template” images, degraded them in image quality, and scaled them in flux, in order to match the geometric scale, point spread function (PSF), and flux of each individual SN image. Then I subtracted the transformed template from the SN image to produce a galaxy subtracted SN image [for more details see Hamuy et al. (1994b)]. Note that in three cases (SNe 1999eg, 1999em, and 2000cb) I could not perform the galaxy subtraction due to the lack of template images. Given that these objects were relatively bright compared to their underlying backgrounds, the systematic errors due to the galaxy background should be small. In our experience this error should be ≤ 0.03 mag.
2. Magnitude extraction: I measured instrumental magnitudes of the SN and several field local standard stars from the galaxy-subtracted images via PSF fitting when the SN was faint (using the ‘daophot’ package), or simple aperture photometry when the object was bright (using the ‘phot’ package). I subtracted the local sky from an

¹IRAF is distributed by the National Optical Astronomy Observatories, which are operated by the Association of Universities for Research in Astronomy, Inc., under cooperative agreement with the National Science Foundation.

annulus around the SN, located typically 5-7 arcsec from the SN. The seeing was typically 1-2 arcsec and always ≤ 3 arcsec so this sample should not be affected by light from the SN.

3. Transformation to the standard system: I performed a linear transformation of the instrumental magnitudes to the standard $UBV(RI)_{KC}$ system through the use of a photometric sequence set up in the same field surrounding the SN [see Hamuy et al. (1993) for further details of the exact photometric transformations employed]. The photometric sequences for the 12 SNe included in the CT/SOIRS photometric follow-up are identified in the finding charts in Figures 2.1, 2.2, and 2.3. The magnitudes for the photometric sequences are listed in Table 2.3 along with the standard error of the mean (in units of mmag) and the number of nights on which each star was observed in the V filter. In every case, I derived these sequences from observations of Landolt standards. This table includes also Z magnitudes for three photometric sequences, each of them measured on one photometric night relative to the Z band standards listed in Appendix B. This band is defined in Appendix A and is centered around 8700 Å.

Table 2.4 lists the final reduced photometry for each SN. The uncertainties correspond to the photon Poisson statistics in each individual observation. I adopted a minimum error of 0.015 mag, which is typical for a single observation of the Landolt standards with CCD detectors. Please note that this table includes a very small subset of the photometry for SN 1999em since the rest of the data will be published separately by Suntzeff et al. (2001). Figures 2.4 and 2.5 shows the B light curves of the 12 CT/SOIRS SNe (for clarity I do not include the light curves in the other bands).

Barbon et al. (1979) divided SNe II into two main subclasses according to their photometric behavior in blue light. They found that the majority of SNe II belong to the “plateau” (SNe II-P) or the “linear” (SNe II-L) class. Their template light curve for

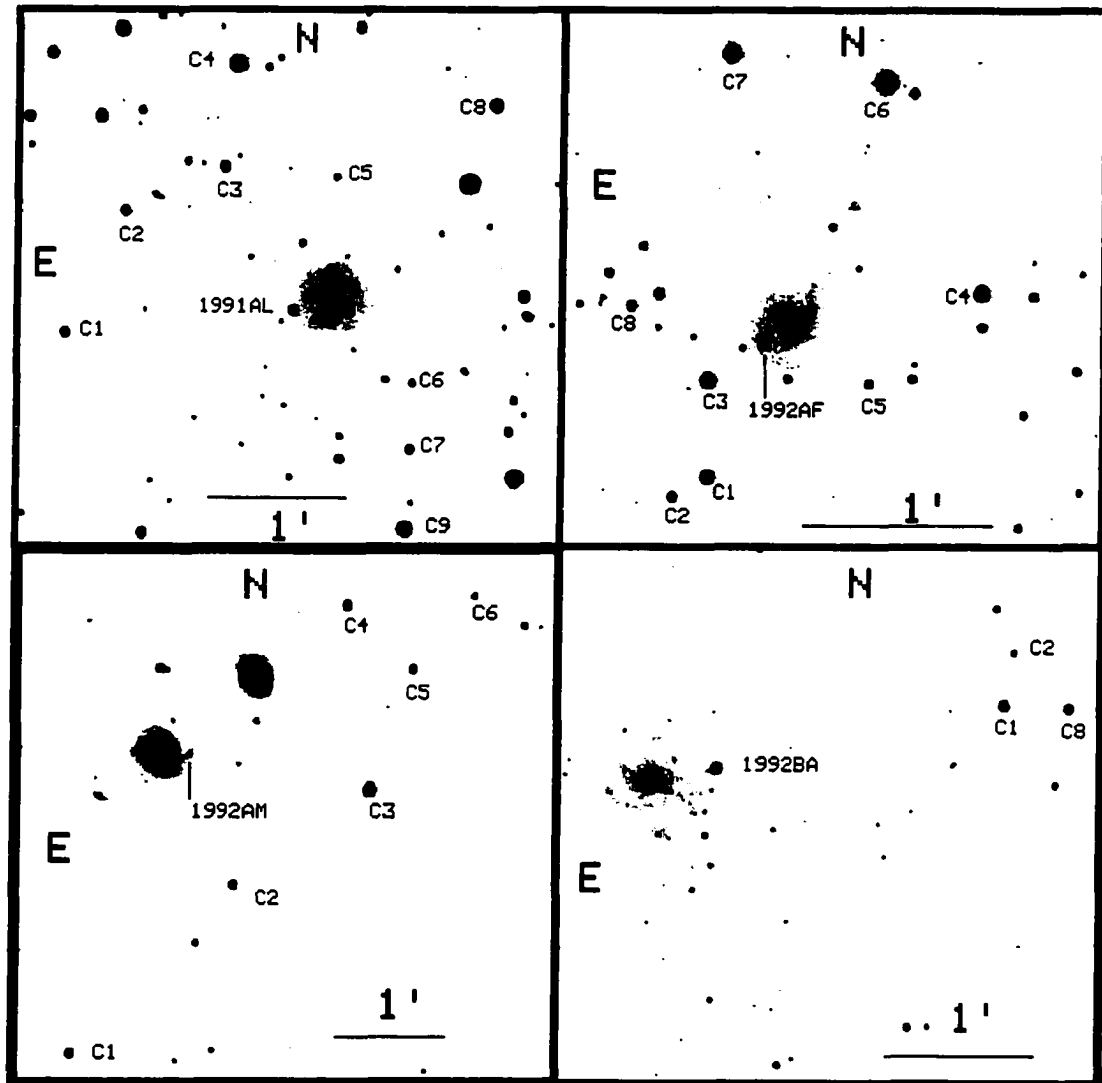


Figure 2.1: V band CCD images of the 12 SNe II included in the CT/SOIRS photometric follow-up (part 1). The photometric stars are labeled along with the SNe.

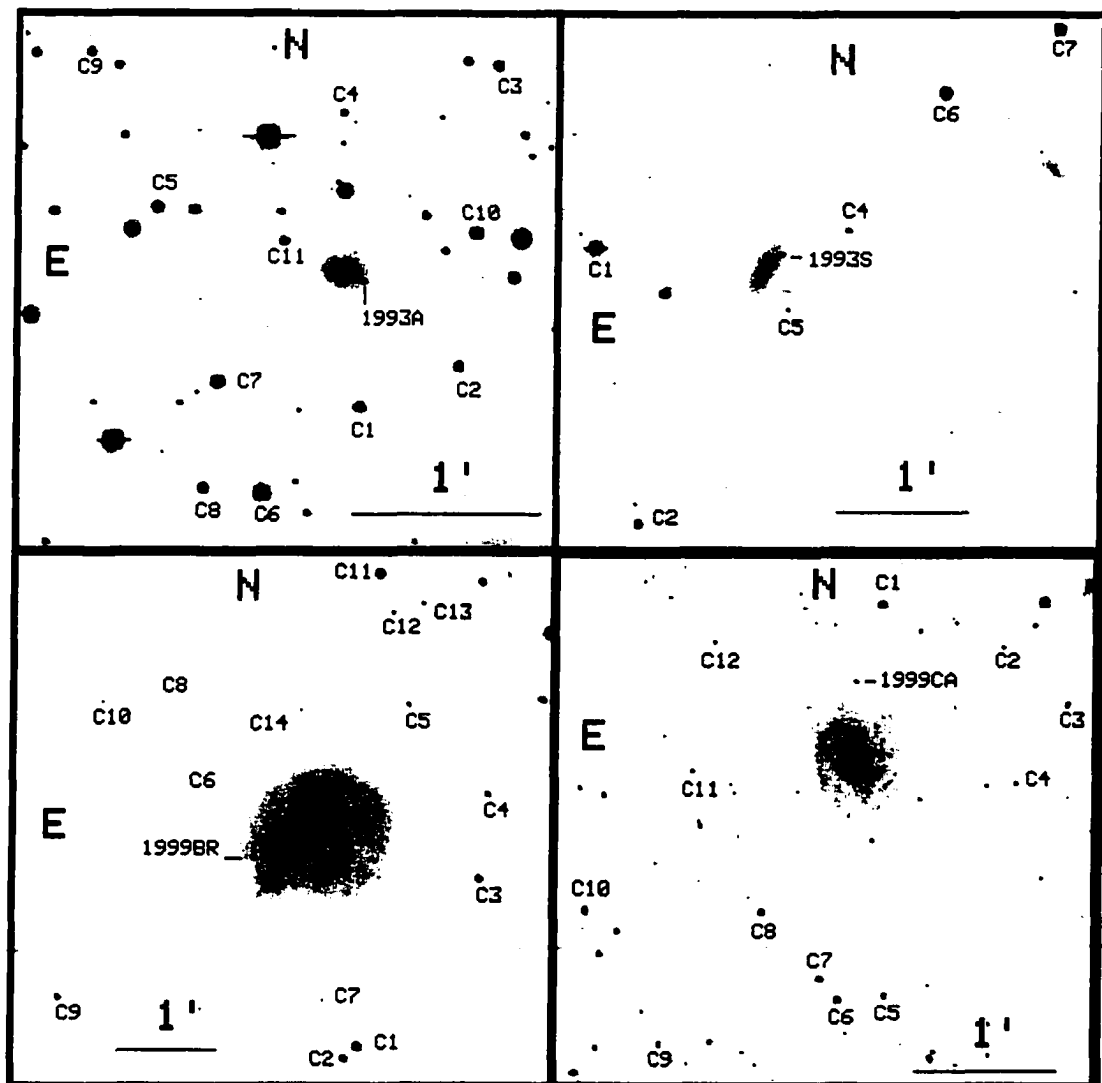


Figure 2.2: V band CCD images of the 12 SNe II included in the CT/SOIRS photometric follow-up (part 2). The photometric stars are labeled along with the SNe.

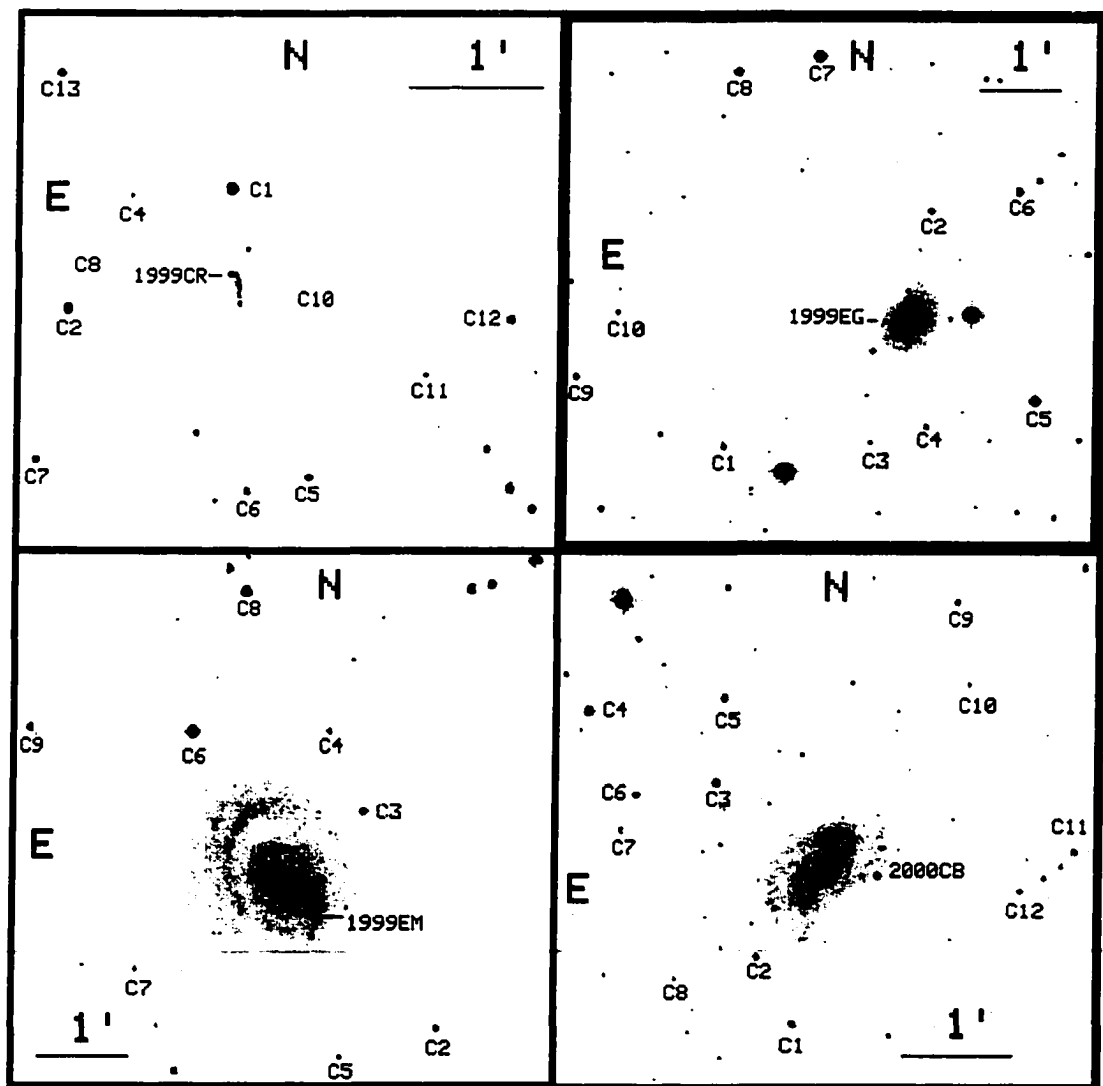


Figure 2.3: V band CCD images of the 12 SNe II included in the CT/SOIRS photometric follow-up (part 3). The photometric stars are labeled along with the SNe.

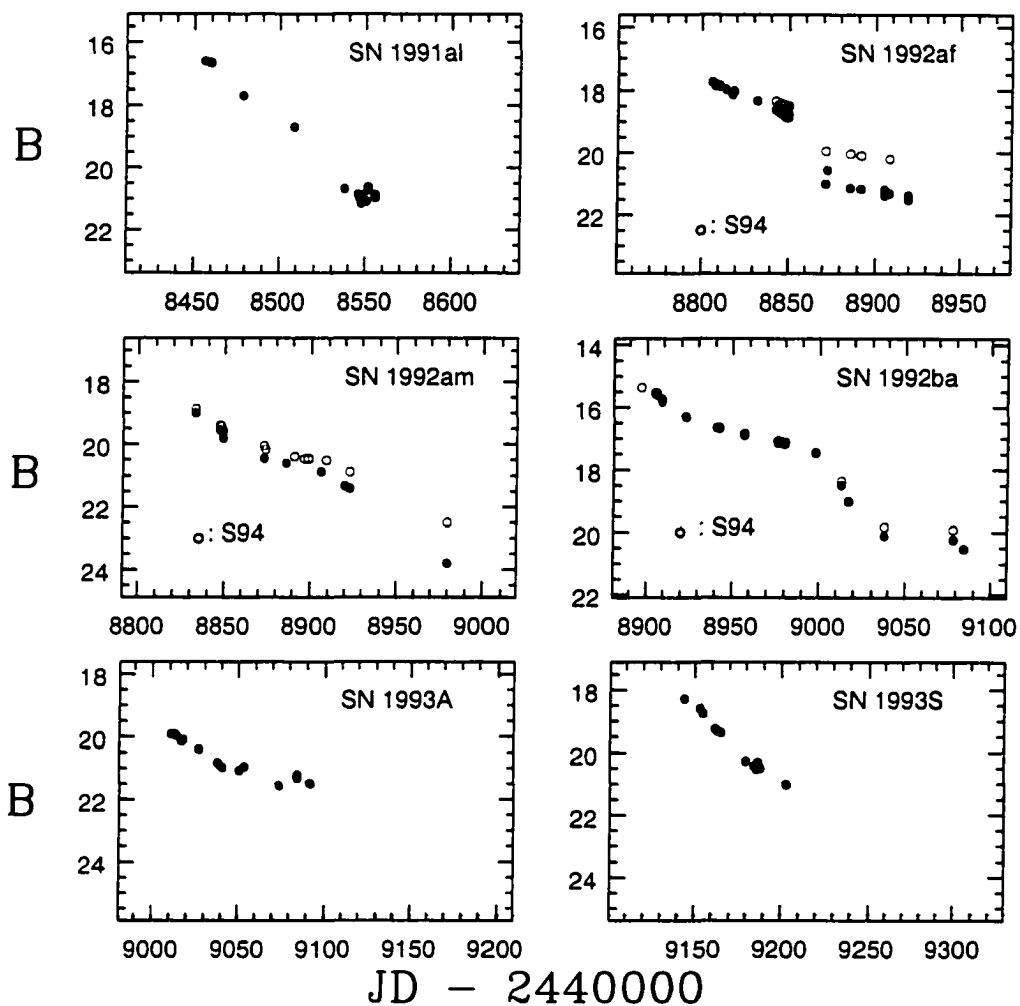


Figure 2.4: *B* band light curves for the 12 CT/SOIRS SNe II (part 2). In all cases the solid dots correspond to the photometry listed in Table 2.4. With open circles are shown, for comparison, photometry by Schmidt et al. (1994a) and Schmidt et al. (1994b).

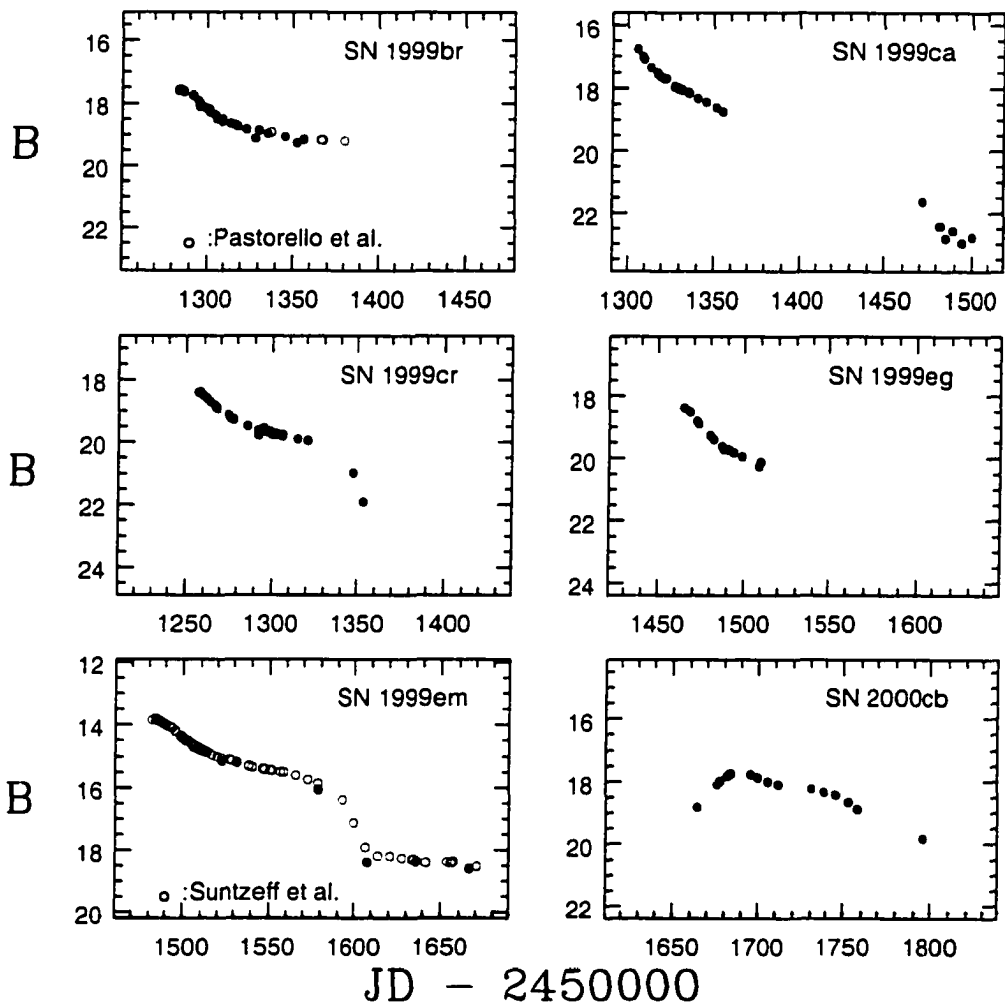


Figure 2.5: *B* band light curves for the 12 CT/SOIRS SNe II (part 2). In all cases the solid dots correspond to the photometry listed in Table 2.4. With open circles are shown, for comparison, photometry by Pastorello et al. (2001), and Suntzeff et al. (2001).

SNe II-P consists of a rapid decline of 1.2 mag during 30-35 days, a plateau phase of nearly constant or slowly-decreasing brightness lasting 50 days, a second brief (~ 10 days) drop of ~ 2.5 mag, and an exponential tail with a decline rate of $0.006 \text{ mag day}^{-1}$. SNe II-L, on the other hand, are characterized by a post-maximum decline during 100 days at a rate of $0.05 \text{ mag day}^{-1}$. In the Barbon et al. sample 2/3 of the objects belong to the SNe II-P group and only 1/5 of the SNe fall in the SNe II-L class. Theoretical modeling of SNe II light curves reveals that SNe II-P are produced by progenitors with massive H envelopes ($< 10 M_{\odot}$), whereas SNe II-L have low mass H mantles ($> 2 M_{\odot}$) (see Chapter 3 for further details).

EPM is currently implemented with dilution factors computed for SNe II-P, so it proves necessary to review the light curve morphology of every object of this sample. Based on the photometric classification of Barbon et al. (1979), an inspection of figures 2.4 and 2.5 reveals the following:

- SN 1991al showed a plateau which is not very evident in blue light, yet quite obvious in the V^* band.
- SN 1992af showed the plateau, a hint of the sudden drop, and the exponential tail, making it a SN II-P. Also shown in Figure 2.4 with open circles is the photometry by Schmidt et al. (1994b) which was obtained from the same CT images that I employed for my measurements, but with a different galaxy subtraction scheme. Their approach consisted in a simple linear interpolation of the galaxy light from nearby pixels to the SN position. Although this technique should work well for slowly varying backgrounds, it can fail to eliminate light from a compact HII region from the SN aperture. This is probably the cause for the systematic difference between both datasets. This example shows the clear advantage of galaxy subtraction in photometric measurements, especially when SNe are at their faint phases.

- SN 1992am displayed a well-defined plateau between JD 2448830-2448930 and a clear drop of ~ 2 mag between JD 2448930-2448980. Schmidt et al. (1994a) published photometry for this object from the CT images, without subtracting a galaxy template from the SN images. Their photometry is included in Figure 2.4 as open circles, which shows that the effect of galaxy subtraction is quite evident, particularly in the last observation where their measurement is 1.3 mag brighter than my estimate.
- SN 1992ba showed a light curve with a long plateau that leaves no doubt that it was a SN II-P. A comparison with the Schmidt et al. (1994b) photometry (open circles) shows an excellent agreement with my measurements.
- SN 1993A displayed a slowly declining light curve during 80 days, a clear indication that it was a SN II-P. Unfortunately the observations ended before the exponential tail.
- SN 1993S was observed for only two months. The *B* light curve showed a decline at a rate of $0.048 \text{ mag day}^{-1}$, quite consistent with the above description of a SN II-L.
- SN 1999br was observed for 100 days, during which it displayed a well-defined plateau. Unfortunately the object went behind the Sun before we could observe the exponential tail. In Figure 2.5 I include with open circles the photometry by Pastorello et al. (2001), which is in excellent agreement with my measurements.
- SN 1999ca showed a plateau of slowly declining brightness during 60 days, and an exponential tail. The extrapolation of the tail to earlier epochs suggests that the SN presumably had a sudden drop from the plateau, sometime when the object was behind the Sun.
- SN 1999cr revealed a well defined plateau and a rapid drop of 1.5 mag. The tail of this SN II-P event could not be observed.
- SN 1999eg had a well-sampled light curve, yet the time coverage was limited to only 60 days in which the object displayed a decline at a rate of $\sim 0.038 \text{ mag day}^{-1}$. Most likely this object was a SN II-P.

- SN 1999em is, after SN 1987A, the second best observed SN. The observations presented here are in excellent agreement with the Suntzeff et al. (2001) data, which reveal that the V light curve was characterized by a plateau of slowly declining brightness during ~ 100 days, followed by a drop of 2 mag in ~ 30 days, and a linear decline at the slow pace of ~ 0.01 mag day $^{-1}$.
- SN 2000cb had a well sampled light curve during 130 days revealing a behavior which defied the classification scheme of Barbon et al. (1979). The B light curve was characterized by a steady brightening during 30 days, a post-maximum decline phase that showed a clear plateau followed by a drop of 1 mag.

2.3.2 Additional optical photometry

Besides the 12 SNe observed by the CT/SOIRS survey, I collected additional optical photometry for SNe 1986L, 1987A, 1988A, 1990E, and 1990K. For completeness and comparison with the CT/SOIRS objects Figure 2.6 shows the light curves of these five SNe, which come from a variety of published papers and unpublished data kindly provided to me. Next I summarize the photometric properties of these objects:

- SN 1986L was intensively observed by M. Phillips and S. Kirhakos with the CTIO 0.9-m and 4.0-m telescopes, BV filters, and CCD detectors. They measured aperture magnitudes for the SN and five local standards properly calibrated on 12 photometric nights. They exercised great care to eliminate the contribution of the background light in the SN aperture by subtracting the flux of the galaxy from images taken in Nov. 1987. The resulting B light curve revealed the great sampling achieved over a period of five months. Although this SN declined somewhat faster than the SNe II-P shown in Figures 2.4 and 2.5, it displayed an evident plateau followed by a fast dimming, and the onset of an exponential decline. Undoubtedly, this object matched well the definition of a SN II-P.
- SN 1987A was the long-awaited naked eye SN. It has been continuously observed by the CTIO staff since its discovery. Here I adopt the $UBVRI$ photoelectric light curves

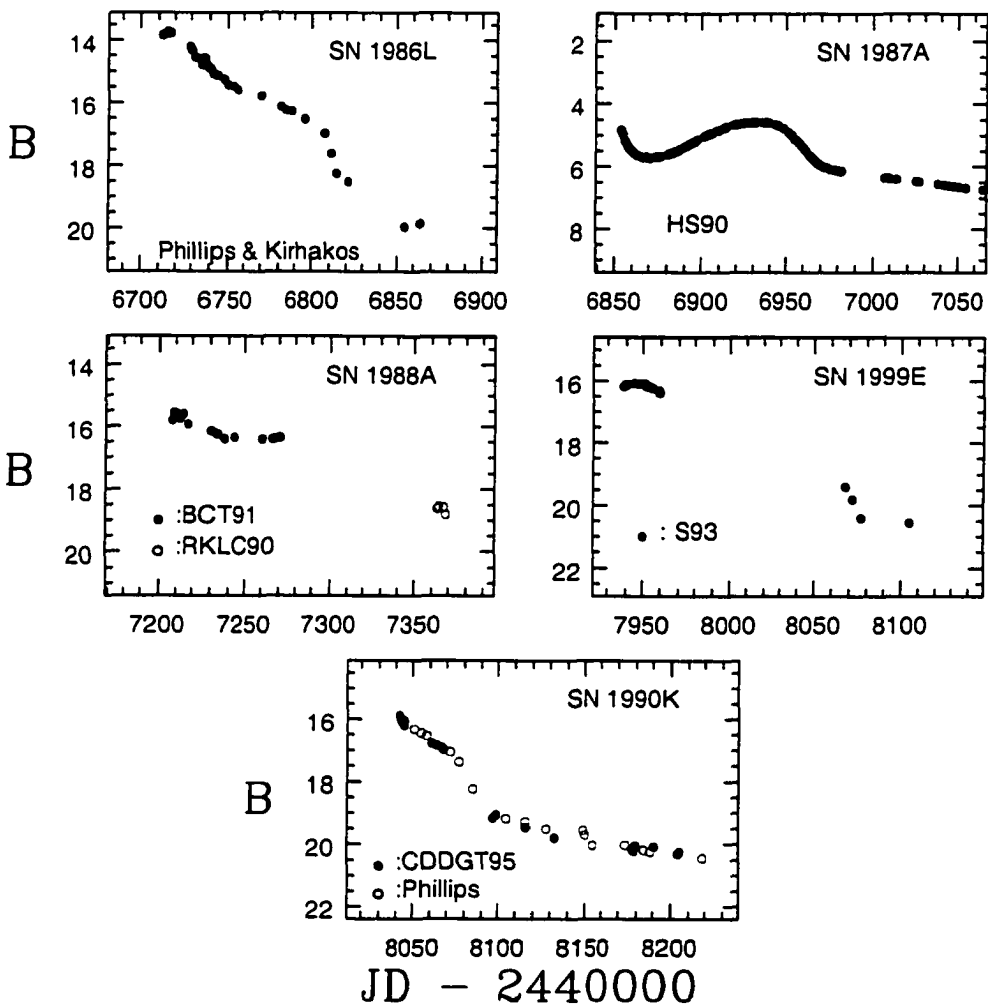


Figure 2.6: *B* band light curves for 5 SNe II from Hamuy & Suntzeff (1990) (HS90), Benetti et al. (1991) (BCT91), Ruiz-Lapuente et al. (1990) (RKLC90), Schmidt et al. (1993) (S93), Capellaro et al. (1995) (CDDGT95), and unpublished photometry by Phillips & Kirhakos.

published by Hamuy & Suntzeff (1990) and the *JHK* photometry reported by Bouchet et al. (1989). Evidently, the optical light curve did not match the classification of a linear or plateau event. Hydrodynamic calculations showed that this behavior was due to the compactness of the blue supergiant progenitor, and that the SN had a massive ($15 M_{\odot}$) H envelope. (Woosley et al., 1987; Arnett, 1996). I include it here in order to test the performance of EPM in this extreme case, although this method has been only developed for genuine SNe II-P (see Chapter 3).

- SN 1988A has BV photometry published by Benetti et al. (1991). The measurements were obtained from photographic plates during a period of 60 days. Besides the usual low precision of photographic photometry (~ 0.1 mag), the SN magnitudes have potential contamination of background light. I include this object in my sample nonetheless, in order to make use of the spectroscopic data that I have for the EPM analysis. Clearly SN 1988A was a SN II-P. Late time CCD BVR photometry for this object was reported by Ruiz-Lapuente et al. (1990) which proves useful to estimate the brightness of the exponential tail and the amount of ^{56}Ni synthesized in the explosion.
- SN 1990E was very well observed by Schmidt et al. (1993) with $UBVRI$ filters and CCDs, for a period of 600 days. Benetti et al. (1994) published late-time CCD BVR photometry for this object, and reported a difference of 0.4 mag in the V magnitudes of Schmidt et al. (1993), presumably owing to different methods in subtracting the galaxy background. In any case, this object clearly showed an early plateau of slightly decreasing brightness before it disappeared behind the Sun. When the observations resumed, SN 1990E was rapidly dimming after which it began the exponential slower decline, leaving no doubts that this was a SN II-P.
- SN 1990K was observed by Capellaro et al. (1995) with $BVRI$ filters and CCDs, for 470 days. Additional (unpublished) photometry was obtained by Phillips from CTIO. The B light curve showed that the SN was caught at the end of a plateau phase of moderate

brightness decrease. The observations clearly showed evidence for the sudden drop off the plateau and a well defined exponential tail, all of which suggested that SN 1990K was a plateau event. Note that this is very different than the conclusion of Capellaro et al. (1995), namely, that this object was a linear event. It seems that they were misled by the poor sampling of the light curves.

2.3.3 Infrared photometry

The SOIRS program yielded JHK_S photometry for SNe 1999br, 1999cr, and 1999em from the CTIO 1-m (YALO), LCO 1.0-m, LCO 2.5-m, SO 2.5-m, and SO 1.5-m telescopes. Considering that SN 1987A (Bouchet et al., 1989) and SN 1980K (Dwek et al., 1983) are virtually the only SNe II with published JHK photometry, this is a significant step forward [although Mattila & Meikle (2000) have recently shown plots with IR light curves for a few other SNe II].

So far, only the 1999em data have been reduced, and the results will be published by Suntzeff et al. (2001). Figure 2.7 presents the JHK photometry along with the optical light curves which reveal the exceptional sampling obtained over a period of 180 days from discovery until the SN went behind the Sun. The U light curve showed that maximum light occurred just after discovery, followed by a phase of rapid decline during which the SN dimmed by ~ 4 mag in 70 days. The B light curve showed that maximum occurred two days later than in U , a rapid decline for ~ 30 days during which the SN dimmed by ~ 1 mag, a phase of 70 days of slowly-decreasing luminosity (plateau) during which the flux decreased by one additional magnitude, a fast drop in flux by 2.5 mag in only 30 days, and a linear decay in magnitude as of JD 2451610 that signaled the onset of the nebular phase. As mentioned above, the V light curve was characterized by a plateau of nearly constant brightness that lasted ~ 100 days. The R , I , Z , J , H , and K light curves had the same basic features of the V light curve, except that the SN gradually got brighter during the plateau. The brightening increased with wavelength, and reached 0.5

mag in the K band. This behavior was probably due to the increasing radius and steady cooling which shifted the peak of the emission toward longer wavelengths.

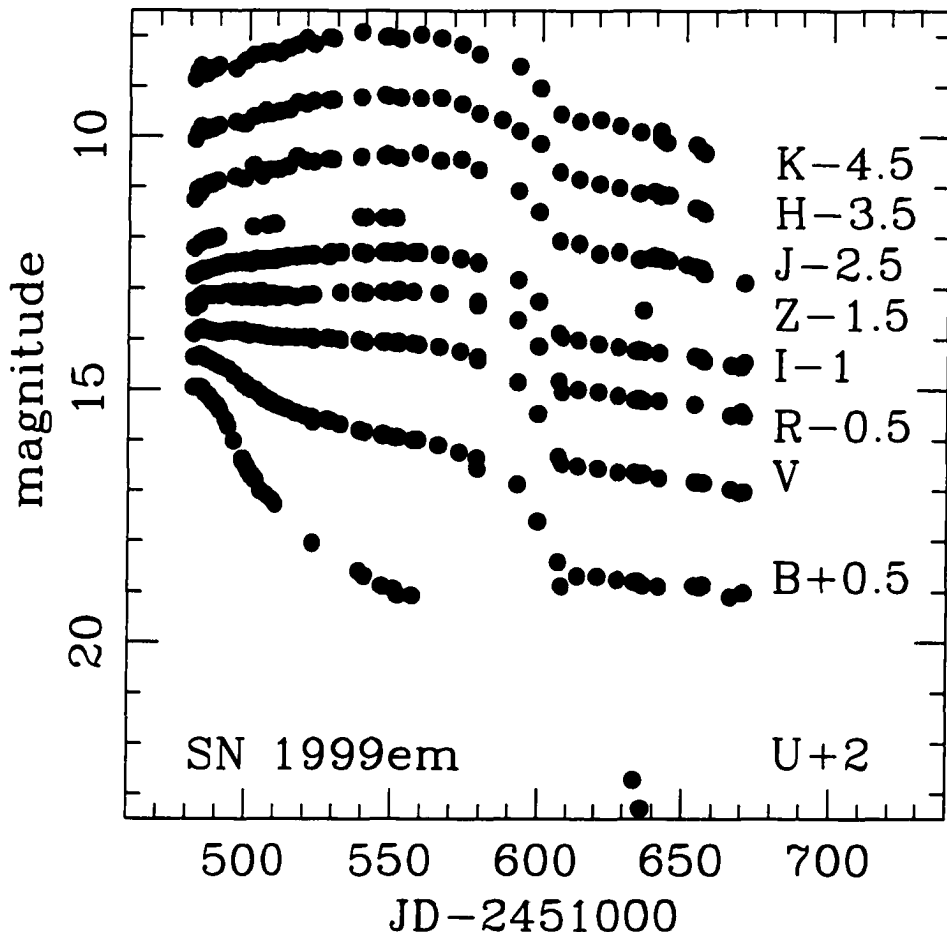


Figure 2.7: $UBV^*RIZJHK^*$ light curves of SN 1999em.

Except for SN 1987A, this dataset is the most complete ever obtained for a Type II SN and affords a great opportunity to test the performance of EPM at IR wavelengths.

2.3.4 Spectroscopy

We obtained follow-up spectroscopy for the 12 CT/SOIRS SNe. We obtained the great majority of the spectra at optical wavelengths (only four in the IR). Thanks to the generous collaboration of M. Della Valle and his collaborators, I was able to complement this database with spectra obtained in the course of the ESO SN key project. Also, I was able to use the impressive spectroscopic sequence of SN 1986L collected by M. Phillips, spectra for SNe 1988A, 1990E and 1990K gathered by the CTIO group, as well as additional observations of recent SNe kindly made by SO astronomers.

In the case of the CT/SOIRS CCD spectra, the data were reduced by myself and my collaborators following a generic procedure comprising 1) overscan/bias subtraction, 2) flat-fielding (duly normalized along the dispersion axis), 3) extraction to 1-D (including background/foreground light subtraction), 4) wavelength calibration using the emission lamp observed at the SN position, 5) atmospheric extinction correction (without including correction for telluric lines), and 6) flux calibration from the flux standards observed during the night. We cleaned the spectra for cosmic rays from the pair of SN observations that we obtained for each SN. Finally, we deredshifted the spectra using the heliocentric redshifts listed in Table 2.1.

A complete list of the 115 spectra that I was able to collect is given in Table 2.5, including: the UT date, the telescope employed, the observatory, the wavelength range covered, the name of the observer(s), and a quality code.

To illustrate some of the data, Figure 2.8 displays early-time spectra of seven SNe obtained \sim 10 days after explosion, after correction for redshift and dust extinction. The time of explosion is estimated for each SN from the EPM analysis and considerations about the time of discovery (as discussed in Chapter 3). This figure reveals that these SNe displayed a great variety of spectral features. For example, while SN 1986L had a nearly featureless blue continuum with weak H α and H γ lines, at the same age SN 1987A

displayed a much redder continuum with strong Balmer P-Cygni profiles and lines due to Fe II $\lambda\lambda$ 5018,5169, Na I λ 5893, Ba II $\lambda\lambda$ 4554,6142, and Sc II λ 5527. Large variations could be seen in the H α line profiles, Doppler shifts, the strength of the He I λ 5876 line (which is only observed at the earliest and hottest phases), and several other features.

To continue with the illustration of the data, Figure 2.9 presents a subsample of spectra obtained \sim 35 days after explosion, for 15 SNe of my sample. Evidently the continuum was quite different among this sample, with SNe 1999br and 1987A having the reddest spectra at this phase relative to the other objects. At this age all SNe displayed strong H lines (including SN 1986L) with significant variations in the line profiles. Note, for example, the relatively narrow H α line of SN 1999br compared to SN 1992am. It is interesting to note also the large differences in the emission/absorption ratio. Weak absorption, for example, could be seen in SNe 1986L, 1990E, 1999ca, 1999cr, and 1999eg. The statistical study of photometric and spectroscopic data of SNe II by Patat et al. (1994) showed that SNe II-L have shallower P-Cygni absorption of H α than SNe II-P, with extreme linear events completely lacking the absorption component. In my sample there is no evident relationship between the emission/absorption ratio and the shape of the light curve, although it must be mentioned that my sample does not include a genuine SN II-L event.

In summary, the optical spectra of my sample show very clearly the heterogeneous nature of SNe II. This has been often remarked in the literature and the reader can find detailed discussions in the papers by Patat et al. (1994) and Schlegel (1996).

As mentioned above we were able to collect some IR spectra during the SOIRS program. We observed SN 1999ca at one epoch and SN 1999em on three different nights with the VLT/ISAAC instrument at Cerro Paranal. I described the observations and reductions procedures in detail in Hamuy et al. (2001) and I will not repeat them here. The combined optical/IR spectra of SN 1999em can be seen in Figure 2.10, which reveals the

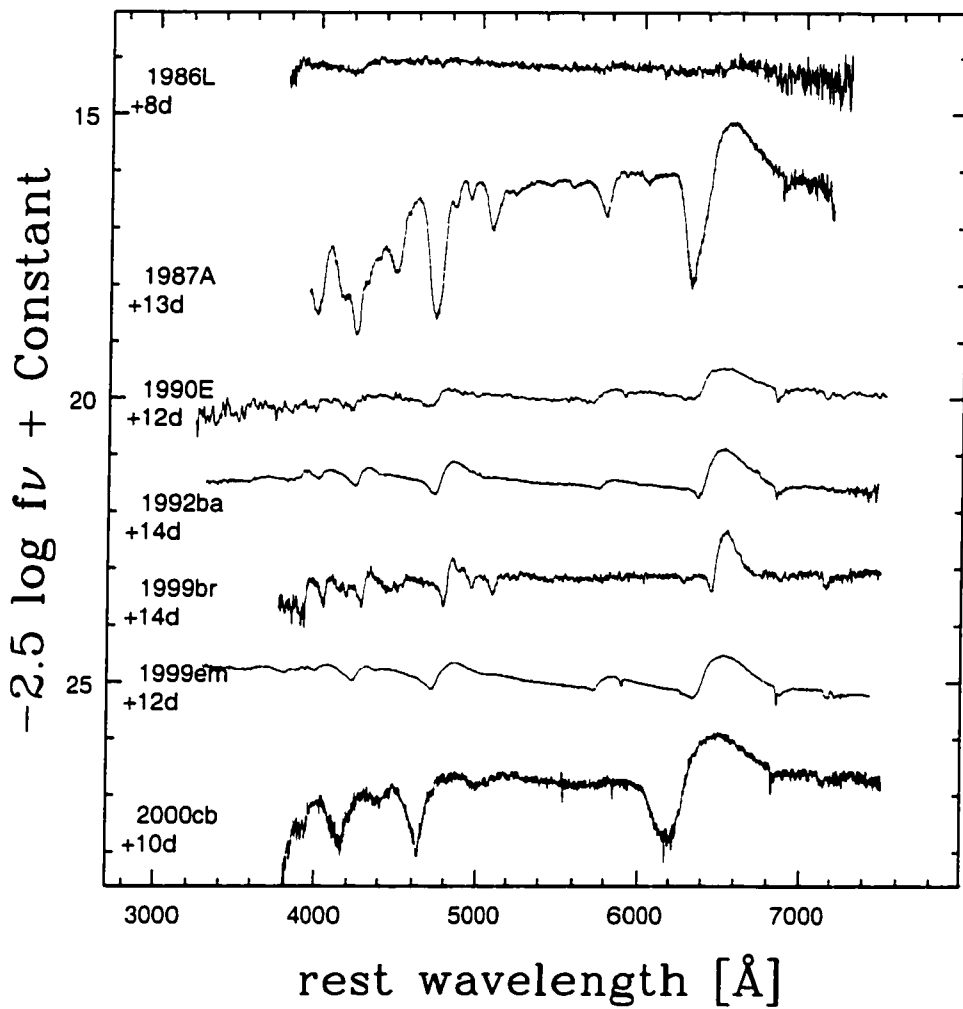


Figure 2.8: Early-time spectra of seven SNe II. The age since explosion is indicated for each spectrum.

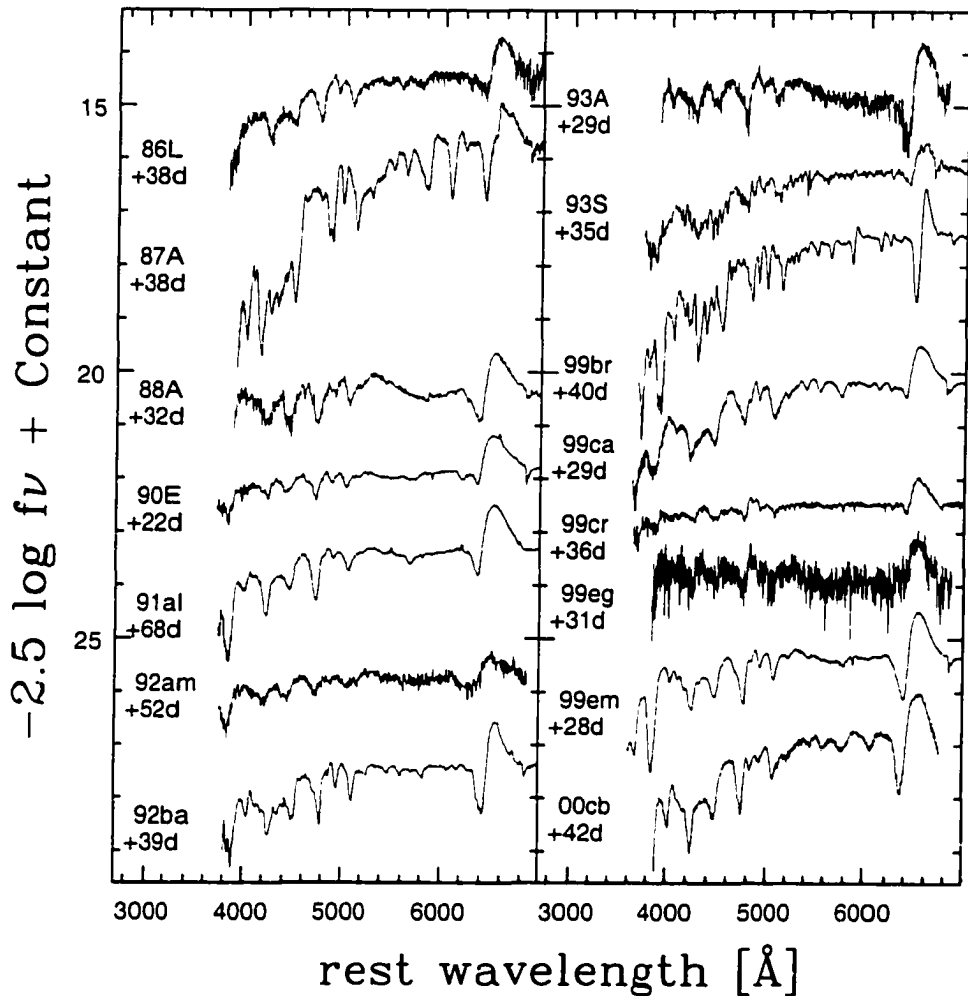


Figure 2.9: Spectra of 15 SNe II, ~ 35 days after explosion. The age is indicated for each spectrum.

exquisite spectral resolution and the superb S/N delivered by ISAAC.

The first spectrum, taken 11.2 days after explosion was characterized by the usual H Balmer lines in the optical and P α , P β , B γ , and B δ in the IR on top of a blue continuum. The He I λ 5876,10830 lines were quite prominent at that phase. The second spectrum (at the age of +27.1 days) was significantly redder and showed strong P γ and P δ lines in lieu of the He I λ 10830 feature, and a few faint lines around 17000 Å from higher transitions in the Brackett series.

2.4 Summary

In this chapter I presented the SN sample considered in this study and the follow-up photometry and spectroscopy gathered for them. The light curves revealed that the majority of the objects in the sample belong to the SN II-P class. Only one object (SN 1993S) seemed to have the basic characteristic of a linear event, although the time coverage of the light curve cast some doubts about its classification. And, as in all SN samples, there were objects that escaped the classical classification schemes: SN 1987A, particularly could not be classified as a linear or plateau event; SN 2000cb presented the same challenge and its photometric similarity to SN 1987A suggested a new class of 87A-like objects. Within the plateau group it was also possible to see significant photometric diversity where each SN showed its own individual character. This could be seen also from the comparison of spectra taken at the same age.

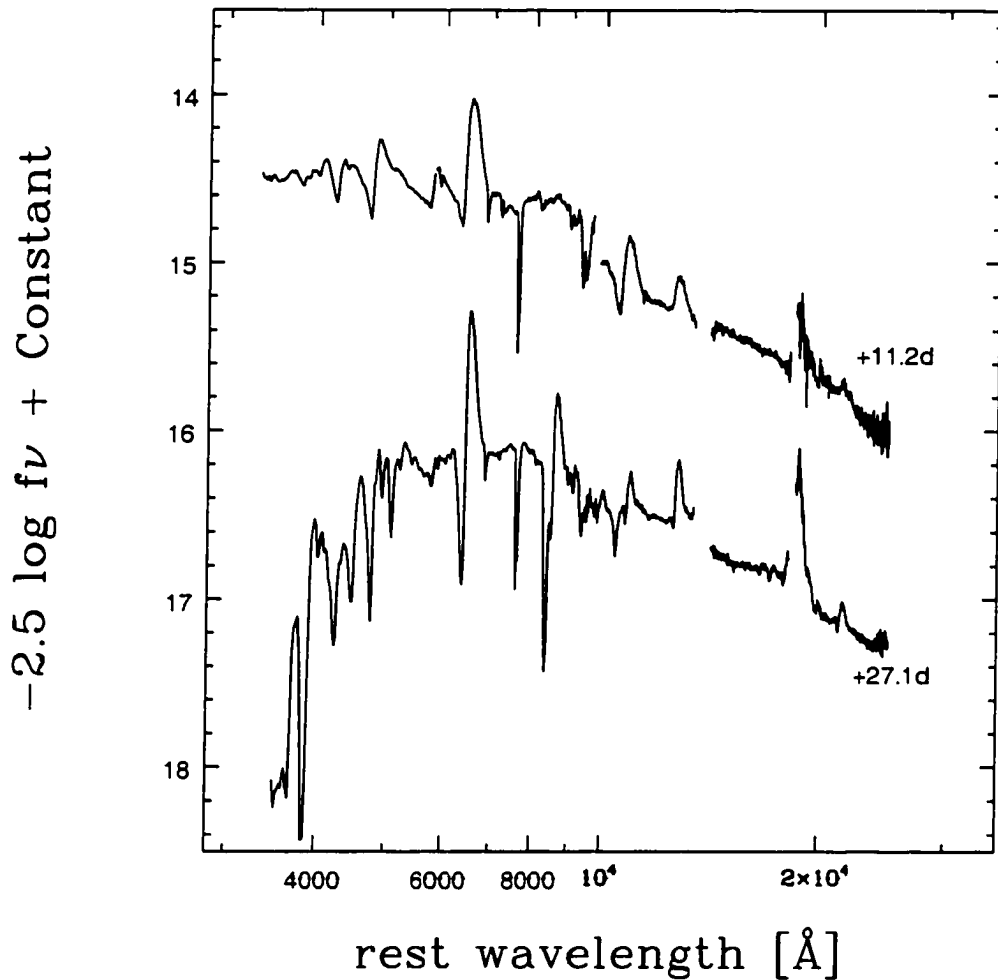


Figure 2.10: Combined optical and IR spectra of SN 1999em. The IR spectra were obtained one day before the optical observations and the mean age is indicated next to each spectrum.

Table 2.1: List of Type II Supernovae

SN	Host Galaxy	z_{helio} (km s $^{-1}$)	source	$A_{\text{GAL}}(V)$ SFD98	$\alpha(2000)$ NED	$\delta(2000)$ NED	Survey/ Discoverer	Date UT
1986L	NGC 1559	1292	NED	0.099	04:17:31.2	-62:47:07	Evans	Oct 7.60
1987A	LMC	278	NED	0.249	05:35:27.9	-69:16:10	Shelton	Feb 24.23
1988A	NGC 4579	1519	NED	0.136	12:37:43.5	+11:48:19	Ikeya/Evans	Jan 18
1990E	NGC 1035	1241	NED	0.082	02:39:28.5	-08:08:04	BASS	Feb 15.12
1990K	NGC 150	1584	NED	0.047	00:34:14.0	-27:47:46	Evans	May 25.80
1991al	LEDA 140858	4572	here	0.168	19:42:24.0	-55:06:23	CT/Wischnjewsky	Jul 16.20
1992af	ESO 340-G038	5611	here	0.171	20:30:40.2	-42:18:35	CT/Antezana	Jun 29.28
1992am	MCG-01-04-039	14310	NED	0.164	01:25:02.7	-04:39:01	CT/Antezana	Jul 26.33
1992ba	NGC 2082	1104	NED	0.193	05:41:47.1	-64:18:01	Evans	Sep 30.75
1993A	anonymous	8790	here	0.572	07:39:17.3	-62:03:14	CT/Wischnjewsky	Jan 17.17
1993S	IRAS F22495-4034	9896	NED	0.054	22:52:23.4	-40:18:37	CT/Antezana	May 26.36
1999br	NGC 4900	969	NED	0.078	13:00:41.8	+02:29:46	LOSS	Apr 12.4
1999ca	NGC 3120	2791	NED	0.361	10:05:22.9	-34:12:41	PARG	Apr 27.55
1999cr	ESO 576-G034	6069	here	0.324	13:20:18.3	-20:08:50	SOIRS/Antezana	Mar 12.20
1999eg	IC 1861	6703	NED	0.388	02:53:08.4	+25:29:24	UKN/SNP	Oct 4.078
1999em	NGC 1637	717	NED	0.130	04:41:27.1	-02:51:46	LOSS	Oct 29.44
2000cb	IC 1158	1927	NED	0.373	16:01:32.1	+01:42:23	LOSS	Apr 27.4

Notes:

SFD98: Schlegel, Finkbeiner & Davis (1998), NED: NASA Extragalactic Database, BAAS: Berkeley Automated Supernova Search, CT: Calán/Tololo, LOSS: Lick Observatory Supernova Search, PARG: Perth Astronomy Research Group, SOIRS: Supernova Optical/IR Survey, UKN/SNP : U.K. Nova/Supernova Patrol

Table 2.2: Journal of the Photometric Observations

Date(UT)	Telescope	Observatory	Supernova(e) Observed	Observer(s)
1991 Jul 18	0.91-m	CTIO	91al	H. Yee/E. Ellingson
1991 Jul 21	0.91-m	CTIO	91al	A. Dey
1991 Jul 22	0.91-m	CTIO	91al	A. Dey
1991 Aug 10	4.0-m	CTIO	91al	M. Navarrete
1991 Aug 22	0.91-m	CTIO	91al	P. Green
1991 Aug 31	0.91-m	CTIO	91al	G. Williger
1991 Sep 09	0.91-m	CTIO	91al	N. Suntzeff
1991 Oct 08	0.91-m	CTIO	91al	N. Suntzeff
1991 Oct 16	0.91-m	CTIO	91al	R. Schommer
1991 Oct 17	0.91-m	CTIO	91al	R. Schommer
1991 Oct 18	0.91-m	CTIO	91al	R. Schommer
1991 Oct 19	0.91-m	CTIO	91al	R. Schommer
1991 Oct 21	0.91-m	CTIO	91al	E. Olszewski
1991 Oct 22	0.91-m	CTIO	91al	M. Hamuy
1991 Oct 26	0.91-m	CTIO	91al	M. Hamuy
1991 Nov 18	0.91-m	CTIO	91al	B. Schmidt/C. Smith
1992 Jul 02	0.91-m	CTIO	92af	K. Wakamatsu/M. Malkan
1992 Jul 04	0.91-m	CTIO	92af	R. Avilés/ M. Hamuy
1992 Jul 06	0.91-m	CTIO	92af	A. Walker
1992 Jul 10	0.91-m	CTIO	92af	A. Walker
1992 Jul 12	1.0-m	LCO	92af	R. Avilés/M. Hamuy
1992 Jul 13	1.0-m	LCO	92af	R. Avilés/M. Hamuy
1992 Jul 14	1.0-m	LCO	92af	R. Avilés/F. Barrientos
1992 Jul 15	1.0-m	LCO	92af	R. Avilés/F. Barrientos
1992 Jul 28	0.91-m	CTIO	92af	N. Tyson

Table 2.2: Journal of Photometric Observations – continued

Date(UT)	Telescope	Observatory	Supernova(e) Observed	Observer(s)
1992 Jul 29	0.91-m	CTIO	92am	N. Tyson
1992 Aug 01	0.91-m	CTIO	91al	R. Avilés/C. Smith
1992 Aug 08	0.91-m	CTIO	92af	R. Avilés
1992 Aug 09	0.91-m	CTIO	92af	R. Avilés
1992 Aug 11	0.91-m	CTIO	92af	R. Avilés
1992 Aug 12	0.91-m	CTIO	92af,92am	M. Hamuy/R. Avilés
1992 Aug 13	0.91-m	CTIO	92af,92am	R. Avilés
1992 Aug 14	0.91-m	CTIO	91al,92af,92am	R. Avilés
1992 Aug 15	0.91-m	CTIO	92af	R. Avilés/F. Barrientos
1992 Sep 03	0.91-m	CTIO	91al	R. Avilés
1992 Sep 06	0.91-m	CTIO	91al,92af	R. Avilés
1992 Sep 07	0.91-m	CTIO	92af,92am	R. Avilés
1992 Sep 20	0.91-m	CTIO	91al,92af,92am	R. Avilés
1992 Sep 26	0.91-m	CTIO	92af	R. Avilés
1992 Oct 09	0.91-m	CTIO	92ba	R. Avilés/M. Hamuy
1992 Oct 10	0.91-m	CTIO	92af,92am,92ba	R. Avilés/M. Hamuy
1992 Oct 13	0.91-m	CTIO	92af,92am,92ba	R. Avilés
1992 Oct 24	4.0-m	CTIO	92af,92am	M. Navarrete
1992 Oct 27	0.91-m	CTIO	92am,92ba	R. Avilés
1992 Nov 14	0.91-m	CTIO	92ba	R. Avilés
1992 Nov 15	0.91-m	CTIO	92ba	R. Avilés
1992 Nov 30	0.91-m	CTIO	92ba	J. Elias/F. Barrientos
1992 Dec 19	0.91-m	CTIO	92ba	R. Avilés
1992 Dec 23	0.91-m	CTIO	92ba	R. Avilés
1992 Dec 23	4.0-m	CTIO	92am	N. Suntzeff

Table 2.2: Journal of Photometric Observations – continued

Date(UT)	Telescope	Observatory	Supernova(e) Observed	Observer(s)
1993 Jan 10	0.91-m	CTIO	92ba	R. Avilés
1993 Jan 20	1.5-m	CTIO	93A	C. Anguita
1993 Jan 23	0.91-m	CTIO	93A	R. Avilés
1993 Jan 25	0.91-m	CTIO	92ba,93A	R. Avilés
1993 Jan 26	0.91-m	CTIO	93A	R. Avilés
1993 Jan 29	0.91-m	CTIO	92ba,93A	R. Avilés
1993 Jan 30	0.91-m	CTIO	93A	R. Avilés
1993 Feb 08	0.91-m	CTIO	93A	M. Hamuy/X. Gómez
1993 Feb 19	0.91-m	CTIO	92ba,93A	R. Avilés
1993 Feb 20	0.91-m	CTIO	93A	R. Avilés
1993 Feb 22	4.0-m	CTIO	93A	N. Suntzeff
1993 Mar 04	0.91-m	CTIO	93A	R. Koopmann
1993 Mar 07	0.91-m	CTIO	93A	R. Avilés
1993 Mar 27	0.91-m	CTIO	93A	R. Avilés
1993 Apr 01	0.91-m	CTIO	92ba	R. Avilés
1993 Apr 07	0.91-m	CTIO	92ba,93A	R. Avilés
1993 Apr 14	0.91-m	CTIO	93A	R. Avilés
1993 Jun 04	0.91-m	CTIO	92af,93S	R. Avilés
1993 Jun 05	0.91-m	CTIO	93S	R. Avilés
1993 Jun 14	0.91-m	CTIO	93S	R. Avilés
1993 Jun 16	0.91-m	CTIO	93S	R. Avilés
1993 Jun 23	0.91-m	CTIO	93S	E. Rubenstein/W. Sherry
1993 Jun 24	4.0-m	CTIO	92af,93S	N. Suntzeff
1993 Jun 26	0.91-m	CTIO	93S	E. Rubenstein/W. Sherry
1993 Jul 11	0.91-m	CTIO	92af,93S	R. Avilés

Table 2.2: Journal of Photometric Observations – continued

Date(UT)	Telescope	Observatory	Supernova(e) Observed	Observer(s)
1993 Jul 16	0.91-m	CTIO	93S	R. Avilés
1993 Jul 17	0.91-m	CTIO	92af,93S	R. Avilés
1993 Jul 18	0.91-m	CTIO	92af,93S	R. Avilés
1993 Jul 19	0.91-m	CTIO	93S	R. Avilés
1993 Aug 03	0.91-m	CTIO	93S	R. Avilés
1994 Nov 09	4.0-m	CTIO	92am	N. Suntzeff
1994 Sep 12	4.0-m	CTIO	93S	R. Avilés
1999 Mar 19	1.0-m	CTIO	99cr	Service Observing
1999 Mar 20	0.91-m	CTIO	99cr	L. Strolger/C. Smith
1999 Mar 22	1.0-m	CTIO	99cr	Service Observing
1999 Mar 24	1.0-m	CTIO	99cr	Service Observing
1999 Mar 26	1.0-m	CTIO	99cr	Service Observing
1999 Mar 29	0.91-m	CTIO	99cr	L. Strolger/C. Smith
1999 Mar 29	1.0-m	CTIO	99cr	Service Observing
1999 Mar 30	0.91-m	CTIO	99cr	L. Strolger
1999 Apr 06	0.91-m	CTIO	99cr	L. Strolger
1999 Apr 07	0.91-m	CTIO	99cr	L. Strolger
1999 Apr 09	1.5-m	CTIO	99cr	L. Strolger
1999 Apr 15	0.91-m	CTIO	99br	M. Hamuy/M.T. Ruiz
1999 Apr 16	0.91-m	CTIO	99br	M. Hamuy/M.T. Ruiz
1999 Apr 17	0.91-m	CTIO	99br,99cr	M. Hamuy/M.T. Ruiz
1999 Apr 18	0.91-m	CTIO	99br	M. Hamuy/M.T. Ruiz
1999 Apr 23	1.5-m	CTIO	99br,99cr	C. Smith
1999 Apr 26	0.91-m	CTIO	99br,99cr	C. Smith
1999 Apr 26	1.5-m	ESO	99br	I. Pérez

Table 2.2: Journal of Photometric Observations – continued

Date(UT)	Telescope	Observatory	Supernova(e) Observed	Observer(s)
1999 Apr 27	1.0-m	CTIO	99br	Service Observing
1999 Apr 28	1.5-m	CTIO	99br,99cr	L. Strolger
1999 Apr 28	1.0-m	CTIO	99cr	Service Observing
1999 Apr 30	1.5-m	CTIO	99cr	S. Wachter
1999 May 01	1.0-m	CTIO	99br,99cr	Service Observing
1999 May 03	1.5-m	CTIO	99br	S. Wachter
1999 May 03	NTT	ESO	99br,99cr	M. Hamuy/S. Brilliant
1999 May 03	1.0-m	CTIO	99br,99cr	Service Observing
1999 May 04	1.5-m	CTIO	99cr	L. Strolger
1999 May 06	1.5-m	CTIO	99br,99cr	L. Strolger
1999 May 07	1.5-m	CTIO	99cr	L. Strolger
1999 May 07	NTT	ESO	99br,99ca,99cr	J. Maza
1999 May 07	1.0-m	CTIO	99br	Service Observing
1999 May 08	1.0-m	CTIO	99br	Service Observing
1999 May 10	1.0-m	CTIO	99ca,99cr	Service Observing
1999 May 11	1.5-m	ESO	99br,99ca	M. Hamuy/A. Pizzella
1999 May 11	1.0-m	CTIO	99br	Service Observing
1999 May 15	1.0-m	CTIO	99ca	Service Observing
1999 May 16	1.0-m	CTIO	99br,99cr	Service Observing
1999 May 19	NTT	ESO	99br,99ca	M. Hamuy/S. Brilliant
1999 May 19	1.0-m	CTIO	99ca	Service Observing
1999 May 20	1.0-m	CTIO	99br	Service Observing
1999 May 21	1.0-m	CTIO	99ca	Service Observing
1999 May 22	1.0-m	CTIO	99cr	Service Observing
1999 May 23	1.0-m	CTIO	99ca	Service Observing

Table 2.2: Journal of Photometric Observations – continued

Date(UT)	Telescope	Observatory	Supernova(e) Observed	Observer(s)
1999 May 24	1.5-m	ESO	99ca	M. Hamuy
1999 May 25	1.0-m	CTIO	99br	Service Observing
1999 May 29	1.0-m	CTIO	99ca	Service Observing
1999 May 30	1.0-m	CTIO	99br	Service Observing
1999 May 31	1.0-m	CTIO	99ca	Service Observing
1999 Jun 01	1.0-m	CTIO	99br	Service Observing
1999 Jun 02	1.0-m	CTIO	99ca	Service Observing
1999 Jun 06	1.0-m	CTIO	99br,99ca	Service Observing
1999 Jun 11	1.0-m	CTIO	99ca	Service Observing
1999 Jun 16	1.0-m	CTIO	99br,99ca	Service Observing
1999 Jun 18	1.0-m	CTIO	99cr	Service Observing
1999 Jun 22	1.0-m	CTIO	99ca	Service Observing
1999 Jun 23	1.0-m	CTIO	99br	Service Observing
1999 Jun 24	1.0-m	CTIO	99cr	Service Observing
1999 Jun 26	1.0-m	CTIO	99ca	Service Observing
1999 Jun 27	1.0-m	CTIO	99br	Service Observing
1999 Oct 13	0.91-m	CTIO	99ca,99eg	M. Hamuy/J. Pérez
1999 Oct 16	0.91-m	CTIO	99eg	M. Hamuy/M.T. Acevedo
1999 Oct 20	0.91-m	CTIO	99ca,99eg	L. Strolger
1999 Oct 21	0.91-m	CTIO	99ca,99eg	L. Strolger
1999 Oct 27	0.91-m	CTIO	99ca	M. Hamuy/M. Wischnjewsky
1999 Oct 28	0.91-m	CTIO	99ca,99eg	M. Wischnjewsky
1999 Oct 29	0.91-m	CTIO	99ca	M. Wischnjewsky
1999 Oct 30	0.91-m	CTIO	99ca,99eg,99em	M. Wischnjewsky
1999 Nov 01	0.91-m	CTIO	99em	M. Wischnjewsky

Table 2.2: Journal of Photometric Observations – continued

Date(UT)	Telescope	Observatory	Supernova(e) Observed	Observer(s)
1999 Nov 02	0.91-m	CTIO	99ca,99em	L. González
1999 Nov 03	0.91-m	CTIO	99em	L. González
1999 Nov 04	0.91-m	CTIO	99eg,99em	L. González
1999 Nov 05	0.91-m	CTIO	99eg,99em	L. González
1999 Nov 06	0.91-m	CTIO	99ca,99em	L. González
1999 Nov 07	0.91-m	CTIO	99ca,99eg,99em	L. González
1999 Nov 08	0.91-m	CTIO	99eg,99em	L. Strolger
1999 Nov 10	0.91-m	CTIO	99em	L. Strolger
1999 Nov 11	0.91-m	CTIO	99ca,99eg,99em	L. Strolger
1999 Nov 13	0.91-m	CTIO	99em	E. Rubenstein
1999 Nov 16	0.91-m	CTIO	99em	E. Rubenstein
1999 Nov 16	1.5-m	CTIO	99eg,99em	L. Strolger
1999 Nov 17	1.5-m	CTIO	99ca,99em	L. Strolger
1999 Nov 18	0.91-m	CTIO	99em	E. Rubenstein
1999 Nov 19	0.91-m	CTIO	99ca,99em	L. Strolger
1999 Nov 19	NTT	ESO	91al	M. Hamuy/V. Doublier
1999 Nov 20	0.91-m	CTIO	99em	E. Rubenstein
1999 Nov 22	0.91-m	CTIO	99em	E. Rubenstein
1999 Nov 24	0.91-m	CTIO	99ca,99em	M. Hamuy/R. Antezana
1999 Nov 26	0.91-m	CTIO	99eg,99em	R. Antezana
1999 Nov 27	0.91-m	CTIO	99eg,99em	R. Antezana
1999 Nov 29	2.5-m	SO	99em	E. Green
1999 Dec 10	1.5-m	SO	99em	T. Pickering/C. Impey
1999 Dec 19	2.5-m	SO	99em	E. Green
1999 Dec 26	0.91-m	CTIO	99em	W. Sherry

Table 2.2: Journal of Photometric Observations – continued

Date(UT)	Telescope	Observatory	Supernova(e) Observed	Observer(s)
1999 Dec 28	0.91-m	CTIO	99em	W. Sherry
2000 Jan 03	0.91-m	CTIO	99em	W. Sherry
2000 Jan 07	0.91-m	CTIO	99em	W. Sherry
2000 Jan 08	0.91-m	CTIO	99em	M. Wischnjewsky
2000 Jan 11	1.5-m	SO	99em	R. de Souza/S. dos Anjos
2000 Jan 13	0.91-m	CTIO	99em	M. Wischnjewsky
2000 Feb 04	1.5-m	SO	99em	R. de Souza/S. dos Anjos
2000 Mar 04	1.5-m	SO	99em	R. de Souza/S. dos Anjos
2000 Apr 02	NTT	ESO	92ba,93A,99br,99em	M. Hamuy
2000 Apr 09	NTT	ESO	99br	M. Hamuy
2000 Apr 29	0.91-m	CTIO	00cb	M. Hamuy
2000 May 02	NTT	ESO	99br,99em	M. Hamuy
2000 May 08	NTT	ESO	99ca	J. Maza
2000 May 11	0.91-m	CTIO	00cb	L. González
2000 May 12	0.91-m	CTIO	00cb	L. González
2000 May 13	0.91-m	CTIO	00cb	L. González
2000 May 17	0.91-m	CTIO	00cb	M. Wischnjewsky/R. Antezana
2000 May 18	0.91-m	CTIO	00cb	M. Wischnjewsky/R. Antezana
2000 May 19	0.91-m	CTIO	00cb	M. Wischnjewsky/R. Antezana
2000 May 20	0.91-m	CTIO	00cb	M. Wischnjewsky/R. Antezana
2000 May 31	NTT	ESO	92af,99cr,00cb	M. Hamuy
2000 Jun 04	0.91-m	CTIO	00cb	Service Observing
2000 Jun 10	0.91-m	CTIO	00cb	Service Observing
2000 Jun 16	0.91-m	CTIO	00cb	Service Observing
2000 Jul 05	0.91-m	CTIO	00cb	Service Observing

Table 2.2: Journal of Photometric Observations – continued

Date(UT)	Telescope	Observatory	Supernova(e) Observed	Observer(s)
2000 Jul 13	0.91-m	CTIO	00cb	Service Observing
2000 Jul 20	0.91-m	CTIO	00cb	Service Observing
2000 Jul 27	0.91-m	CTIO	00cb	Service Observing
2000 Aug 01	0.91-m	CTIO	00cb	Service Observing
2000 Sep 08	0.91-m	CTIO	00cb	J.C. Seguel/D. Geisler

Table 2.3: $UBVRIZ$ Sequences

Star	<i>U</i>	<i>B</i>	<i>V</i>	<i>R</i>	<i>I</i>	<i>Z</i>	<i>n</i>
SN 1991al							
c1	...	17.908(008)	17.036(012)	16.560(008)	16.074(010)	...	5
c2	...	17.633(010)	16.770(006)	16.273(010)	15.808(008)	...	5
c3	...	17.428(008)	16.619(011)	16.144(012)	15.710(009)	...	5
c4	...	15.390(009)	14.427(010)	13.889(015)	13.391(009)	...	5
c5	...	19.075(015)	18.358(007)	17.939(011)	17.522(016)	...	5
c6	...	18.846(012)	18.365(006)	18.039(007)	17.676(012)	...	5
c7	...	18.371(012)	17.332(016)	16.682(009)	16.098(009)	...	5
c8	...	16.436(010)	15.558(010)	15.058(012)	14.572(013)	...	5
c9	...	15.799(006)	14.965(007)	14.490(012)	14.026(005)	...	5
SN 1992af							
c1	...	16.873(010)	16.230(008)	15.855(015)	15.499(009)	...	4
c2	...	18.338(010)	17.685(008)	17.312(015)	16.947(009)	...	4
c3	...	16.452(009)	15.853(008)	15.498(015)	15.150(009)	...	4
c4	...	16.503(008)	15.855(008)	15.478(015)	15.126(009)	...	4
c5	...	19.570(043)	18.558(010)	17.861(015)	17.295(011)	...	4
c6	...	14.772(009)	14.166(009)	13.816(015)	13.468(011)	...	4
c7	...	15.613(009)	14.904(008)	14.516(015)	14.164(009)	...	4
c8	...	18.745(012)	17.648(008)	16.954(015)	16.358(020)	...	4

Table 2.3: $UBVRIZ$ Sequences – continued

Star	<i>U</i>	<i>B</i>	<i>V</i>	<i>R</i>	<i>I</i>	<i>Z</i>	<i>n</i>
SN 1992am							
c1	...	17.730(008)	16.637(008)	...	15.408(009)	...	2
c2	...	18.083(010)	16.927(009)	...	15.576(008)	...	4
c3	...	15.302(011)	14.883(009)	...	14.345(011)	...	3
c4	...	17.282(006)	16.531(006)	...	15.728(006)	...	5
c5	...	18.577(006)	17.075(007)	...	14.995(007)	...	4
c6	...	18.778(016)	18.208(008)	...	17.472(016)	...	3
SN 1992ba							
c1	...	16.269(007)	15.543(006)	15.121(015)	14.702(006)	...	8
c2	...	18.011(010)	16.902(007)	...	15.695(006)	...	7
c8	...	16.448(012)	15.280(009)	...	13.908(010)	...	3
SN 1993A							
c1	...	18.121(012)	17.086(008)	...	15.951(007)	...	11
c2	...	18.560(013)	17.526(008)	...	16.456(009)	...	11
c3	...	17.922(012)	17.092(007)	...	16.188(006)	...	11
c4	...	19.728(013)	18.823(007)	...	17.854(012)	...	11
c5	...	17.595(010)	16.779(006)	...	15.821(007)	...	11
c6	...	15.765(015)	14.671(015)	2
c7	...	17.101(011)	15.925(008)	...	14.644(008)	...	10
c8	...	17.836(014)	17.147(007)	...	16.349(009)	...	9

Table 2.3: *UBVRIZ* Sequences – continued

Star	<i>U</i>	<i>B</i>	<i>V</i>	<i>R</i>	<i>I</i>	<i>Z</i>	<i>n</i>
c9	...	19.303(015)	17.768(007)	...	15.823(008)	...	9
c10	...	17.221(012)	16.240(007)	...	15.190(007)	...	9
c11	...	18.831(012)	17.674(009)	...	16.442(006)	...	9
SN 1993S							
c1	...	14.126(008)	13.395(009)	...	12.806(015)	...	3
c2	...	17.302(007)	16.490(006)	...	15.637(007)	...	5
c4	...	18.652(006)	17.946(006)	...	17.108(007)	...	5
c5	...	18.929(006)	17.736(007)	...	16.365(013)	...	5
c6	...	14.970(006)	14.447(006)	...	13.772(007)	...	5
c7	...	14.752(006)	14.013(006)	...	13.224(008)	...	5
SN 1999br							
c1	16.931(014)	15.847(007)	14.778(005)	14.167(006)	13.684(006)	13.445(015)	7
c2	18.157(020)	17.233(007)	16.186(005)	15.533(006)	14.992(005)	14.742(015)	7
c3	16.723(013)	16.940(006)	16.479(005)	16.161(006)	15.832(006)	...	5
c4	20.160(063)	18.934(011)	17.460(008)	16.463(010)	15.383(006)	...	5
c5	18.700(022)	18.686(009)	17.923(006)	17.453(007)	17.002(008)	16.796(015)	7
c6	19.749(046)	20.006(016)	19.466(013)	19.136(015)	18.795(021)	18.755(071)	7
c7	20.321(082)	19.824(014)	18.911(008)	18.384(010)	17.915(014)	17.700(027)	7
c8	...	21.049(061)	19.493(012)	18.233(009)	16.671(006)	16.072(015)	6
c9	19.114(040)	18.010(006)	16.729(005)	15.896(007)	15.129(006)	14.815(015)	7
c10	19.477(034)	19.482(014)	18.887(009)	18.500(011)	18.146(014)	17.915(033)	7

Table 2.3: $UBVRIZ$ Sequences – continued

Star	<i>U</i>	<i>B</i>	<i>V</i>	<i>R</i>	<i>I</i>	<i>Z</i>	<i>n</i>
c11	15.497(010)	15.431(005)	14.788(005)	14.420(007)	14.067(006)	13.889(015)	7
c12	20.768(107)	19.712(017)	18.316(006)	17.405(010)	16.543(009)	16.145(015)	7
c13	19.449(067)	19.070(013)	18.293(007)	17.822(010)	17.419(008)	17.251(019)	6
c14	21.294(184)	21.266(054)	20.567(036)	20.079(042)	19.604(059)	19.438(132)	5
SN 1999ca							
c1	15.493(016)	15.148(010)	14.407(008)	13.965(015)	13.584(011)	13.422(015)	3
c2	19.217(027)	19.084(010)	18.318(007)	17.878(007)	17.433(009)	17.250(037)	3
c3	17.880(018)	17.727(016)	17.027(008)	16.595(015)	16.155(009)	...	3
c4	19.448(028)	18.456(008)	17.403(009)	16.775(007)	16.234(008)	15.978(015)	3
c5	19.388(027)	18.087(010)	16.819(009)	16.052(008)	15.419(009)	15.157(015)	2
c6	14.787(016)	14.781(013)	14.155(015)	13.235(015)	1
c7	16.025(012)	15.981(010)	15.336(011)	14.929(015)	14.558(015)	14.384(015)	2
c8	16.601(011)	16.319(011)	15.607(007)	15.175(011)	14.776(008)	14.588(015)	3
c9	16.874(009)	16.731(010)	16.069(009)	15.661(009)	15.271(009)	15.089(015)	2
c10	15.555(009)	15.367(010)	14.707(008)	14.300(015)	13.943(011)	13.787(015)	2
c11	19.104(022)	18.395(009)	17.337(007)	16.741(007)	16.178(008)	15.915(015)	3
c12	18.400(031)	18.380(015)	17.742(007)	17.303(007)	16.882(008)	16.696(022)	3
SN 1999cr							
c1	...	14.468(005)	13.898(005)	13.534(005)	13.172(006)	...	6
c2	...	16.022(004)	15.320(004)	14.888(004)	14.457(005)	...	11
c4	...	20.035(015)	18.745(007)	17.904(005)	17.161(010)	...	11

Table 2.3: *UBVRIZ* Sequences – continued

Star	<i>U</i>	<i>B</i>	<i>V</i>	<i>R</i>	<i>I</i>	<i>Z</i>	<i>n</i>
c5	...	17.083(004)	16.061(004)	15.448(004)	14.874(004)	...	11
c6	...	16.843(004)	16.126(004)	15.690(004)	15.259(004)	...	11
c7	...	16.677(004)	16.063(004)	15.685(004)	15.297(005)	...	11
c8	...	20.522(025)	20.053(016)	19.762(015)	19.437(020)	...	11
c10	...	20.320(019)	19.818(013)	19.471(011)	19.067(019)	...	11
c11	...	19.227(007)	18.548(015)	18.164(008)	17.784(005)	...	11
c12	...	15.814(004)	15.141(004)	14.735(004)	14.335(005)	...	11
c13	...	16.759(004)	15.909(004)	15.411(004)	14.953(004)	...	11
SN 1999eg							
c1	...	17.159(018)	16.030(011)	15.357(011)	14.765(011)	...	4
c2	...	16.934(009)	15.956(009)	15.378(009)	14.833(009)	...	4
c3	...	18.627(007)	17.813(009)	17.336(009)	16.862(010)	...	4
c4	...	18.112(009)	17.543(011)	17.175(009)	16.788(009)	...	4
c5	...	15.134(015)	13.783(015)	3
c6	...	15.407(011)	14.467(011)	13.929(015)	13.391(015)	...	2
c7	...	14.253(015)	13.478(015)	1
c8	...	15.614(011)	14.560(011)	13.956(015)	13.404(015)	...	3
c9	...	16.710(017)	15.964(011)	15.545(011)	15.145(011)	...	2
c10	...	18.256(012)	17.550(011)	17.114(011)	16.697(011)	...	2

Table 2.3: *UBVRIZ* Sequences – continued

Star	<i>U</i>	<i>B</i>	<i>V</i>	<i>R</i>	<i>I</i>	<i>Z</i>	n
SN 1999em							
c2	17.717(037)	17.569(025)	16.980(012)	16.581(011)	16.237(011)	16.123(014)	2
c3	15.773(012)	15.728(010)	15.132(010)	14.765(011)	14.430(011)	14.290(011)	2
c4	17.530(028)	16.732(010)	15.781(011)	15.205(011)	14.726(011)	14.515(011)	2
c5	18.875(102)	18.623(028)	17.840(014)	17.396(016)	16.973(017)	16.813(025)	2
c6	14.949(012)	13.627(010)	12.410(011)	11.754(015)	11.181(015)	10.904(011)	2
c7	17.622(034)	17.691(012)	17.155(011)	16.806(011)	16.477(012)	16.368(017)	1
c8	15.457(012)	14.189(010)	13.019(010)	12.405(011)	11.887(011)	11.638(011)	1
c9	16.084(012)	15.668(010)	14.885(011)	14.447(011)	14.059(011)	13.896(011)	2
SN 2000cb							
c1	17.094(017)	16.910(008)	16.210(008)	15.806(008)	15.416(008)	...	4
c2	16.936(017)	16.991(008)	16.557(008)	16.282(008)	15.972(008)	...	4
c3	16.841(017)	16.435(008)	15.609(008)	15.141(008)	14.704(008)	...	4
c4	15.521(017)	15.321(008)	14.626(008)	14.232(008)	13.851(008)	...	4
c5	16.467(017)	16.054(008)	15.244(008)	14.791(008)	14.356(008)	...	4
c6	16.895(017)	16.904(008)	16.291(008)	15.913(008)	15.524(008)	...	4
c7	17.837(021)	17.788(008)	17.182(008)	16.827(008)	16.459(009)	...	4
c8	19.397(073)	18.831(038)	18.003(009)	17.507(008)	17.018(021)	...	4
c9	18.226(028)	17.961(008)	17.264(009)	16.845(008)	16.435(008)	...	1
c10	19.280(074)	19.150(020)	18.481(010)	18.064(010)	17.683(012)	...	1
c11	16.957(017)	17.003(009)	16.411(009)	16.051(009)	15.676(009)	...	1
c12	17.711(018)	17.550(008)	16.853(010)	16.446(008)	16.039(008)	...	1

Table 2.4: *UBVRIZ* Photometry for 12 CT/SOIRS SNe II

JD- 2400000	<i>U</i>	<i>B</i>	<i>V</i>	<i>R</i>	<i>I</i>	<i>Z</i>	D/P
SN 1991al							
48455.67	...	16.608(018)	...	16.230(015)	P
48458.77	...	16.660(018)	16.570(016)	16.286(015)	16.126(015)	...	P
48459.60	...	16.664(018)	16.604(016)	16.300(015)	16.138(015)	...	P
48478.65	...	17.703(017)	16.907(015)	16.468(015)	16.341(015)	...	P
48478.66	...	17.702(017)	16.907(015)	16.466(015)	16.342(015)	...	P
48490.70	17.051(023)	...	16.380(015)	...	P
48490.72	17.077(018)	P
48499.56	17.195(030)	16.731(015)	16.465(015)	...	P
48508.63	...	18.702(018)	17.378(016)	16.848(015)	16.568(015)	...	P
48537.65	...	20.683(141)	19.206(037)	18.333(023)	17.842(032)	...	D
48545.53	...	20.864(349)	19.308(076)	D
48545.55	19.177(070)	D
48546.52	...	20.984(200)	19.309(041)	D
48547.52	...	21.158(169)	19.292(043)	D
48548.55	...	20.893(175)	19.311(054)	D
48550.54	...	21.088(198)	19.391(034)	...	18.007(022)	...	D
48550.56	18.023(020)	...	D
48551.53	...	20.627(276)	19.579(090)	18.516(029)	17.965(036)	...	D
48551.54	...	20.716(232)	...	18.545(032)	18.032(034)	...	D
48555.52	...	20.971(113)	19.406(034)	18.516(016)	18.072(027)	...	D
48555.53	...	20.887(099)	19.492(039)	18.544(025)	18.042(024)	...	D
48578.53	19.694(104)	18.767(051)	18.247(065)	...	D
48835.68	21.598(106)	D

Table 2.4: *UBVRIZ* SN Photometry – continued

JD 2400000	<i>U</i>	<i>B</i>	<i>V</i>	<i>R</i>	<i>I</i>	<i>Z</i>	D/P
48848.60	21.395(251)	D
48868.62	22.567(285)	D
48871.64	22.318(518)	D
48885.61	22.740(209)	D
SN 1992af							
48805.81	...	17.756(017)	17.145(015)	D
48805.80	17.146(015)	D
48807.62	...	17.835(031)	17.172(018)	...	16.185(188)	...	D
48807.64	...	17.862(050)	D
48809.90	...	17.867(017)	17.173(016)	D
48813.85	...	17.991(025)	17.206(016)	D
48815.82	17.327(111)	D
48816.88	17.328(057)	D
48816.90	17.289(034)	D
48817.67	...	18.147(098)	17.210(024)	...	16.662(030)	...	D
48818.67	...	18.042(052)	17.249(024)	D
48831.84	...	18.346(017)	17.257(016)	D
48842.60	...	18.631(043)	17.369(015)	D
48843.65	...	18.658(044)	17.394(015)	...	16.711(016)	...	D
48845.53	...	18.745(048)	17.437(015)	...	16.729(015)	...	D
48846.66	...	18.785(042)	17.423(015)	...	16.734(016)	...	D
48847.59	...	18.754(039)	17.459(015)	...	16.720(015)	...	D
48848.63	...	18.882(038)	17.478(015)	D

Table 2.4: *UBVRIZ* SN Photometry – continued

JD 2400000	<i>U</i>	<i>B</i>	<i>V</i>	<i>R</i>	<i>I</i>	<i>Z</i>	D/P
48849.70	...	18.769(043)	17.535(015)	...	16.794(017)	...	D
48849.69	...	18.858(050)	D
48871.58	...	21.010(145)	19.035(031)	...	17.909(019)	...	D
48871.60	17.879(017)	...	D
48872.57	...	20.562(323)	19.213(072)	...	17.933(059)	...	D
48885.69	...	21.149(071)	19.387(017)	...	18.183(017)	...	D
48891.57	...	21.172(072)	19.420(019)	...	18.243(016)	...	D
48905.60	...	21.380(322)	19.554(059)	...	18.444(031)	...	D
48905.59	...	21.194(344)	D
48908.59	...	21.312(166)	19.564(026)	...	18.398(017)	...	D
48919.61	...	21.526(051)	19.758(015)	...	18.572(015)	...	D
48919.64	...	21.376(054)	D
SN 1992am							
48832.93	...	19.002(017)	18.494(016)	D
48846.88	...	19.549(044)	18.608(020)	D
48847.82	...	19.573(052)	18.585(016)	...	18.037(016)	...	D
48848.87	...	19.814(076)	18.649(021)	...	18.055(020)	...	D
48872.79	...	20.454(178)	18.938(028)	...	18.119(028)	...	D
48885.89	...	20.604(066)	19.059(019)	...	18.181(054)	...	D
48905.68	...	20.881(287)	19.233(061)	...	18.246(043)	...	D
48908.68	19.280(063)	...	18.309(043)	...	D
48919.68	...	21.336(021)	19.454(015)	...	18.322(015)	...	D
48922.59	...	21.412(089)	19.482(016)	...	18.357(018)	...	D

Table 2.4: *UBVRIZ* SN Photometry – continued

JD 2400000	<i>U</i>	<i>B</i>	<i>V</i>	<i>R</i>	<i>I</i>	<i>Z</i>	D/P
48979.65	...	23.805(308)	21.601(056)	...	20.053(035)	...	D
SN 1992ba							
48904.76	...	15.532(019)	15.241(015)	14.951(015)	14.838(015)	...	D
48904.77	...	15.575(019)	15.226(015)	14.951(015)	14.858(015)	...	D
48904.78	14.945(015)	D
48905.83	...	15.613(019)	15.226(015)	14.977(015)	14.870(015)	...	D
48908.81	...	15.828(019)	15.296(015)	15.007(015)	14.860(015)	...	P
48922.80	...	16.305(017)	15.421(015)	...	14.831(015)	...	P
48940.77	...	16.654(017)	15.509(015)	...	14.787(015)	...	P
48941.79	...	16.678(017)	15.522(015)	...	14.787(015)	...	P
48956.80	...	16.905(016)	15.606(016)	...	14.845(015)	...	P
48975.86	...	17.147(017)	15.760(015)	P
48979.67	...	17.176(017)	15.806(015)	...	14.954(015)	...	P
48979.69	...	17.164(017)	15.801(015)	...	14.957(015)	...	P
48997.77	...	17.480(019)	16.090(015)	...	15.224(015)	...	P
49012.69	...	18.497(017)	16.882(015)	...	15.803(015)	...	P
49016.72	...	19.022(022)	17.332(015)	...	16.160(015)	...	D
49037.69	...	20.117(065)	18.169(015)	...	16.777(015)	...	D
49078.63	...	20.238(077)	18.543(016)	...	17.124(015)	...	D
49084.55	...	20.533(126)	18.558(022)	...	17.162(015)	...	D

Table 2.4: *UBVRIZ* SN Photometry – continued

JD 2400000	<i>U</i>	<i>B</i>	<i>V</i>	<i>R</i>	<i>I</i>	<i>Z</i>	D/P
SN 1993A							
49007.74	19.489(021)	D
49010.74	...	19.924(028)	19.487(016)	...	19.004(028)	...	D
49012.73	...	19.910(022)	19.500(015)	...	18.963(024)	...	D
49013.76	...	19.961(028)	19.455(017)	...	18.847(029)	...	D
49016.76	...	20.143(024)	19.457(015)	...	19.001(023)	...	D
49017.68	...	20.095(020)	19.517(018)	...	18.927(026)	...	D
49026.74	...	20.403(162)	19.587(085)	...	18.767(061)	...	D
49037.72	...	20.834(040)	19.724(018)	...	18.906(020)	...	D
49038.68	...	20.891(046)	19.671(017)	...	18.824(027)	...	D
49040.73	...	20.988(024)	19.725(015)	...	18.902(015)	...	D
49050.75	...	21.081(075)	19.704(029)	D
49053.70	...	20.962(353)	19.634(112)	...	18.921(079)	...	D
49073.68	...	21.561(096)	20.008(036)	...	19.002(029)	...	D
49084.58	...	21.219(270)	19.850(065)	...	18.948(046)	...	D
49084.63	...	21.328(271)	19.836(069)	D
49091.63	...	21.497(157)	19.840(064)	...	18.855(088)	...	D
SN 1993S							
49142.86	18.150(024)	D
49143.85	...	18.289(020)	18.142(042)	...	17.875(026)	...	D
49152.86	...	18.603(019)	18.176(016)	...	17.872(020)	...	D
49154.83	...	18.765(019)	18.239(019)	...	17.842(018)	...	D

Table 2.4: *UBVRIZ* SN Photometry – continued

JD 2400000	<i>U</i>	<i>B</i>	<i>V</i>	<i>R</i>	<i>I</i>	<i>Z</i>	D/P
49161.84	...	19.258(027)	18.465(016)	...	17.919(023)	...	D
49162.82	...	19.324(015)	18.513(015)	...	18.008(017)	...	D
49164.90	...	19.372(075)	18.546(045)	D
49179.90	...	20.279(050)	18.925(016)	...	18.241(015)	...	D
49184.75	...	20.443(030)	19.057(015)	...	18.291(015)	...	D
49185.83	...	20.533(035)	19.073(015)	...	18.357(015)	...	D
49186.79	...	20.322(170)	19.125(022)	...	18.336(033)	...	D
49187.89	...	20.510(032)	19.093(015)	...	18.331(019)	...	D
49202.81	...	21.024(336)	19.350(051)	...	18.530(039)	...	D
SN 1999br							
51283.70	...	17.583(015)	17.615(019)	D
51284.72	...	17.568(015)	17.541(015)	...	17.295(015)	...	D
51285.71	...	17.587(015)	17.509(015)	17.343(015)	17.271(021)	...	D
51286.69	...	17.633(015)	17.544(015)	17.323(015)	17.220(015)	...	P
51291.80	...	17.751(017)	17.496(016)	17.210(017)	17.052(017)	...	D
51294.67	...	17.944(017)	17.513(017)	17.225(015)	17.044(015)	...	D
51294.69	...	17.921(016)	17.531(019)	17.206(015)	17.029(015)	...	D
51294.73	17.848(035)	17.921(019)	17.506(015)	17.240(016)	17.087(016)	16.946(047)	D
51294.74	17.753(043)	17.963(018)	17.523(015)	17.246(015)	17.075(015)	16.845(046)	D
51294.75	16.896(038)	D
51294.75	16.903(037)	D
51295.59	...	18.111(031)	17.549(029)	17.313(020)	17.102(043)	...	P
51296.67	...	18.039(033)	17.641(035)	17.276(031)	17.073(026)	...	D

Table 2.4: *UBVRIZ* SN Photometry – continued

JD 2400000	<i>U</i>	<i>B</i>	<i>V</i>	<i>R</i>	<i>I</i>	<i>Z</i>	D/P
51296.68	...	18.072(023)	17.605(023)	17.289(024)	D
51299.48	...	18.156(063)	17.602(042)	17.265(025)	17.065(052)	...	P
51301.51	...	18.190(026)	17.555(026)	17.230(016)	17.023(034)	...	P
51301.53	17.621(016)	D
51301.54	...	18.281(021)	17.626(016)	17.258(015)	17.007(018)	...	D
51301.61	18.792(029)	18.267(015)	17.613(015)	17.264(015)	17.045(016)	16.890(015)	D
51304.73	...	18.369(020)	17.607(015)	17.215(015)	16.977(017)	...	D
51305.70	19.037(031)	18.413(021)	17.613(015)	17.237(015)	16.988(016)	16.821(015)	D
51305.74	...	18.500(024)	17.609(015)	P
51306.66	17.195(015)	16.953(023)	...	P
51309.61	...	18.594(020)	17.587(015)	17.183(015)	16.869(018)	...	P
51309.66	...	18.514(017)	17.614(015)	D
51309.66	17.623(015)	D
51309.67	17.624(015)	D
51309.73	17.594(015)	D
51309.74	17.611(017)	D
51309.75	17.621(015)	D
51314.57	...	18.651(020)	17.542(015)	17.110(015)	16.885(029)	...	P
51317.65	19.643(035)	18.693(023)	17.625(015)	17.140(015)	16.805(016)	16.606(015)	D
51318.60	...	18.743(021)	17.565(015)	17.126(015)	16.764(023)	...	P
51323.49	...	18.830(070)	17.595(039)	17.104(022)	16.662(043)	...	P
51328.49	...	19.127(103)	17.548(034)	17.099(018)	16.729(037)	...	P
51330.49	...	18.867(032)	17.575(021)	17.062(015)	16.618(024)	...	P
51335.49	...	18.976(027)	17.588(015)	17.069(015)	16.649(021)	...	P
51345.49	...	19.069(017)	17.572(026)	17.030(021)	16.674(085)	...	P

Table 2.4: *UBVRIZ* SN Photometry – continued

JD 2400000	<i>U</i>	<i>B</i>	<i>V</i>	<i>R</i>	<i>I</i>	<i>Z</i>	D/P
51352.46	...	19.266(068)	17.604(025)	17.026(017)	16.515(029)	...	P
51356.48	...	19.155(058)	17.658(024)	17.073(015)	16.574(021)	...	P
SN 1999ca							
51305.50	17.107(016)	16.755(015)	15.959(015)	15.537(015)	15.315(016)	15.171(015)	P
51308.56	17.754(034)	17.001(017)	16.067(015)	15.639(015)	15.379(016)	...	D
51309.50	17.665(016)	17.083(017)	16.100(015)	15.641(015)	15.399(015)	...	D
51309.51	17.628(016)	...	16.108(015)	D
51309.51	16.116(015)	D
51309.55	16.108(015)	D
51313.47	18.298(054)	17.359(017)	16.244(015)	15.768(015)	15.465(016)	...	D
51317.52	18.621(074)	17.565(017)	16.371(015)	15.869(015)	15.576(016)	...	D
51317.54	18.382(016)	17.527(015)	16.392(015)	15.832(015)	15.580(016)	15.357(015)	P
51319.46	18.964(137)	17.651(017)	16.425(015)	15.910(015)	15.611(016)	...	D
51321.46	18.879(111)	17.715(017)	16.469(015)	15.957(015)	15.641(016)	...	D
51322.50	18.850(064)	17.704(017)	16.515(015)	15.942(015)	15.679(015)	15.448(104)	D
51322.47	16.474(021)	D
51322.47	16.495(017)	D
51322.47	16.535(015)	D
51322.54	16.519(037)	D
51322.54	16.510(058)	D
51327.46	19.144(306)	17.958(017)	16.592(015)	16.049(015)	15.727(016)	...	D
51329.46	19.468(218)	18.015(017)	16.612(015)	16.063(015)	15.761(016)	...	D
51331.46	19.293(177)	18.064(017)	16.636(015)	16.086(015)	15.768(016)	...	D

Table 2.4: $UBVRIZ$ SN Photometry – continued

ID	U	B	V	R	I	Z	D/P
2400000							
51335.45	19.544(277)	18.157(017)	16.701(015)	16.134(015)	15.852(016)	...	D
51340.46	19.862(284)	18.323(017)	16.819(015)	16.208(015)	15.894(016)	...	D
51345.46	...	18.442(017)	16.868(015)	16.256(015)	15.925(016)	...	D
51351.47	...	18.614(046)	16.984(015)	16.319(015)	15.977(019)	...	D
51355.46	...	18.746(017)	17.100(015)	16.449(015)	16.126(016)	...	D
51464.86	20.685(141)	19.645(034)	D
51471.87	...	21.641(258)	D
51478.86	20.857(092)	19.858(043)	19.373(091)	...	D
51480.86	19.477(123)	...	D
51481.83	...	22.428(428)	21.217(110)	19.935(039)	19.580(054)	...	D
51484.85	...	22.821(236)	21.097(057)	19.931(027)	19.667(065)	...	D
51488.83	...	22.572(148)	21.293(043)	20.084(022)	D
51489.83	19.718(035)	19.331(056)	D
51493.85	...	22.969(167)	21.291(071)	...	19.776(149)	...	D
51506.85	21.393(114)	D
51499.86	...	22.781(174)	21.327(065)	20.247(032)	19.951(130)	...	D
SN 1999cr							
51256.78	...	18.402(017)	18.068(015)	17.777(015)	17.562(016)	...	D
51257.82	...	18.393(015)	18.054(015)	17.746(015)	17.510(015)	...	D
51257.85	...	18.436(015)	18.070(015)	17.800(015)	17.570(015)	...	D
51259.82	...	18.509(017)	18.097(015)	17.807(015)	17.558(016)	...	D
51261.82	...	18.603(017)	18.131(015)	17.818(015)	17.545(016)	...	D
51263.77	...	18.702(017)	18.169(015)	17.827(015)	17.569(016)	...	D

Table 2.4: *UBVRIZ* SN Photometry – continued

JD 2400000	<i>U</i>	<i>B</i>	<i>V</i>	<i>R</i>	<i>I</i>	<i>Z</i>	D/P
51266.73	...	18.860(017)	18.244(015)	17.867(015)	17.604(016)	...	D
51266.78	...	18.834(021)	18.216(020)	17.839(015)	17.568(015)	...	D
51266.81	...	18.825(021)	18.210(018)	17.848(015)	17.553(020)	...	D
51267.82	...	18.928(030)	18.174(020)	17.852(015)	17.589(015)	...	D
51267.84	...	18.890(026)	18.260(021)	17.846(017)	D
51274.83	...	19.130(021)	18.376(017)	17.912(015)	17.652(017)	...	D
51274.84	...	19.144(030)	D
51275.82	...	19.234(017)	18.379(015)	17.975(015)	17.677(015)	...	D
51277.78	...	19.259(015)	18.401(015)	17.961(015)	17.698(016)	...	D
51277.80	...	19.278(016)	18.444(015)	18.000(015)	D
51285.68	...	19.477(028)	18.531(022)	18.039(017)	17.749(015)	...	D
51291.82	...	19.616(018)	18.592(015)	18.081(015)	17.802(017)	...	D
51291.86	...	19.779(069)	18.618(037)	18.114(015)	17.779(029)	...	D
51294.74	...	19.547(050)	18.587(015)	18.101(015)	17.766(015)	...	D
51294.78	...	19.576(024)	D
51296.70	...	19.669(042)	18.597(015)	18.103(015)	17.765(015)	...	D
51296.71	...	19.672(047)	18.655(023)	18.176(015)	17.855(025)	...	D
51298.53	...	19.662(121)	18.662(034)	...	17.775(044)	...	D
51299.51	...	19.756(068)	18.636(039)	18.175(018)	17.910(045)	...	D
51301.55	...	19.751(051)	18.640(024)	18.170(015)	17.845(023)	...	D
51301.68	...	19.718(029)	D
51302.79	...	19.756(127)	18.638(037)	18.166(027)	17.793(019)	...	D
51304.74	...	19.751(020)	18.665(015)	18.143(015)	17.831(015)	...	D
51305.60	...	19.806(019)	18.689(015)	18.126(015)	17.832(016)	...	D
51305.79	...	19.751(021)	18.632(015)	18.077(015)	17.798(015)	...	D

Table 2.4: $UBVRIZ$ SN Photometry – continued

JD	<i>U</i>	<i>B</i>	<i>V</i>	<i>R</i>	<i>I</i>	<i>Z</i>	D/P
2400000							
51308.76	18.693(017)	18.174(015)	17.800(017)	...	D
51308.78	17.852(019)	...	D
51314.59	...	19.902(048)	18.671(022)	18.169(015)	D
51320.57	...	19.947(031)	18.768(017)	18.230(015)	17.907(019)	...	D
51347.47	...	20.982(059)	19.514(022)	18.887(015)	18.508(026)	...	D
51353.47	...	21.917(326)	20.286(090)	19.418(043)	19.148(069)	...	D
SN 1999eg							
51464.76	...	18.394(015)	18.201(019)	17.943(023)	17.744(041)	...	P
51467.75	...	18.508(017)	18.207(026)	17.902(032)	17.647(046)	...	P
51471.76	...	18.804(021)	18.279(017)	17.974(018)	17.791(031)	...	P
51472.72	...	18.891(029)	18.322(020)	17.978(021)	17.786(036)	...	P
51479.73	...	19.272(045)	18.475(024)	18.086(023)	17.858(035)	...	P
51481.73	...	19.398(035)	18.513(021)	18.115(023)	17.909(033)	...	P
51486.75	...	19.620(064)	18.589(044)	18.069(045)	17.916(089)	...	P
51487.80	...	19.720(030)	18.662(022)	P
51489.80	...	19.715(027)	18.682(016)	18.213(021)	17.993(036)	...	P
51490.71	...	19.724(028)	18.709(021)	18.233(021)	17.938(033)	...	P
51493.72	...	19.823(036)	18.732(021)	18.249(024)	17.941(034)	...	P
51498.71	...	19.949(036)	18.795(022)	18.302(020)	P
51508.68	...	20.267(136)	18.936(038)	18.424(032)	18.109(047)	...	P
51509.72	...	20.125(120)	18.887(038)	18.352(034)	18.122(057)	...	P

Table 2.4: *UBVRIZ* SN Photometry – continued

JD 2400000	<i>U</i>	<i>B</i>	<i>V</i>	<i>R</i>	<i>I</i>	<i>Z</i>	D/P
SN 1999em							
51481.76	13.703(015)	P
51483.72	13.607(015)	P
51484.76	13.570(015)	P
51485.79	13.542(015)	P
51486.80	13.549(015)	P
51487.76	13.512(015)	P
51488.80	13.514(015)	P
51489.81	13.489(015)	P
51498.78	14.420(017)	14.357(015)	13.869(015)	13.600(015)	13.483(015)	...	P
51499.81	14.522(017)	14.414(015)	13.894(015)	13.599(015)	13.482(015)	...	P
51501.75	13.296(015)	P
51506.77	13.265(015)	P
51508.82	13.241(015)	P
51509.86	13.234(015)	P
51511.85	...	14.833(015)	13.968(015)	13.633(015)	13.414(015)	...	P
51522.70	16.043(015)	15.142(015)	14.016(015)	13.618(015)	13.351(015)	...	P
51531.76	...	15.185(015)	14.011(015)	13.577(015)	13.284(015)	...	P
51538.56	13.090(015)	P
51540.55	13.102(015)	P
51546.55	13.112(015)	P
51550.55	13.108(015)	P
51578.63	...	16.060(015)	14.409(015)	13.828(015)	13.492(015)	...	P
51607.64	...	18.388(040)	16.467(015)	15.541(015)	14.956(015)	...	P

Table 2.4: *UBVRIZ* SN Photometry – continued

JD 2400000	<i>U</i>	<i>B</i>	<i>V</i>	<i>R</i>	<i>I</i>	<i>Z</i>	D/P
51636.04	21.300(400)	18.370(030)	16.658(015)	15.721(015)	15.239(015)	14.924(015)	P
51665.97	...	18.600(035)	16.968(015)	15.999(015)	15.503(025)	...	P
SN 2000cb							
51663.81	19.423(060)	18.819(016)	18.082(015)	17.684(015)	17.581(020)	...	P
51675.70	...	18.088(015)	17.200(015)	16.752(015)	16.533(015)	...	P
51676.76	...	18.018(015)	17.135(015)	16.686(015)	16.463(015)	...	P
51677.77	...	17.976(015)	17.076(015)	16.620(015)	16.399(015)	...	P
51681.74	...	17.823(015)	16.901(015)	16.434(015)	16.202(015)	...	P
51682.81	...	17.770(016)	16.863(015)	16.395(015)	16.145(015)	...	P
51683.78	...	17.738(015)	16.822(015)	16.351(015)	16.114(015)	...	P
51683.75	...	17.750(015)	16.811(015)	P
51684.75	18.571(067)	...	16.791(015)	16.308(015)	16.074(015)	...	P
51695.57	...	17.773(015)	16.625(015)	16.085(015)	15.820(016)	...	P
51699.72	...	17.877(015)	16.594(015)	16.047(015)	15.738(015)	...	P
51705.70	...	18.010(015)	16.591(015)	16.009(015)	15.675(015)	...	P
51711.77	...	18.099(029)	P
51730.67	...	18.228(015)	16.606(015)	15.960(015)	15.563(015)	...	P
51738.64	...	18.332(018)	16.662(015)	15.991(015)	15.587(015)	...	P
51745.66	...	18.425(016)	16.763(015)	16.069(015)	15.654(015)	...	P
51752.70	...	18.666(015)	16.964(015)	16.207(015)	P
51757.64	...	18.893(015)	17.181(015)	16.390(015)	15.956(015)	...	P
51795.49	...	19.832(076)	18.043(015)	17.083(015)	16.632(015)	...	P

Table 2.5: Journal of the Spectroscopic Observations

Date(UT)	Telescope	Observatory	Rest-frame Wavelength	Observer(s)	Quality
SN 1986L					
1986 Oct 9	1.0-m	CTIO	3700-7700	P. Vader	E
1986 Oct 11	1.0-m	CTIO	3750-7130	P. Vader	E
1986 Oct 12	1.0-m	CTIO	3780-7270	M. Phillips	E
1986 Oct 13	1.0-m	CTIO	3670-4950	B. Bohannan/J. Doggett	P
1986 Oct 14	1.0-m	CTIO	3660-4960	B. Bohannan/J. Doggett	P
1986 Oct 15	1.0-m	CTIO	3680-4950	B. Bohannan/J. Doggett	G
1986 Oct 20	1.0-m	CTIO	3710-4980	S. Heathcote	G
1986 Oct 26	1.0-m	CTIO	3830-7140	M. Phillips	E
1986 Oct 28	1.0-m	CTIO	3580-5070	M. Navarrete	E
1986 Oct 28	4.0-m	CTIO	3580-5100	S. Heathcote	E
1986 Oct 29	4.0-m	CTIO	3680-5200	S. Heathcote	E
1986 Nov 01	2.5-m	LCO	3300-7120	J. Maza/M.T. Ruiz	E
1986 Nov 02	2.5-m	LCO	3300-7120	J. Maza/M.T. Ruiz	E
1986 Nov 03	2.5-m	LCO	3300-7120	J. Maza/M.T. Ruiz	E
1986 Nov 03	1.0-m	CTIO	3900-7260	M. Phillips/A. Phillips	E
1986 Nov 04	2.5-m	LCO	3300-7120	J. Maza/M.T. Ruiz	E
1986 Nov 04	1.0-m	CTIO	4200-7420	J. Steiner/S. Kirhakos	E
1986 Nov 05	2.5-m	LCO	3300-7120	J. Maza/M.T. Ruiz	E
1986 Nov 06	2.5-m	LCO	3300-7120	J. Maza/M.T. Ruiz	E
1986 Nov 07	2.5-m	LCO	3300-7120	J. Maza/M.T. Ruiz	E
1986 Nov 10	1.0-m	CTIO	4170-7380	J. Steiner/S. Kirhakos	E
1986 Nov 11	1.0-m	CTIO	3800-7100	M. Phillips/A. Phillips	E
1986 Nov 14	1.5-m	CTIO	3700-6400	P. Bergeron/G. Fontaine	E

Table 2.5: Journal of Spectroscopic Observations – cont.

Date(UT)	Telescope	Observatory	Rest-frame Wavelength	Observer(s)	Quality
1986 Nov 16	1.5-m	CTIO	3700-6400	P. Bergeron/G. Fontaine	E
1986 Nov 25	1.0-m	CTIO	3500-6100	S. Heathcote	G
1986 Dec 09	1.0-m	CTIO	3690-6630	B. Bohannan	E
1986 Dec 10	1.52-m	ESO	3800-7300	D. Pelat	E
1986 Dec 23	1.52-m	ESO	4000-7470	D. Pelat	E
1987 Jan 01	1.52-m	ESO	4000-7470	D. Pelat	E
1987 Jan 23	1.0-m	CTIO	3500-6890	S. Heathcote	G
1987 Jan 30	1.5-m	CTIO	5580-7950	J. Maza/M.T. Ruiz	E
SN 1988A					
1988 Jan 28	1.5-m	CTIO	3270-7670	S. Heathcote/M. Hamuy	E
1988 Jan 29	1.5-m	CTIO	3240-7690	S. Heathcote/M. Hamuy	E
1988 Feb 02	1.5-m	CTIO	5770-10160	M. Hamuy	E
1988 Feb 03	1.5-m	CTIO	3650-7340	M. Phillips/M. Hamuy	G
1988 Mar 06	4.0-m	CTIO	7680-10150	M. Phillips/S. Heathcote	E
SN 1990E					
1990 Feb 23	...	CTIO	3360-7830	...	G
1990 Mar 04	...	CTIO	3550-9000	...	E
1990 Jul 03	...	CTIO	3540-7680	...	G

Table 2.5: Journal of Spectroscopic Observations – cont.

Date(UT)	Telescope	Observatory	Rest-frame Wavelength	Observer(s)	Quality
SN 1990K					
1990 May 31	4.0-m?	CTIO	3200-9500	R. Williams/M. Phillips?	E
1990 Jun 07	...	CTIO	3600-7670	...	E
1990 Jun 08	...	CTIO	6060-10100	...	E
1990 Jun 12	...	CTIO	3900-7670	...	G
1990 Jun 18	...	CTIO	6070-9000	...	P
1990 Jul 03	...	CTIO	3800-7690	...	G
1990 Aug 13	...	CTIO	4360-7660	...	G
1990 Aug 17	...	CTIO	4000-7660	...	G
SN 1991al					
1991 Aug 05	3.6-m	ESO	3600-9800	E. Capellaro	E
1991 Aug 06	3.6-m	ESO	3830-6950	E. Capellaro	G
1991 Aug 10	3.6-m	ESO	3690-9860	E. Capellaro	E
1991 Aug 13	2.2-m	ESO	4450-7030	E. Capellaro	E
1991 Sep 02	1.5-m	CTIO	3600-7620	M. Hamuy	E
1991 Sep 14	4.0-m	CTIO	3600-7400	M. Phillips	E
1991 Oct 10	1.5-m	CTIO	4500-7600	M. Hamuy	G/P
1991 Nov 07	4.0-m	CTIO	3700-7350	M. Hamuy/R. Smith	E

Table 2.5: Journal of Spectroscopic Observations – cont.

Date(UT)	Telescope	Observatory	Rest-frame Wavelength	Observer(s)	Quality
SN 1992af					
1992 Jul 09	1.5-m	CTIO	4700-7030	K. Wakamatsu/M. Malkan	P
1992 Jul 10	1.5-m?	CTIO	4700-7010	K. Wakamatsu/M. Malkan?	P
1992 Jul 29	4.0-m	CTIO	3600-7360	M. Phillips/A. Alonso	E
1992 Oct 01	4.0-m	CTIO	3800-7350	M. Phillips	E
1992 Oct 31	4.0-m	CTIO	3800-7280	M. Phillips	E
SN 1992am					
1992 Jul 29	4.0-m	CTIO	3200-6880	M. Phillips/A. Alonso	E
1992 Oct 01	4.0-m	CTIO	3680-7110	M. Phillips	E
SN 1992ba					
1992 Oct 01	4.0-m	CTIO	3280-7450	M. Phillips	E
1992 Oct 01	4.0-m	CTIO	6160-9440	M. Phillips	G
1992 Oct 05	4.0-m	CTIO	3250-7300	J. Maza	E
1992 Oct 05	1.5-m	CTIO	5970-9820	M. Hamuy	G
1992 Oct 27	1.5-m	CTIO	3200-7660	M. Hamuy	E
1992 Nov 23	4.0-m	CTIO	3200-7410	J. Maza	E
1992 Dec 18	4.0-m	CTIO	3200-7450	M. Phillips	E
1993 Jan 28	4.0-m	CTIO	3700-6950	M. Phillips	E
1993 Feb 27	2.2-m	ESO	4000-9050	M. Della Valle	E
1993 Mar 21	4.0-m	CTIO	5800-9120	M. Phillips	E

Table 2.5: Journal of Spectroscopic Observations – cont.

Date(UT)	Telescope	Observatory	Rest-frame Wavelength	Observer(s)	Quality
SN 1993A					
1993 Jan 28	4.0-m	CTIO	3590-6800	M. Phillips	E
1993 Apr 21	4.0-m	CTIO	3760-7210	M. Hamuy	P
SN 1993S					
1993 Jun 26	1.5-m	CTIO	3400-7450	M. Hamuy	G
1993 Jun 28	NTT	ESO	3880-9310	M. Della Valle	G
1993 Jul 23	1.5-m	CTIO	4180-7440	M. Hamuy	G/P
1993 Aug 24	3.6-m	ESO	3600-9540	E. Capellaro	E
SN 1999br					
1999 Apr 23	2.5-m	LCO	3830-9170	M. Phillips/Peralta	E
1999 Apr 26	1.5-m	ESO	3490-9660	I. Pérez	E
1999 Apr 29	NTT	ESO	3370-10080	M. Hamuy/V. Doublier	E
1999 May 03	NTT	ESO	3300-10040	M. Hamuy/S. Brillant	E
1999 May 11	1.5-m	ESO	3740-10080	M. Hamuy/A. Pizzella	E
1999 May 19	NTT	ESO	3460-10010	M. Hamuy/S. Brillant	E
1999 May 21	3.6-m	ESO	3400-10200	F. Patat/M. Turatto ?	E
1999 Jul 21	1.5-m	ESO	3700-9000	M. Turatto/A. Pizzella ?	E
SN 1999ca					

Table 2.5: Journal of Spectroscopic Observations – cont.

Date(UT)	Telescope	Observatory	Rest-frame Wavelength	Observer(s)	Quality
1999 May 06	VLT/Antu	ESO	10790-13400	M. Hamuy/C. Lidman	E
1999 May 07	NTT	ESO	3250-9970	J. Maza	E
1999 May 11	1.5-m	ESO	3360-10030	M. Hamuy/A. Pizzella	E
1999 May 19	NTT	ESO	3280-9780	M. Hamuy/S. Brillant	E
				SN 1999cr	
1999 Mar 20	2.5-m	LCO	3560-9060	M. Phillips/H. Olivares?	E
1999 Mar 30	4.0-m	CTIO	3450-8780	G. Aldering	G
1999 Apr 23	2.5-m	LCO	3730-9070	M. Phillips/F. Peralta ?	E
1999 May 03	NTT	ESO	3350-9470	M. Hamuy/S. Brillant	G
1999 May 07	NTT	ESO	3350-9440	J. Maza	E
				SN 1999eg	
1999 Oct 16	2.5-m	LCO	3700-8970	M. Phillips	G
1999 Nov 19	NTT	ESO	4590-9200	M. Hamuy/V. Doublier	G/P

Table 2.5: Journal of Spectroscopic Observations – cont.

Date(UT)	Telescope	Observatory	Rest-frame Wavelength	Observer(s)	Quality
SN 1999em					
1999 Oct 30	1.5-m	CTIO	3300-9700	C. Smith	E
1999 Nov 02	VLT/Antu	ESO	9920-24900	M. Hamuy/C. Lidman/M. Petr	E
1999 Nov 03	NTT	ESO	3300-10040	J. Maza	E
1999 Nov 09	NTT	ESO	3310-9700	M. Hamuy/S. Brillant	E
1999 Nov 14	NTT	ESO	3330-10060	M. Hamuy/V. Doublier	E
1999 Nov 18	VLT/Antu	ESO	9880-25170	Service Observing	E
1999 Nov 19	NTT	ESO	3380-10010	M. Hamuy/V. Doublier	E
1999 Nov 28	VLT/Antu	ESO	9830-25120	M. Hamuy/C. Lidman/? Chadid	E
1999 Dec 16	2.5-m	SO	4910-9250	C. Corbally/A. Omizzolo	E
1999 Dec 31	2.5-m	SO	3350-7100	D. Burstein/Y. Li	E
SN 2000cb					
2000 Apr 29	4.0-m	CTIO	3240-8970	G. Aldering/A. Conley	E
2000 May 02	NTT	ESO	3800-9440	M. Hamuy	E
2000 May 08	NTT	ESO	3780-9500	J. Maza	E
2000 May 25	1.0-m	LCO	4470-6670	H. Rivera	E
2000 May 29	2.5-m	SO	3840-5560	D. McIntosh	E
2000 May 30	2.5-m	SO	3840-5560	D. McIntosh	E
2000 May 31	NTT	ESO	3300-10020	M. Hamuy	E
2000 Jul 03	2.5-m	SO	3890-6890	J. Liebert/E. Mamajeck	E

Quality Code: E: excellent, G: Good, P:Poor

CHAPTER 3 THE EXPANDING PHOTOSPHERE METHOD

3.1 Introduction

In this chapter I summarize the physics of SN II light curves and the essential ideas of the expanding photosphere method. Then I describe my implementation of the method, i.e., my prescriptions to compute photometric angular radii, spectroscopic physical sizes, dust extinction, and uncertainties in the derived distances. With all these ingredients and the data presented in Chapter 2 I proceed to show EPM results for the 17 SNe. As opposed to the previous work of Schmidt et al. (1994b), I find that great caution must be exercised in order to derive reliable EPM distances, and that the method does not always yield consistent distances at different epochs (e.g. SNe 1986L and 1999cr). In the next chapter I perform a detailed assessment of EPM.

3.2 The physics of SN II light curves

The presence of neutron stars in SN remnants has given support to the original idea by Baade & Zwicky that SNe II result from the collapse of the core of a massive star (Falk & Arnett, 1977; Weaver & Woosley, 1980; Arnett, 1996). The gravitational energy released during the collapse ($\sim 10^{53}$ ergs) is mainly radiated in the form of neutrinos. Such an explosion mechanism was first confirmed with the detection of neutrinos from SN 1987A (Svoboda, 1987). A very small fraction of the neutrino energy goes into accelerating a shock wave which heats and accelerates the matter. After a few hours of propagation through the star, the shock emerges at the surface, the photospheric temperature rises to

$10^5\text{-}10^6$ K, and the surface begins to expand at $v > 3 \times 10^4$ km s $^{-1}$. The presence of broad P-Cygni profiles in SN II spectra provides unambiguous evidence for a high-velocity expanding atmosphere.

The first phase of SN evolution consists of a period of several (~ 20) days during which a cooling wave proceeds inward in mass but in which the photosphere is swept outward by the expansion of the ejecta. Despite the increase in radius the supernova luminosity declines owing to the temperature decrease. Since much of the opacity is due to Thomson scattering by ionized electrons the opacity suddenly drops when the photospheric temperature reaches the value of H recombination at $\sim 6,000$ K. At this point, a longer-lasting era begins during which a recombination wave moves inward in mass, uncovering the inner material and releasing radiation trapped in the ejecta. The photosphere is expected to be nearly coincident with the recombination front and, to zero order, remains constant in radius and temperature, giving rise to the extended plateau. Since the ionization potential varies from ion to ion, the photospheric temperature is expected to change with the He/H mixture, from 6,000 K for pure H to 12,000 K for pure He. As the photosphere recedes, the SN eventually reaches the point where nearly all of the ejected matter becomes transparent (nearly ~ 120 days after explosion) and the bolometric luminosity begins to track the instantaneous energy input from the radioactive elements freshly synthesized in the explosion. According to hydrodynamic models the source of radioactivity is ^{56}Ni which decays to ^{56}Co with a half-life of 6.1 days. The daughter then decays to ^{56}Fe with a half-life of 77.1 days. The exponential tail of SNe II observed at optical wavelengths is attributed to thermalized γ rays from the radioactive decay of ^{56}Co (Weaver & Woosley, 1980).

In the frame of the model just outlined, it is thought that variations in the H envelope mass are responsible for the different light curve shapes displayed by linear and plateau SNe. Typical models of plateau SNe consist of a massive ($< 10 M_{\odot}$) H-rich mantle,

while linear SNe are thought to be due to progenitors that undergo substantial loss of their H outer layers, either by mass transfer or pre-supernova stellar winds. With little H in the envelope the recombination wave phase is shortened significantly, thus leading to a weak or absent plateau. Litvinova & Nadezhin (1983) estimated $\sim 0.1\text{-}0.3 M_{\odot}$ of H for linear SNe, while the models of Swartz et al. (1991) required the envelope mass to range from 0.5 to $5 M_{\odot}$. More recent models computed by Arnett (1996) for the linear SN 1980K suggested $2.2 M_{\odot}$ for the H envelope. Blinnikov & Bartunov (1993) argued that an extended circumstellar medium around the SN was also required to reproduce the light curves of the linear SN 1979C. Its role is to absorb ultraviolet photons and reradiate them at longer wavelengths. This hypothesis is supported by the high radio luminosity of SN 1979C (Weiler et al., 1981), presumably due to the collision of the SN ejecta with the circumstellar material ejected by the SN progenitor. Among SNe II-P, 1999em has been the first and only radio detected event and the least radio luminous (except for the unusual SN 1987A) (Pooley et al., 2001; Weiler et al., 1998), thus suggesting that this type of SN undergoes less mass loss before the explosion compared to linear events.

Also relevant to the morphology of the light curve is the radius of the SN progenitor. Smaller progenitors must spend a larger fraction of their explosion energy in adiabatic expansion and, thus are expected to produce dimmer plateaus (Arnett, 1980). A classical SN II-P requires an initial radius like that of a red supergiant ($R_0 \sim 10^{13}$ cm). On the other hand, if the progenitor is a blue supergiant, the plateau becomes dim enough that the luminosity due to radioactive heating can promptly exceed that due to shock-deposited energy. In the models of Arnett (1996) and Blinnikov et al. (2000) for SN 1987A, for example, a compact blue supergiant with $R_0=3\times 10^{12}$ cm and $15 M_{\odot}$ of ejected matter yielded a light curve with a steady brightening of 3 mag during 60 days, a broad peak, a fast decline phase in 30 days, and the exponential tail.

3.3 Basic ideas of EPM

EPM involves measuring a photometric angular radius and a spectroscopic physical radius from which a SN distance can be derived. Assuming that continuum radiation arises from a spherically-symmetric photosphere, a photometric measurement of its color and magnitude determines its angular radius θ ,

$$\theta = \frac{R}{D} = \sqrt{\frac{(1+z)f_\lambda}{\zeta_{\lambda'}^2 \pi B_{\lambda'}(T) 10^{-0.4[A(\lambda') + A(\lambda)]}}}, \quad (3.1)$$

where R is the photospheric radius, D is the luminosity distance to the SN, $B_{\lambda'}(T)$ is the Planck function at the color temperature of the blackbody radiation in the SN rest-frame, f_λ is the observed flux density, $A(\lambda')$ is the dust extinction in the host galaxy, $A(\lambda)$ is the foreground extinction in the Galaxy, λ' is the wavelength of light in the source frame, and $\lambda=(1+z)\lambda'$ is the corresponding redshifted wavelength in the observer's frame. This equation includes the two redshift effects usually incorporated in the K -term (Oke & Sandage, 1968), namely, the $(1+z)$ shift of photons to longer wavelengths and the corresponding flux reduction by a factor $(1+z)$ owing to the spread of light emitted in wavelength interval $d\lambda'$ to the observer's interval $d\lambda$. The two other $(1+z)$ factors due to time dilation and the decrease in energy of each photon are not included here since they are incorporated in the definition of luminosity distance used to determine cosmological parameters.

The factor $\zeta_{\lambda'}$ accounts for the fact that a real SN does not radiate like a blackbody at a unique color temperature. The SN atmosphere has a large ratio of scattering to absorptive opacity, a ratio which varies with wavelength due to line blanketing and varying continuous absorption. The result is that the photosphere, which lies at a larger radius than the thermalization depth where the color temperature is set, radiates less strongly than a blackbody at that temperature, and the color temperature itself depends upon the photometric bands employed to measure it and the redshift of the SN. $\zeta_{\lambda'}$ is known as the “flux

dilution correction”, though it takes into account departures from a blackbody SN arising from all effects. Its role is to convert the observed angular radius into the photospheric angular radius, defined as the region of total optical depth $\tau=2/3$ or the last scattering surface. Since the continuum opacity in the optical and near IR is dominated by electron scattering, the total opacity is grey, and the photospheric angular radius is independent of wavelength (E96), which explains why θ does not have a wavelength subscript.

A measurement of the photospheric radius R can then convert the angular radius to the distance to the SN. Because SNe are strong point explosions, they rapidly attain a state of homologous expansion in which the radius at a time t is given by

$$R = R_0 + \frac{v(t - t_0)}{(1 + z)}, \quad (3.2)$$

where v is the photospheric velocity measured from spectral lines, t_0 is the time of explosion, and R_0 is the initial radius of the shell. The $(1 + z)$ factor accounts for the effects of time dilation in an expanding Universe. Combining these equations I get

$$\theta_i = \frac{R_0 + \frac{v_i(t_i - t_0)}{(1+z)}}{D}, \quad (3.3)$$

where θ_i and v_i are the observed quantities measured at time t_i . Because the expansion is so rapid (typically $\sim 10^9$ cm s $^{-1}$), R_0 rapidly becomes insignificant. Even for a large progenitor with $R_0=5\times 10^{13}$ cm [2× larger than the largest luminosity class I star known, van Belle et al. (1999)], the initial radius is only 10% of the SN radius at an age of five days (and less at later times), so it is safe to use the following approximation for all but the first days,

$$\frac{\theta_i}{v_i} \approx \frac{(t_i - t_0)}{(1 + z)D}. \quad (3.4)$$

This equation shows that photometric and spectroscopic data at two or more epochs are needed to solve for D and t_0 .

Clearly, the determination of distances relies on our knowledge of $\zeta_{\lambda'}$. EPM was first applied to SNe II by Kirshner & Kwan (1974), assuming that SNe II emitted like perfect blackbodies ($\zeta_{\lambda'}=1$). SKE92 corrected this situation by computing dilution factors from SNe II atmosphere models and optical distance correction factors derived empirically from SN 1987A. A major step forward in the knowledge of the dilution factors was achieved by E96 from detailed NLTE models of SNe II-P encompassing a wide range in luminosity, density structure, velocity, and composition. They found that the most important variable determining $\zeta_{\lambda'}$ was the effective temperature; for a given temperature, $\zeta_{\lambda'}$ changed by only 5-10% over a very large variation in the other parameters. This result implied that EPM has the potential to measure accurate distances without the need for a specially-crafted model for each SN. Because their models were only valid for H-rich massive atmospheres, they recommended to limit the application of the dilution factors to SNe II-P during the plateau phase of H recombination. This excluded linear SNe, not only due to their low-mass H mantle, but because of the effects caused by circumstellar material which were not part of the E96 models.

One great advantage of distances determined by EPM is that they are independent of the “cosmic distance ladder.” Photometric and spectroscopic observations at two epochs and a physical model for the SN atmosphere lead directly to a distance. Moreover, additional observations of the same SN are essentially independent distance measurements as the properties of the photosphere change over time. This provides a valuable internal consistency check.

Next I use the model atmospheres of E96 (kindly provided to me by R. Eastman), to compute dilution factors for the 17 SNe with the purpose to assess the performance of the method, both at optical and IR wavelengths.

3.4 The measurement of angular radii

EPM involves measuring the photometric angular radius of the SN (equation 3.1) by fitting Planck curves [$B_{\lambda'}(T_S)$] to the observed magnitudes. Here S is the filter combination used, i.e., $S = \{BV\} = \{VI\} = \{BVI\}, \dots$. With two wavelengths the solution is exact (two equations and two unknowns). For three or more wavelengths I use the method of least-squares at each epoch to find the color temperature T_S and the parameter $\theta\zeta_{S,z}$ that minimize the quantity

$$\chi^2 = \sum_{\bar{\lambda} \in S} \frac{[m_{\bar{\lambda}} + 5 \log(\theta\zeta_{S,z}) - b_{\bar{\lambda}}(T_S, z)]^2}{\sigma_m^2}. \quad (3.5)$$

In this equation $m_{\bar{\lambda}}$ is the SN's apparent magnitude in a photometric band with central wavelength $\bar{\lambda}$, σ_m is the corresponding photometric error, and $b_{\bar{\lambda}}(T_S, z)$ is the synthetic magnitude of $\pi B_{\lambda'}(T_S) 10^{-0.4[A(\lambda') + A(\lambda)]}/(1+z)$, i.e.,

$$b_{\bar{\lambda}}(T_S, z) = -2.5 \log_{10} \int \frac{\pi \lambda B_{\lambda}(T_S) 10^{-0.4[A(\lambda') + A(\lambda)]}}{hc(1+z)} S(\lambda) d\lambda + ZP. \quad (3.6)$$

The λ/hc factor has the role to convert energy flux into photon flux, to account for the fact that photometric observations are obtained with photon detectors.

The integration scheme, filter functions, and zero points for the computation of synthetic magnitudes are all crucial for the determination of angular radii and EPM distances. The details about the computation of synthetic magnitudes can be found in Appendix A. Color-temperature calibrations can be derived for any filter pair in this photometric system by computing $b_{\bar{\lambda}}(T, z=0)$. Following E96, I fit a polynomial of the form

$$b_{\bar{\lambda}}(T, z=0) = \sum_{i=0}^5 c_i(\lambda) \left\{ \frac{10^4 K}{T} \right\}^i \quad (3.7)$$

in the range $4,000 \text{ K} < T < 25,000 \text{ K}$. I choose this high order so that the magnitude residuals are always below 0.01 mag. Figure 3.1 shows $b_{\bar{\lambda}}(T, z=0)$ for the B filter (top),

and the magnitude residuals from the polynomial fit (bottom). Table 3.1 gives the resulting coefficients $c_i(\lambda)$ for the $BVRIJHK$ filters. From these fits it is straightforward to compute the color temperature from any pair of magnitudes. Figure 3.2 (top) illustrates some of these temperature-color curves. Note that, as expected, all these curves intersect at $T \sim 10,000$ K, which corresponds to the photospheric temperature of Vega which has nearly zero colors at all wavelengths. The bottom panel shows the temperature difference between my calibration and that of E96. This comparison reveals that significant differences in color temperatures can be obtained depending on the photometric system adopted. The disagreement is particularly large at high temperatures where a small difference in color translates into a large variation in temperature. Since the angular radius $\theta\zeta_{S,z}$ must be corrected for a dilution factor computed from atmosphere models, $\zeta_{S,z}$ must be computed in the same photometric system described above.

In general, the dilution factor is the ratio of the luminosity of the atmosphere model and its corresponding blackbody luminosity, i.e.,

$$\zeta_{\lambda'} = \sqrt{\frac{L_{\lambda'}}{\pi B_{\lambda'}(T) 4\pi R^2}}. \quad (3.8)$$

In practice, the dilution factor must be determined for the same photometric system employed in the observations. Since the angular radius and color temperature of the SN are determined from filters which are effectively shifted to the blue, both the model and the blackbody must be redshifted. My calculation of $\zeta_{S,z}$ begins by performing this operation to the model spectra of E96, fitting them with blackbody curves $B_{\lambda'}(T_S)$, and solving for T_S and $\zeta_{S,z}$ by minimizing the quantity

$$\sum_{\bar{\lambda} \in S} [M_{\bar{\lambda}} + 5 \log(R/D_{10}) + 5 \log \zeta_{S,z} - b_{\bar{\lambda}}(T_S, z)]^2. \quad (3.9)$$

R is the photospheric radius (defined as the last scattering surface), and $M_{\bar{\lambda}}$ is the redshifted broadband absolute magnitude of the atmosphere model for a filter with central

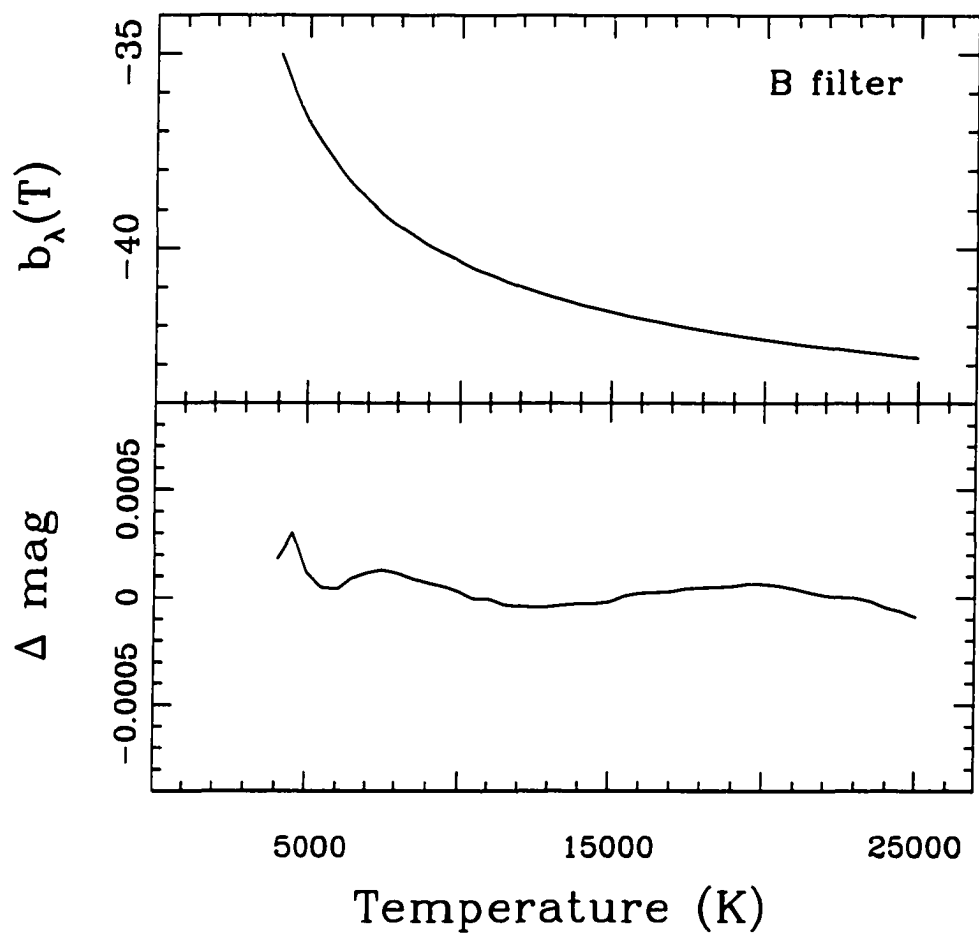


Figure 3.1: (top) Relation between $b_\lambda(T, z = 0)$ and color temperature for the B filter.
(bottom) Magnitude residuals between $b_\lambda(T, z = 0)$ and the polynomial fit.

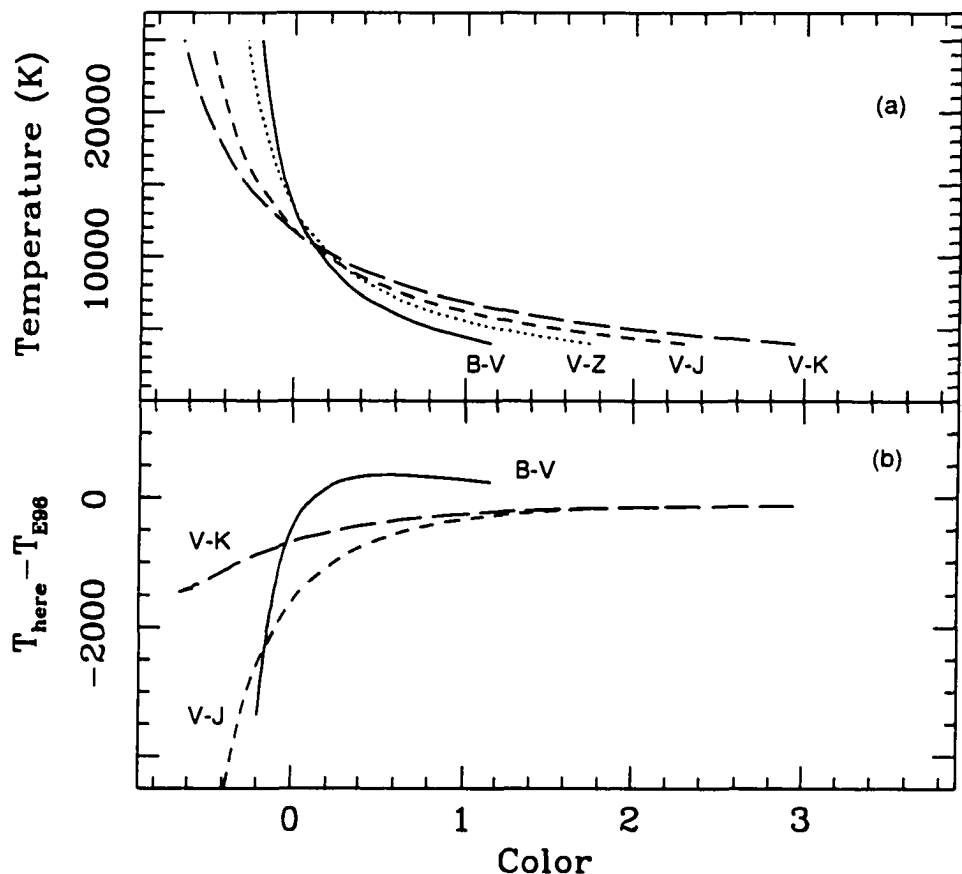


Figure 3.2: (a) Relation between color temperature and four different colors in my photometric system. (b) Difference in color temperature between my calibration and that of E96. Note that the colors become nearly degenerate at high temperatures. Because the hottest SN temperature used in this study is $< 15,000$ K, the discrepancy between the two calibrations is negligible.

wavelength $\bar{\lambda}$, i.e.,

$$M_{\bar{\lambda}} = -2.5 \log_{10} \int \frac{\lambda L_{\lambda'}}{hc(1+z)4\pi D_{10}^2} S(\lambda) d\lambda + ZP. \quad (3.10)$$

Here $L_{\lambda'}$ is the luminosity of the model, λ' is the rest-frame wavelength, and D_{10} is the standard 10 pc distance used in the definition of absolute magnitudes.

Clearly, the resulting dilution factor is a function of z and is only valid for the specific redshift of the SN. Figure 3.3 shows ζ factors for eight filter combinations for the specific case of $z = 0$. The differences between the new dilution factors and those of E96 are less than 5% and, not surprisingly, I recover the result that ζ is primarily determined by temperature. For convenience, therefore, I perform polynomial fits to $\zeta(T_S)$, i.e.,

$$\zeta(T_S) = \sum_{i=0}^2 a_{S,i} \left\{ \frac{10^4 K}{T_S} \right\}^i. \quad (3.11)$$

Table 3.2 gives the resulting coefficients $a_{S,i}$ for the eight filter subsets and in Figure 3.3 I compare these fits to the individual ζ factors. Following E96, I remove the peculiar models s15.5.1, s25.5.1, and h10.30.1 (shown with crosses), as they are not appropriate models for SNe II-P.

For the general case of a SN at redshift z , the procedure to obtain the photospheric radius consists in:

- 1) obtaining the parameters $\theta\zeta_{S,z}$ and T_S (equation 3.5),
- 2) computing $\zeta_{S,z}$ from the E96 models (equation 3.9),
- 3) performing polynomial fits to $\zeta(T_S)$,
- 4) using T_S to get $\zeta_{S,z}$ (equation 3.11), and
- 5) solving for θ from $\theta\zeta_{S,z}$.

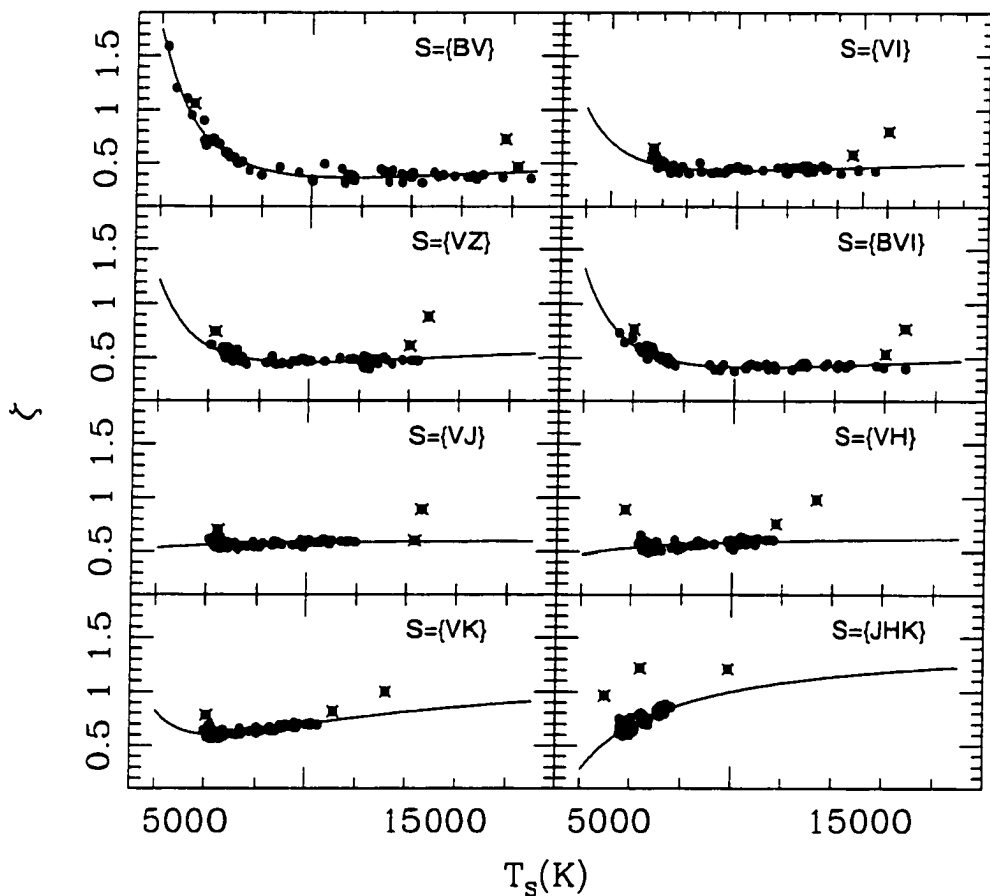


Figure 3.3: Dilution factors ζ computed from E96 atmosphere models vs. color temperature derived from eight different filter subsets ($z=0$). The solid lines correspond to a polynomial fit to $\zeta(T_s)$, from which three deviant models (shown with crosses) are removed.

3.5 The determination of dust extinction in the host galaxies

Equation 3.1 shows that the derivation of angular radii requires one to know the amount of extinction suffered by the SN along the line-of-sight in the host galaxy and the Galaxy.

E96 pointed out that dust is far less of a problem than it is for the standard-candle technique because, while dust makes the SN to appear fainter, it also makes it appear cooler and therefore with a lower intrinsic luminosity. They also showed that, to first order, the two effects tend to cancel out and that the uncertainty in angular radius is less than 10% for a 1 mag uncertainty in visual extinction. Their analysis, however, did not include the effects of dust in the dilution factors which are mainly determined by temperature and thus, by the adopted $A(V)$. Hence, the sensitivity of EPM to dust might be larger than previously suspected so it proves necessary to come up with a method to estimate $A(V)$.

The estimate of the amount of foreground visual extinction is under good control ($\sigma=0.06$ mag) thanks to the IR dust maps of Schlegel et al. (1998) (see Table 2.1 for the adopted values). The determination of absorption in the host galaxy, on the other hand, is more challenging. Since SNe II occur near HII regions, this is potentially a significant problem. In principle, the reddening caused by dust can be determined, provided I know the intrinsic color of the source and the extinction law. For the latter I adopt the mean curve of Cardelli et al. (1989) ($R_V=3.1$) which is valid for dense and diffuse regions of the interstellar medium. The more challenging aspect of the extinction correction is the determination of intrinsic colors. To zero order SNe II should all reach the same temperature of H recombination during the plateau phase. Unfortunately, significant variations between 6,000-12,000 K are expected for the photosphere depending on the H/He abundance ratio (Arnett, 1996) which limits the precision of the method to estimate color excesses. Keeping this caveat in mind, I proceed now to use the observed colors to estimate $A_{host}(V)$, using the well-studied SN 1987A as the reference for the intrinsic color.

For this purpose I adopt $A_{GAL}(V)=0.249$ and $A_{host}(V)=0.216$, which corresponds to a total color excess of $E(B-V)=0.15\pm0.05$ for SN 1987A (Suntzeff & Bouchet, 1990).

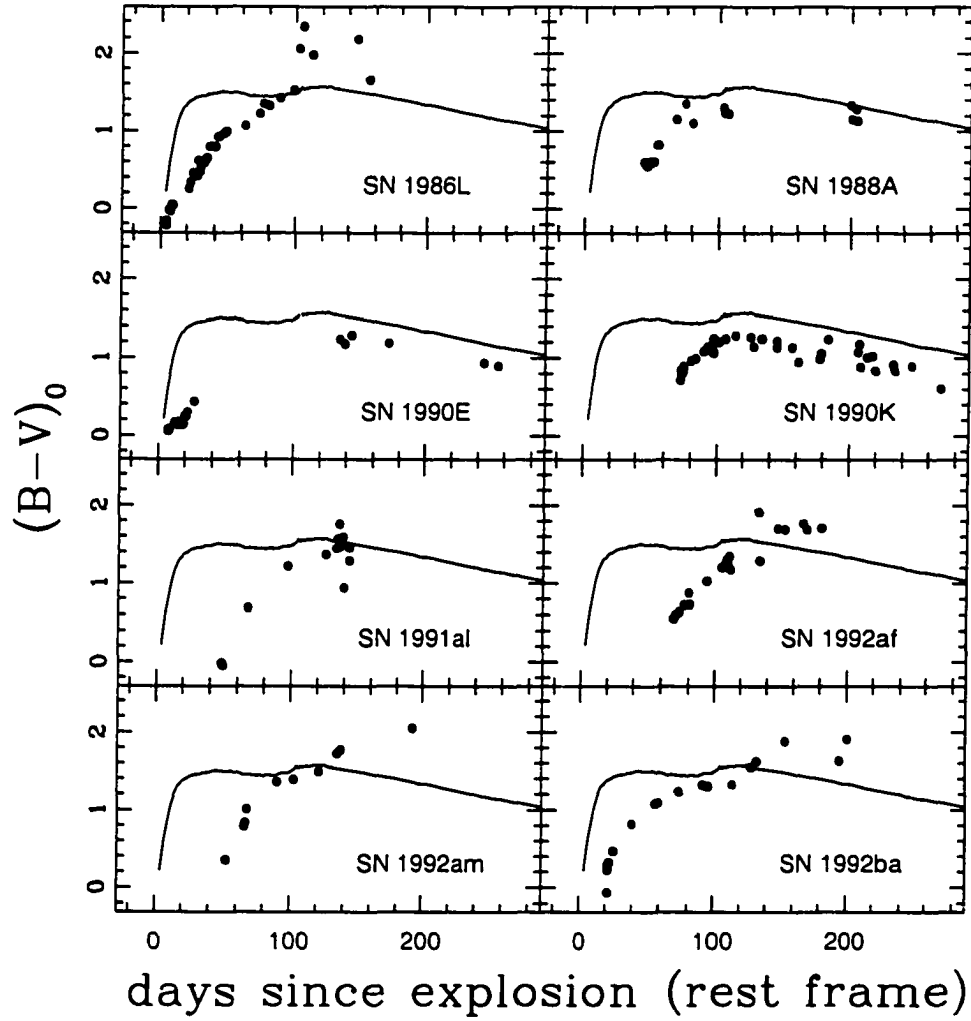


Figure 3.4: $(B-V)_0$ color curve of SNe II. The solid line corresponds to SN 1987A (part 1).

Figures 3.4 and 3.5 display intrinsic $(B-V)_0$ color curves for the 17 SNe of my sample as a function of time since explosion (derived from the EPM analysis given below), compared to that of SN 1987A (solid line). Clearly SN 1987A displayed a much faster

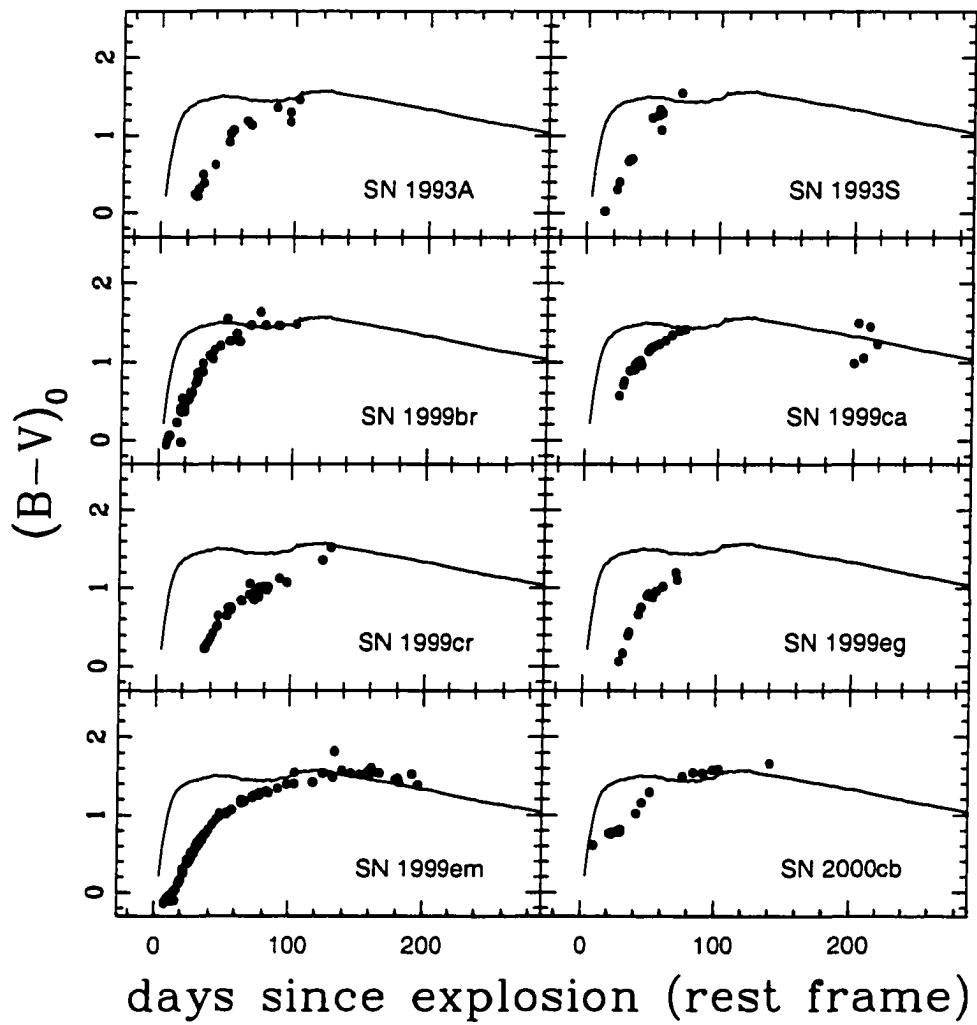


Figure 3.5: $(B - V)_0$ color curve of SNe II. The solid line corresponds to SN 1987A (part 2).

cooling than any of the other SNe and promptly reached $(B - V)_0 \sim 1.5$ during the plateau (until day 120). All other SNe had a color behavior consistent with a gradual reddening during the recombination phase and a slow decrease in color during the nebular phase (it is difficult to generalize, however, due to the incompleteness of photometric data in some cases). The very different cooling rates of these SNe make it difficult to estimate a color excess. Lacking other possibilities I assume here the hypothesis that SNe II asymptotically cool down to the same photospheric temperature before the onset of the nebular phase. For the cases lacking sufficient data, I assume also that the color during the nebular phase should be roughly the same for all SNe. With these criteria and a simple eye-ball fitting I adjust the observed color curve to match the color curve of SN 1987A and obtain the intrinsic color curves shown in Figures 3.4 and 3.5. An inspection of these plots clearly reveals some problems. In particular, while SNe 1990E and 1990K appeared too blue compared to SN 1987A in the nebular phase, SN 1992af looked too red.

The explanation to these problems can be found in the analysis of the $(V - I)_0$ colors curves which are shown in Figures 3.6 and 3.7. Again, all objects showed the photospheric cooling during the recombination phase, followed by a tail of nearly constant color. Adopting the same criteria outlined above for the $(B - V)$ color, I derive color excesses for the objects of my sample relative to SN 1987A. It is possible to see that the two SNe that appear "blue" in $(B - V)$ look red now. This means that it is not possible to derive a consistent reddening from both colors and that it proves necessary to adopt an intermediate value that minimizes the discrepancies. Obviously the opposite argument applies to SN 1992af.

In the three most challenging cases the discrepancy in the derived $A_{host}(V)$ values is ± 0.6 mag. In the other cases the agreement is much better and usually $A_{host}(V)$ agree within ± 0.2 mag. It is reasonable, therefore, to assume a global uncertainty of ± 0.3 mag in the $A_{host}(V)$ values determined from the $(B - V)$ and $(V - I)$ color curves. Note that

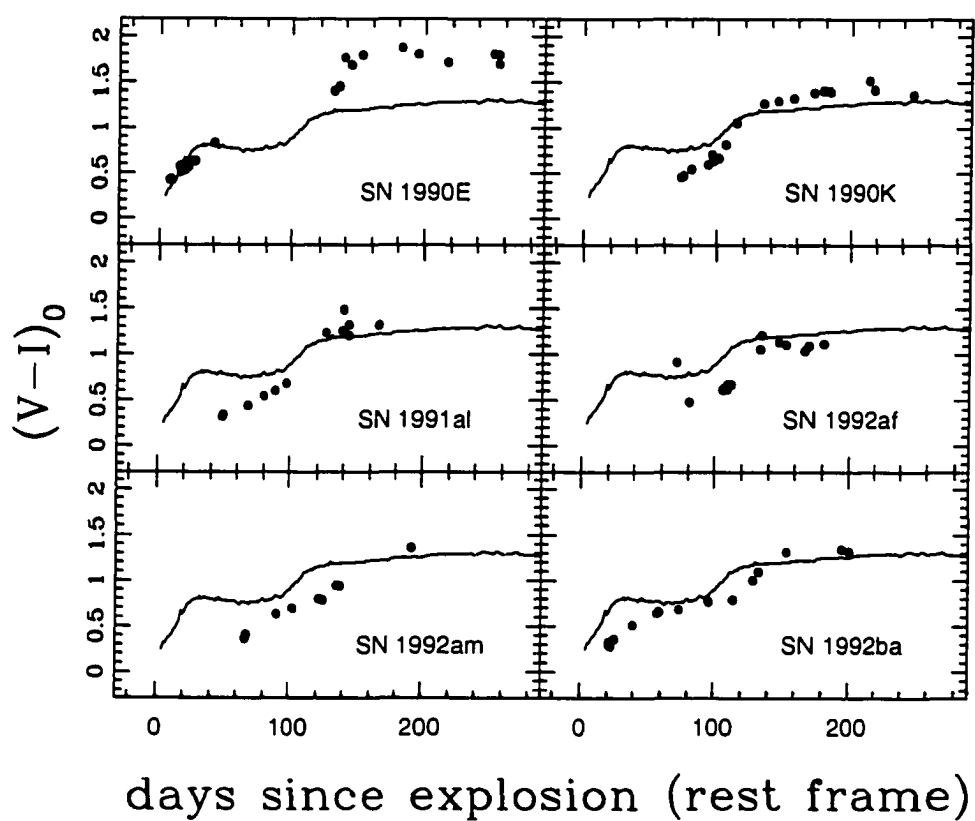


Figure 3.6: $(V - I)_0$ color curve of SNe II. The solid line corresponds to SN 1987A (part 1).

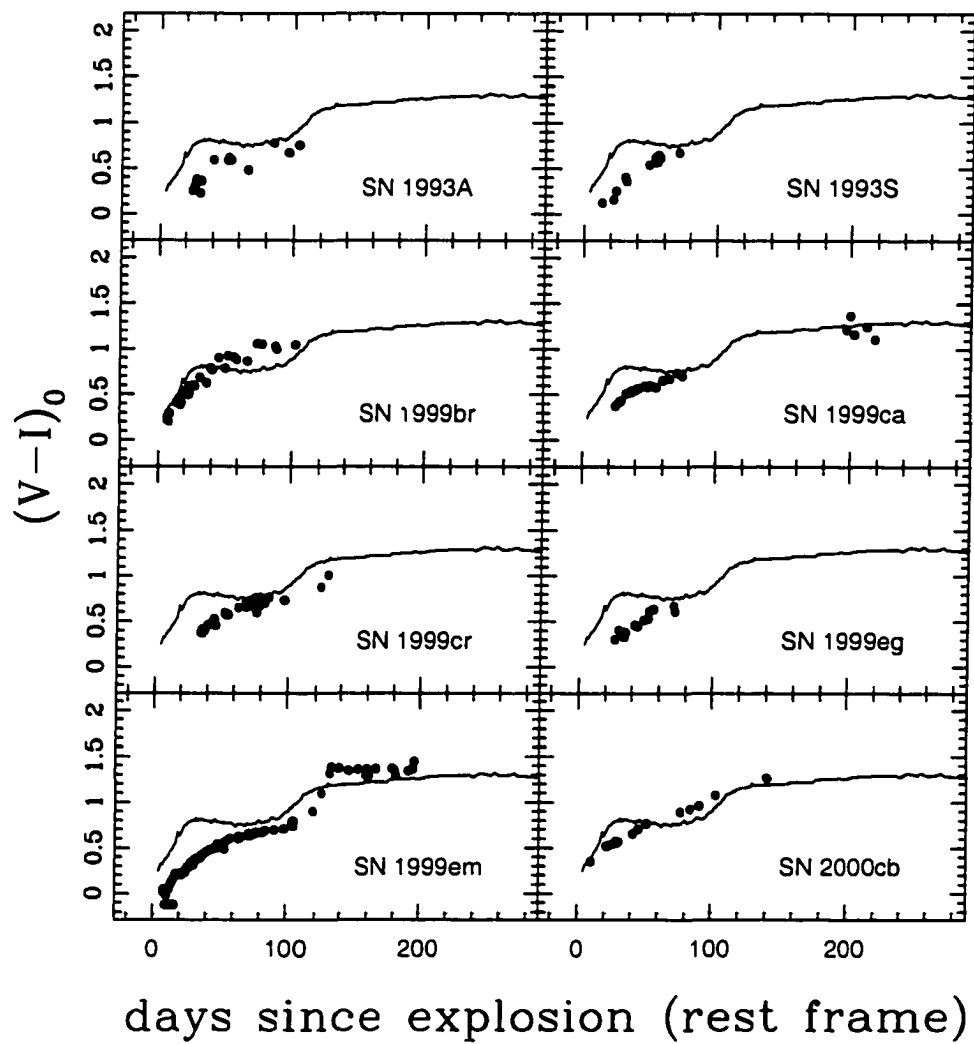


Figure 3.7: $(V - I)_0$ color curve of SNe II. The solid line corresponds to SN 1987A (part 2).

the uncertainty of 0.16 mag in the intrinsic color of SN 1987A becomes negligible. The adopted $A_{host}(V)$ values are given in Table 3.3. I also include in this table the $A(V)$ values computed from the equivalent width of the interstellar Na I D line measured from my spectra. For this purpose I employ the conversion $E(B - V) = 0.25 \times W_\lambda(\text{Na I D})$ (Barbon et al., 1990). Within the uncertainties, the agreement between $A_{host}(V)$ and $A(V)$ is reasonable, but note the large disagreement between $A(V) = 1.55$ and $A_{host}(V) = 0.18$ for SN 1999em. The independent estimate of $A_{host}(V) \approx 0.03\text{--}0.18$ and $A_{host}(V) < 0.34$ from theoretical modeling of the spectra of SN 1999em (Baron et al., 2000) suggests that the light of SN 1999em was likely absorbed by a gas cloud with relatively large gas to dust ratio, perhaps ejected by the supernova progenitor in an episode of mass loss. SN 1999cr seems to be another example where the Na I D line appeared to be too strong for the amount of reddening. There are other examples that demonstrate the difficulty of using the equivalent width of interstellar lines to estimate dust extinction. The spectra of the highly reddened Type Ia SN 1986G revealed interstellar Na I D absorption with an equivalent width of 4.1 Å (Phillips et al., 1987) which implies $A(V) \sim 3.2$, yet the analysis of its colors yielded only $A(V) = 1.9$ (Phillips et al., 1999).

3.6 The measurement of physical radii

The next step in deriving an EPM distance involves the determination of photospheric velocities from the SN spectra. To date the photospheric velocities have been estimated from the minimum of weak spectral absorption features (SKE92, S94). There are several problems with this approach, however. First, the location of the line minimum shifts toward bluer wavelengths (higher velocity) as the optical depth of the line increases. This is a prediction of line profile models in homologously expanding scattering atmospheres [see Fig. 3 of Jeffery & Branch (1990), for example]. Second, even if the observed velocities could be extrapolated to zero strength, the inferred velocity would correspond to that

of the thermalization surface (where the radiation field forms) and not to the photosphere (the last scattering surface). Since the dilution factors computed by E96 correspond to the ratio of the luminosity of the SN model to that of a blackbody with the *photospheric* radius of such model, the use of the velocity of the thermalization surface is inappropriate, even though it has been common practice in the past. Third, velocities derived from absorption lines are affected by line blending or possible line misidentifications, both of which can lead to an erroneous estimate of the photospheric velocity.

To get around these problems I adopt an approach based on cross-correlating the SN spectrum with the models of E96 (with known photospheric velocities) using the IRAF “fxcor” task. Before applying this technique to the observed spectra, it proves necessary to test it with the model spectra of E96. In doing so I cross-correlate models with other models having *BVI* color temperatures within $\pm 1,000$ K of each other. For each pair of models I end up with a relative velocity derived from the cross-correlation (CC, hereafter) technique which can then be compared with the actual value. The hope is that the whole set of pairs can be used to derive a relationship between the CC relative velocity and the actual value. I carry out tests separately in the optical and the IR in order to apply this method to spectra observed in different spectral windows. In the optical I select two wavelength ranges (3000-5000, 5700-6700 Å) and a NIR a window between 10000-13500 Å. I end up with these ranges after numerous experiments which show that beyond 13500 Å there are too few spectral lines to help me constraining the expansion velocity. In the optical these tests suggest the elimination of the red wings of the strong H α and H β , which have the potential to bias the derivation of expansion velocities from the CC procedure.

Figure 3.8 compares the CC relative velocities and the actual values, both in the optical and NIR, from the whole set of models (except for s15.5.1 and s25.5.1 which are not appropriate for SNe II-P, E96). In both cases I get a reasonable correlation which permits

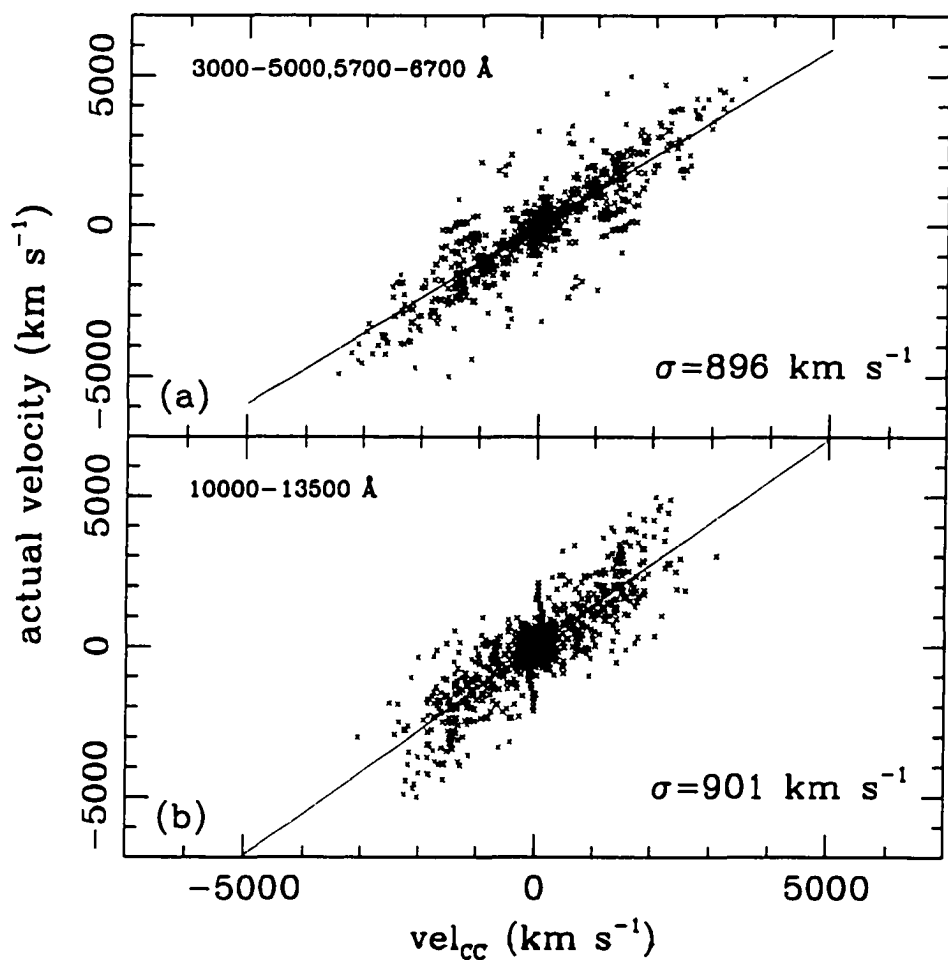


Figure 3.8: (a) Relative expansion velocities derived from the cross-correlation technique for pairs of model spectra with similar color temperatures, versus the actual relative velocities. The cross-correlation was restricted to the range 3000-5000, 5700-6700 Å. The ridge line is a linear least-squares fit to the points. (b) Same as (a) but for the range 10000-13500 Å.

me to convert the velocity offsets measured from cross-correlation into a photospheric velocity. The scatter in these relationships is 900 km s^{-1} which provides an estimate of the precision in the derivation of a photospheric velocity from a single model. The data in Figure 3.8 can be adequately modeled with straight lines, both in the optical and IR. Least-squares fits yield slopes of 1.18 in the optical and 1.38 in the NIR, and zero points of -3 km s^{-1} in both cases. This implies that the magnitude of the relative velocity is *smaller* than the actual value. Overall, this is an encouraging result, although it must be mentioned that the points with the largest scatter in Figure 3.8 correspond to pairs with the largest temperatures. This means that the precision of the CC technique drops to $\sim 2000 \text{ km s}^{-1}$ when $T_{BVI} > 8,000 \text{ K}$.

The general procedure to measure the CC velocity from a SN spectrum begins by selecting atmosphere models with BVI color temperatures within $\pm 1,000 \text{ K}$ of each observed spectrum, after which I cross-correlate the SN spectrum and the subsample of models in the aforementioned wavelength windows. The outcome of this operation is a cross-correlation function (CCF) with a well-defined peak whose location in velocity space gives the relative velocity of the observed and reference spectrum. The height of the CCF is a measure of how well the spectral features of the two spectra match each other. Figure 3.9 shows examples of the CC technique. Panel (a) compares an optical spectrum of SN 1999em with four models of similar color temperature, and panel (b) shows the corresponding CCFs. The two models that best match the observed spectrum, p6.60.1 and p6.40.2, are the ones that give the highest CCF peaks. Models s15.43.3 and s15.46.2, on the other hand, provide poorer matches to the observed spectrum and, consequently, the lowest CCF peaks. For each cross-correlation I get a relative velocity which I proceed to correct using the calibrations shown in Figure 3.8, in order to get the actual relative velocity. Since the photospheric velocities of the models are known, I can derive independent photospheric velocities for each SN spectrum. After multiple measurements

of SN spectra, I find that the scatter in velocity yielded by multiple cross-correlations varies between 5-20%. The errors in the average velocities are probably smaller than this because I make use of various models to compute such averages. To be conservative I hereby adopt the rms uncertainty in velocity yielded by the various models.

In general, there are fewer spectroscopic observations of SNe than photometric points. This leads to the need to interpolate velocities to the time of the photometric observations. After numerous tests I realized that the EPM distance is very sensitive to the adopted velocity curve. For example, a high order polynomial has the potential to introduce wiggles which can then bias the distance estimates. My approach is to fit a function with the fewest possible free parameters, since in some cases I only have two spectra available for a fit. After several experiments with the best observed SNe I find that a power law of the form

$$v = a \left\{ \frac{t - t_0}{1 + z} \right\}^\alpha \quad (3.12)$$

reproduces the data reasonably well. Although there are three free parameters in this equation (a , t_0 , α), the time of explosion, t_0 , can be determined from the photometry via the EPM analysis through equation 3.4. Hence, t_0 can be fixed in the velocity fit, thus reducing the number of free parameters in equation 3.12 to only two. The clear advantage is that this allows me to fit the velocity points even with a coarse sampling. The only problem is that, in order to obtain t_0 from the EPM analysis, it proves necessary to know the velocity curve. The solution to this problem is to adopt an iterative approach. In general, convergence is achieved after 2-3 iterations. There are some problematic cases when the photometric/spectroscopic sampling is poor, as shown below in this Chapter.

For comparison with the CC method I include in this study velocities determined from the conventional method of measuring the wavelength of weak Fe lines. For simplicity I use only Fe II $\lambda 5169$ instead of multiple lines. Numerous tests show that other Fe lines

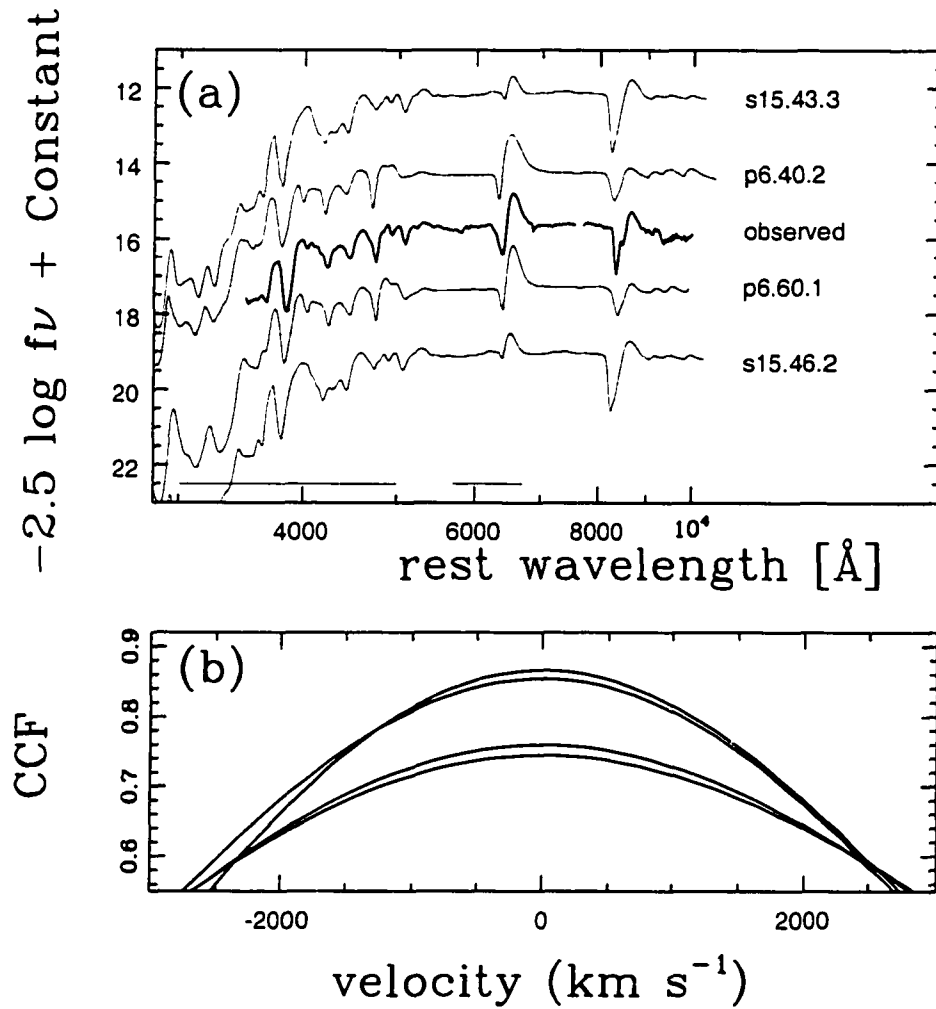


Figure 3.9: (a) Optical spectrum of SN 1999em taken on JD 2451501.66 (thick line) compared to four models with similar color temperature. The horizontal bars show the wavelength ranges (3000-5000, 5700-6700 Å) used in the derivation of relative velocities from the CC technique. (b) Cross correlation function between the observed spectrum and the four models shown above. The two curves with the highest peaks correspond to models p6.60.1 and p6.40.2, both of which match well the observed spectrum. The two lower curves correspond to models s15.43.3 and s15.46.2 which provide a poorer match to the observed spectrum.

give the same velocity as this line. Fe II $\lambda 5169$ also has the advantage that it is promptly measurable in the spectroscopic evolution of SNe II. I also adopt the technique of fitting a power law to the velocities derived from Fe II $\lambda 5169$.

Figure 3.10 illustrates an example of the techniques outline above. The top panel shows CC velocities derived from SN 1999em (filled dots) and the corresponding power law fit (solid line), which is characterized by an exponent (α) of -0.766. The fit does a good job over a period of 70 days. With open dots are plotted the velocities derived from Fe 5169. The fit is performed over the entire plateau phase (~ 120 days) and proves to match very well all points ($\alpha=-0.697$). The bottom panel displays the ratio of the Fe 5169 and CC velocity fits. While the CC velocity initially exceeds the Fe velocity by 10%, at later times the Fe velocity is large by 10%. Admittedly, this is somewhat counter-intuitive since the minimum of the Fe line is expected to form near the thermalization surface which, in an homologous expansion should expand slower than the last scattering surface (Jeffery & Branch, 1990; Kirshner & Kwan, 1974). The CC technique is designed to measure the photospheric expansion velocity so I would expect $V_{CC} > V_{Fe}$ at all epochs in an electron scattering dominated atmosphere. Further examples are given below that reveal that the V_{CC}/V_{Fe} ratio varies significantly from SN to SN, making it harder to come up with a physical interpretation of this variation.

3.7 The determination of errors

Before showing results of the EPM analysis, it is necessary to mention the general procedure to determine errors in the derived distances.

To compute the distance it suffices, in principle, to perform a least-squares fit to the $(\theta_i/v_i, t_i)$ points (equation 3.4). To perform such a fit it is necessary to know the uncertainty in each of the θ_i/v_i points. In this case this is rendered difficult by the lack of knowledge of the systematic errors in ζ which are needed to obtain the θ/v parameter. In

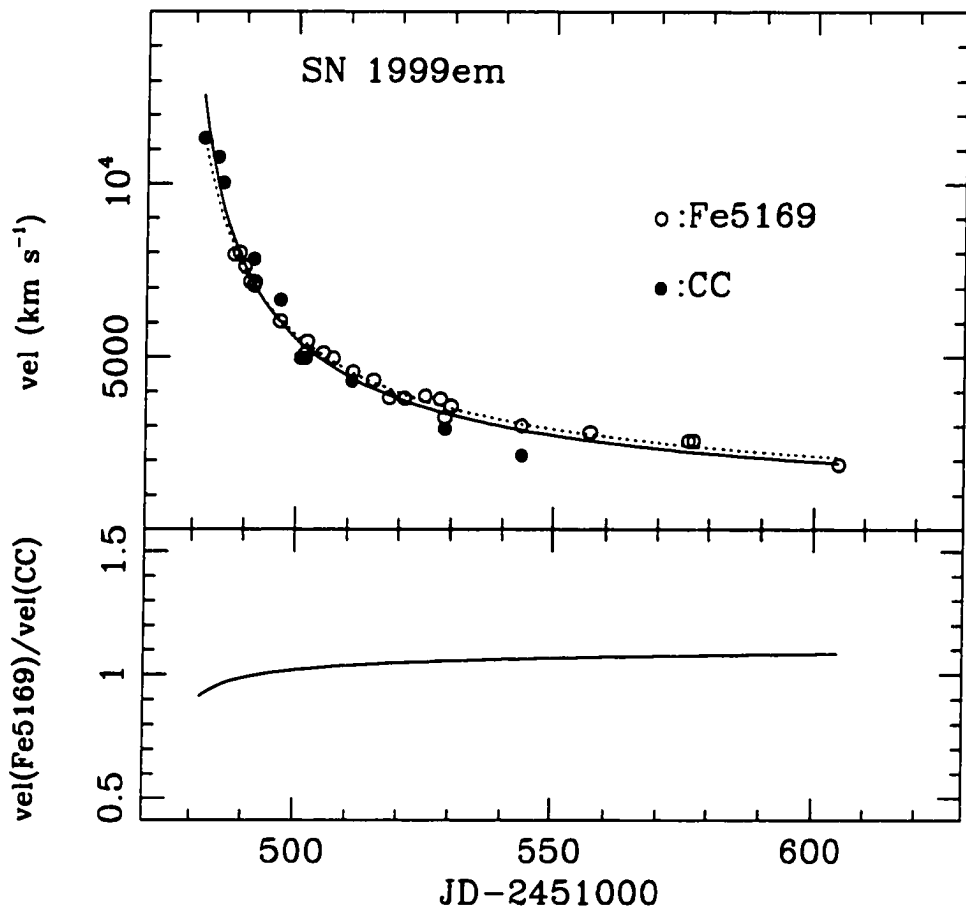


Figure 3.10: The top panel shows CC velocities derived from SN 1999em with a power law fit to the data (solid line), and the Fe 5169 velocities with the corresponding fit (dotted line). The bottom panel shows the ratio of the two fits.

the case of constant photometric errors during the plateau phase, the fractional uncertainty in θ_i/v_i proves approximately constant. Because θ_i/v_i increases linearly with time, the absolute error in θ_i/v_i also increases linearly. Hence, by weighting the fits by the errors, the fits are going to be biased significantly to the earlier data. Equal weighting seems to be a more reasonable way to derive an “average” distance. To estimate the uncertainties in the distance and explosion time I use the Monte Carlo method to randomly vary the photometric points (according to the photometric errors) and the adopted velocities (with an adopted uncertainty of 5%). With the new synthetic dataset I proceed to recompute D and t_0 iteratively with equations 3.4 and 3.12. From 50 simulations I obtain average parameters and estimates of the uncertainties in t_0 and D from the dispersion among all the realizations.

Below I apply the approach just outlined to the 17 SNe. Note that the resulting uncertainties provide only an estimate of the internal errors owing to random uncertainties in the photometry and spectroscopy. The systematic errors due to the dilution factors and the adopted extinction can be estimated from an external comparison, which is the topic of Chapter 4.

3.8 Results

In this section I present the EPM analysis for the 17 SNe, seven of which were also studied by Schmidt et al. In each subsection I discuss specific results for each SN and a comparison with previous EPM analysis.

3.8.1 SN 1986L

Figure 3.11 shows the BV light curves and velocities of SN 1986L (listed in Table 3.4). The ratio between $v(CC)$ and $v(Fe5169)$ reveals a large initial difference, which is probably caused by the extrapolation of the $v(Fe5169)$ points. The extrapolation is a consequence of the absence of the Fe II $\lambda 5169$ feature in the early hot spectra of the SN. For

comparison the velocity curve adopted by S94 is included (dashed line) in this figure. The agreement with my $v(Fe5169)$ points is good, but their extrapolation is well below our extrapolation and the $v(CC)$ points. This comparison illustrates that the fitting procedure to the velocities can have dramatic consequences in the EPM analysis (especially in the extrapolation region) and, hence, in the derived distance.

Table 3.5 summarizes the EPM quantities derived for SN 1986L and the $\{BV\}$ filter subset, following the prescription described in section 3.4. For each epoch are given the color temperature T_{BV} , the uncorrected angular radius $\theta\zeta_{BV}$, the dilution factor ζ_{BV} , the expansion velocity obtained from the power-law fits to $v(Fe5169)$ and $v(CC)$, and the quantity θ/v required to solve for the distance. Figure 3.12 shows θ/v as a function of time, both for the case of Fe 5169 and CC velocities.

In theory, θ/v should increase linearly with time and the slope of the relation gives the distance. This plot reveals that the run of θ/v changes in slope at JD 2446740, both for the Fe and the CC cases. Since no Fe velocity information is available before JD 2446732 it is possible that the inflection is due to extrapolation. However, the CC velocity curve is well constrained so that the inflection must be due to a poor performance of dilution factors. After JD 2446805 the dispersion is even larger but this is not a worry since that epoch is the onset of the optically thin phase in which EPM cannot be applied.

Using the earliest CC points between JD 2446712.4-2446738.4, I obtain a distance of 11.2 Mpc and an explosion time on JD 2446707.9 (see Table 3.6). The discovery (Evans, 1986) happened on JD 2446711.1 and the featureless spectra revealed that SN 1986L was caught soon after explosion, which agrees well with this EPM solution. On the other hand, if I fit the data between JD 2446740-2446800 I obtain a much earlier explosion time at JD 2446633, which is highly inconsistent with the spectroscopic information. I do not derive a solution from the Fe points due to the lack of velocity information before JD 2446732.

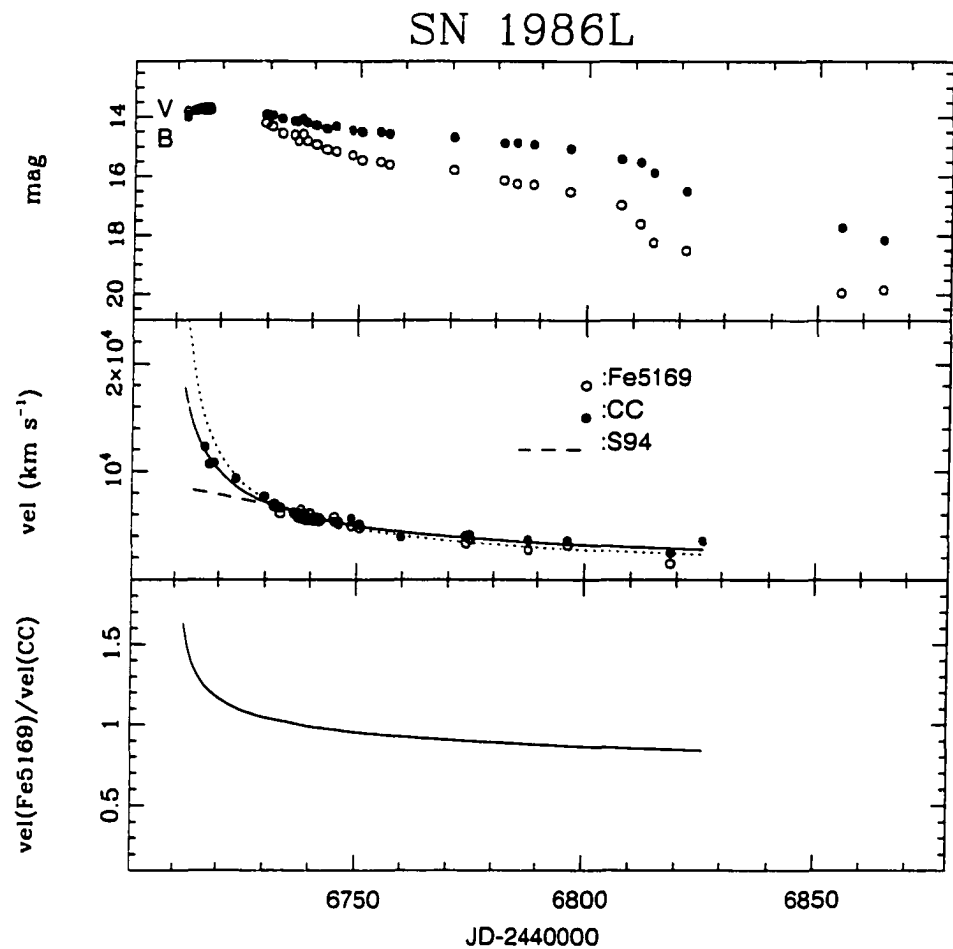


Figure 3.11: Top: *BV* light curves of SN 1986L. Middle: CC velocities (closed dots) and the power-law fit (solid line); open dots show Fe 5169 velocities and the dotted line the corresponding fit. For comparison the velocity curve adopted by S94 is included (dashed line). Bottom: The ratio of the velocity fits.

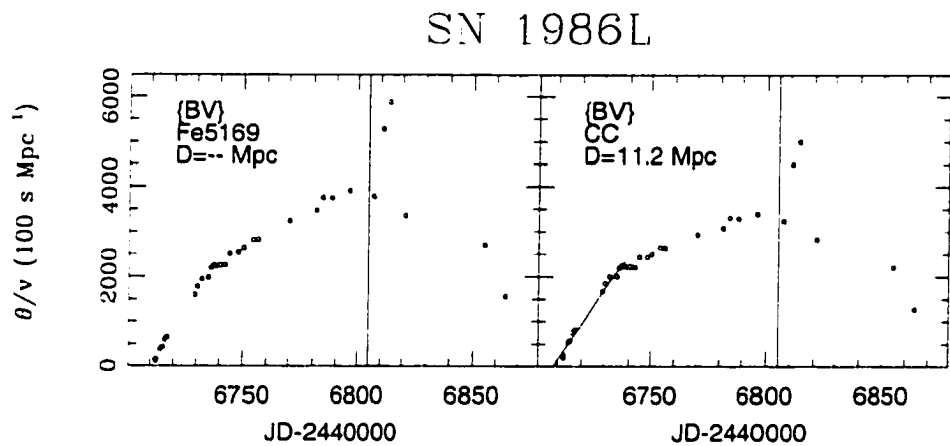


Figure 3.12: θ/v as a function of time for SN 1986L, obtained from filter subset $\{BV\}$. The ridge line corresponds to an unweighted least-squares fit to the CC points between JD 2446712.4-2446738.4. The vertical line corresponds to the end of the plateau phase. No solution was derived from the Fe points due to the lack of velocity information before JD 2446732.

This SN has a well sampled velocity curve so that it is possible to interpolate magnitudes to the time of the spectroscopic observations. Because the light curves are so well sampled, the interpolation is almost exact so that this approach is almost equivalent to no interpolation and provides a mean to check the errors introduced by the power-law fit. Using the CC points between JD 2446716 and 2446739 I obtain $D=11.5$ Mpc (see Table 3.6), in very good agreement with the 11.2 Mpc solution derived from velocity interpolations.

S94 did an EPM analysis of SN 1986L using Fe velocities. They did not mention the presence of the inflection, but presumably they noticed it because they restricted the data points to the first linear part and ignored the data beyond JD 2446742.3. They derived a distance of 16 ± 2 Mpc, which can be compared to my CC estimate of 11.2 Mpc. Their greater value was a consequence of the very shallow velocity curve adopted (shown in Figure 3.11), which was an extrapolation from velocities measured after JD 2446732. Hence, their EPM solution must be taken with great care.

3.8.2 SN 1987A

SN 1987A was not a classical SN II-P. Its progenitor was a compact blue supergiant that led to a dim initial plateau. The light curve promptly became powered by radioactivity. I include it here for curiosity although it must be kept in mind that the models of E96 were intended to represent only genuine SNe II-P with initially extended H envelopes.

Figure 3.13 shows the BVI light curves (Hamuy & Suntzeff, 1990) and velocities of SN 1987A (listed in Table 3.7) measured from the CTIO catalogue of spectra (Phillips et al., 1988). Although not shown in this figure, I also make use of the IR photometry obtained at ESO by Bouchet et al. (1989). While the power law fit to $v(Fe\bar{5}169)$ (dotted line) matches the points very well, the fit to $v(CC)$ has difficulties to follow the steeper initial slope and gives residuals of up to 20%. The ratio between $v(CC)$ and $v(Fe\bar{5}169)$ reveals that $v(CC)$ is 10% greater than $v(Fe\bar{5}169)$, at all epochs. For comparison the velocity curve adopted by SKE92 is included (dashed line) in this figure, and proves to agree closely to my estimates from the Fe I $\lambda 5169$ line.

Table 3.8 summarizes the EPM quantities derived for SN 1987A from the $\{BVI\}$ filter subset (Tables for $\{VI, BVI, JHK\}$ are also available in electronic form). Figure 3.14 shows θ/v as a function of time, for all four filter combinations and both velocity curves.

In all cases θ/v increases linearly with time, at least during the first 60 days of SN evolution. At JD 2446940 the departure from linearity is quite evident, which corresponds to the end of optically thick phase. This is quite remarkable considering that 1987A is not a typical plateau SN like those modeled by E96. Using the data between JD 2446853.6-2446909.5, I obtain a distance between 28-46 kpc, and an explosion time between JD 2446849.4 and 2446850.7 (see Table 3.9) which is in excellent agreement with the prompt optical discovery by I. Shelton on JD 2446850.73 (Kunkel & Madore, 1987), only a few hours after the time of core collapse detected by neutrino observations at JD 2446849.82 (Svoboda, 1987). Hereafter, I adopt the neutrino event as the time of explosion which

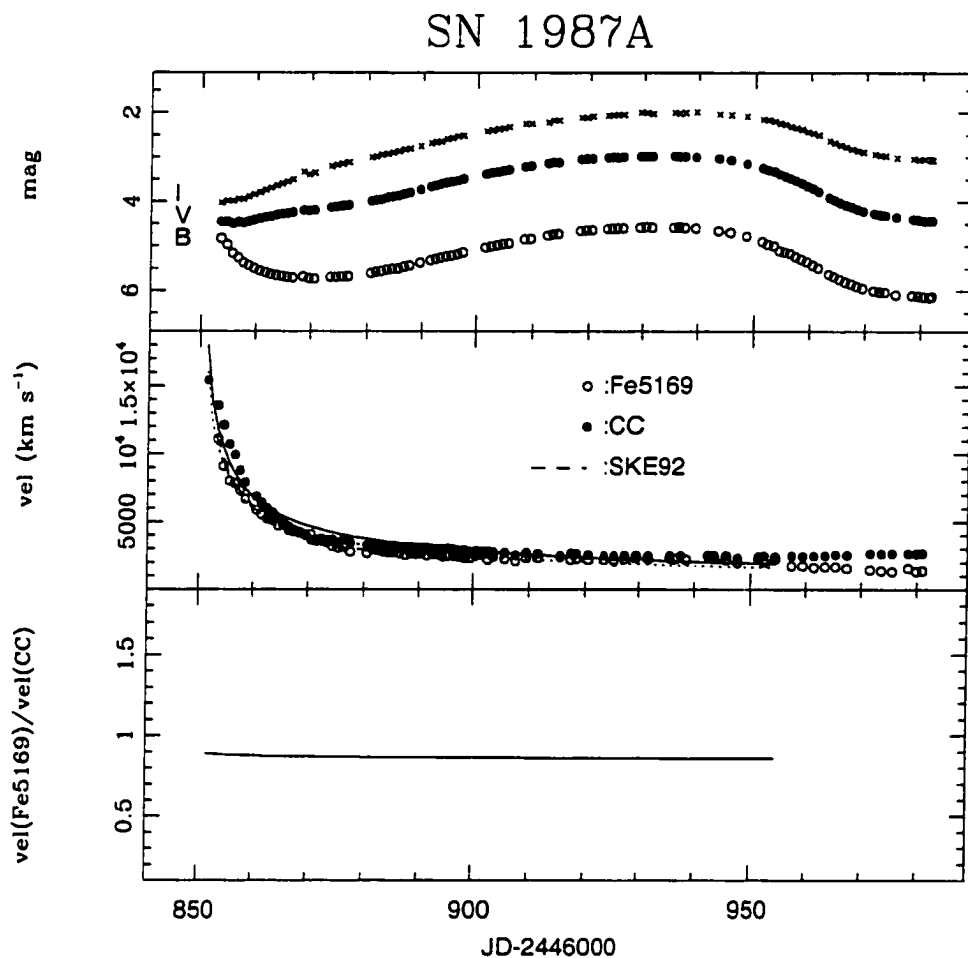


Figure 3.13: Top: BVI light curves of SN 1987A. Middle: CC velocities (closed dots) and the power-law fit (solid line); open dots show Fe 5169 velocities and the dotted line the corresponding fit. For comparison the velocity curve adopted by SKE92 is included (dashed line). Bottom: The ratio of the velocity fits.

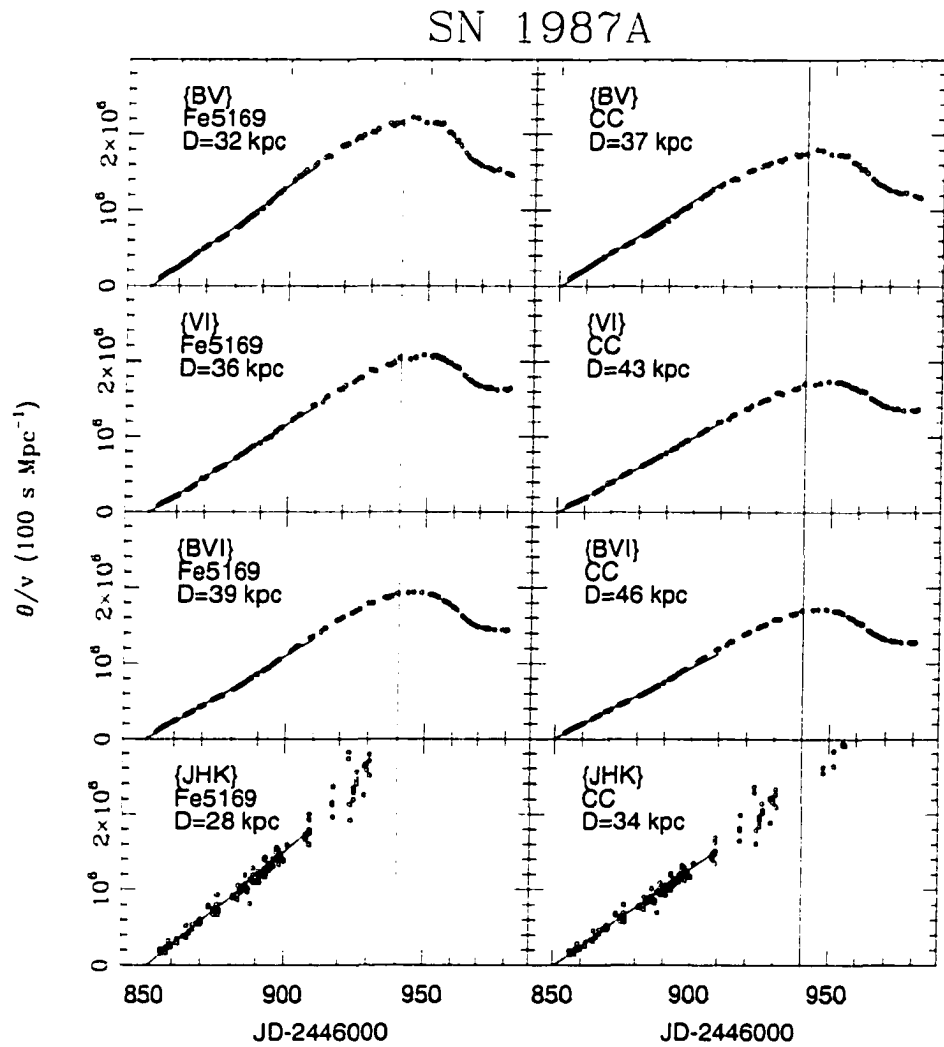


Figure 3.14: θ/v as a function of time for SN 1987A from filter subsets $\{BV, VI, BVI, JHK\}$. The ridge lines correspond to unweighted least-squares fits to the points between JD 2446853.6-2446909.5. The vertical line corresponds to the end of the optically thick phase where EPM is valid.

occurred less than one hour before shock emergence (Arnett, 1996).

For a given velocity curve, the distances derived from different filter subsets show a dispersion of $\sim 15\%$, which proves far greater than the 1-2% formal errors. This SN provides a sense of the internal consistency of the dilution factors. The distances derived from the Fe velocities are $\sim 20\%$ smaller than those obtained from the CC velocities. On average I obtain $D(CC)=39$ kpc which proves to be 22% shorter than the 50 kpc Cepheid distance to the LMC. This external comparison gives a sense of the accuracy of EPM (provided the Cepheid distance is right), although this discrepancy could be due to the fact that the dilution factors computed by E96 are only valid for genuine SNe II-P.

The great sampling of the velocity curve permits me to interpolate magnitudes to the time of the spectroscopic observations and check the solutions derived from the power-law fits. The solutions from JD 2446854-2446910 are listed in Table 3.9 for all eight filter/velocity combinations. The resulting distances prove very similar to those obtained from velocity interpolations.

SKE92 obtained a distance of 53 ± 4 kpc from the $V\,I$ filters but, since they used dilution factors partially determined from SN 1987A and assuming a distance of 50 kpc to the LMC, their EPM distance was not an independent solution. Also, they used JHK photometry to derive a value of 49 ± 3 kpc, assuming $\zeta=1$ at all times. This assumption might have been correct (in fact, it gives the correct distance) but was clearly in conflict with the $\zeta=0.5-0.6$ range implied by the E96 models.

Eastman & Kirshner (1989) obtained an EPM distance of 49 ± 6 kpc using $V\,I$ photometry for the first 10 days since core collapse and specific atmosphere models for SN 1987A. Their dilution factors for this filter combination ranged between 0.45-0.60 which were moderately higher than those published by E96 ($\zeta \approx 0.45$) and used here. Since ζ enters linearly in the EPM distance formula, this explains why I obtain a lower value of $D(CC)=43$ kpc from the same filters. It is the price paid for using average di-

lution factors and not specific models for SN 1987A. In any event it would be easy to distinguish such a radioactively-powered light curve from photometry.

3.8.3 SN 1988A

Table 3.10 presents the velocities measured from our spectra and three velocities derived by Turatto et al. (1993) from the Fe II $\lambda 5169$ line. Figure 3.15 shows the BV photometry and velocities of SN 1988A. The fit to $v(CC)$ yields a steeper curve than that obtained from $v(Fe5169)$. For comparison the velocity curve adopted by SKE92 is included as a dashed line in this figure.

Table 3.11 summarizes the EPM quantities derived for SN 1988A from the $\{BV\}$ filter subset, and Figure 3.16 shows θ/v as a function of time for both cases. Although the run of θ/v is quite linear over the entire period of the photometric observations, I restrict the CC sample to epochs earlier than JD 2447243.6, in order to avoid the risks of large extrapolations in the velocity curves. Clearly the dilution factors yield an excellent internal consistency in both cases. The resulting fitting parameters are given in Table 3.12.

The explosion time proves to be at JD 2447155.7 and 2447170.3 from Fe 5169 and CC, respectively. SN 1988A was independently discovered by Ikeya (Kosai, 1988) and Evans (1988). The earliest detection was recorded on JD 2447176.2. The EPM solutions are consistent with this observation and suggest that the SN was ~ 2 weeks old at discovery. In what follows I adopt $t_0=2447163$.

EPM yields distances of 23.8 and 15.3 Mpc from Fe 5169 and CC, respectively. The large Fe 5169 value is clearly due to the shallower velocity curve. My Fe 5169 estimate of 23.8 ± 2 Mpc can be compared with that obtained by SKE92 (23 ± 4 Mpc) and their revised value of 20 ± 3 Mpc (S94). The difference between SKE92 and S94 is mainly due to the use of different dilution factors. The latter should be preferred in the comparison with our analysis since both were derived from the dilution factors of E96.

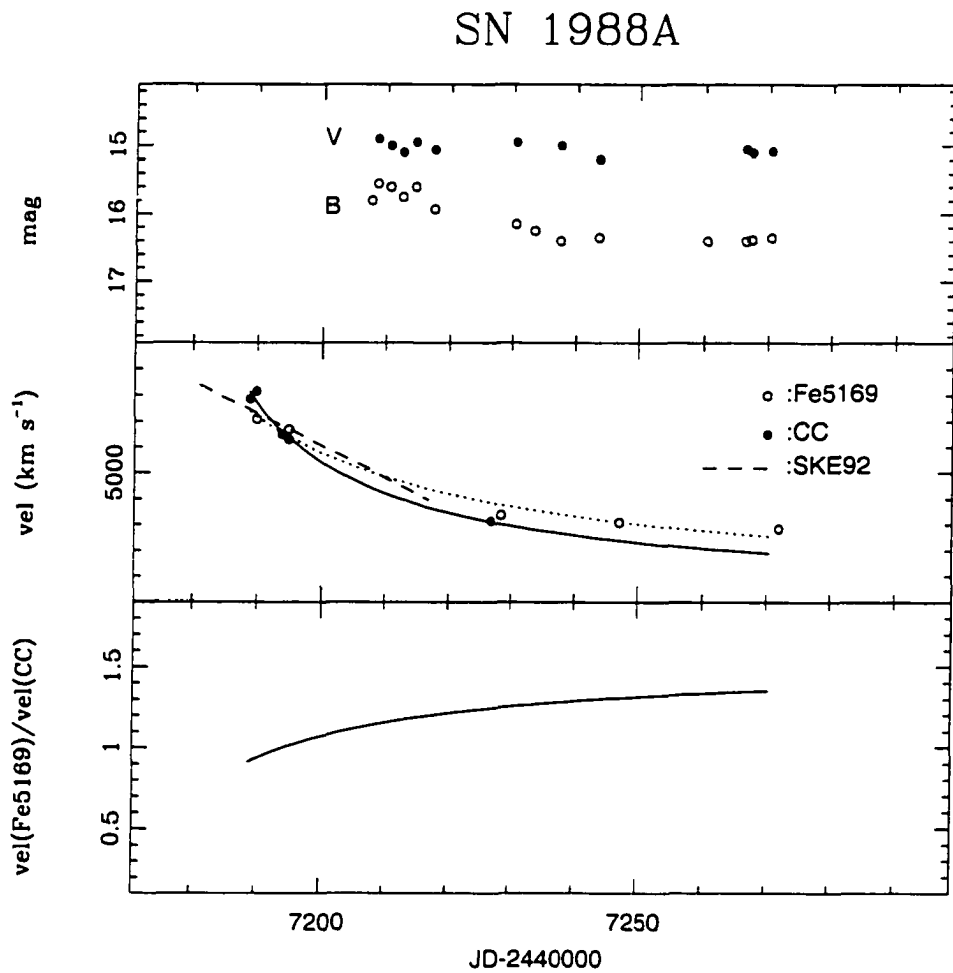


Figure 3.15: Top: *BV* light curves of SN 1988A. Middle: CC velocities (closed dots) and the power-law fit (solid line); open dots show Fe 5169 velocities and the dotted line the corresponding fit. For comparison the velocity curve adopted by SKE92 is included (dashed line). Bottom: The ratio of the velocity fits.

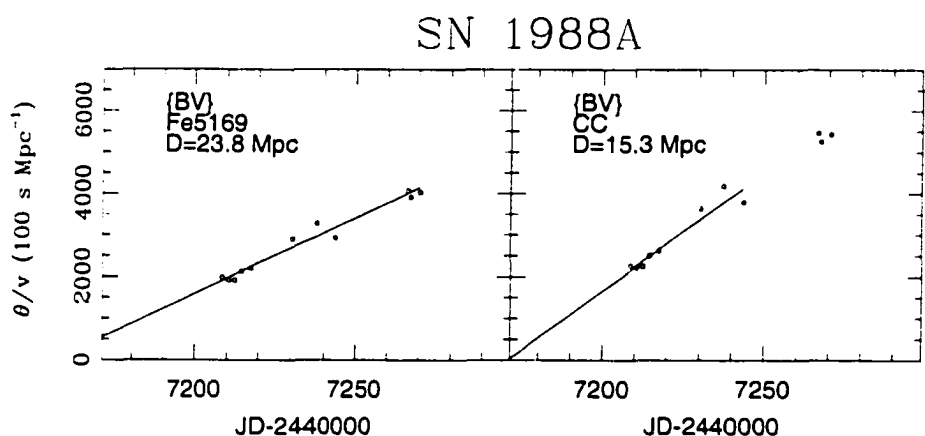


Figure 3.16: θ/v as a function of time for SN 1988A, obtained from filter subset $\{BV\}$. The ridge lines correspond to unweighted least-squares fits to the Fe points between JD 2447208.5-2447270.4, and between JD 2447208.5-2447243.6 for the CC points.

3.8.4 SN 1990E

Figure 3.17 shows the BVI light curves of SN 1990E. Also shown are the velocities measured from our spectra, and those computed from the wavelengths of the Fe II $\lambda 5169$ line published by Schmidt et al. (1993) (see Table 3.13). The velocity curve adopted by SKE92 for this SN is included as a dashed line. Clearly their adopted curve matches well my estimates from Fe II $\lambda 5169$ after JD 2447955, but their initial velocities are much lower than my $v(Fe5169)$ points. The power-law fits have nearly the same shape so that the ratio $v(Fe5169)/v(CC)$ is almost constant. $v(Fe5169)$ proves to be $\sim 10\%$ larger than $v(CC)$.

Table 3.14 gives the EPM quantities derived for SN 1990E from the $\{VI\}$ filter subset (the tables for $\{BV, BVI\}$ are available in electronic form). Figure 3.18 is a plot of θ/v versus time for the six filter/velocity combinations. Linear relationships can be seen only over a limited period of 20 days of plateau evolution (note the discrepant point at JD 2447973.3 in the middle panels). Since the color temperature at this time (5,600 K) is $\sim 1,000$ K lower than the coolest models of E96 (see Figure 3.3), the dilution factor at this epoch is obtained from extrapolation in temperature. This might explain the prompt departure from linearity of θ/v . Table 3.15 presents the EPM solutions from the fits to the data between JD 2447939.6-2447959.6 (excluding the last data point).

The explosion time shows a small scatter between JD 2447917.6-2447930.4. This SN was discovered by the BASS program with a magnitude of 16 on JD 2447937.62 (Penny-packer & Perlmutter, 1990). The discovery report mentioned that the SN was not present down to a limiting magnitude of 19 in a pre-discovery image taken on 2447932.62, setting thus a lower limit to the time of explosion. The EPM analysis yields values somewhat lower than this. Considering that SNe II are promptly visible after explosion, hereafter I adopt $t_0=2447932.62$.

The EPM distances from the three different filter combinations range between 16

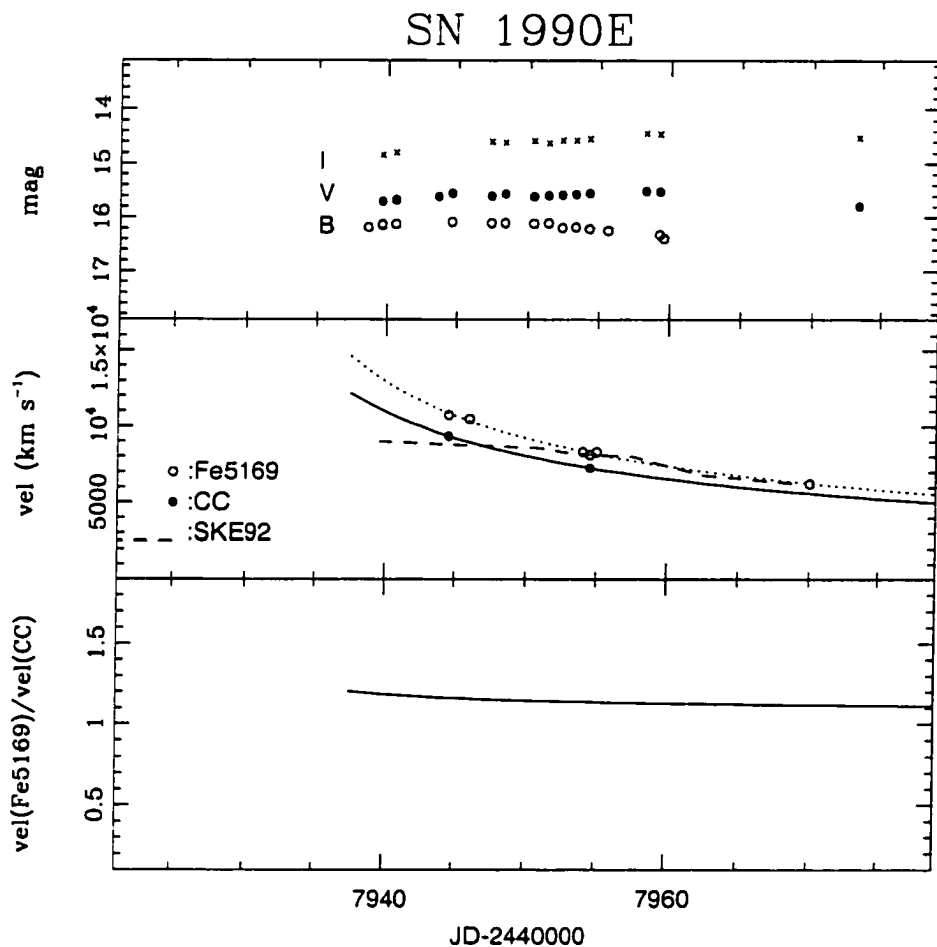


Figure 3.17: Top: *BVI* light curves of SN 1990E. Middle: CC velocities (closed dots) and the power-law fit (solid line); open dots show Fe 5169 velocities and the dotted line the corresponding fit. For comparison the velocity curve adopted by SKE92 is included (dashed line). Bottom: The ratio of the velocity fits.

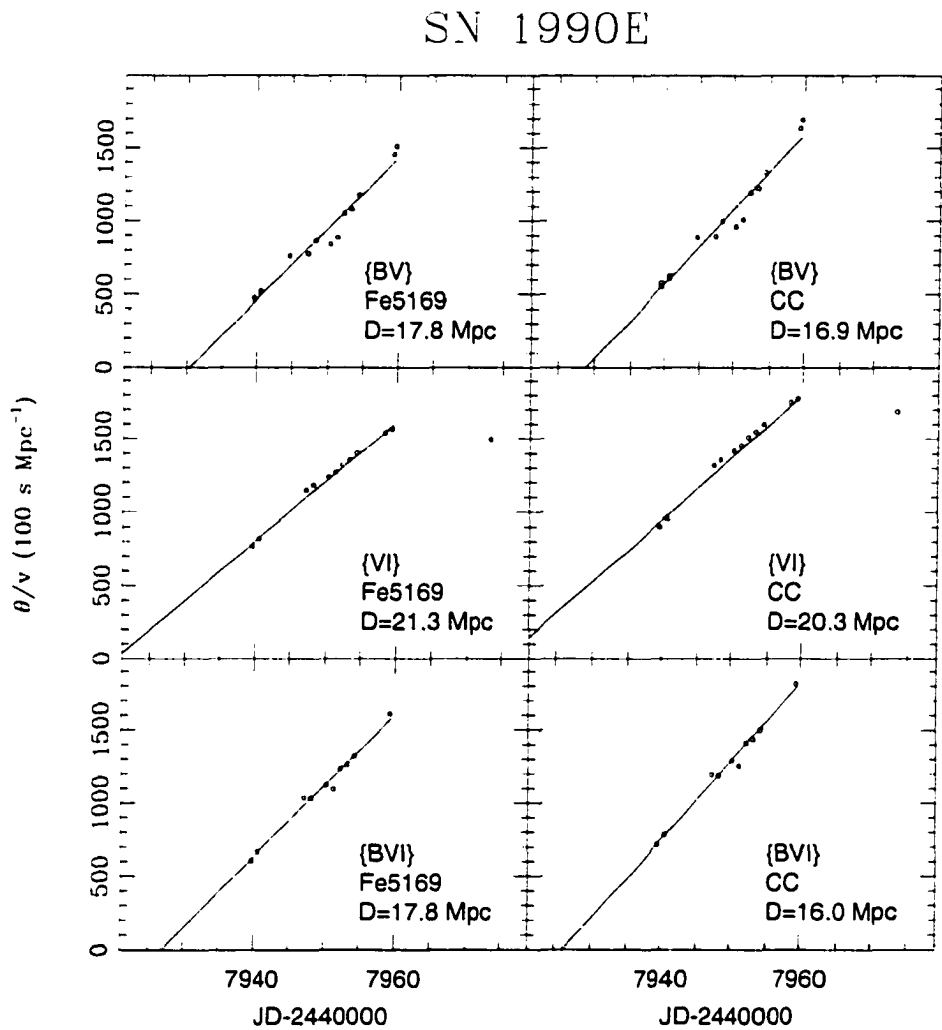


Figure 3.18: θ/v as a function of time for SN 1990E, obtained from filter subsets $\{BV, VI, BVI\}$. The ridge lines correspond to unweighted least-squares fits to the points between JD 2447939.6-2447959.6.

and 21 Mpc, or 15% about the average. The CC distances are \sim 10% lower than the Fe distances owing to the smaller velocities yielded by the CC method. Table 3.15 also lists distances derived from photometric interpolations to the time of the spectroscopic observations obtained between JD 2447944-2447955. Despite the poor velocity sampling and the small baseline, the resulting distances prove only 7% larger than those yielded by the power-law fits.

My values of 17.8 Mpc from the $\{BV\}$ filters and $v(Fe5169)$ velocities can be compared to the EPM distance of 21 ± 3 given by SKE92 and their revised value of 18 ± 2.5 Mpc (S94).

3.8.5 SN 1990K

Table 3.16 summarizes the velocities measured from our spectra. Figure 3.19 shows the BVI light curves and velocities of SN 1990K. The velocity curve adopted by S94 for this SN is included as a dashed line. Their curve is steeper than the power-law fit to the $v(Fe5169)$ data. Unfortunately, the scatter in the measured velocities makes it hard to judge which curve better represents the observations. The two power-law fits have nearly the same shape, with the CC curve being $\sim 10\%$ higher than the Fe fit.

The EPM quantities derived from the BV filters can be found in Table 3.17 (tables for $\{VI, BVI\}$ are available in electronic form). Figure 3.20 illustrates the run of θ/v for the six filter/velocity combinations. Contrary to expectations, this parameter remains quite flat before the end of the plateau phase at JD 2448080, probably owing to extrapolations of dilution factors to temperatures lower than those encompassed by the models of E96 (see Figure 3.3). If I limit the EPM fits to the plateau phase (JD 2448041.9-2448071.9) in neither of these cases does the iteration procedure to solve for the EPM parameters give convergence. In other words, a moderate change in t_0 causes a slight change in the velocity curve which, in turn, leads to a very different t_0 from the fit to the (θ_i, t_i) points. This problem is certainly a consequence that the SN was caught quite old on JD 2448037.3 (Evans, 1990). In fact, only 40 days after discovery the SN started to fall off the plateau. Assuming that the plateau lasted ~ 110 days I adopt JD 2447970 as the time of explosion.

S94 reported a distance of 20 ± 5 Mpc from the same data that I employ here, but an adopted velocity curve somewhat steeper than that yielded by the power-law fit to the $v(Fe5169)$ points. Given that slightly different velocities can lead to dramatically different EPM solutions, and because the dilution factors used by S94 do not cover the range in color temperature displayed by SN 1990K, I believe that these data are not useful for an EPM analysis.

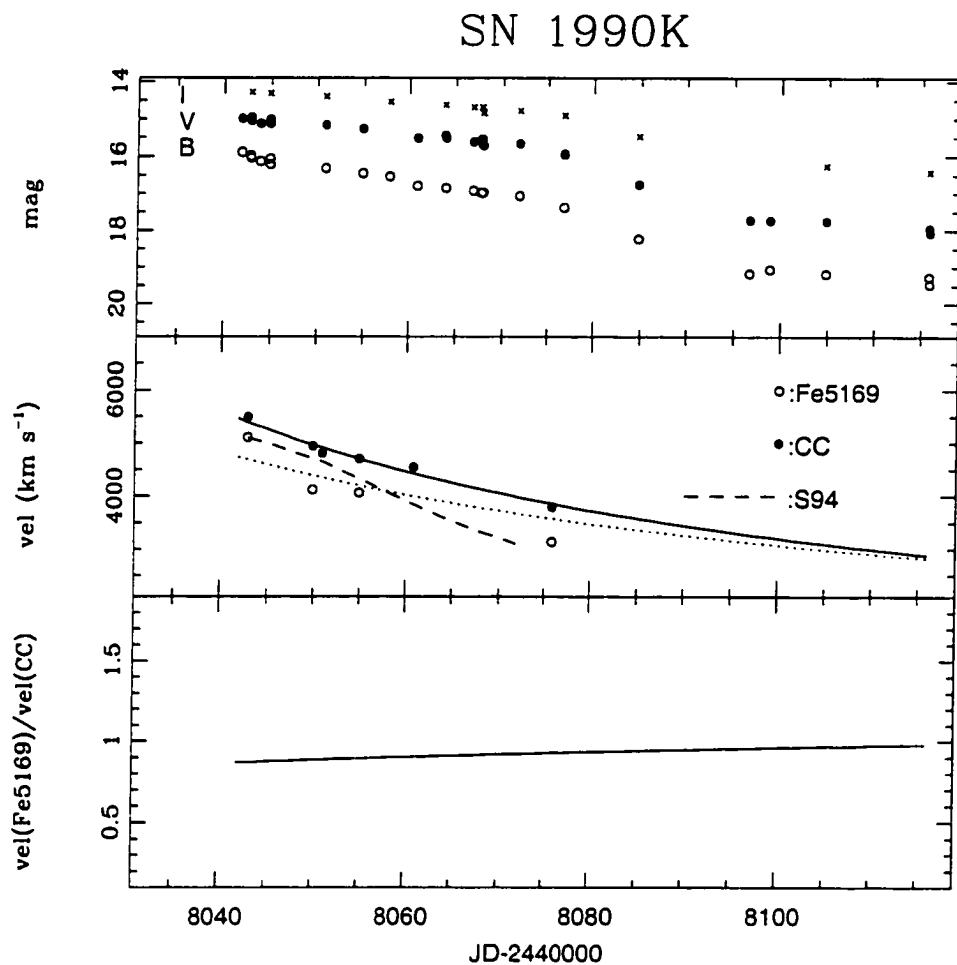


Figure 3.19: Top: *BVI* light curves of SN 1990K. Middle: CC velocities (closed dots) and the power-law fit (solid line); open dots show Fe 5169 velocities and the dotted line the corresponding fit. For comparison the velocity curve adopted by S94 is included (dashed line). Bottom: The ratio of the velocity fits.

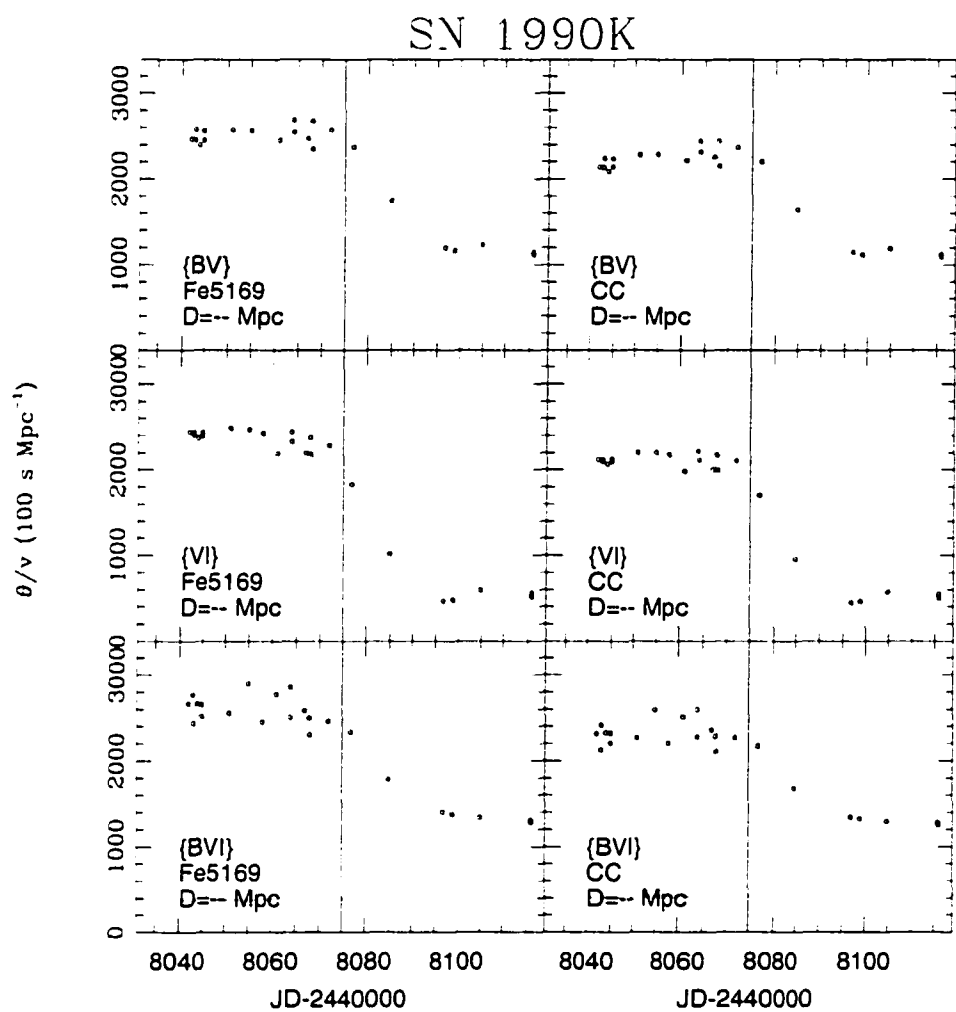


Figure 3.20: θ/v as a function of time for SN 1990K, obtained from filter subsets $\{BV, VI, BVI\}$. The vertical line corresponds to the end of the plateau phase.

3.8.6 SN 1991al

Table 3.18 gives the velocities measured for SN 1991al. Figure 3.21 shows the BVI light curves of SN 1991al and the velocity curves. The bottom panel shows that the ratio $v(Fe5169)/v(CC)$ is almost constant and that $v(CC)$ is $\sim 10\%$ larger than $v(Fe5169)$.

Table 3.19 presents EPM quantities derived for SN 1991al from the $\{BVI\}$ filter subset (the tables for $\{BV\}$ and $\{VI\}$ are available in electronic form). Figure 3.22 shows θ/v versus time for the four filter/velocity combinations. θ/v increases steadily until the onset of the nebular phase between JD 2448510 and 2448530, although a curvature of the θ/v versus time relation can be clearly seen. Since the early points are not well constrained by the $v(t)$ fits it proves hard to attribute this curvature to dilution factors. Hence, to avoid the risks of extrapolations I restrict the fits to JD 2448478.7-2448508.6. When I do this I find no convergence in the iterative approach, a likely consequence of the lack of constraints at early epochs.

Assuming that the plateau lasted ~ 110 days I adopt $t_0=2448410$. The discovery of SN 1991al by Wishniewsky on JD 2448453.7 (Wells & Maza, 1991) suggests that the SN was found ~ 40 days after explosion.

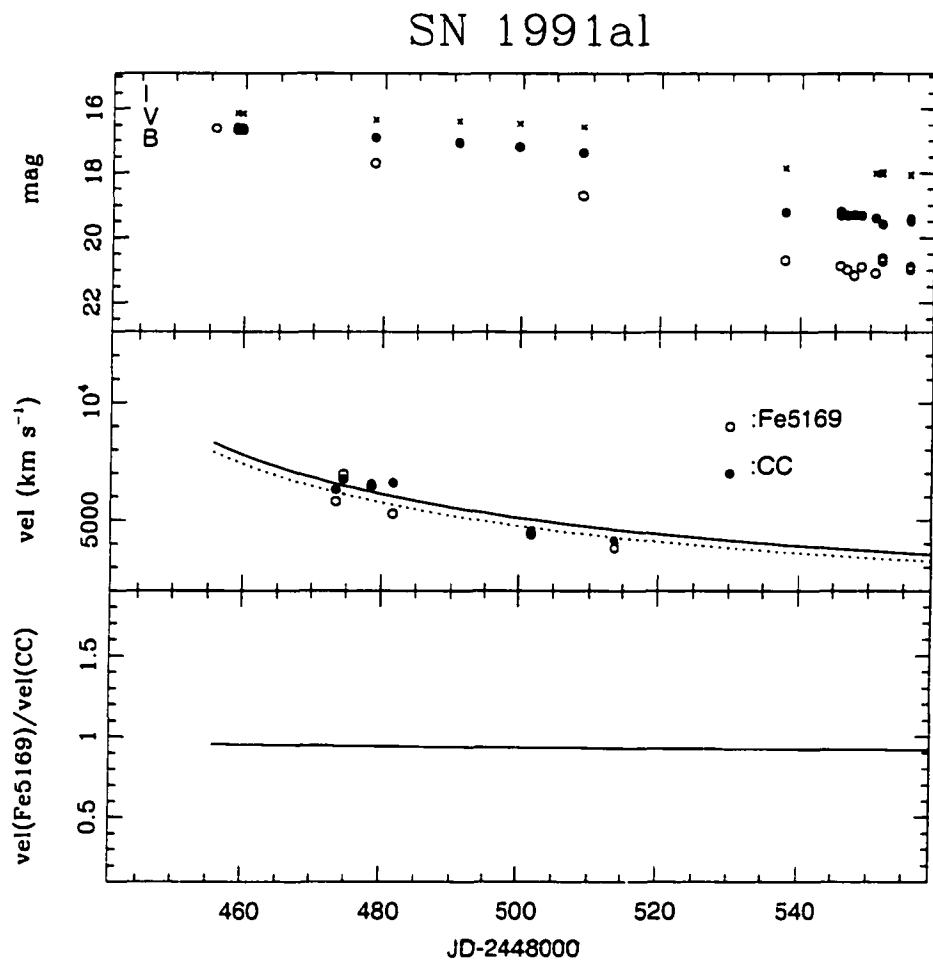


Figure 3.21: Top: BVI light curves of SN 1991al. Middle: CC velocities (closed dots) and the power-law fit (solid line); open dots show Fe 5169 velocities and the dotted line the corresponding fit. Bottom: The ratio of the velocity fits.

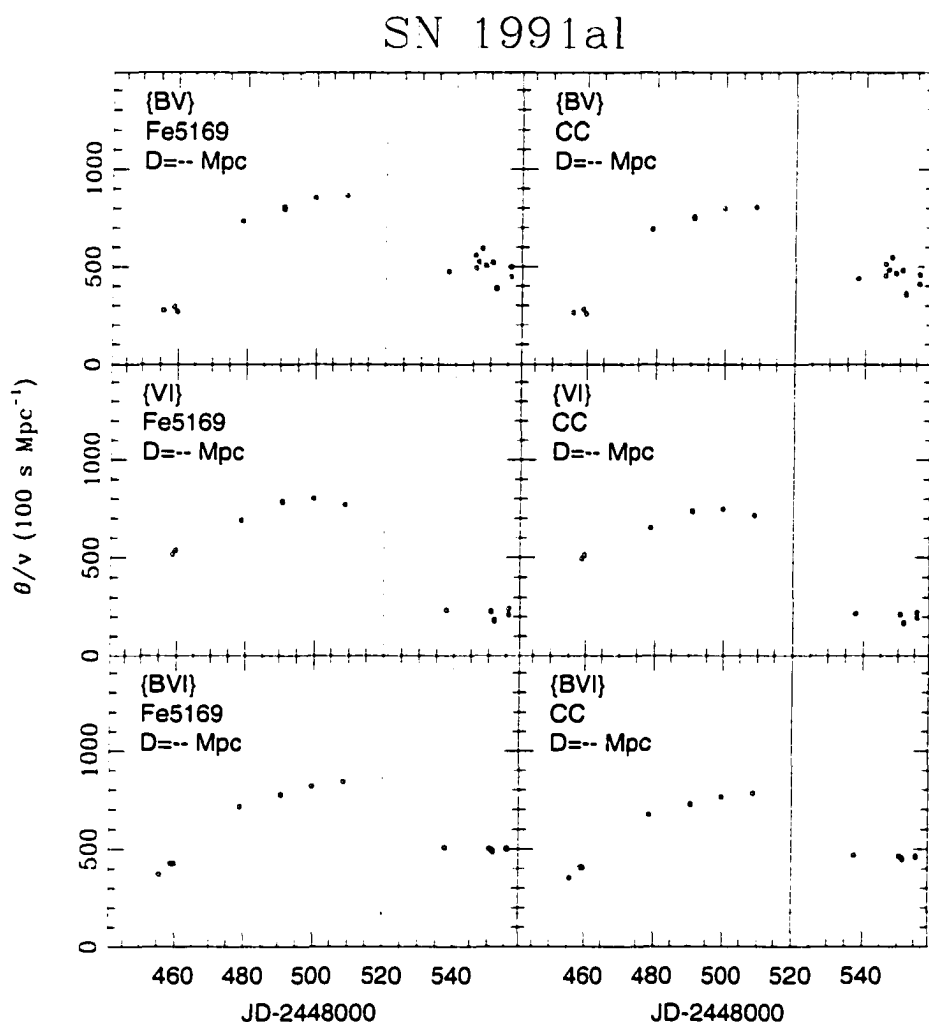


Figure 3.22: θ/v as a function of time for SN 1991al, obtained from filter subsets $\{BV, BVI\}$. The vertical line shows the end of the plateau phase.

3.8.7 SN 1992af

Table 3.20 summarizes the velocities measured from our three spectra, of which only one allows me to get a Fe velocity. Since the minimum for an EPM solution is two spectra, I can only get a power-law fit from the CC velocities. Figure 3.23 shows the BVI light curves (top panel) and velocities (middle panel) of SN 1992af. The velocity curve adopted by S94 for this SN is included as a dashed line. Their curve is 30% higher than the single $v(Fe5169)$ point I have.

The EPM quantities derived from the BVI filters and the CC velocities can be found in Table 3.21. Figure 3.23 (bottom panel) illustrates the corresponding run of θ/v . This parameter increases quite linearly until the end of the plateau at JD 2448850. If I restrict the EPM fits to the early part of the plateau where the dilution factors can be obtained without extrapolations in temperature (JD 2448805.8-2448831.8), it proves impossible to get an iterative solution for any of the filter subsets. The reason is the same as for SN 1990K: a moderate change in t_0 causes a slight change in the velocity curve which, in turn, leads to a very different t_0 from the fit to the (θ_i, t_i) points. The cause is again due to the fact that the SN was caught too late. The discovery by Antezana on JD 2448802.78 (Wells & Maza, 1992) and the fall from the plateau 50 days later confirm this conclusion. I hereafter adopt JD 2448736 as the time of explosion, assuming that the end of the plateau occurred at an age of ~ 110 days.

S94 found a distance of 55 ± 23 Mpc from the same data that I employ here, but an adopted velocity curve somewhat steeper and higher than that implied by the power-law fit to the $v(CC)$ points. The lack of convergence in my EPM analysis reveals that any slight change in the adopted velocity leads to widely different solutions. Like in the case of SN 1990K, I believe that these data cannot be used for an EPM analysis.

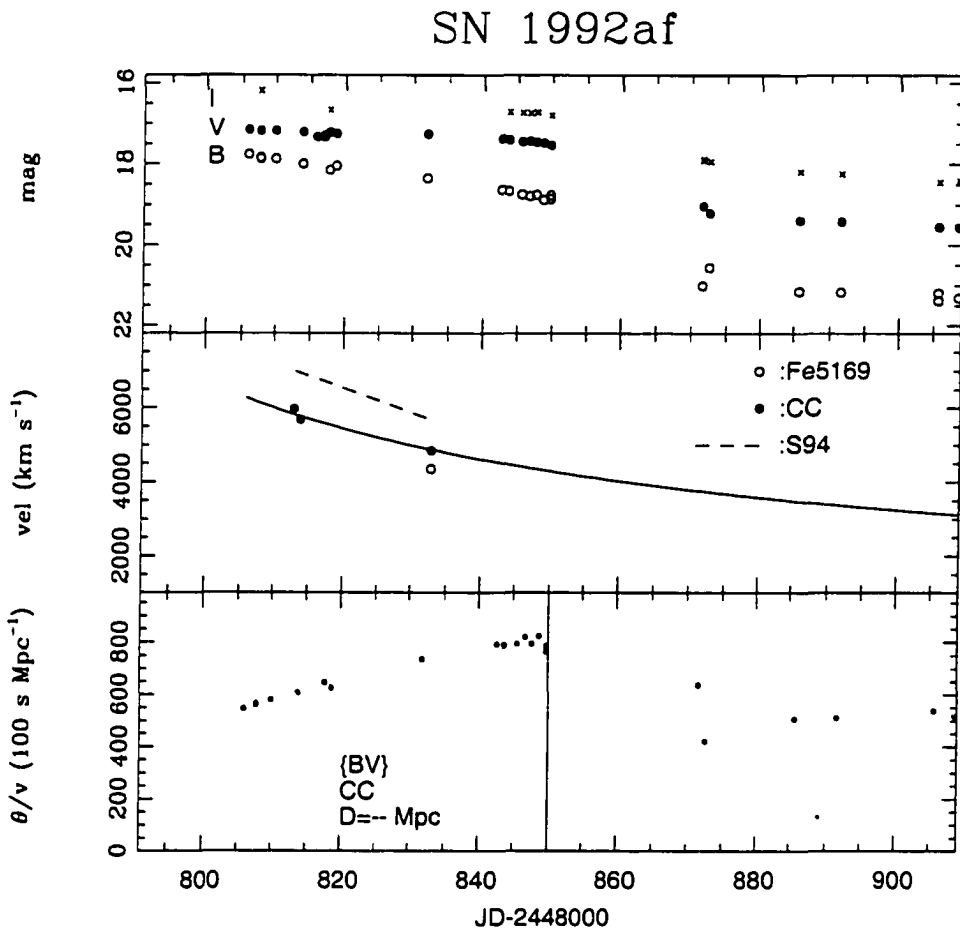


Figure 3.23: Top: BVI light curves of SN 1992af. Middle: CC velocities (closed dots) and the power-law fit (solid line); the open dot shows the only Fe 5169 velocity measured. For comparison the velocity curve adopted by S94 is included (dashed line). Bottom: θ/v as a function of time, obtained from filter subset $\{BV\}$. The vertical line shows the end of the plateau phase.

3.8.8 SN 1992am

Table 3.22 presents the velocities measured from our two spectra of SN 1992am (the minimum required for EPM). Figure 3.24 shows the BVI light curves and the velocities. Included is the curve adopted by Schmidt et al. (1994a) (dashed line). The bottom panel shows that the ratio $v(Fe\lambda 5169)/v(CC)$ is almost constant at all epochs.

Table 3.23 presents EPM quantities derived for SN 1992am from the $\{VI\}$ filter subset (the table for $\{BV, BVI\}$ are available in electronic form). Figure 3.25 shows θ/v versus time for the six filter/velocity combinations. θ/v increases steadily until the end of the plateau (between JD 2448930-70), though not in a linear form. Beyond JD 2448900 the photospheric temperature was below the range encompassed by the dilution factors and the velocities resulted from extrapolation in time, both of which might explain the departure from linearity. To avoid incurring in errors due to extrapolations I choose to restrict the fits to JD 2448832.9-2448859. Table 3.24 presents the EPM solutions for the $\{BV, VI, BVI\}$ combinations.

SN 1992am was discovered by Antezana (Phillips & Maza, 1992) on JD 2448829.83 in the course of the CT survey. This object was found at $z=0.048$ and proves to be the most distant to which EPM has been applied. The explosion time yielded by EPM is in the range JD 2448767-2448789 (~ 50 days before discovery). Hereafter I adopt $t_0=2448778.1$.

The EPM distance has a spread of 15% (168-230 Mpc) among the different filter subsets. The small differences in the velocity curves derived from the CC method and the Fe II $\lambda 5169$ line produce results which are insignificantly different. Table 3.24 also includes the solutions for $\{BVI\}$ from interpolating magnitudes to the time of the two velocity measurements. The distances prove 8% smaller than those yielded by the power-law fits.

The analysis of Schmidt et al. (1994a) gave $D=180\pm28$ Mpc from the $\{BVI\}$ filters,

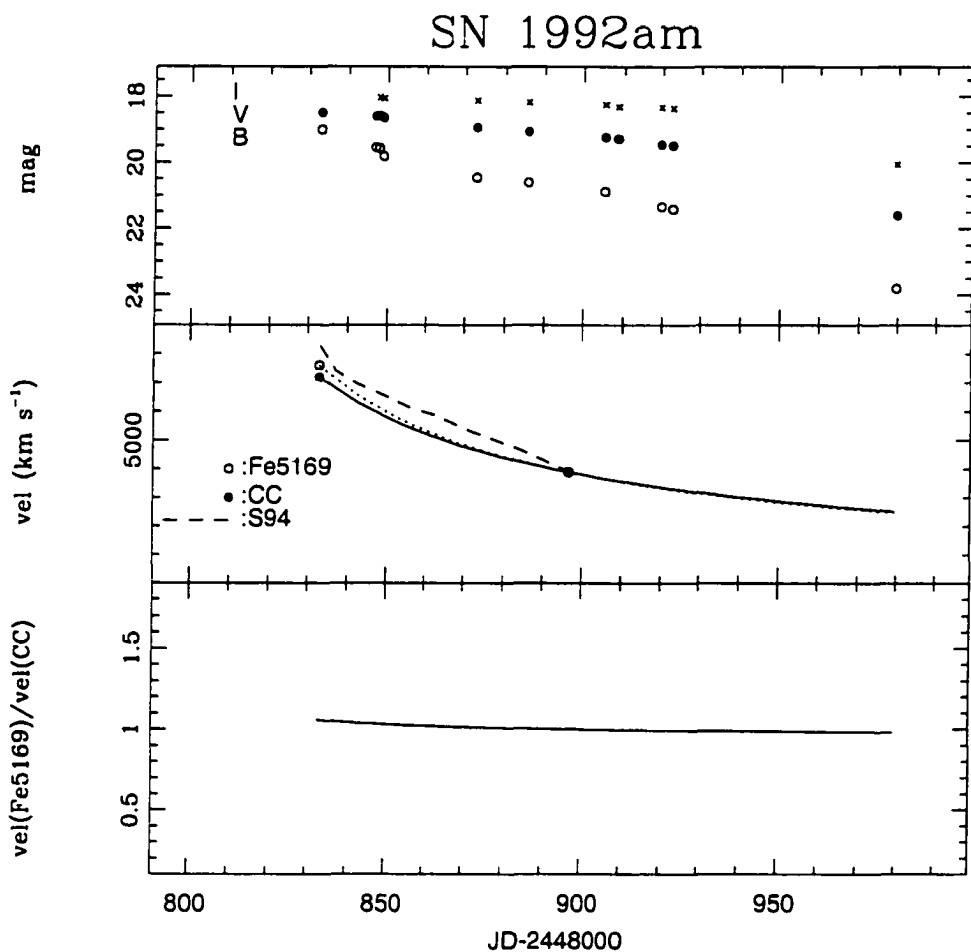


Figure 3.24: Top: *BVI* light curves of SN 1992am. Middle: CC velocities (closed dots) and the power-law fit (solid line); open dots show Fe 5169 velocities and the dotted line the corresponding fit. For comparison the velocity curve adopted by Schmidt et al. (1994a) is included (dashed line). Bottom: The ratio of the velocity fits.

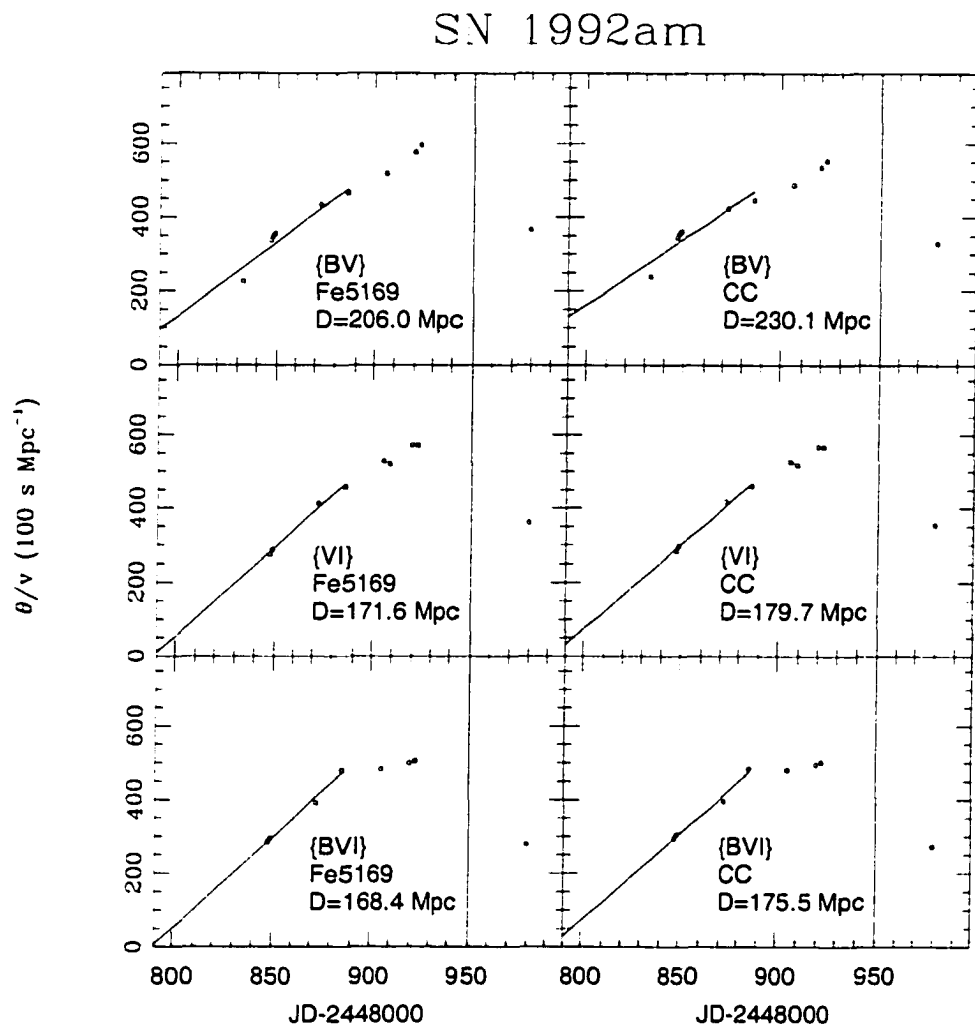


Figure 3.25: θ/v as a function of time for SN 1992am, obtained from filter subsets $\{BV, VI, BVI\}$. The ridge lines correspond to unweighted least-squares fits to the points between JD 2448832.9-244885.9. The vertical line shows the end of the plateau phase.

in good agreement with the distance of 168 Mpc derived here from the Fe curve and the same filters.

3.8.9 SN 1992ba

Table 3.25 gives the velocities measured from our spectra of SN 1992ba. Figure 3.26 shows the BVI light curves and the velocities. The curve adopted by S94 is included (dashed line) for comparison, which reveals that their velocities are $\sim 10\%$ lower than the $v(Fe)$ points. The bottom panel presents the ratio $v(Fe5169)/v(CC)$, which proves close to unity at all times.

Table 3.26 summarizes the EPM quantities derived for SN 1992ba from the $\{BVI\}$ filter subset (the tables for $\{BV, BVI\}$ are available in electronic form). Figure 3.27 shows θ/v versus time for all six filter/velocity combinations, which reveals very linear relationships until approximately JD 2448950, and small departures from linearity until the onset of the nebular phase at JD 2449000. As mentioned earlier for other SNe, these non-linearities can be due to extrapolations of dilution factors to temperatures lower than those of the model spectra. By restricting the fitting sample to JD 2448904.8-2448956.8, I obtain the EPM solutions summarized in Table 3.27.

SN 1992ba was discovered by Evans (1992) on JD 2448896.25. McNaught (1992) reported that the SN was not present on a plate taken on JD 244883.2 with limiting magnitude 19. This provides a well constrained range for the time of explosion between JD 244883.2-244896.25. The EPM analysis yields $t_0=2448869-2448879$ which is 14-4 days earlier than the observation by McNaught (1992). In what follows I adopt $t_0=2448883.2$.

EPM produces a distance between 21.0-23.4 Mpc from the different filter subsets, which corresponds to a small spread of 5% about the average. The small differences in the two velocity curves (CC and Fe) have negligible effects on the solution. The analysis of S94 gave $D=14\pm1.5$ Mpc from the $\{BVI\}$ filters. This contrasts with the value of 23.3 Mpc that I get from the same filters and the Fe velocity curve. With their velocity curve and their preferred values for extinction of $A_{GAL}=0.11$ and $A_{host}(V)=0.3$. I obtain

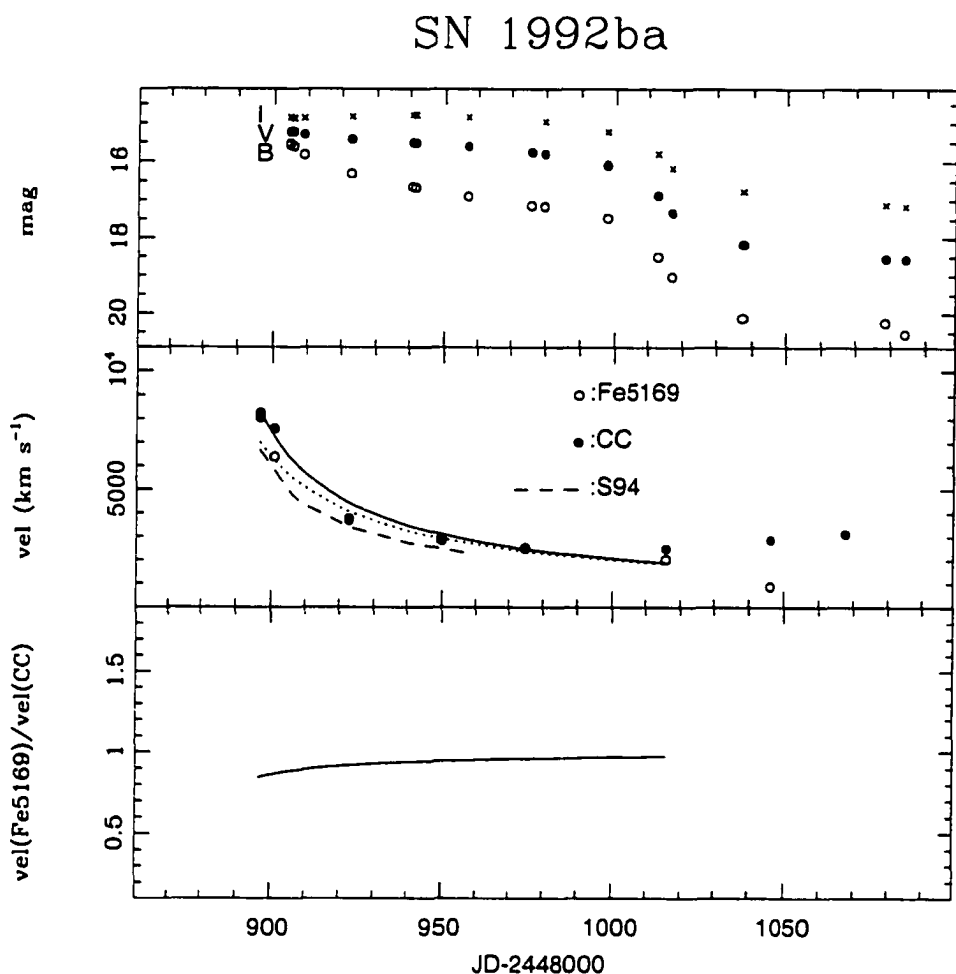


Figure 3.26: Top: *BVI* light curves of SN 1992ba. Middle: CC velocities (closed dots) and the power-law fit (solid line); open dots show Fe 5169 velocities and the dotted line the corresponding fit. For comparison the velocity curve adopted by S94 is included (dashed line). Bottom: The ratio of the velocity fits.

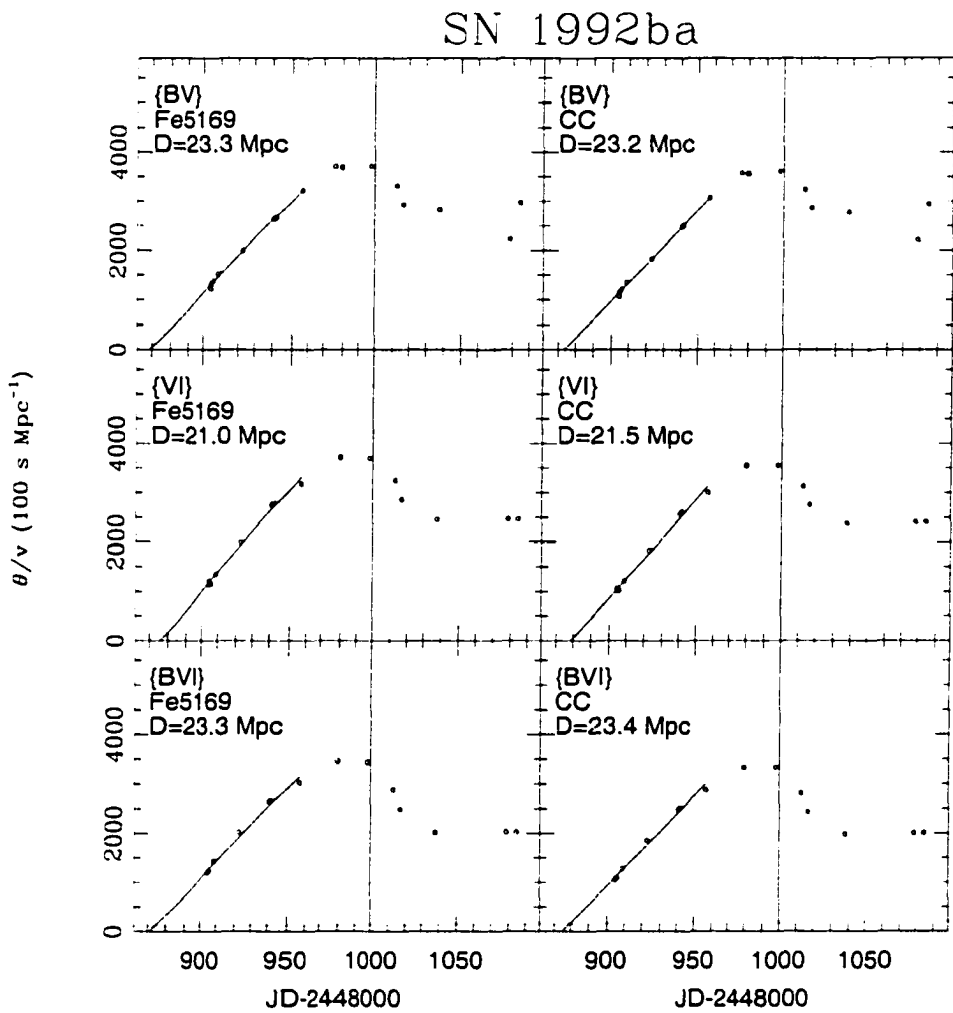


Figure 3.27: θ/v as a function of time for SN 1992ba, obtained from filter subsets $\{BV, VI, BVI\}$. The ridge lines correspond to unweighted least-squares fits to the points between JD 2448904.8-2448956.8. The vertical line shows the end of the plateau phase.

$D=16.2\pm0.7$ Mpc, which is only 1.3σ higher than their result.

This SN is a perfect example to illustrate the type of data needed for EPM. The observations began soon after explosion and covered the entire evolution along the plateau. The frequency of the observations was typically one photometric point every 10 days, and one spectrum every 15-20 days. This analysis demonstrates that it is possible to get a very consistent distance without using vast amounts of telescope time.

3.8.10 SN 1993A

Table 3.28 lists the velocities measured from our two spectra of SN 1993A (the minimum required by EPM). Figure 3.28 shows the BVI light curves and the velocities. The $v(Fe\lambda 5169)/v(CC)$ ratio (bottom panel) shows a $\sim 10\%$ difference between the two power-law fits.

Table 3.29 summarizes the EPM quantities derived for SN 1993A from the $\{VI\}$ filter subset (the tables for $\{BV, BVI\}$ are available in electronic form). Figure 3.29 shows θ/v versus time for all six filter/velocity combinations. It is possible to notice some curvature in these plots. It is possible that this is due to the velocity curves employed (which are derived from only two spectra) and not to dilution factors. Without more information I proceed to fit all the data between JD 2449010.7-2449091.6. The EPM solutions are summarized in Table 3.30.

The discovery of SN 1993A by Wischnjewsky occurred on JD 2449004.67 (Maza & Hamuy, 1993a). No sign of the SN could be seen down to a limiting magnitude of 20 on a pre-discovery plate taken on JD 2448985.5, thus restricting the time of explosion to JD 2448985.5-2449004.67. This does not compare too well with the range $t_0=2448952-2448977$ given by EPM. I hereafter adopt $t_0=2448985.5$.

The EPM distance yielded by the CC curve and the three different filter subsets varies within the range 194-282 Mpc. This corresponds to an 18% range about the average. From the Fe curve I obtain 15% lower distances owing to the smaller velocities implied by the Fe II $\lambda 5169$ line.

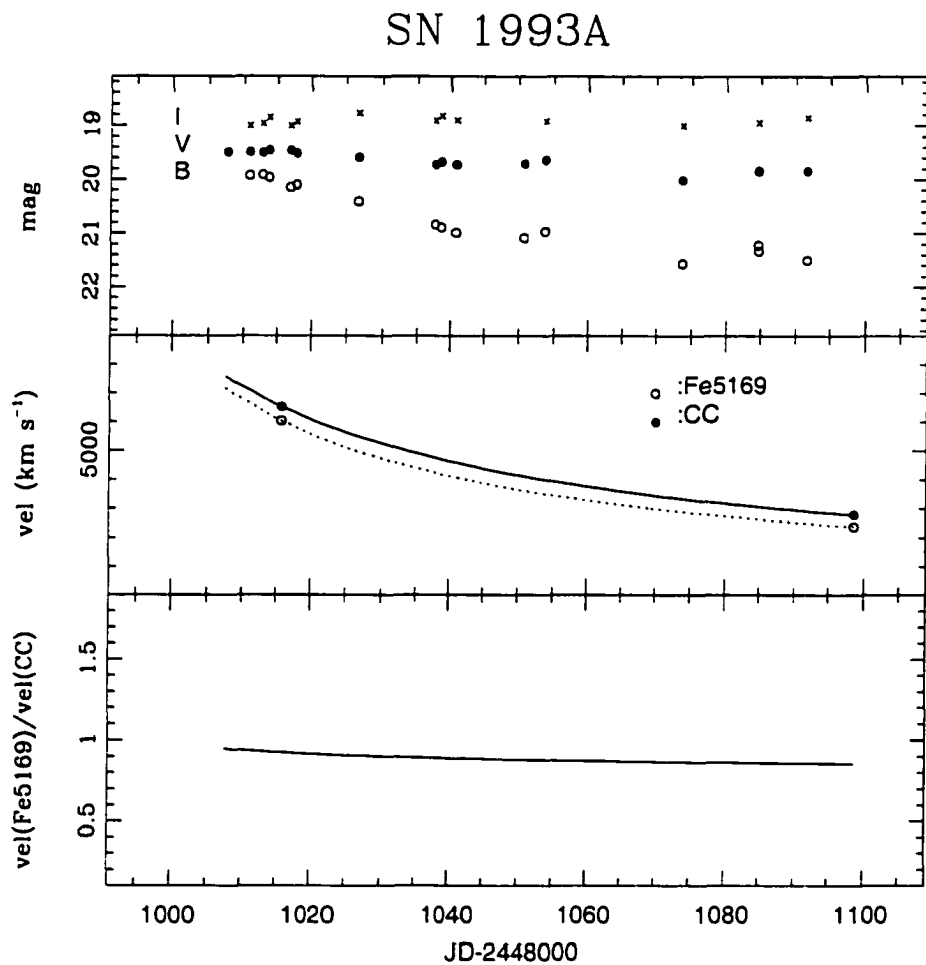


Figure 3.28: Top: BVI light curves of SN 1993A. Middle: CC velocities (closed dots) and the power-law fit (solid line); open dots show Fe 5169 velocities and the dotted line the corresponding fit. Bottom: The ratio of the velocity fits.

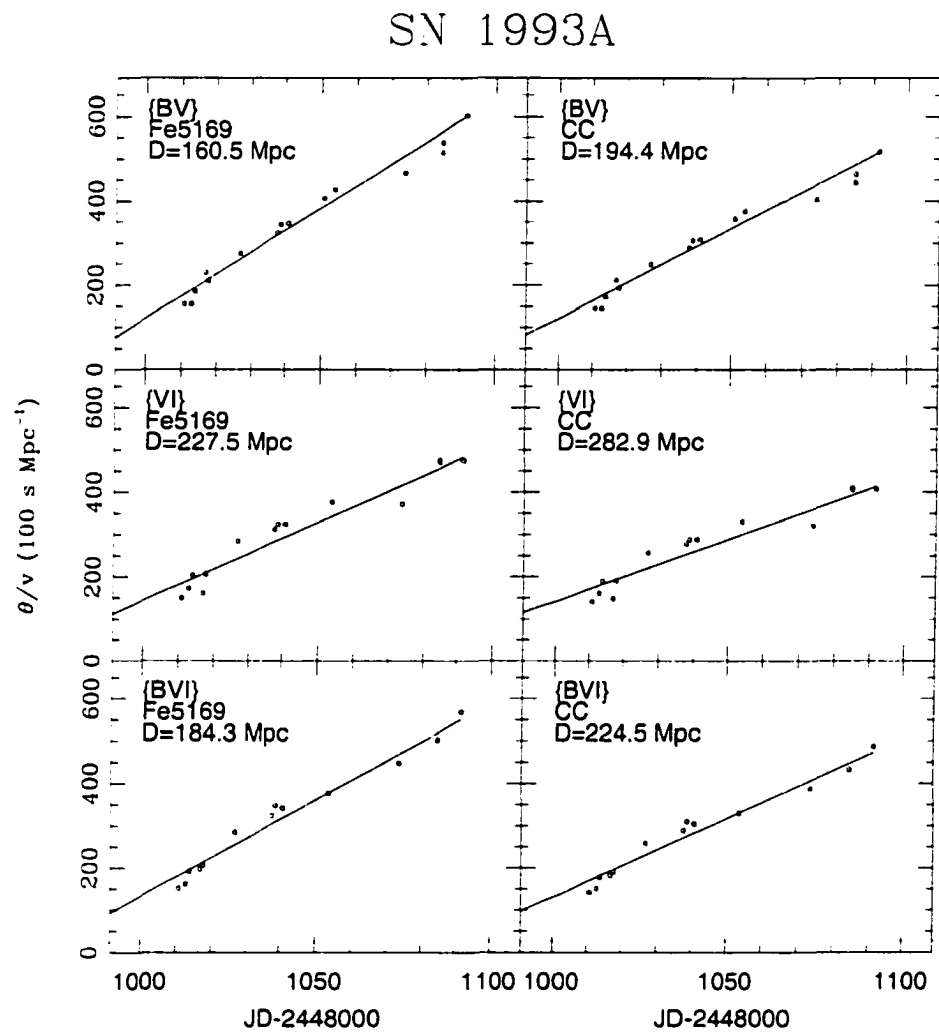


Figure 3.29: θ/v as a function of time for SN 1993A, obtained from filter subsets $\{BV, VI, BVI\}$. The ridge lines correspond to unweighted least-squares fits to the points between JD 2449010.7-2449091.6.

3.8.11 SN 1993S

Table 3.31 presents the velocities measured from our spectra of SN 1993S. Figure 3.30 shows the BVI light curves and the velocity curves. The bottom panel is a plot of the $v(Fe5169)/v(CC)$ ratio which reveals that $v(CC)$ exceeds $v(Fe5169)$ by $\sim 10\%$.

Table 3.32 summarizes the EPM quantities derived for SN 1993S from the $\{BVI\}$ filter subset (the tables for $\{BV, VI\}$ are available in electronic form). Figure 3.31 shows the run of θ/v as a function of time for the six filter/velocity combinations. Evidently there is an inflection around JD 2449165 in all filter subsets, both in the Fe and CC cases. Since the points before this epoch are obtained by extrapolating $v(t)$, it is not possible to comment on the behavior of the dilution factors before JD 2449165. After that day, however, the velocity curves are reasonably constrained, yet the θ/v parameter shows a flat behavior. Clearly EPM is not performing well in this case, perhaps because this object was not a plateau event. Evidently no EPM solutions can be obtained for SN 1993S.

This SN was discovered by Antezana on JD 2449133.86 (Maza & Hamuy, 1993b). The blue color measured a few days later suggested that the SN was found quite young, so I adopt $t_0=2449130$.

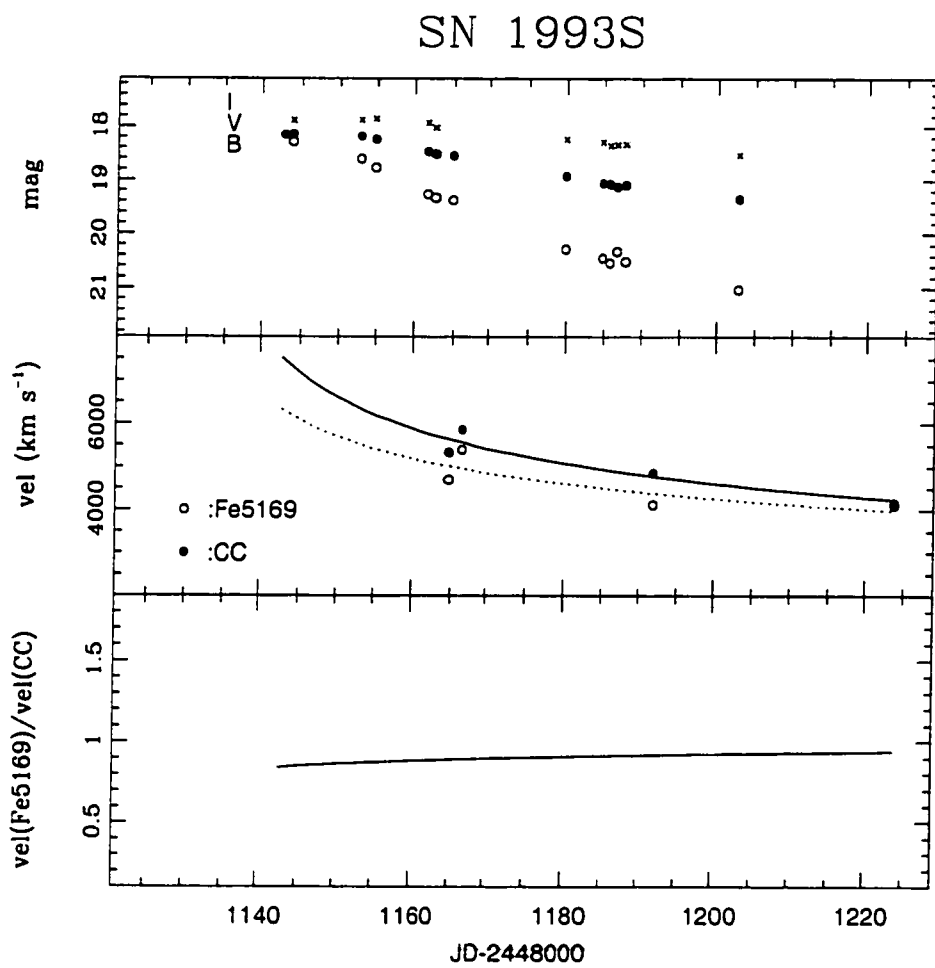


Figure 3.30: Top: *BVI* light curves of SN 1993S. Middle: CC velocities (closed dots) and the power-law fit (solid line); open dots show Fe 5169 velocities and the dotted line the corresponding fit. Bottom: The ratio of the velocity fits.

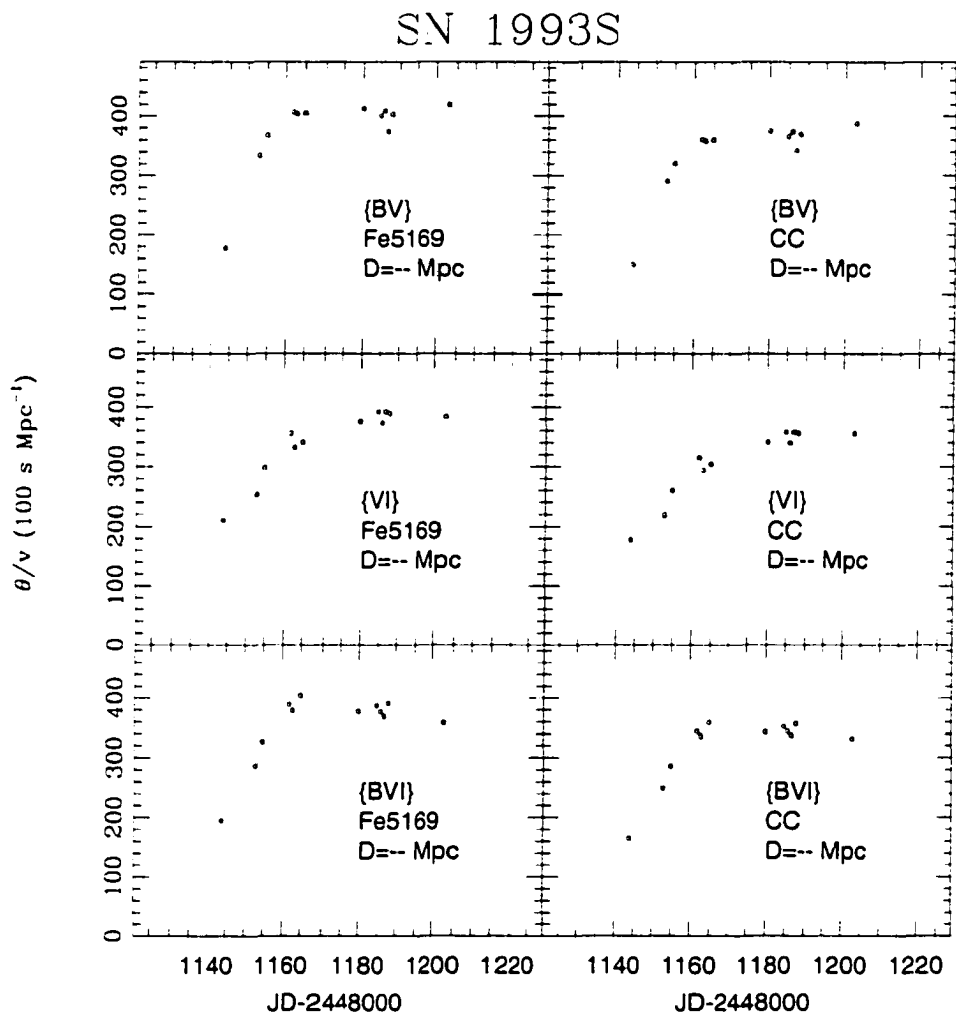


Figure 3.31: θ/v as a function of time for SN 1993S, obtained from filter subsets $\{BV, VI, BVI\}$.

3.8.12 SN 1999br

Table 3.33 lists the velocities measured from our spectra of SN 1999br and one late spectrum kindly provided by A. Pastorello. Figure 3.32 shows the $BVIZ$ light curves and the velocity curves. The $v(Fe\lambda 5169)/v(CC)$ ratio, shown in the bottom panel, varies from 0.8 to 1.5. This anticipates very different EPM solutions depending on the method used to estimate the photospheric velocity.

The EPM quantities for the $\{VI\}$ filter subset are given in Table 3.34. (the tables for $\{BV, BVI, VZ\}$ are available in electronic form). Figure 3.33 shows the EPM results for the eight filter/velocity combinations. θ/v evolves quite linearly over the entire plateau phase until the last observations on JD 2451380. This is quite remarkable, considering that after JD 2451320 the photospheric temperature was low enough that it proves necessary to extrapolate the dilution factors. EPM performs very well in this case, at all epochs and over a broad wavelength range encompassed by the $BVIZ$ filters. To avoid extrapolations in dilution factors and velocities I proceed to apply EPM in the range JD 2451291.8-2451330.5. The solutions are given in Table 3.35.

SN 1999br was discovered at 17th mag by the Lick Observatory Supernova Search (LOSS, hereafter) on JD 2451280.9 (King, 1999). A pre-discovery image taken on JD 2451264.9 showed nothing at the SN position down to a limiting magnitude of 18.5 (Li, 1999a), which implies that the SN exploded between JD 2451264.9-2451280.9. A spectrum taken three days after discovery (Garnavich et al., 1999) revealed a blue continuum and the presence of He I $\lambda 5876$ line, which suggested that the SN was indeed very young. From the EPM analysis I get a time of explosion of JD 2451277.9 and JD 2451285.0 from Fe and CC, respectively. While the CC curve predicts an explosion five days after discovery, the Fe solution agrees very well with the spectroscopic information. I adopt $t_0=2451277.9$, the value derived from the Fe curve.

The distance derived from the CC points varies within 11-12.1 Mpc. There is great

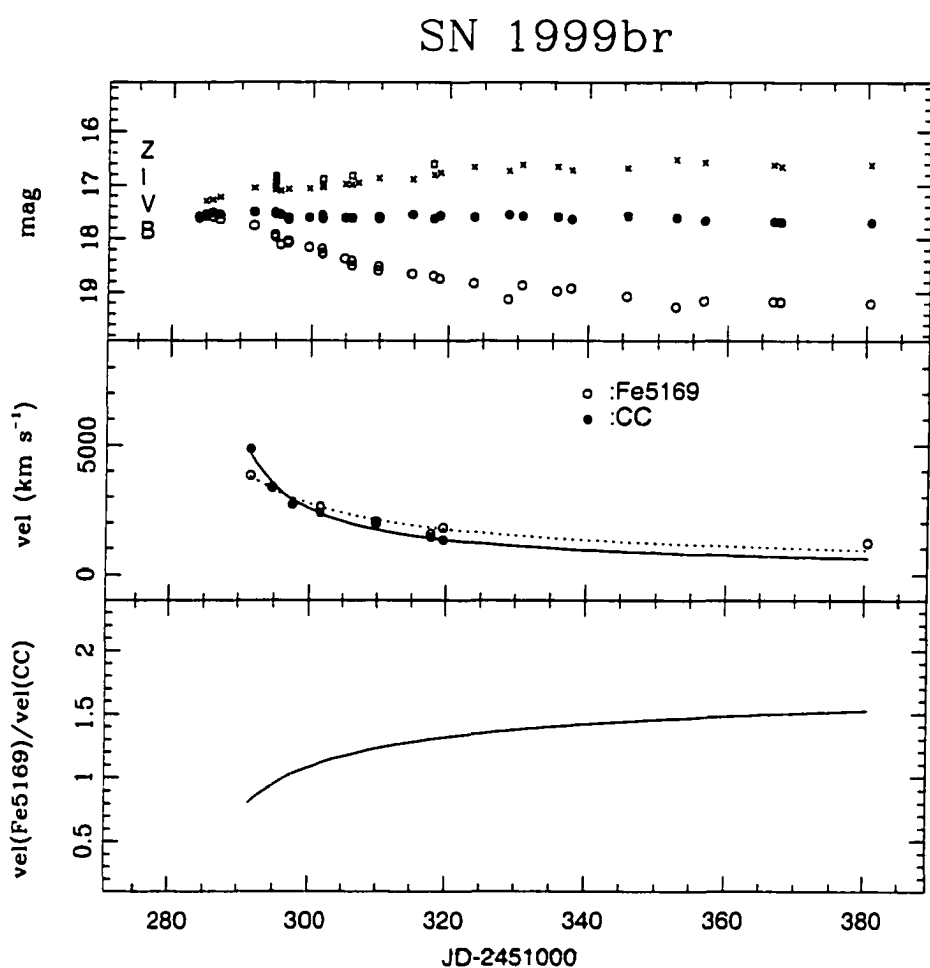


Figure 3.32: Top: *BVIZ* light curves of SN 1999br. Middle: CC velocities (closed dots) and the power-law fit (solid line); open dots show Fe 5169 velocities and the dotted line the corresponding fit. Bottom: The ratio of the velocity fits.

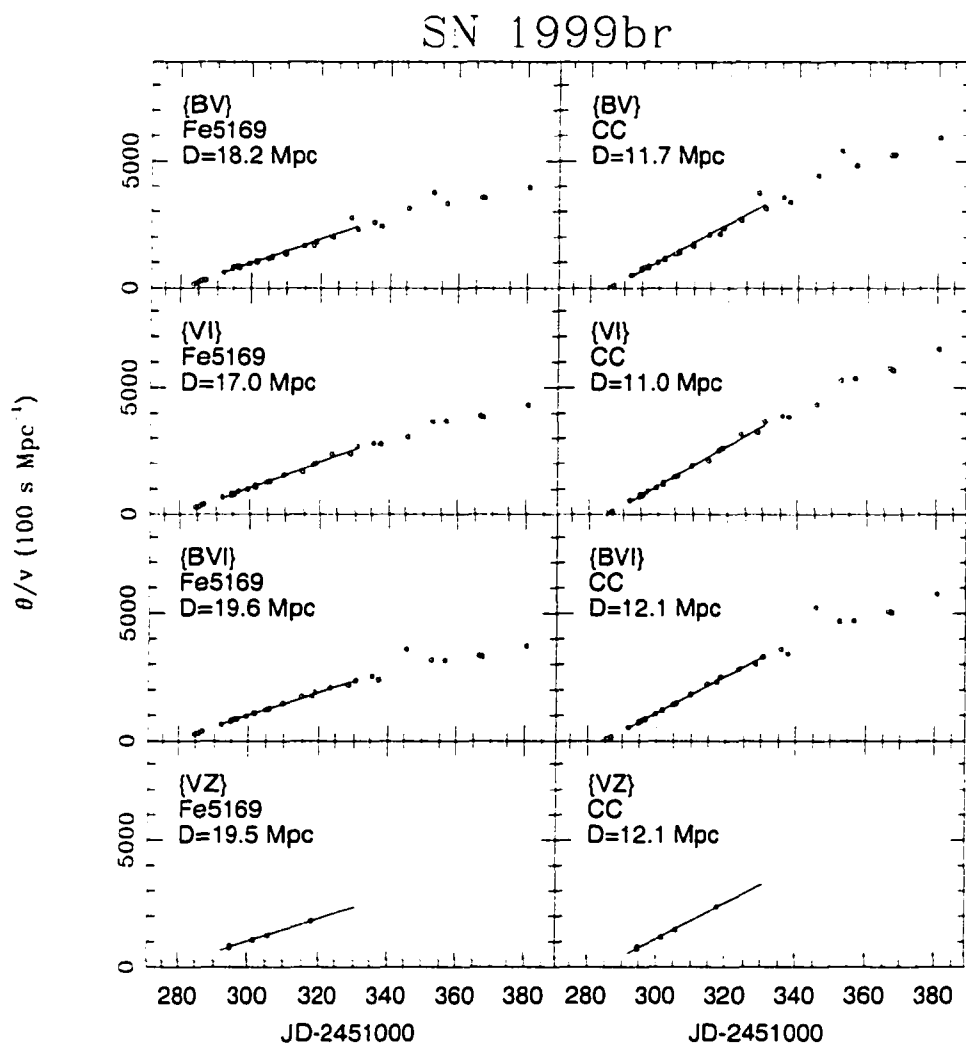


Figure 3.33: θ/v as a function of time for SN 1999br, obtained from filter subsets $\{BV, VI, BVI, VZ\}$. The ridge lines correspond to unweighted least-squares fits to the points between JD 2451291.8-2451330.5.

internal consistency at all epochs and over a wide wavelength range. However, there is a large discrepancy with the Fe solution which lies between 17-19.5 Mpc. If I remove the first CC velocity point which appears too high, the resulting distance increases by 10% which is not enough to explain the difference with the Fe solution. This example reveals the relevance of the method used to derive photospheric velocities in the EPM analysis.

This SN also permits me to derive solutions from magnitude interpolations to the time of the spectroscopy and check the power-law fits. Table 3.35 lists the solutions derived from JD 2451291-2451320. Although the resulting distances vary by up to $\pm 20\%$ with respect to the power-law solutions, on average there is no significant difference between the two methods. This comparison gives an idea of the error introduced by the power-law method.

3.8.13 SN 1999ca

Table 3.36 summarizes the velocities measured from our spectra. Figure 3.34 shows the BVI light curves (top panel) and velocity curves (middle panel) of SN 1999ca. Evidently, our spectra covered a very small baseline of 13 days, so that the velocity curves shown here are obtained from a large extrapolation. Over the period covered by our spectroscopic observations, $v(Fe5169)$ shows a very shallow slope compared to $v(CC)$, which is responsible for the large $v(Fe5169)/v(CC)$ ratio (shown in the bottom panel). It is hard to ascertain the reality of this difference with so few data points, but it is possible to anticipate that the EPM solutions must be very uncertain.

The EPM quantities derived from the BV filters and the CC velocities can be found in Table 3.37 (the tables for $\{VI, BVI\}$ are available in electronic form). Figure 3.35 shows the corresponding run of θ/v for the six filter/velocity combinations. Note the very flat evolution of θ/v when the Fe velocity curve is used. This is clearly a symptom of the shallow velocity curve which, naturally, prevents to obtain an EPM solution. When the CC curve is employed, instead, θ/v increases roughly linearly with time, thus suggesting a good behavior of the dilution factors. However, it proves impossible to get convergence from my iterative procedure for any of the filter subsets. Like in the case of SNe 1990K and 1992af, I find that a moderate change in t_0 causes a slight change in the velocity curve, which leads to a very different t_0 from the fit to the (θ_i, t_i) points. In the case of those SNe the problem is caused by the fact that the objects were caught too late. Here, instead, the problem is caused by the small baseline of our spectroscopic observations. This is certainly a shame given the great photometric sampling obtained.

SN 1999ca was discovered by the Perth Astronomy Research Group (Woodings et al., 1999) on JD 2451296.05. Their report pointed out that the SN was not present down to 19th mag on an image taken on JD 2451270.5. Below I adopt an explosion time of JD 2451280.

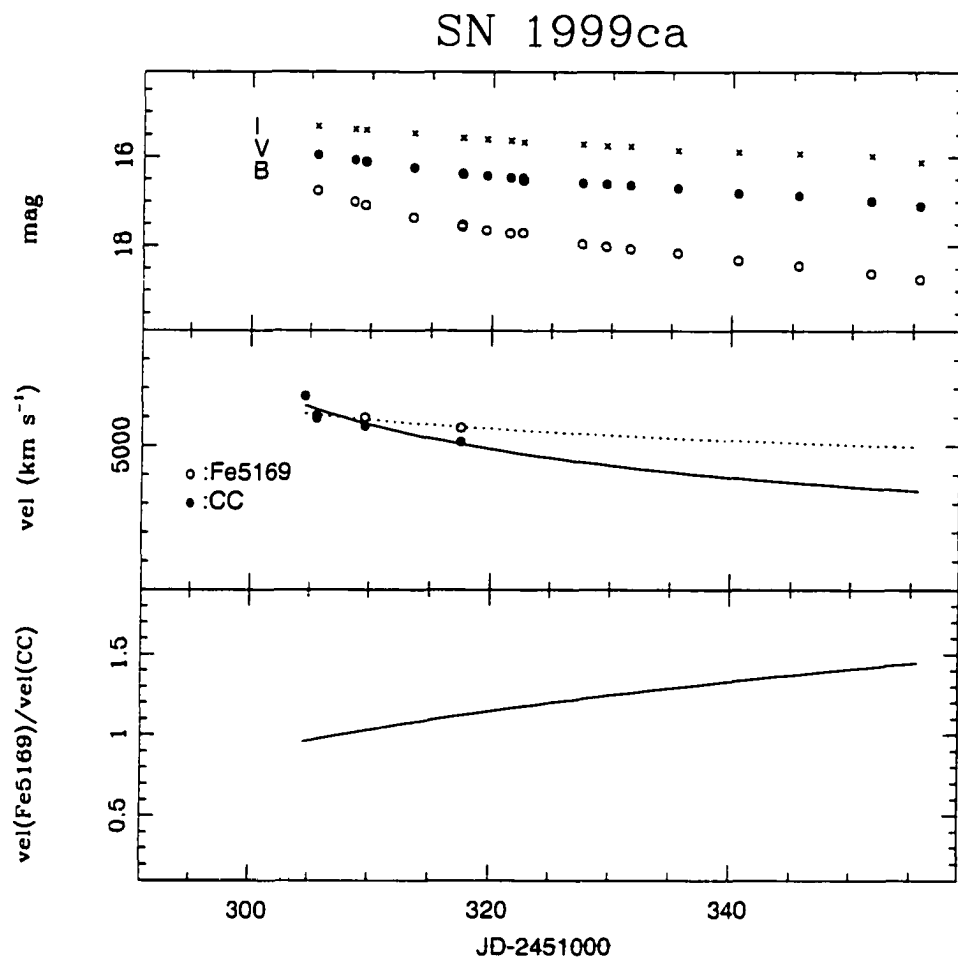


Figure 3.34: Top: *BVI* light curves of SN 1999ca. Middle: CC velocities (closed dots) and the power-law fit (solid line); open dots show Fe 5169 velocities and the dotted line the corresponding fit. Bottom: The ratio of the velocity fits.

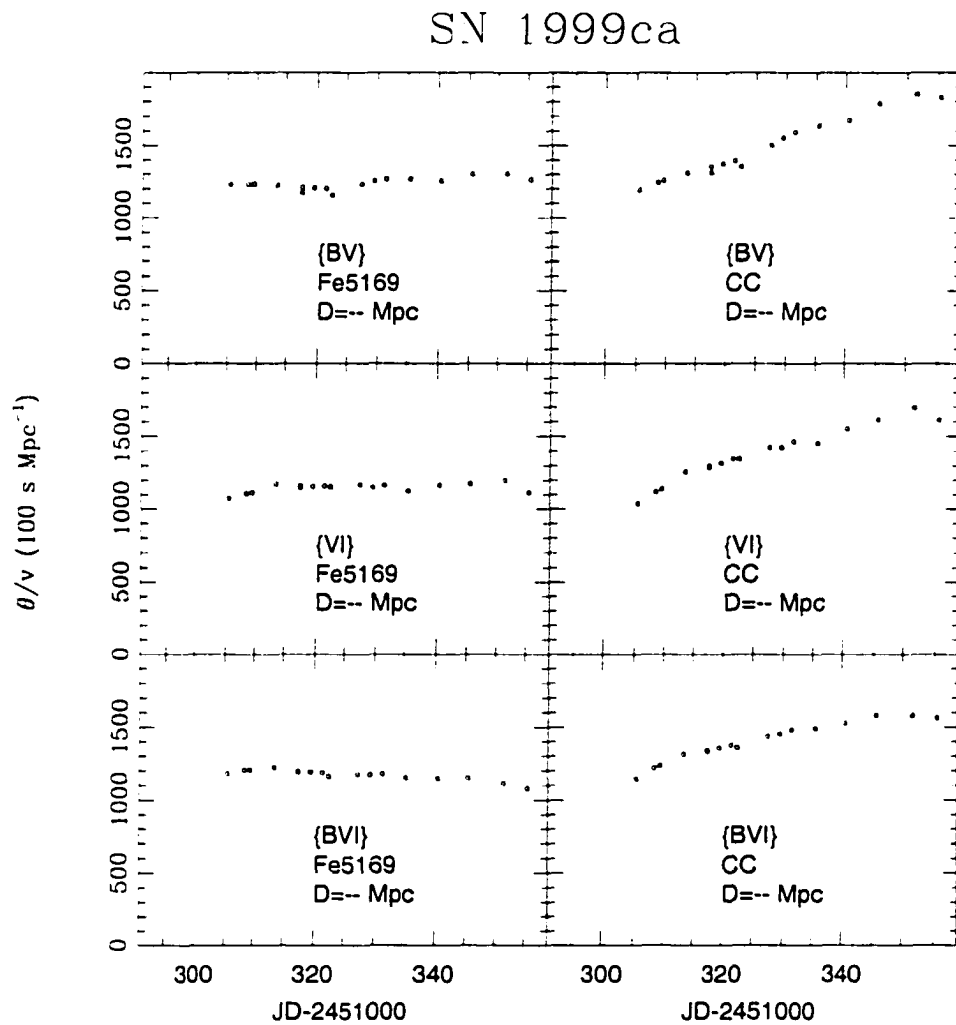


Figure 3.35: θ/v as a function of time for SN 1999ca, obtained from filter subsets $\{BV, VI, BVI\}$. No EPM solution could be obtained in this case.

3.8.14 SN 1999cr

Table 3.38 gives the velocities measured from our spectra of SN 1999cr. Figure 3.36 shows the BV^I light curves and the velocity curves. The $v(Fe5169)/v(CC)$ ratio, shown in the bottom panel, is quite constant and close to unity at all times.

The EPM quantities for the $\{VI\}$ filter subset are given in Table 3.39. (the tables for $\{BV, BV^I\}$ are available in electronic form). Figure 3.37 shows the EPM results for the six filter/velocity cases. The sudden drop of θ/v corresponds to the end of the plateau at JD 2451330. Evidently, the run of θ/v shows a change in slope around JD 2451270, well before the end of the plateau, for all six filter/velocity combinations. Although the velocity curves were reasonably sampled on five epochs and the power-law fits work reasonably well, it is fair to ask if this problem could be due to an artifact introduced by the velocity interpolation. If I replace the power-law fit with a linear interpolation scheme the inflection does not go away, which suggests that the problem is probably caused by dilution factors. Over most of the plateau the color temperature of the SN was higher than those of E96 models, so that almost no extrapolations are required to obtain ζ . Like in the case of SN 1986L, the inevitable conclusion in this case is that the dilution factors perform poorly. An examination of the spectra of this object does not show an unusual behavior of the line profiles, making it hard to explain the poor performance of the dilution factors. Despite the difficulties, I choose to carry out fits to the early-time points between JD 2451256.8-2451267.8. The solutions are given in Table 3.40.

SN 1999cr was discovered by Antezana on JD 2451249.7 in the course of the SOIRS survey (Maza & Hamuy, 1999). The EPM analysis yields a time of explosion between JD 2451208-2451229, implying that the SN was found at an approximate age of 30 days. Below I adopt $t_0=2451221.5$, the average of the six EPM solutions.

The distance from the CC points and the three subsets agree quite well between 72-95 Mpc ($\sim 15\%$ about the average). Given the similarity between the two velocity curves the

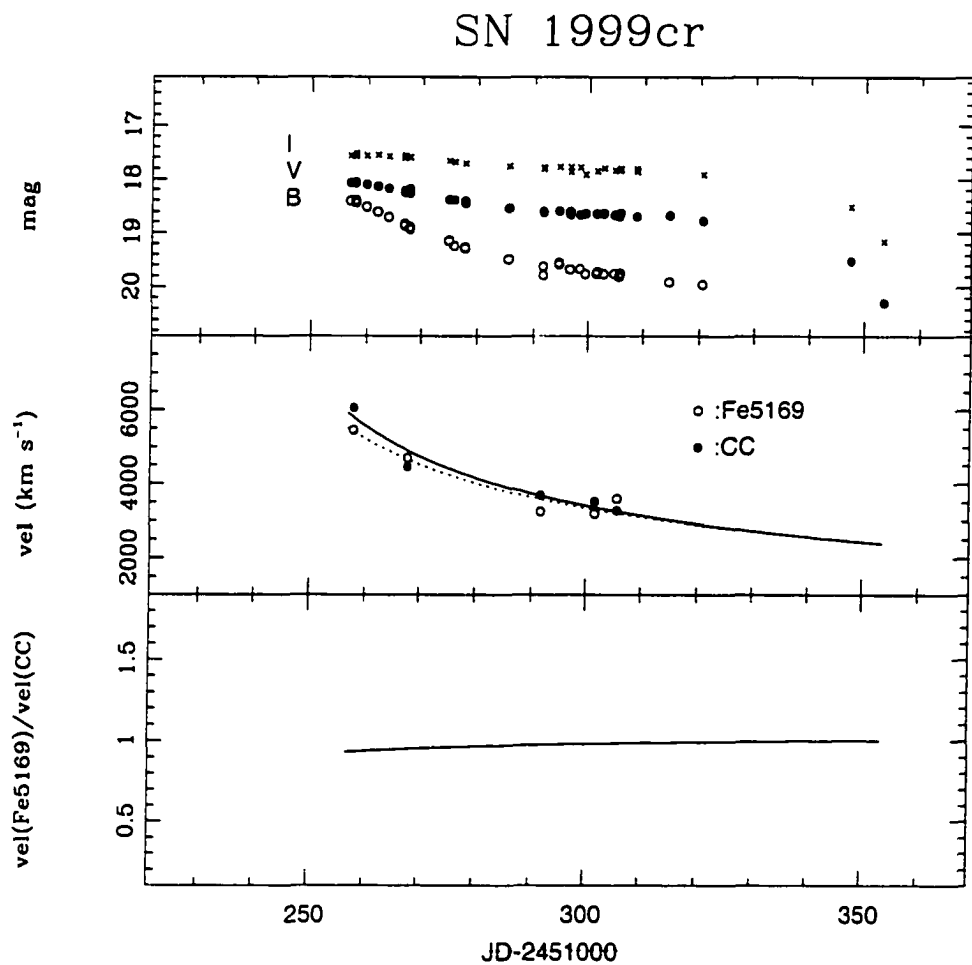


Figure 3.36: Top: BVI light curves of SN 1999cr. Middle: CC velocities (closed dots) and the power-law fit (solid line); open dots show Fe 5169 velocities and the dotted line the corresponding fit. Bottom: The ratio of the velocity fits.

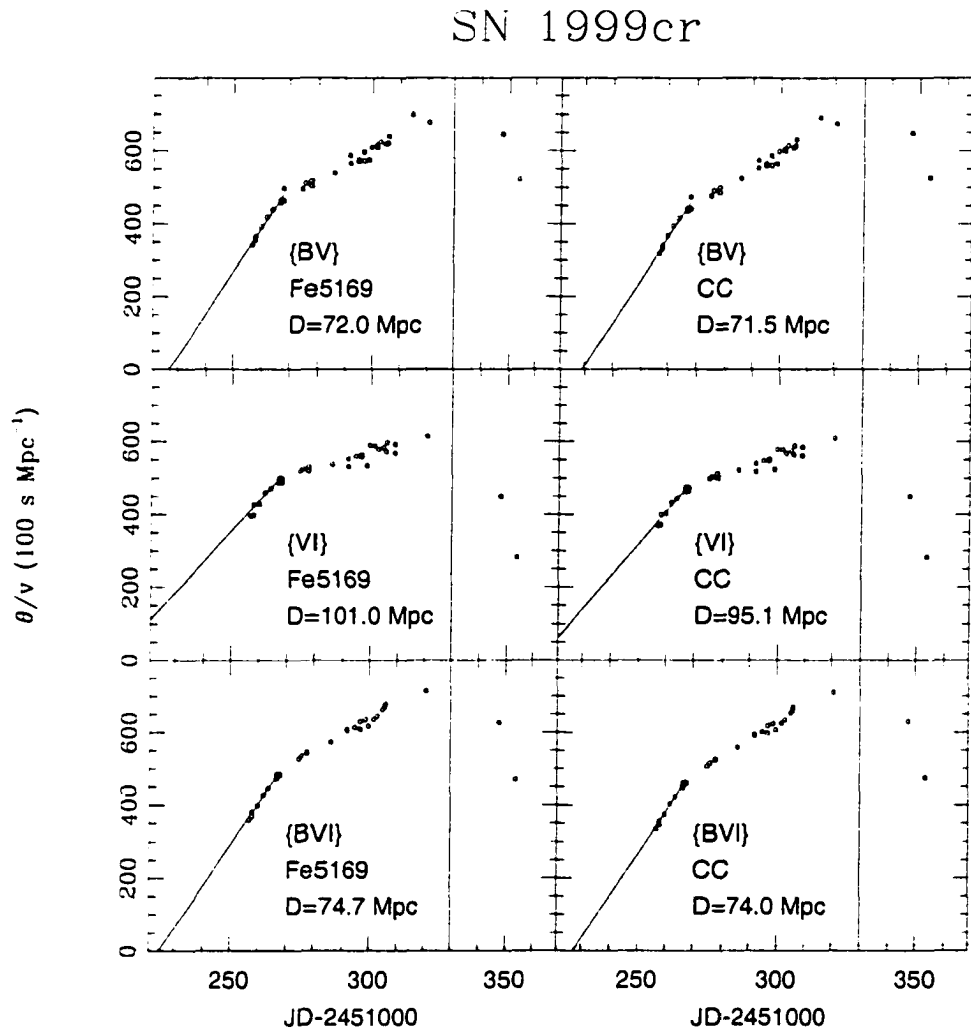


Figure 3.37: θ/v as a function of time for SN 1999cr, obtained from filter subsets $\{BV, VI, BVI\}$. The ridge lines correspond to unweighted least-squares fits to the points between JD 2451256.8-2451267.8. The vertical line shows the end of the plateau phase.

Fe distances prove insignificantly different than those given above, namely, $D(Fe)=72\text{-}101 \text{ Mpc}$.

3.8.15 SN 1999eg

Table 3.41 presents the velocities measured from our two spectra of SN 1999eg. Figure 3.38 shows the BVI light curves and the velocity curves. The bottom panel shows that the ratio $v(Fe5169)/v(CC)$ decreases from unity to 0.8, which is expected to cause some differences in the EPM solutions.

Table 3.42 presents EPM quantities derived for SN 1999eg from the $\{BV\}$ filter subset (the table for $\{VI, BVI\}$ are available in electronic form). Figure 3.39 shows θ/v versus time for the six filter/velocity combinations. While θ/v increases quite linearly for $\{VI\}$, it shows evident curvatures in $\{BV, BVI\}$. Given the poorly constrained $v(t)$ curve it proves hard to attribute the departure from linearity to the dilution factors, especially at the epochs of the first and last observations where the velocities have to be extrapolated. To avoid problems due to extrapolated velocities I proceed to get a solution from JD 2451467.8-2451493.7. Table 3.43 presents the EPM solutions for $\{BV, VI, BVI\}$. Also included in this table are the results from interpolating the magnitudes to the time of the two spectroscopic observations. This approach yields distances 7% higher than the power-law method.

SN 1999eg was discovered by Armstrong (Hurst, 1999) on JD 2451455.57. in the course of the U. K. Nova/Supernova Patrol program. The explosion time yielded by EPM lies between JD 2451429-2451445, which is about 2-3 weeks before discovery. Taking the average from the six solutions I hereafter adopt $t_0=2451437.2$.

The EPM distance derived from the CC velocities has a spread of only 12% (97-121 Mpc) among the different filter subsets. This proves surprisingly small given the curvature displayed by θ/v . The steeper Fe velocity curve produces a smaller distance between 68-84 Mpc.

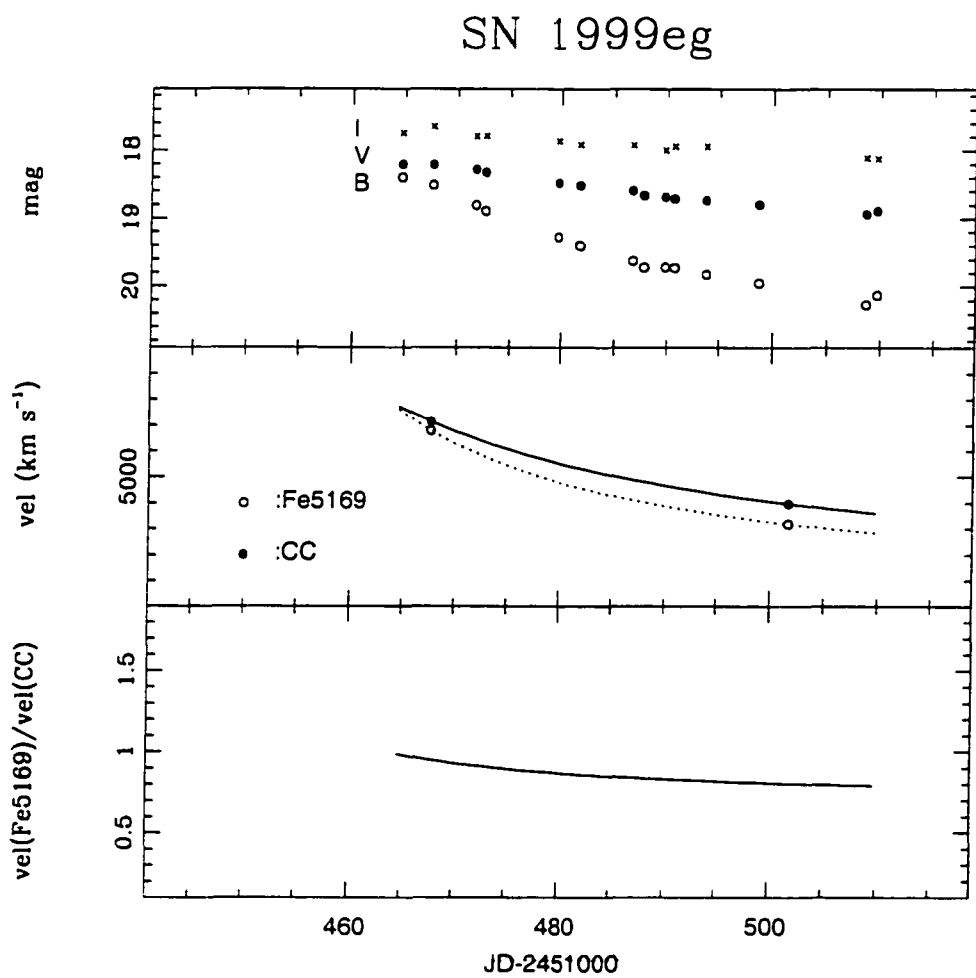


Figure 3.38: Top: *BVI* light curves of SN 1999eg. Middle: CC velocities (closed dots) and the power-law fit (solid line); open dots show Fe 5169 velocities and the dotted line the corresponding fit. Bottom: The ratio of the velocity fits.

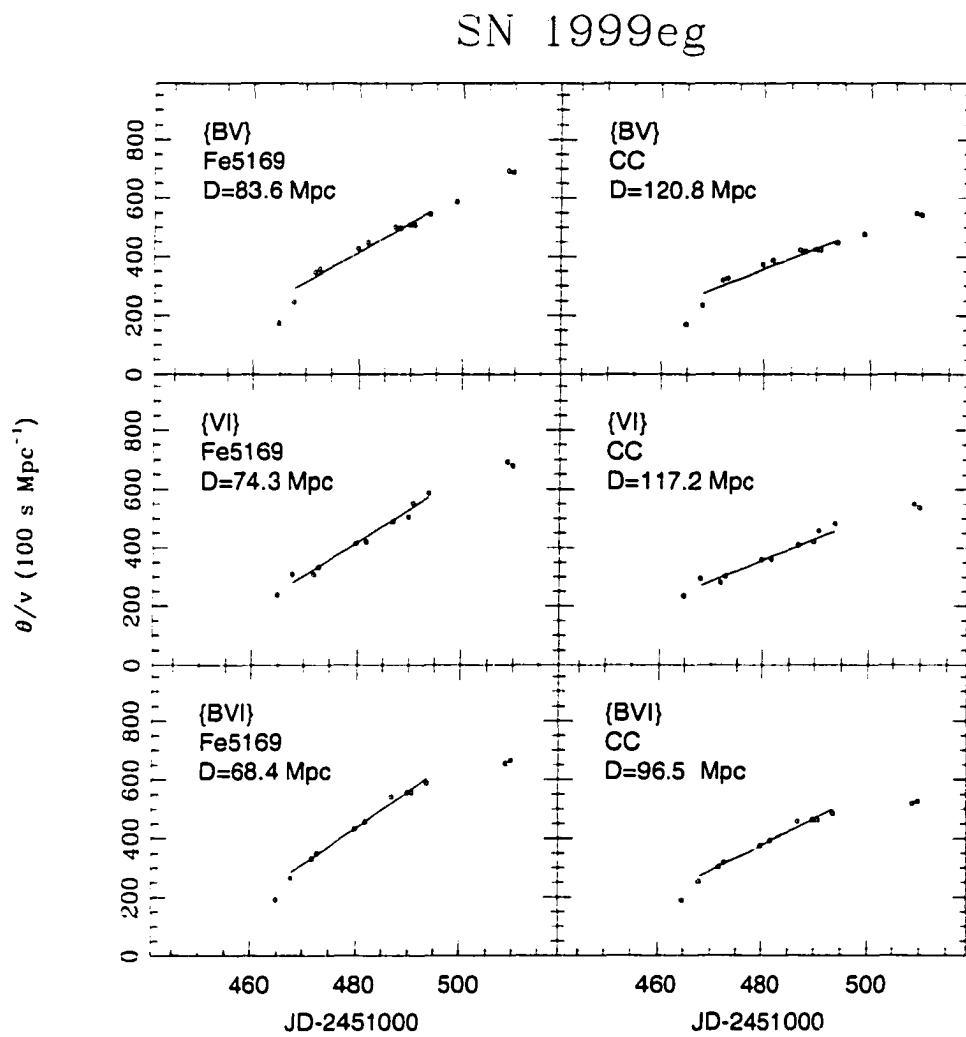


Figure 3.39: θ/v as a function of time for SN 1999eg, obtained from filter subsets $\{BV, VI, BVI\}$. The ridge lines correspond to unweighted least-squares fits to the points between JD 2451467.8-2451493.7.

3.8.16 SN 1999em

Table 3.44 presents the velocities measured from our spectra of SN 1999em. This table also includes the Fe velocities derived from the absorption line measurements published by Leonard et al. (2001), corrected to a heliocentric redshift of 717 km s^{-1} . Figure 3.40 shows the BVI light curves and the velocity curves. In a recent paper (Hamuy et al., 2001) I published a detailed EPM analysis for this SN, employing a polynomial fit to the $v(CC)$ points instead of the power-law fit used here. For comparison, the polynomial fit for this SN is included in this figure as a dashed line. Because of the high order of the polynomial, the fit went almost through all points. The bottom panel shows the ratio $v(Fe5169)/v(CC)$ which reveals differences of the order of $\pm 10\%$ between the two power-law fits.

Table 3.45 presents EPM quantities derived for SN 1999em from filter subset $\{VH\}$ (the tables for subsets $\{BV, BVI, VI, VZ, VJ, VK, JHK\}$ are available in electronic form). Figure 3.41 shows θ/v versus time for filters $\{BV, BVI, VI, VZ\}$. The daily sampling of the light curves permits us to appreciate in great detail the evolution of θ/v . Overall, this parameter increases linearly with time until the end of the plateau around JD 2451580. However, a curvature can be appreciated which becomes more pronounced as the plateau approaches its end. In $\{BV\}$ there is a kink in the θ/v curve between JD 2451590-2451600. Since all these features vary from subset to subset, most likely they are due to dilution factors. Figure 3.42 presents the EPM results for subsets $\{VJ, VH, VK, JHK\}$. For $\{VJ, VH, VK\}$ the dilution factors behave remarkably well over a period of 100 days of SN evolution until the very end of the plateau phase. In $\{JHK\}$ the scatter increases considerably because the errors in the derived color temperatures increase as the Rayleigh-Jeans limit is approached. These plots confirm the internal consistency of the dilution factors computed by E96 from IR wavelengths. Because the photospheric temperature of SN 1999em fell below the temperature limit of

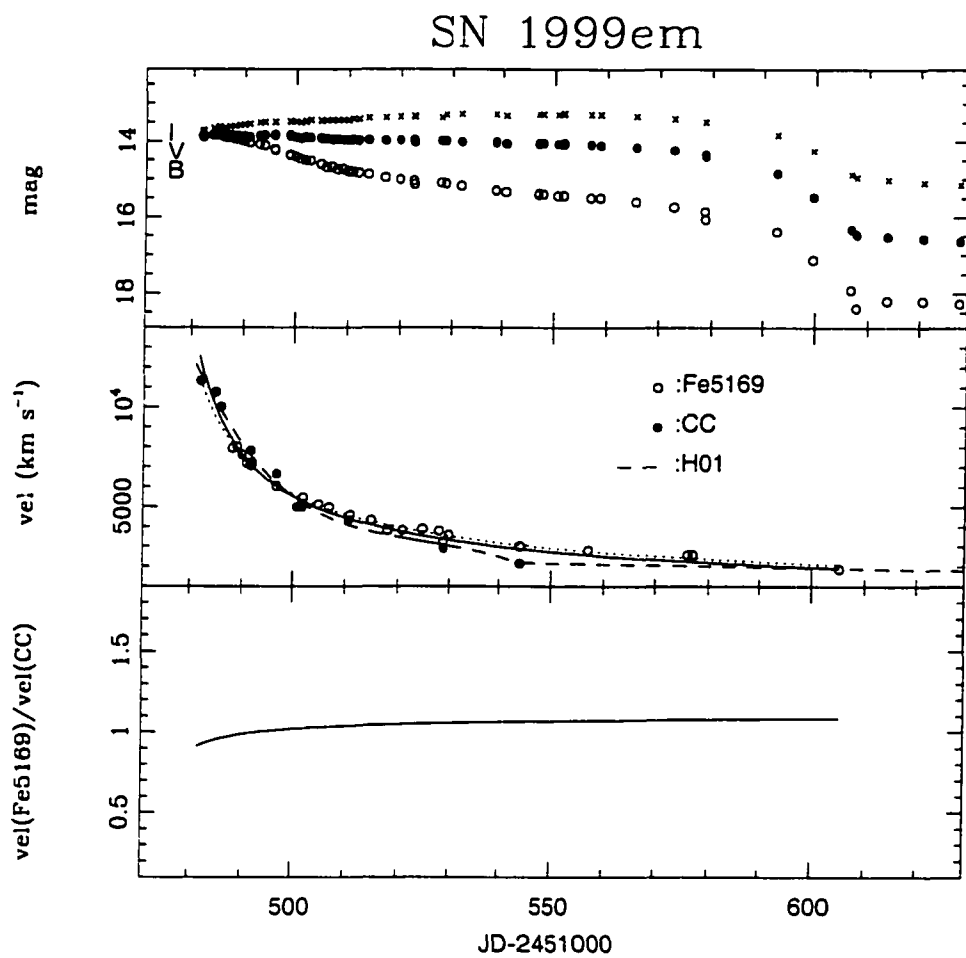


Figure 3.40: Top: BVI light curves of SN 1999em. Middle: CC velocities (closed dots) and the power-law fit (solid line); open dots show Fe 5169 velocities and the dotted line the corresponding fit. For comparison the velocity curve adopted by Hamuy et al. (2001) is included (dashed line). Bottom: The ratio of the power-law velocity fits.

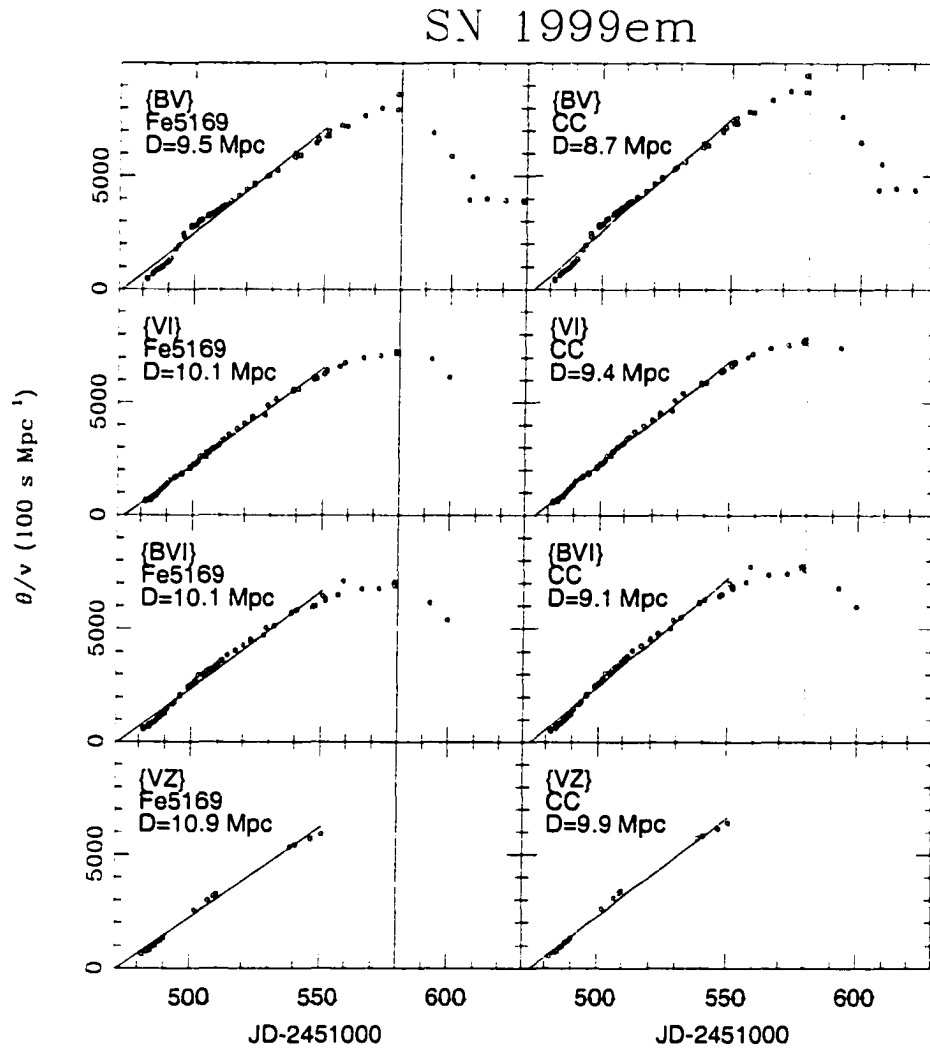


Figure 3.41: θ/v as a function of time for SN 1999em, obtained from filter subsets $\{BV, VI, BVI, VZ\}$. The ridge lines correspond to unweighted least-squares fits to the points between JD 2451481.8-2451550.6. The vertical line shows the end of the plateau phase.

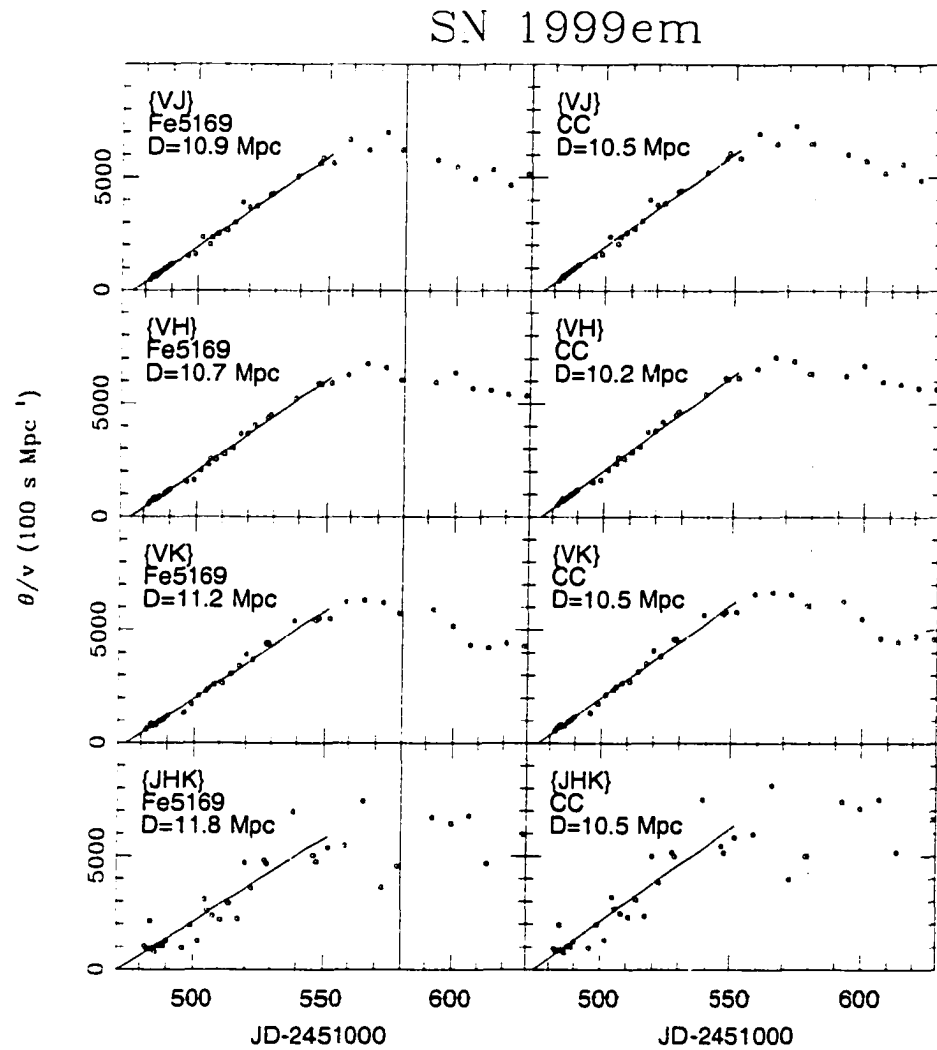


Figure 3.42: θ/v as a function of time for SN 1999em, obtained from filter subsets $\{VJ, VH, VK, JHK\}$. The ridge lines correspond to unweighted least-squares fits to the points between JD 2451481.8-2451551.7. The vertical line shows the end of the plateau phase.

the E96 models at JD 2451550, I proceed to fit the data in a restricted range between JD 2451481.8-2451551.7. Table 3.46 presents the EPM solutions for all filter subsets.

SN 1999em was discovered on JD 2451480.94 in the course of the LOSS program (Li, 1999b). A pre-discovery image taken on JD 2451471.95 showed nothing at the position of SN 1999em (with a limiting magnitude of ~ 19.0), which indicated that the SN was caught at an early stage. The explosion time yielded by EPM varies in a narrow range between JD 2451471-2451476, which proves in great agreement with the pre-discovery observation. Taking the average from all solutions I hereafter adopt $t_0=2451474$.

The EPM distance derived from the CC velocities has a spread of 10% (8.7-10.5 Mpc) among the different filter subsets. This range can be compared with that obtained by Hamuy et al. (2001) from the polynomial fit to the CC velocities, namely, 6.9-8.6 Mpc. This 25% difference is quite significant and is entirely due to the different schemes employed to fit the velocity points. More insight about interpolation schemes can be obtained from interpolating magnitudes to the epoch of the spectroscopic observations which, given the great sampling of the light curves, is almost equivalent to no interpolation. The results are listed in Table 3.46 which reveal, again, that the CC distances are 27% lower than the values yielded by the power-law fits. These comparisons demonstrate the high sensitivity of EPM to the fitting scheme used to interpolate velocities, even in a case like this where the velocity curve was well-sampled.

When the Fe velocity curve is adopted the resulting distance lies between 9.5-11.8 Mpc, which is only 5% larger than the solution derived from the power-law fit to the $v(CC)$ points. This is a reasonable agreement considering that the first week of the Fe curve is obtained from extrapolation of the first $v(Fe)$ point.

Leonard et al. (2001) have recently derived an EPM distance to SN 1999em from magnitude interpolations to the epoch of the spectroscopy. Using velocities derived from the Fe II λ 4924, 5018, 5169 lines they derived distances of 8.2, 9.7, and 9.2 Mpc from

$\{BV, VI, BVI\}$, respectively. These compare well with my solutions of 9.2, 9.8, and 9.5 Mpc derived from magnitude interpolation and Fe velocities.

3.8.17 SN 2000cb

Table 3.47 presents the velocities measured from our spectra of SN 2000cb. Figure 3.43 illustrates the BVI light curves and the velocity curves. The light curves are reminiscent of SN 1987A. Perhaps this SN also had a compact progenitor and might not be a good candidate for an EPM analysis, but I include here to explore the application of the method to another non-standard plateau SN. The $v(Fe5169)/v(CC)$ ratio, shown in the bottom panel, reveals that the CC curve is somewhat steeper than the Fe curve. Initially $v(CC)$ is 25% higher than $v(Fe)$ and at later times they approach each other.

The EPM quantities for the $\{BVI\}$ filter subset are given in Table 3.48. (the tables for $\{BV, VI\}$ are available in electronic form). Figure 3.44 shows the EPM results for the six filter/velocity combinations. During the first 35 days θ/v grows linearly in all filter subsets. The departure from linearity first occurs in $\{VI\}$ at JD 2451690, which coincides with the time at which the color temperature dropped below the range encompassed by the E96 models. The linear phase lasts at least 15 more days in $\{BV\}$ and $\{BVI\}$ which, again, is the time when the dilution factors are obtained from extrapolation. Beyond JD 2451730 the drop of θ/v is quite evident but this is not a problem given that this is the time when the SN began to loose its photosphere. Overall, it is remarkable how well the dilution factors perform, especially considering that SN 2000cb is far from a typical plateau event. Next I present EPM solutions from the early evolution of the SN (JD 2451663.8-2451705.7). For $\{VI\}$ I restrict the sample even more to JD 2451663.8-2451684.8 to avoid extrapolations of dilution factors in temperature. The solutions are given in Table 3.49.

SN 2000cb was discovered (at a magnitude of 18.5) by the LOSS program on JD 2451657.91 (Papenkova & Li, 2000). A pre-discovery image taken on JD 2451642.91 showed no evidence of the SN down to 18.5 mag. The EPM analysis yields an excellent agreement with these observation, with the explosion time ranging between JD 2451651-

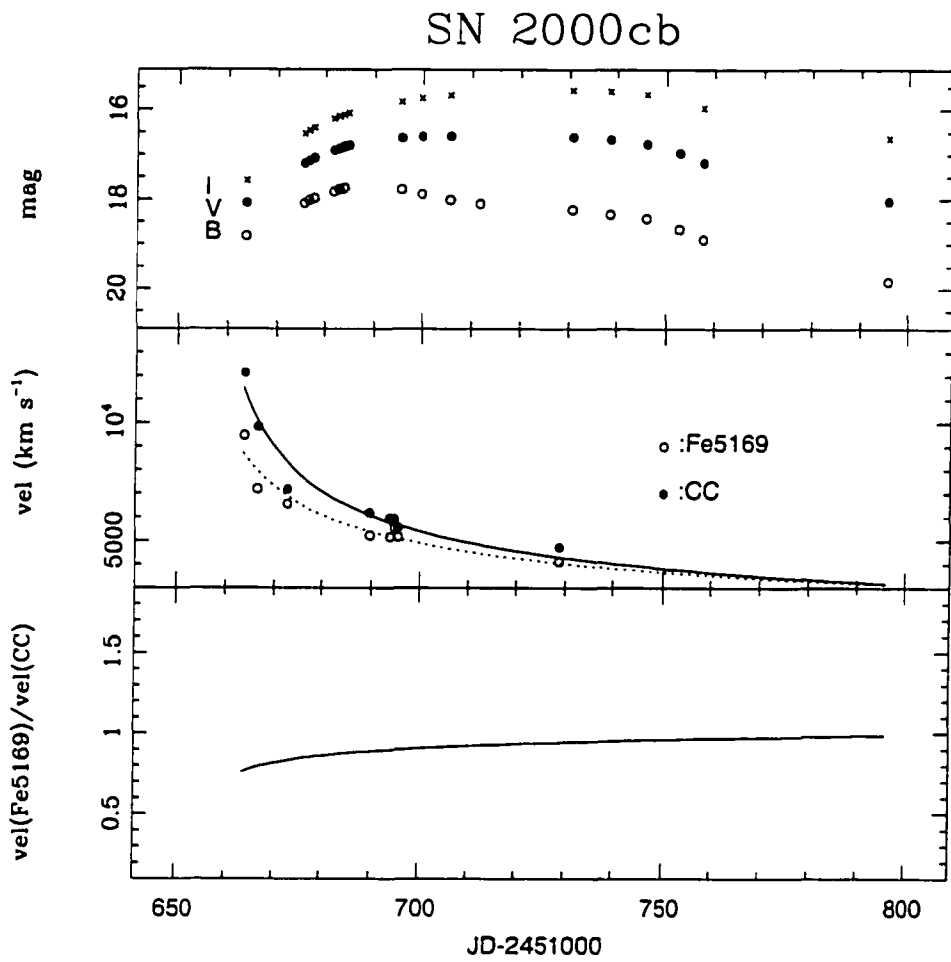


Figure 3.43: Top: *BVI* light curves of SN 2000cb. Middle: CC velocities (closed dots) and the power-law fit (solid line); open dots show Fe 5169 velocities and the dotted line the corresponding fit. Bottom: The ratio of the velocity fits.

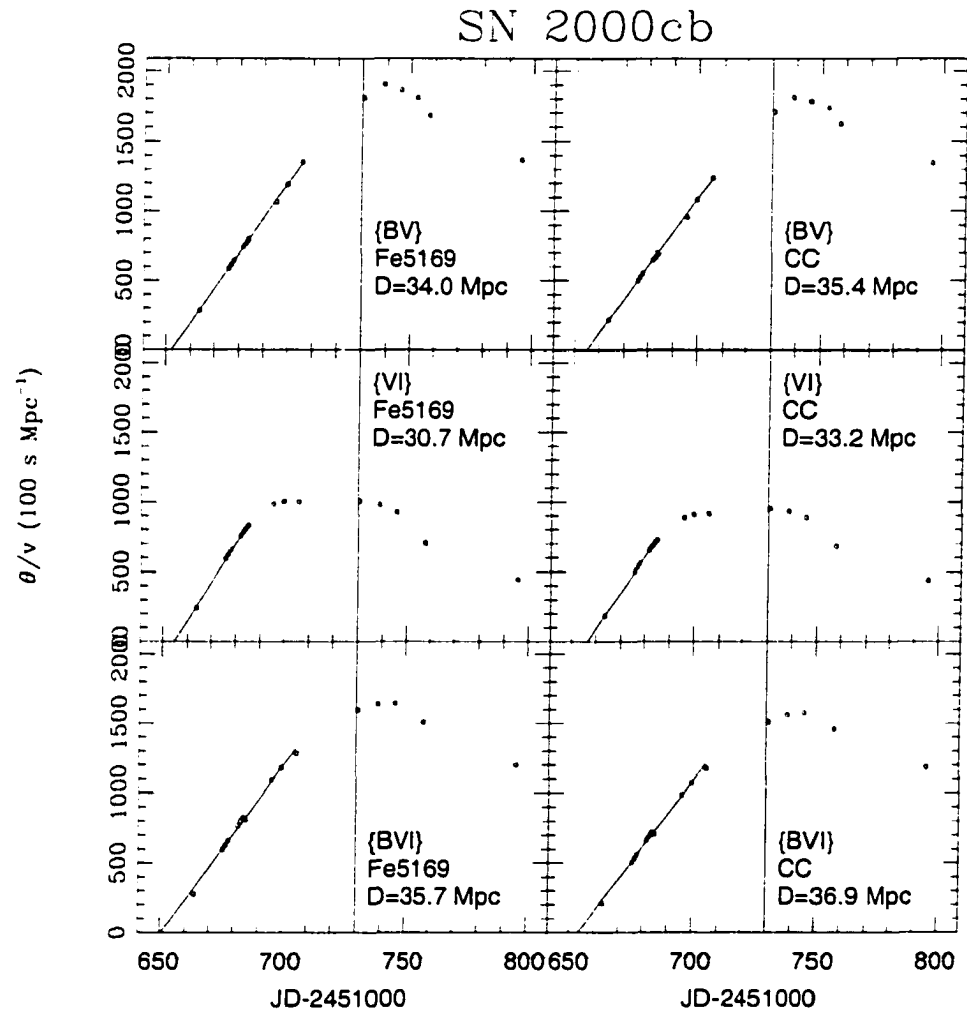


Figure 3.44: θ/v as a function of time for SN 2000cb, obtained from filter subsets $\{BV, VI, BVI\}$. The ridge lines correspond to unweighted least-squares fits to the points between JD 2451663.8-2451705.7 ($\{BV, BVI\}$) and JD 2451663.8-2451684.8 ($\{VI\}$). The vertical line shows the end of the optically thick phase where EPM is valid.

2451656. Below I adopt $t_0=2451653.8$, the average of the six EPM solutions.

The observations began so early after explosion that the EPM analysis gives very consistent solutions. From the CC curve I obtain a distance of 33.2-36.9 Mpc (or only 5% about the average). The distances from the Fe curve are somewhat shorter with $D(Fe)=31\text{-}36$ Mpc. I can compare the power-law distances to those derived from interpolating magnitudes to the epoch of the spectroscopy. The solutions from the data obtained between JD 2451663-2451696 are given in Table 3.49; the distances prove 10% higher than those yielded by the power-law fits.

3.9 Summary

In this chapter I summarized our current understanding about the physics of the light curves of Type II SNe. In this frame it is thought that progenitors with large H-rich envelopes undergo a long (~ 100 days) phase of expansion, cooling, and recombination, during which the SN has a well-defined photosphere near the recombination front. To zero order the radiative outcome of the recombination phase is a plateau of nearly constant luminosity. Then I gave the essential ideas of the expanding photosphere method which offers the potential to produce distances from the optically thick plateau phase of SNe II-P. Next I described all the details regarding the implementation of the method, namely, the determination of angular radii, reddening due to dust in the host galaxy, and photospheric velocities. Finally, I applied EPM to the 17 SNe and reported all the results on a SN-to-SN basis. I showed that 12 of these objects have sufficient data to produce reliable distances, which I proceed to discuss below.

Table 3.1: Fits to $b_{\bar{\lambda}}(T, z = 0)^a$

i	$c_i(B)$	$c_i(V)$	$c_i(R)$	$c_i(I)$	$c_i(Z)$	$c_i(J_S)$	$c_i(H)$	$c_i(K_S)$
0	-45.144	-44.766	-44.597	-44.345	-44.232	-43.913	-43.767	-43.638
1	7.159	6.793	6.628	6.347	6.262	6.022	5.878	5.737
2	-4.301	-4.523	-4.693	-4.732	-4.810	-4.859	-4.914	-4.881
3	2.639	2.695	2.770	2.739	2.778	2.772	2.797	2.757
4	-0.811	-0.809	-0.831	-0.811	-0.825	-0.819	-0.829	-0.813
5	0.098	0.096	0.099	0.096	0.098	0.097	0.098	0.096

^a $b_{\bar{\lambda}}(T, z = 0) = \sum_i c_i(\lambda) T_4^{-i}$, $T_4 = T/10^4 K$.

Table 3.2: Fits to $\zeta(T_S)$ ^a

<i>S</i>	<i>a</i> ₀	<i>a</i> ₁	<i>a</i> ₂	<i>σ</i> ^b
{BV}	0.7557	-0.8997	0.5199	0.048
{BVI}	0.7336	-0.6942	0.3740	0.027
{VI}	0.7013	-0.5304	0.2646	0.029
{VZ}	0.8185	-0.7137	0.3510	0.031
{VJ}	0.6104	-0.0323	0.0000	0.025
{VH}	0.6548	-0.0737	0.0000	0.031
{VK}	1.2865	-0.8571	0.2700	0.051
{JHK}	1.4787	-0.4799	0.0000	0.046

^a $\zeta(T_S) = \sum_i a_{S,i} (\frac{10^4 K}{T_S})^i, (z=0).$

^b $σ$ is the rms of the fit.

Table 3.3: Adopted Host Galaxy Reddenings

SN	$A_{host}(V)$	$A(V)$
	± 0.3	Na ID
1986L	0.000	0.00
1987A	0.216	0.62
1988A	0.000	0.00
1990E	1.000	1.45
1990K	0.500	0.78
1991al	0.150	0.47
1992af	0.000	0.00
1992am	0.300	...
1992ba	0.000	0.00
1993A	0.000	...
1993S	0.300	0.62
1999br	0.000	0.00
1999ca	0.300	0.78
1999cr	0.000	0.78
1999eg	0.000	...
1999em	0.180	1.55
2000cb	0.000	0.00

Table 3.4: Expansion Velocities of SN 1986L

JD- 2440000	Date(UT)	$v(CC)$ (km s $^{-1}$)	$v(Fe5169)$ (km s $^{-1}$)
6716.86	1986 Oct 13	12257(346)
6717.83	1986 Oct 14	10657(793)
6718.80	1986 Oct 15	10783(626)
6723.72	1986 Oct 20	9344(471)
6729.73	1986 Oct 26	7645(605)
6731.65	1986 Oct 28	6971(634)
6731.65	1986 Oct 28	6714(757)
6732.83	1986 Oct 29	6621(756)	6094
6735.83	1986 Nov 01	6064(546)	6152
6736.83	1986 Nov 02	5698(577)	5746
6737.70	1986 Nov 03	6098(500)	6442
6737.70	1986 Nov 03	5602(573)	6036
6738.81	1986 Nov 04	5869(414)	5978
6738.81	1986 Nov 04	5441(564)	5746
6739.81	1986 Nov 05	5462(568)	6094
6740.81	1986 Nov 06	5377(527)	5688
6741.81	1986 Nov 07	5377(547)	5514
6744.78	1986 Nov 10	5322(491)	5746
6745.71	1986 Nov 11	5080(529)	5281
6748.77	1986 Nov 14	5632(285)	4933
6750.71	1986 Nov 16	5090(683)	4759
6759.73	1986 Nov 25	3911(532)
6773.73	1986 Dec 09	4018(500)	3308
6774.70	1986 Dec 10	4084(576)	3714
6787.72	1986 Dec 23	3650(586)	2728
6796.62	1987 Jan 01	3566(583)	3134
6818.62	1987 Jan 23	2423(491)	1451
6825.58	1987 Jan 30	3543(792)

Table 3.5: EPM Quantities Derived for SN 1986L

JD- 2440000	T_{BV} K	$\theta\zeta_{BV}$ $10^{11} \text{ cm Mpc}^{-1}$	ζ_{BV}	$v(Fe)$ km s^{-1}	$\theta/v(Fe)$ 100 s Mpc^{-1}	$v(CC)$ km s^{-1}	$\theta/v(CC)$ 100 s Mpc^{-1}
6712.40	26333(3059)	145(14)	0.426	28416	120(13)	17611	193(21)
6712.40	20913(1829)	182(15)	0.410	28416	156(15)	17611	252(25)
6714.30	13848(722)	299(19)	0.385	20052	387(32)	14419	538(44)
6715.30	14311(777)	294(19)	0.387	17611	432(36)	13277	573(47)
6716.20	12049(529)	364(22)	0.384	15955	594(47)	12439	762(60)
6717.30	12191(543)	360(22)	0.384	14383	651(51)	11591	808(64)
6729.30	8673(258)	521(28)	0.427	7643	1596(117)	7264	1679(123)
6730.40	7818(207)	612(32)	0.467	7369	1780(129)	7061	1857(135)
6732.40	6876(158)	737(38)	0.547	6927	1943(139)	6727	2001(143)
6735.20	7138(171)	660(34)	0.520	6407	1981(142)	6326	2007(144)
6736.20	5923(117)	970(49)	0.708	6244	2195(156)	6198	2211(157)
6737.40	6686(150)	780(40)	0.571	6062	2254(161)	6054	2257(161)
6738.40	6181(127)	864(44)	0.653	5919	2236(159)	5940	2228(159)
6740.30	6017(121)	878(45)	0.686	5670	2257(161)	5740	2229(159)
6742.30	5737(110)	927(47)	0.754	5434	2261(161)	5548	2215(157)
6744.30	5103(87)	1286(65)	0.980	5221	2514(179)	5373	2443(174)
6748.20	5111(87)	1208(61)	0.977	4860	2545(181)	5071	2440(173)
6750.30	4669(73)	1512(76)	1.223	4690	2637(187)	4927	2510(178)
6754.20	4530(69)	1641(83)	1.323	4410	2813(200)	4687	2647(188)
6756.20	4452(73)	1672(91)	1.385	4281	2820(208)	4575	2639(195)
6770.30	4242(69)	1831(103)	1.578	3584	3238(244)	3956	2933(221)
6781.30	3852(57)	2295(130)	2.067	3204	3466(262)	3608	3078(233)
6784.20	3584(50)	2979(170)	2.546	3119	3750(285)	3529	3315(252)
6788.20	3636(52)	2756(157)	2.442	3012	3748(285)	3428	3292(250)
6796.30	3443(47)	3156(181)	2.865	2819	3908(298)	3246	3394(259)

Table 3.5: EPM Quantities for SN 1986L – continued

JD- 2440000	T_{BV} K	$\theta\zeta_{BV}$ $10^{11} \text{cm Mpc}^{-1}$	ζ_{BV}	$v(Fe)$ km s^{-1}	$\theta/v(Fe)$ 100s Mpc^{-1}	$v(CC)$ km s^{-1}	$\theta/v(CC)$ 100s Mpc^{-1}
6807.20	3264(42)	3301(191)	3.354	2603	3781(289)	3039	3239(248)
6811.10	2556(27)	9384(564)	7.024	2535	5270(412)	2973	4494(351)
6814.10	2284(22)	14477(887)	9.903	2486	5880(465)	2925	4998(395)
6821.20	2643(29)	5059(302)	6.338	2379	3356(261)	2819	2831(221)
6855.00	2425(51)	4433(539)	8.242	1991	2702(355)	2431	2213(291)
6864.10	3057(77)	1217(143)	4.082	1911	1560(199)	2349	1269(162)

Table 3.6: EPM Solutions for SN 1986L

Filter Subset	$t_0(Fe)$ JD	$D(Fe)$ (Mpc)	$t_0(CC)$ JD	$D(CC)$ (Mpc)	interpolation
{BV'}	2446707.9(2.4)	11.2(0.2)	velocity
{BV'}	2446706.5(0.7)	11.5(0.5)	photometry

Table 3.7: Expansion Velocities of SN 1987A

JD- 2446000	Date(UT)	$v(CC)$ (km s $^{-1}$)	$v(Fe5169)$ (km s $^{-1}$)
851.67	1987 Feb 25	15423(1116)	...
853.53	1987 Feb 27	13572(851)	11085.3
854.52	1987 Feb 28	12124(1137)	9112.01
855.57	1987 Mar 01	10709(337)	8009.29
856.56	1987 Mar 02	9935(154)	7835.17
857.54	1987 Mar 03	8788(769)	7312.83
858.52	1987 Mar 04	7915(589)	6674.41
860.58	1987 Mar 06	6863(573)	5861.87
861.52	1987 Mar 07	6401(573)	5513.64
862.50	1987 Mar 08	5975(550)	5223.45
863.50	1987 Mar 09	5656(520)	5107.37
864.51	1987 Mar 10	5251(530)	4701.1
865.50	1987 Mar 11	4966(546)	4759.14
866.51	1987 Mar 12	4644(554)	4352.87
867.50	1987 Mar 13	4234(616)	4352.87
868.52	1987 Mar 14	4215(494)	4178.76
869.53	1987 Mar 15	4003(503)	4004.64
870.55	1987 Mar 16	3614(939)	4062.68
871.51	1987 Mar 17	3670(525)	3598.37
872.53	1987 Mar 18	3562(538)	3714.45
873.51	1987 Mar 19	3622(581)	3482.3
874.51	1987 Mar 20	3679(599)	3192.11
875.51	1987 Mar 21	3434(626)	3076.03
876.50	1987 Mar 22	3665(644)	3134.07
877.58	1987 Mar 23	3452(691)	2785.84
880.52	1987 Mar 26	3281(658)	2669.76
881.49	1987 Mar 27	3239(621)	2959.95
882.50	1987 Mar 28	3311(619)	2901.92
883.51	1987 Mar 29	3259(606)	2785.84
884.51	1987 Mar 30	3173(584)	2727.8
885.50	1987 Mar 31	3232(601)	2785.84
886.50	1987 Apr 01	3120(572)	2669.76
887.50	1987 Apr 02	3133(564)	2553.69
888.48	1987 Apr 03	3136(555)	2669.76
889.49	1987 Apr 04	3081(539)	2611.72
890.50	1987 Apr 05	3063(529)	...
891.49	1987 Apr 06	3060(520)	2495.65

Table 3.7: Expansion Velocities of SN 1987A – continued

JD- 2446000	Date(UT)	$v(CC)$ (km s $^{-1}$)	$v(Fe5169)$ (km s $^{-1}$)
892.50	1987 Apr 07	2996(507)	2611.72
893.49	1987 Apr 08	2975(505)	2611.72
894.52	1987 Apr 09	2967(496)	2437.61
895.51	1987 Apr 10	3011(503)	2495.65
896.54	1987 Apr 11	2961(482)	2495.65
897.51	1987 Apr 12	2863(467)	2437.61
898.53	1987 Apr 13	2893(470)	2321.53
899.50	1987 Apr 14	2768(454)	2321.53
900.54	1987 Apr 15	2829(468)	2495.65
901.49	1987 Apr 16	2800(453)	2611.72
902.53	1987 Apr 17	2806(455)	2205.46
903.46	1987 Apr 18	2768(444)	2437.61
905.47	1987 Apr 20	2724(436)	2263.49
907.51	1987 Apr 22	2535(438)	2089.38
909.47	1987 Apr 24	2715(434)	2321.53
911.47	1987 Apr 26	2626(427)	2321.53
915.54	1987 Apr 30	2506(400)	2437.61
917.50	1987 May 02	2676(423)	2205.46
918.47	1987 May 03	2623(420)	2263.49
920.48	1987 May 05	2542(410)	2205.46
923.48	1987 May 08	2490(406)	2205.46
925.48	1987 May 10	2486(405)	2089.38
927.47	1987 May 12	2518(407)	2263.49
929.47	1987 May 14	2514(401)	2321.53
931.49	1987 May 16	2488(400)	2263.49
935.47	1987 May 20	2393(400)	2321.53
935.47	1987 May 21	2504(411)	...
937.45	1987 May 23	2496(411)	...
942.48	1987 May 27	2506(402)	2495.65
943.47	1987 May 28	2494(411)	2263.49
945.47	1987 May 30	2502(413)	2205.46
947.48	1987 Jun 01	2333(416)	1973.3
951.45	1987 Jun 05	2434(415)	2263.49
952.52	1987 Jun 06	2458(412)	2031.34
954.45	1987 Jun 08	2416(409)	2263.49
957.45	1987 Jun 11	2472(412)	1741.15
959.46	1987 Jun 13	2444(412)	1741.15
961.44	1987 Jun 15	2455(414)	1625.07

Table 3.7: Expansion Velocities of SN 1987A – continued

JD- 2446000	Date(UT)	$v(CC)$ (km s $^{-1}$)	$v(Fe\bar{5}169)$ (km s $^{-1}$)
963.49	1987 Jun 17	2489(416)	1683.11
965.45	1987 Jun 19	2571(419)	1683.11
967.45	1987 Jun 21	2529(421)	1567.03
971.48	1987 Jun 25	2643(437)	1450.96
973.48	1987 Jun 27	2631(428)	1392.92
975.47	1987 Jun 29	2648(440)	1334.88
978.45	1987 Jul 02	2642(430)	1567.03
979.88	1987 Jul 03	2637(431)	1334.88
980.89	1987 Jul 04	2663(429)	1392.92

Table 3.8: EPM Quantities Derived for SN 1987A

JD- 2446000	T_{BIV} K	$\theta\zeta_{BIV}$ $10^{14} \text{cm Mpc}^{-1}$	ζ_{BIV}	$n(Fr)$ km s^{-1}	$\theta/v(Fr)$ 10^5s Mpc^{-1}	$n(CC)$ km s^{-1}	$\theta/v(CC)$ 10^5s Mpc^{-1}
853.58	9043(357)	45(3)	0.397	10685	106(8)	11312	100(8)
854.64	7537(242)	61(3)	0.477	9150	140(11)	9812	130(10)
855.62	6445(175)	81(5)	0.612	8173	162(13)	8846	150(12)
856.64	5719(138)	107(6)	0.772	7428	187(15)	8104	171(13)
857.62	5298(119)	127(8)	0.910	6868	204(16)	7542	186(14)
858.61	4926(103)	156(9)	1.072	6413	227(18)	7083	206(16)
859.61	4592(90)	192(12)	1.262	6032	253(20)	6695	228(18)
860.61	4333(81)	232(14)	1.449	5710	280(22)	6357	251(20)
861.62	4150(74)	268(16)	1.607	5431	307(24)	6081	274(22)
862.59	3997(69)	305(19)	1.759	5196	334(26)	5839	297(24)
863.61	3864(65)	347(22)	1.910	4978	365(29)	5615	323(26)
864.64	3778(62)	378(24)	2.017	4784	392(31)	5414	346(28)
865.62	3696(60)	411(26)	2.128	4617	418(33)	5240	369(29)
866.65	3621(58)	447(28)	2.236	4461	448(36)	5077	394(32)
868.53	3579(57)	476(30)	2.301	4209	492(40)	4813	430(34)
869.55	3522(55)	503(32)	2.393	4089	514(41)	4688	448(36)
870.59	3479(54)	528(34)	2.465	3976	539(43)	4568	469(38)
873.59	3436(52)	570(36)	2.541	3695	607(49)	4271	525(42)
874.56	3409(52)	592(38)	2.591	3615	632(51)	4187	546(44)
875.57	3387(51)	613(39)	2.632	3538	658(53)	4105	567(46)
876.58	3380(51)	622(40)	2.646	3465	678(55)	4027	583(47)
880.59	3342(50)	675(43)	2.719	3214	773(63)	3758	661(54)
881.58	3349(50)	678(43)	2.705	3159	793(64)	3700	677(55)
882.57	3344(50)	687(44)	2.715	3107	814(66)	3644	694(56)
883.59	3335(50)	708(45)	2.733	3057	848(69)	3590	722(59)

Table 3.8: EPM Quantities for SN 1987A – continued

JD- 2446000	T_{BIV} K	$\theta\zeta_{BIV}$ $10^{14} \text{ cm Mpc}^{-1}$	ζ_{BIV}	$v(Fe)$ km s^{-1}	$\theta/v(Fe)$ 10^5 s Mpc^{-1}	$v(CC)$ km s^{-1}	$\theta/v(CC)$ 10^5 s Mpc^{-1}
884.58	3328(50)	721(46)	2.747	3009	872(71)	3539	742(60)
885.60	3299(49)	755(48)	2.807	2963	908(74)	3488	771(63)
886.60	3307(49)	759(49)	2.789	2919	933(76)	3441	791(64)
887.58	3299(49)	779(50)	2.807	2878	964(78)	3397	817(66)
889.55	3300(49)	800(51)	2.803	2801	1019(83)	3314	861(70)
891.53	3273(48)	853(55)	2.861	2729	1093(89)	3235	922(75)
892.53	3275(48)	863(55)	2.857	2695	1121(91)	3198	945(77)
893.51	3259(48)	893(57)	2.890	2662	1162(95)	3162	978(80)
894.53	3256(48)	910(59)	2.897	2629	1195(97)	3127	1005(82)
895.52	3251(47)	925(60)	2.908	2599	1225(100)	3093	1029(84)
896.55	3270(48)	913(59)	2.868	2568	1239(101)	3060	1040(85)
897.51	3271(48)	928(60)	2.864	2540	1275(104)	3029	1069(87)
901.52	3280(48)	963(62)	2.846	2433	1391(113)	2912	1163(95)
902.50	3266(48)	995(64)	2.875	2409	1437(117)	2885	1200(98)
903.55	3283(48)	984(63)	2.839	2383	1454(119)	2857	1213(99)
904.52	3282(48)	998(64)	2.843	2361	1487(121)	2833	1240(101)
905.55	3263(48)	1033(67)	2.882	2337	1534(125)	2807	1277(104)
908.49	3309(49)	1006(65)	2.785	2274	1588(129)	2737	1319(107)
909.54	3292(49)	1035(67)	2.821	2253	1629(133)	2714	1352(110)
912.50	3321(49)	1027(66)	2.761	2196	1695(138)	2650	1404(114)
913.49	3332(50)	1026(66)	2.740	2177	1720(140)	2630	1424(116)
914.48	3360(50)	991(64)	2.684	2159	1710(139)	2610	1414(115)
918.51	3342(50)	1046(67)	2.719	2091	1840(150)	2534	1518(124)
919.48	3348(50)	1044(67)	2.708	2076	1857(151)	2517	1531(125)
920.49	3351(50)	1041(67)	2.701	2060	1871(152)	2499	1542(126)

Table 3.8: EPM Quantities for SN 1987A – continued

JD- 2446000	T_{BV} K	$\theta\zeta_{BV}$ $10^{14} \text{ cm Mpc}^{-1}$	ζ_{BV}	$v(Fe)$ km s^{-1}	$\theta/v(Fe)$ 10^5 s Mpc^{-1}	$v(CC)$ km s^{-1}	$\theta/v(CC)$ 10^5 s Mpc^{-1}
923.50	3365(51)	1036(66)	2.673	2015	1924(157)	2449	1582(129)
924.48	3353(50)	1057(68)	2.698	2000	1959(160)	2433	1611(131)
925.49	3376(51)	1027(66)	2.653	1986	1949(159)	2417	1601(130)
926.50	3358(50)	1053(68)	2.687	1972	1987(162)	2402	1632(133)
929.49	3367(51)	1046(67)	2.670	1933	2028(165)	2358	1662(135)
930.48	3389(51)	1020(65)	2.629	1920	2021(165)	2343	1656(135)
931.53	3362(50)	1056(68)	2.680	1907	2066(168)	2329	1691(138)
935.53	3348(50)	1077(69)	2.708	1859	2140(174)	2275	1748(142)
936.47	3385(51)	1025(66)	2.636	1848	2105(171)	2263	1719(140)
937.49	3365(51)	1048(67)	2.673	1837	2135(174)	2250	1743(142)
939.49	3365(51)	1042(67)	2.673	1815	2147(175)	2226	1751(143)
943.47	3311(49)	1095(70)	2.782	1774	2219(181)	2179	1806(147)
945.47	3311(49)	1077(69)	2.782	1754	2208(180)	2157	1795(146)
948.48	3318(49)	1025(66)	2.768	1725	2148(175)	2124	1744(142)
951.46	3263(48)	1048(67)	2.882	1698	2141(175)	2094	1737(142)
952.45	3228(47)	1073(69)	2.959	1690	2146(175)	2084	1740(142)
953.51	3231(47)	1053(68)	2.952	1680	2124(174)	2074	1721(141)
954.49	3163(45)	1112(72)	3.109	1672	2140(175)	2064	1733(142)
956.47	3213(46)	1001(65)	2.993	1655	2021(165)	2046	1636(134)
957.47	3179(46)	1022(66)	3.071	1647	2020(165)	2036	1634(134)
958.46	3176(45)	1000(65)	3.079	1639	1981(162)	2027	1602(131)
959.47	3197(46)	942(61)	3.030	1631	1906(156)	2018	1541(126)
960.49	3159(45)	965(62)	3.117	1623	1908(156)	2009	1542(126)
961.47	3169(45)	923(60)	3.094	1616	1847(151)	2000	1492(122)
963.48	3161(45)	876(57)	3.113	1601	1758(144)	1983	1419(116)

Table 3.8: EPM Quantities for SN 1987A – continued

JD- 2446000	T_{BV} K	$\theta\zeta_{BV}$ $10^{14} \text{ cm Mpc}^{-1}$	ζ_{BV}	$v(Fe)$ km s^{-1}	$\theta/v(Fe)$ 10^5 s Mpc^{-1}	$v(CC)$ km s^{-1}	$\theta/v(CC)$ 10^5 s Mpc^{-1}
964.46	3169(45)	844(55)	3.094	1593	1714(140)	1975	1382(113)
965.46	3172(45)	818(53)	3.086	1586	1671(137)	1967	1347(110)
966.48	3158(45)	813(52)	3.121	1579	1651(135)	1958	1330(109)
967.47	3153(45)	804(52)	3.132	1572	1633(134)	1950	1316(108)
968.47	3148(45)	789(51)	3.144	1565	1604(131)	1942	1292(106)
969.47	3153(45)	768(50)	3.132	1558	1575(129)	1934	1268(104)
971.48	3144(45)	759(49)	3.155	1544	1560(128)	1919	1255(103)
972.47	3152(45)	743(48)	3.136	1537	1542(126)	1911	1240(101)
973.47	3166(45)	723(47)	3.102	1531	1524(125)	1904	1225(100)
975.48	3134(44)	741(48)	3.178	1518	1538(126)	1889	1235(101)
978.48	3179(46)	684(44)	3.071	1499	1488(122)	1867	1194(980)
979.46	3190(46)	670(43)	3.045	1493	1474(120)	1860	1183(970)
980.47	3198(46)	655(42)	3.026	1487	1457(119)	1853	1169(958)

Table 3.9: EPM Solutions for SN 1987A

Filter Subset	$t_0(Fe)$ JD	$D(Fe)$ (kpc)	$t_0(CC)$ JD	$D(CC)$ (kpc)	interpolation
{BV}	2446850.5(0.2)	32.0(0.4)	2446850.5(0.3)	37.0(0.6)	velocity
{VI}	2446850.6(0.4)	36.4(0.5)	2446850.3(0.5)	42.7(0.5)	velocity
{BVI}	2446849.6(0.6)	39.4(0.6)	2446849.4(0.3)	45.8(0.8)	velocity
{JHK}	2446850.7(0.5)	28.4(0.6)	2446850.3(0.7)	33.7(0.9)	velocity
{BV}	2446850.4(0.4)	30.5(0.7)	2446848.8(0.4)	37.1(0.8)	photometry
{VI}	2446850.9(0.6)	33.9(0.5)	2446849.3(0.5)	41.2(0.6)	photometry
{BVI}	2446849.0(0.2)	38.3(0.8)	2446847.2(0.6)	46.5(0.9)	photometry
{JHK}	2446850.8(1.2)	27.2(1.3)	2446848.7(1.4)	33.4(1.7)	photometry

Table 3.10: Expansion Velocities of SN 1988A

JD- 2440000	Date(UT)	$v(CC)$ (km s $^{-1}$)	$v(Fe5169)$ (km s $^{-1}$)	Source
7188.86	1988 Jan 28	7851(682)	...	here
7189.86	1988 Jan 29	8160(683)	7081	here
7193.86	1988 Feb 02	6489(388)	...	here
7194.86	1988 Feb 03	6292(396)	6674	here
7226.84	1988 Mar 06	3134(601)	...	here
7228.5	1988 Mar 08	...	3370	Turatto et al. (1993)
7247.0	1988 Mar 25-28	...	3080	Turatto et al. (1993)
7272.0	1988 Apr 20-21	...	2840	Turatto et al. (1993)

Table 3.11: EPM Quantities Derived for SN 1988A

JD- 2440000	T_{BV} K	$\theta\zeta_{BV}$ $10^{11}\text{cm Mpc}^{-1}$	ζ_{BV}	$v(Fe)$ km s^{-1}	$\theta/v(Fe)$ 100 s Mpc^{-1}	$v(CC)$ km s^{-1}	$\theta/v(CC)$ 100 s Mpc^{-1}
7208.53	5987(561)	679(157)	0.693	4960	1976(468)	4341	2258(535)
7210.53	6263(614)	588(137)	0.637	4805	1919(456)	4154	2220(528)
7212.47	5987(561)	619(143)	0.693	4664	1917(454)	3988	2241(531)
7214.57	5987(561)	664(154)	0.693	4521	2119(502)	3824	2505(593)
7217.52	5013(395)	971(224)	1.023	4335	2189(516)	3616	2625(619)
7230.43	4019(260)	1955(456)	1.833	3685	2894(690)	2934	3635(867)
7237.50	3580(210)	2848(672)	2.555	3411	3268(788)	2665	4183(1009)
7243.57	4145(275)	1578(367)	1.682	3208	2925(696)	2473	3794(903)
7266.42	3681(221)	2517(592)	2.356	2631	4061(977)	1955	5465(1314)
7267.37	3832(238)	2139(501)	2.099	2612	3902(935)	1939	5258(1260)
7270.41	3854(240)	2117(496)	2.064	2553	4017(962)	1888	5433(1301)

Table 3.12: EPM Solutions for SN 1988A

Filter Subset	$t_0(Fe)$ JD	$D(Fe)$ (Mpc)	$t_0(CC)$ JD	$D(CC)$ (Mpc)	interpolation
{BVI}	2447155.7(5.5)	23.8(2.1)	2447170.3(5.7)	15.3(2.5)	velocity

Table 3.13: Expansion Velocities of SN 1990E

JD- 2440000	Date(UT)	$v(CC)$ (km s $^{-1}$)	$v(Fe5169)$ (km s $^{-1}$)	Source
7944.51	1990 Feb 23	9341(597)	10737	here
7945.6	1990 Feb 23	...	10469	Schmidt et al. (1993)
7953.6	1990 Mar 03	...	8322	Schmidt et al. (1993)
7954.53	1990 Mar 04	7258(392)	8125	here
7954.5	1990 Mar 04	...	8322	Schmidt et al. (1993)
7969.6	1990 Mar 19	...	6232	Schmidt et al. (1993)

Table 3.14: EPM Quantities Derived for SN 1990E

JD- 2440000	T_{VI} K	$\theta\zeta_{VI}$ $10^{11}\text{cm Mpc}^{-1}$	ζ_{VI}	$v(Fe)$ km s^{-1}	$\theta/v(Fe)$ 100 s Mpc^{-1}	$v(CC)$ km s^{-1}	$\theta/v(CC)$ 100 s Mpc^{-1}
7939.60	7788(384)	434(34)	0.438	12887	768(72)	10968	902(84)
7940.60	7712(481)	447(45)	0.440	12395	819(91)	10586	959(107)
7947.30	6797(241)	585(36)	0.513	9946	1146(91)	8635	1320(104)
7948.30	7158(319)	539(41)	0.472	9671	1181(108)	8410	1358(124)
7950.30	6685(198)	602(33)	0.531	9168	1237(92)	7997	1418(105)
7951.30	7033(357)	550(50)	0.484	8939	1271(132)	7807	1455(151)
7952.30	6797(205)	590(33)	0.513	8722	1319(98)	7627	1509(112)
7953.30	6855(209)	583(32)	0.505	8517	1356(101)	7457	1549(115)
7954.30	6797(205)	599(33)	0.513	8322	1402(104)	7294	1599(119)
7958.30	6474(184)	673(37)	0.572	7636	1541(114)	6717	1752(129)
7959.30	6474(184)	670(36)	0.572	7484	1566(116)	6588	1778(131)
7973.30	5600(212)	815(63)	0.924	5900	1495(138)	5230	1687(155)
8063.90	4074(165)	905(87)	3.888	2721	855(92)	2422	961(104)
8067.90	3980(164)	838(87)	4.332	2663	727(84)	2370	816(94)
8071.90	3482(259)	1078(222)	7.931	2608	521(111)	2321	585(124)
8076.90	3598(150)	762(94)	6.852	2543	437(58)	2263	492(65)
8084.90	3440(179)	843(131)	8.366	2447	412(67)	2176	463(76)
8115.90	3333(237)	791(170)	9.604	2140	385(85)	1900	434(96)

Table 3.15: EPM Solutions for SN 1990E

Filter Subset	$t_0(Fe)$ JD	$D(Fe)$ (kpc)	$t_0(CC)$ JD	$D(CC)$ (kpc)	interpolation
{BV}	2447930.4(1.5)	17.8(1.4)	2447928.7(4.2)	16.9(2.6)	velocity
{VI}	2447920.1(3.9)	21.3(2.9)	2447917.6(6.8)	20.3(4.4)	velocity
{BVI}	2447926.9(3.9)	17.8(1.6)	2447926.1(3.6)	16.0(3.0)	velocity
{BV}	2447927.9(4.6)	19.4(3.1)	2447925.6(7.7)	18.3(4.6)	photometry
{VI}	2447918.0(7.3)	22.3(4.3)	2447915.9(9.8)	20.6(6.1)	photometry
{BVI}	2447924.3(4.1)	19.6(2.8)	2447923.4(6.9)	17.6(3.8)	photometry

Table 3.16: Expansion Velocities of SN 1990K

JD- 2440000	Date(UT)	$v(CC)$ (km s $^{-1}$)	$v(Fe\delta 169)$ (km s $^{-1}$)
8042.90	1990 May 31	5493(392)	5107
8049.88	1990 Jun 07	4943(534)	4121
8050.89	1990 Jun 08	4804(601)	...
8054.90	1990 Jun 12	4701(614)	4063
8060.85	1990 Jun 18	4543(755)	...
8075.83	1990 Jul 03	3787(715)	3134

Table 3.17: EPM Quantities Derived for SN 1990K

JD- 2440000	T_{BV} K	$\theta\zeta_{BV}$ $10^{11}\text{cm Mpc}^{-1}$	ζ_{BV}	$v(Fe)$ km s^{-1}	$\theta/v(Fe)$ 100 s Mpc^{-1}	$v(CC)$ km s^{-1}	$\theta/v(CC)$ 100 s Mpc^{-1}
8041.91	5396(253)	1007(124)	0.861	4739	2465(327)	5459	2140(284)
8042.89	5069(109)	1147(72)	0.996	4693	2454(197)	5393	2135(171)
8042.90	4884(193)	1320(146)	1.091	4692	2577(312)	5392	2243(272)
8043.89	4993(158)	1150(108)	1.033	4646	2396(255)	5327	2090(223)
8044.90	4848(100)	1310(82)	1.111	4600	2561(206)	5262	2239(180)
8044.92	4711(214)	1347(187)	1.195	4599	2451(362)	5261	2143(317)
8050.90	4487(86)	1520(96)	1.357	4348	2577(207)	4909	2283(184)
8054.90	4398(83)	1541(97)	1.432	4197	2564(206)	4699	2290(184)
8060.90	4148(74)	1643(104)	1.679	3992	2451(198)	4419	2215(179)
8063.80	3831(64)	2202(140)	2.100	3901	2687(218)	4295	2441(198)
8063.92	3996(69)	1853(118)	1.864	3898	2550(206)	4290	2317(187)
8066.92	4071(127)	1666(181)	1.769	3809	2472(296)	4170	2258(271)
8067.80	3765(62)	2234(143)	2.209	3784	2673(217)	4136	2445(198)
8067.92	4201(97)	1440(121)	1.621	3780	2349(229)	4132	2150(210)
8071.90	3854(65)	1950(124)	2.065	3672	2572(208)	3986	2369(192)
8076.80	3765(79)	1858(145)	2.209	3548	2371(220)	3820	2202(204)
8084.80	3679(76)	1387(109)	2.361	3365	1746(162)	3579	1642(153)
8096.71	3721(77)	856(67)	2.284	3130	1198(111)	3274	1145(106)
8098.82	3996(132)	670(75)	1.864	3093	1162(142)	3226	1114(136)
8104.80	3765(98)	811(77)	2.209	2992	1227(131)	3096	1186(127)
8115.80	4021(144)	593(74)	1.832	2825	1146(154)	2885	1122(151)
8115.86	3831(113)	662(72)	2.100	2824	1116(134)	2883	1093(132)

Table 3.18: Expansion Velocities of SN 1991al

JD- 2448000	Date(UT)	$v(CC)$ (km s $^{-1}$)	$v(Fe5169)$ (km s $^{-1}$)
473.50	1991 Aug 05	6307(465)	5803
474.50	1991 Aug 06	6737(459)	6965
478.50	1991 Aug 10	6540(486)	6442
481.50	1991 Aug 13	6596(425)	5281
501.67	1991 Sep 02	4531(706)	4411
513.69	1991 Sep 14	4134(700)	3831

Table 3.19: EPM Quantities Derived for SN 1991al

JD- 2448000	T_{BVI} K	$\theta\zeta_{BVI}$ $10^{11} \text{ cm Mpc}^{-1}$	ζ_{BVI}	$v(Fe)$ km s^{-1}	$\theta/v(Fe)$ 100 s Mpc^{-1}	$v(CC)$ km s^{-1}	$\theta/v(CC)$ 100 s Mpc^{-1}
455.67	11264(864)	124(15)	0.422	7918	372(48)	8298	354(46)
458.77	10318(176)	136(3)	0.422	7537	427(24)	7916	407(22)
459.60	10345(177)	134(3)	0.422	7442	428(24)	7821	407(22)
478.65	6679(66)	221(4)	0.530	5831	715(38)	6193	673(36)
478.66	6685(66)	220(4)	0.529	5831	714(38)	6192	673(36)
490.70	6774(141)	208(7)	0.521	5165	773(47)	5514	724(44)
490.72	6719(121)	211(7)	0.526	5164	775(46)	5513	726(43)
499.56	6252(138)	226(8)	0.578	4776	818(51)	5117	764(48)
508.63	5073(38)	318(6)	0.852	4443	841(45)	4774	782(42)
537.65	4366(97)	230(13)	1.235	3661	508(39)	3967	469(36)
550.54	4358(84)	213(10)	1.242	3406	504(35)	3702	464(32)
550.56	4393(84)	208(9)	1.215	3406	502(34)	3702	462(31)
551.53	4034(157)	257(25)	1.537	3388	493(53)	3684	453(49)
551.54	4130(156)	236(21)	1.438	3388	485(50)	3684	446(46)
555.52	4373(84)	206(10)	1.230	3318	506(36)	3611	465(33)
555.53	4188(76)	229(11)	1.384	3318	498(34)	3611	458(31)

Table 3.20: Expansion Velocities of SN 1992af

JD- 2448000	Date(UT)	$v(CC)$ (km s $^{-1}$)	$v(Fe\bar{5}169)$ (km s $^{-1}$)
812.88	1992 Jul 09	5970(380)	...
813.82	1992 Jul 10	5680(441)	...
832.77	1992 Jul 29	4841(529)	4353

Table 3.21: EPM Quantities Derived for SN 1992af

JD- 2448000	T_{BV} K	$\theta\zeta_{BV}$ $10^{11} \text{cm Mpc}^{-1}$	ζ_{BV}	$v(CC)$ km s^{-1}	$\theta/v(CC)$ 100s Mpc^{-1}
805.81	6348(133)	217(11)	0.632	6271	546(38)
807.62	6058(191)	237(18)	0.687	6148	561(51)
807.64	5917(569)	250(65)	0.719	6147	566(151)
809.90	5897(118)	252(13)	0.724	6001	580(41)
813.85	5470(129)	296(19)	0.846	5764	608(49)
817.67	4877(352)	399(80)	1.109	5555	647(134)
818.67	5435(246)	295(35)	0.858	5503	625(80)
831.84	4397(67)	526(27)	1.455	4908	736(53)
842.60	3950(107)	704(66)	1.967	4521	791(84)
843.65	3945(109)	698(66)	1.973	4486	789(85)
845.53	3844(112)	747(77)	2.126	4427	794(91)
846.66	3728(94)	838(77)	2.327	4392	820(86)
847.59	3874(94)	721(62)	2.080	4363	794(79)
848.63	3641(82)	889(75)	2.494	4332	823(81)
849.70	4016(110)	616(57)	1.875	4301	765(81)
849.69	3811(114)	736(78)	2.180	4301	785(92)
871.58	2748(180)	1403(441)	5.866	3753	637(203)
872.57	3755(706)	358(240)	2.277	3732	421(283)
885.69	3030(105)	765(117)	4.342	3477	507(81)
891.57	3045(108)	738(115)	4.279	3375	511(84)
905.60	2940(448)	809(554)	4.763	3157	538(369)
908.59	3051(246)	685(239)	4.254	3114	517(182)

Table 3.22: Expansion Velocities of SN 1992am

JD- 2448000	Date(UT)	$v(CC)$ (km s $^{-1}$)	$v(Fe\bar{5}169)$ (km s $^{-1}$)
832.90	1992 Jul 29	7193(457)	7603
896.79	1992 Oct 01	3888(611)	3889

Table 3.23: EPM Quantities Derived for SN 1992am

JD- 2448000	$T_{V,I}$ K	$\theta\zeta_{V,I}$ $10^{11} \text{ cm Mpc}^{-1}$	$\zeta_{V,I}$	$v(Fr)$ km s^{-1}	$\theta/v(Fe)$ 100 s Mpc^{-1}	$v(CC)$ km s^{-1}	$\theta/v(CC)$ 100 s Mpc^{-1}
847.82	8644(207)	72(3)	0.427	6112	275(17)	5912	284(17)
848.87	8244(239)	75(3)	0.434	6032	288(19)	5842	297(20)
872.79	6757(211)	96(5)	0.497	4693	413(31)	4637	418(31)
885.89	6458(276)	100(9)	0.520	4211	458(47)	4190	460(47)
905.68	5975(304)	110(11)	0.569	3665	528(57)	3677	526(57)
908.68	6041(318)	105(10)	0.561	3596	520(57)	3612	518(57)
919.68	5441(71)	125(4)	0.648	3368	572(33)	3394	568(33)
922.59	5464(81)	122(4)	0.644	3313	571(34)	3341	567(34)
979.65	4343(138)	88(7)	0.958	2540	361(34)	2592	354(33)

Table 3.24: EPM Solutions for SN 1992am

Filter Subset	$t_0(Fe)$ JD	$D(Fe)$ (Mpc)	$t_0(CC)$ JD	$D(CC)$ (Mpc)	interpolation
{BV}	2448766.9(13)	206(35)	2448754.5(14)	230(36)	velocity
{VI}	2448788.9(9)	172(25)	2448784.0(11)	180(31)	velocity
{BVI}	2448789.4(6)	168(18)	2448784.9(7)	176(19)	velocity
{BV}	2448779.9(12)	196(36)	2448774.0(14)	207(41)	photometry

Table 3.25: Expansion Velocities of SN 1992ba

JD- 2448000	Date(UT)	$v(CC)$ (km s $^{-1}$)	$v(Fe5169)$ (km s $^{-1}$)
896.86	1992 Oct 01	8253(415)	...
896.90	1992 Oct 01	8025(440)	...
900.83	1992 Oct 05	7589(349)	...
900.89	1992 Oct 05	7564(360)	6384
922.82	1992 Oct 27	3677(464)	3772
949.80	1992 Nov 23	2959(481)	2844
974.84	1992 Dec 18	2543(495)	2496
1015.69	1993 Jan 28	2477(398)	2031

Table 3.26: EPM Quantities Derived for SN 1992ba

JD- 2448000	T_{BVI} K	$\theta\zeta_{BVI}$ $10^{11}\text{cm Mpc}^{-1}$	ζ_{BVI}	$v(Fc)$ km s^{-1}	$\theta/v(Fc)$ 100 s Mpc^{-1}	$v(CC)$ km s^{-1}	$\theta/v(CC)$ 100 s Mpc^{-1}
904.76	8737(127)	293(7)	0.430	5685	1201(66)	6478	1054(58)
904.77	8676(125)	295(7)	0.431	5683	1203(66)	6477	1056(58)
905.83	8574(121)	298(7)	0.434	5548	1241(68)	6298	1093(60)
908.81	7611(94)	350(7)	0.468	5205	1437(78)	5852	1278(70)
922.80	6079(55)	497(10)	0.604	4074	2022(109)	4439	1856(100)
940.77	5283(41)	648(12)	0.759	3231	2642(141)	3441	2481(133)
941.79	5240(40)	658(13)	0.771	3195	2671(143)	3399	2511(134)
956.80	4939(35)	717(13)	0.861	2751	3031(162)	2891	2884(154)
979.67	4726(33)	744(14)	0.938	2289	3465(185)	2374	3341(179)
979.69	4748(33)	736(14)	0.930	2288	3462(185)	2373	3338(178)
997.77	4730(35)	654(13)	0.936	2030	3442(185)	2090	3344(180)
1012.69	4136(25)	667(13)	1.239	1862	2888(154)	1907	2820(151)
1016.72	4059(27)	585(12)	1.291	1822	2488(134)	1863	2432(131)
1037.69	4068(38)	425(11)	1.285	1641	2015(113)	1669	1981(112)
1078.63	4098(40)	354(9)	1.265	1383	2024(115)	1395	2007(114)
1084.55	4143(51)	338(11)	1.234	1353	2026(119)	1363	2012(119)

Table 3.27: EPM Solutions for SN 1992ba

Filter Subset	$t_0(Fe)$ JD	$D(Fe)$ (Mpc)	$t_0(CC)$ JD	$D(CC)$ (Mpc)	interpolation
$\{BVI\}$	2448868.8(3.9)	23.3(1.6)	2448873.8(1.6)	23.2(1.2)	velocity
$\{VI\}$	2448875.6(2.7)	21.0(1.2)	2448878.6(1.3)	21.5(1.0)	velocity
$\{BVI\}$	2448871.0(3.2)	23.3(1.5)	2448874.9(1.2)	23.4(1.0)	velocity

Table 3.28: Expansion Velocities of SN 1993A

JD- 2448000	Date(UT)	$v(CC)$ (km s $^{-1}$)	$v(Fe5169)$ (km s $^{-1}$)
1015.73	1993 Jan 28	6525(414)	6036
1098.60	1993 Apr 21	2781(312)	2380

Table 3.29: EPM Quantities Derived for SN 1993A

JD- 2448000	T_{VI} K	$\theta\zeta_{VI}$ $10^{11}\text{cm Mpc}^{-1}$	ζ_{VI}	$v(Fe)$ km s^{-1}	$\theta/v(Fe)$ 100 s Mpc^{-1}	$v(CC)$ km s^{-1}	$\theta/v(CC)$ 100 s Mpc^{-1}
1010.74	9600(382)	42(2)	0.422	6646	150(11)	7093	141(11)
1012.73	9005(291)	46(2)	0.418	6388	173(12)	6855	161(11)
1013.76	8336(290)	54(3)	0.418	6263	204(15)	6738	190(14)
1016.76	9933(352)	41(2)	0.426	5924	161(11)	6419	149(10)
1017.68	8495(285)	50(3)	0.417	5827	207(15)	6327	191(14)
1026.74	6862(588)	72(10)	0.504	5018	285(43)	5543	258(39)
1037.72	6873(152)	67(3)	0.502	4294	313(20)	4817	279(18)
1038.68	6714(171)	73(4)	0.527	4241	325(23)	4762	289(20)
1040.73	6845(119)	68(2)	0.506	4131	325(19)	4650	289(17)
1053.70	7527(944)	59(11)	0.441	3548	377(75)	4043	331(66)
1073.68	5965(192)	80(5)	0.740	2912	372(29)	3365	322(26)
1084.58	6432(389)	73(8)	0.585	2653	470(55)	3082	405(47)
1084.63	6502(414)	72(8)	0.569	2652	476(57)	3081	410(49)
1091.63	6053(466)	84(13)	0.704	2508	475(79)	2923	407(67)

Table 3.30: EPM Solutions for SN 1993A

Filter Subset	$t_0(Fe)$ JD	$D(Fe)$ (Mpc)	$t_0(CC)$ JD	$D(CC)$ (Mpc)	interpolation
$\{BV\}$	2448976.5(6)	161(19)	2448971.9(7)	194(24)	velocity
$\{VI\}$	2448960.5(11)	227(31)	2448952.1(14)	283(45)	velocity
$\{BVI\}$	2448970.6(5)	184(15)	2448964.9(6)	224(19)	velocity

Table 3.31: Expansion Velocities of SN 1993S

JD- 2448000	Date(UT)	$v(CC)$ (km s $^{-1}$)	$v(Fe5169)$ (km s $^{-1}$)
1164.76	1993 Jun 26	5332(479)	4701
1166.5	1993 Jun 28	5860(309)	5398
1191.93	1993 Jul 23	4858(578)	4121
1223.77	1993 Aug 24	4163(546)	4121

Table 3.32: EPM Quantities Derived for SN 1993S

JD- 2448000	T_{BVI} K	$\theta\zeta_{BVI}$ $10^{11} \text{ cm Mpc}^{-1}$	ζ_{BVI}	$v(F_C)$ km s^{-1}	$\theta/v(F_C)$ 100 s Mpc^{-1}	$v(CC)$ km s^{-1}	$\theta/v(CC')$ 100 s Mpc^{-1}
1143.85	12093(348)	52(2)	0.431	6219	195(12)	7356	165(10)
1152.86	9522(172)	69(2)	0.433	5532	287(16)	6366	249(14)
1154.83	8506(127)	79(2)	0.447	5427	327(18)	6216	286(16)
1161.84	7027(112)	101(3)	0.507	5120	389(23)	5785	344(20)
1162.82	6920(71)	99(2)	0.514	5084	379(21)	5735	336(18)
1164.90	6666(356)	108(12)	0.536	5012	404(50)	5634	359(45)
1179.90	6374(90)	99(3)	0.566	4610	378(21)	5082	343(19)
1184.75	5610(58)	121(3)	0.692	4512	387(21)	4948	352(19)
1185.83	5822(66)	110(3)	0.649	4491	377(21)	4920	344(19)
1186.79	5681(143)	112(6)	0.677	4473	369(28)	4896	337(25)
1187.89	5529(65)	124(3)	0.711	4453	391(22)	4869	357(20)
1202.81	6201(278)	89(7)	0.588	4221	358(35)	4557	332(32)

Table 3.33: Expansion Velocities of SN 1999br

JD- 2451000	Date(UT)	$v(CC)$ (km s $^{-1}$)	$v(Fe\bar{5}169)$ (km s $^{-1}$)
291.72	1999 Apr 23	4861(467)	3831
294.66	1999 Apr 26	3351(437)	3366
297.66	1999 Apr 29	2708(436)	...
301.62	1999 May 03	2376(482)	2612
309.71	1999 May 11	1955(359)	2031
317.67	1999 May 19	1436(467)	1567
319.52	1999 May 21	1319(472)	1799
380.47	1999 Jul 21	...	1218

Table 3.34: EPM Quantities Derived for SN 1999br

JD- 2451000	T_{VI} K	$\theta\zeta_{VI}$ $10^{11} \text{ cm Mpc}^{-1}$	ζ_{VI}	$v(Fe)$ km s^{-1}	$\theta/v(Fe)$ 100 s Mpc^{-1}	$v(CC)$ km s^{-1}	$\theta/v(CC)$ 100 s Mpc^{-1}
284.72	9768(269)	81(3)	0.434	6536	285(17)
285.71	9870(335)	81(4)	0.434	5862	318(21)	56833	33(2)
286.69	8879(217)	93(3)	0.439	5344	398(24)	15883	134(8)
291.80	7815(180)	118(4)	0.455	3792	684(42)	4666	556(34)
294.67	7628(165)	122(4)	0.460	3312	802(48)	3541	750(45)
294.69	7395(165)	128(4)	0.467	3309	829(50)	3536	776(47)
294.73	8013(178)	112(4)	0.451	3303	755(46)	3524	708(43)
294.74	7784(162)	117(4)	0.456	3302	780(46)	3521	731(43)
295.59	7792(396)	116(10)	0.456	3188	797(77)	3301	769(74)
296.67	6974(261)	136(8)	0.484	3056	920(72)	3063	918(72)
299.48	7165(424)	132(13)	0.476	2770	998(113)	2597	1065(120)
301.51	7197(274)	133(9)	0.475	2601	1080(89)	2351	1195(98)
301.53	6800(213)	144(9)	0.493	2599	1126(87)	2349	1246(97)
301.54	6683(131)	149(5)	0.500	2599	1148(70)	2348	1271(78)
301.61	6974(131)	138(4)	0.484	2593	1098(65)	2340	1217(72)
304.73	6624(121)	153(5)	0.503	2380	1279(77)	2055	1481(89)
305.70	6651(118)	152(5)	0.502	2322	1301(77)	1982	1524(90)
309.61	6187(108)	178(6)	0.535	2120	1572(95)	1740	1915(115)
314.57	6483(166)	165(8)	0.513	1919	1677(119)	1517	2122(151)
317.65	5753(86)	206(6)	0.579	1816	1961(115)	1408	2529(148)
318.60	5829(111)	206(8)	0.570	1787	2019(130)	1379	2617(168)
323.49	5342(195)	250(20)	0.636	1654	2373(223)	1246	3152(296)
328.49	5757(198)	213(15)	0.578	1542	2392(206)	1138	3242(279)
330.49	5263(104)	262(11)	0.649	1502	2684(179)	1100	3663(244)
335.49	5322(86)	253(9)	0.639	1412	2801(174)	1018	3885(241)

Table 3.34: EPM Quantities for SN 1999br – continued

JD- 2451000	T_{VI} K	$\theta\zeta_{VI}$ $10^{11}\text{cm Mpc}^{-1}$	ζ_{VI}	$v(Fe)$ km s^{-1}	$\theta/v(Fe)$ 100 s Mpc^{-1}	$v(CC)$ km s^{-1}	$\theta/v(CC)$ 100 s Mpc^{-1}
337.50	5403(22)	239(2)	0.626	1380	2761(139)	989	3852(195)
345.49	5463(313)	239(33)	0.617	1268	3053(443)	891	4347(631)
352.46	4867(106)	317(17)	0.729	1187	3659(264)	821	5287(382)
356.48	4881(89)	307(13)	0.726	1146	3685(239)	787	5366(348)
366.47	4948(44)	293(6)	0.711	1058	3897(213)	714	5769(315)
367.45	5033(123)	279(13)	0.693	1050	3835(265)	708	5686(392)
380.48	4897(44)	299(6)	0.722	959	4318(230)	635	6515(347)

Table 3.35: EPM Solutions for SN 1999br

Filter Subset	$t_0(Fe)$ JD	$D(Fe)$ (Mpc)	$t_0(CC)$ JD	$D(CC)$ (Mpc)	interpolation
{BV}	2451279.2(1.5)	18.2(1.3)	2451285.6(0.7)	11.7(0.6)	velocity
{VI}	2451279.2(1.1)	17.0(0.9)	2451285.5(0.7)	11.0(0.6)	velocity
{BVI}	2451276.7(1.8)	19.6(1.2)	2451284.5(0.9)	12.1(0.7)	velocity
{VZ}	2451276.6(1.4)	19.5(1.1)	2451284.3(0.8)	12.1(0.7)	velocity
{BV}	2451278.4(1.5)	18.7(1.3)	2451283.4(1.0)	13.6(0.8)	photometry
{VI}	2451280.6(0.9)	15.3(0.7)	2451284.9(0.9)	11.3(0.7)	photometry
{BVI}	2451278.8(1.2)	17.4(1.0)	2451284.0(0.8)	12.5(0.7)	photometry
{VZ}	2451282.2(1.9)	15.1(1.3)	2451282.7(1.8)	13.6(1.3)	photometry

Table 3.36: Expansion Velocities of SN 1999ca

JD- 2451000	Date(UT)	$v(CC)$ (km s $^{-1}$)	$v(Fe\bar{5}169)$ (km s $^{-1}$)
304.60	1999 May 06	6731(369)	...
305.54	1999 May 07	5940(343)	6036
309.56	1999 May 11	5678(345)	5978
317.54	1999 May 19	5141(423)	5630

Table 3.37: EPM Quantities Derived for SN 1999ca

JD- 2451000	T_{BV} K	$\theta\zeta_{BV}$ $10^{11}\text{cm Mpc}^{-1}$	ζ_{BV}	$v(Fe)$ km s^{-1}	$\theta/v(Fe)$ 100 s Mpc^{-1}	$v(CC)$ km s^{-1}	$\theta/v(CC)$ 100 s Mpc^{-1}
305.50	6097(117)	512(24)	0.684	6077	1231(85)	6268	1194(82)
308.56	5419(99)	641(32)	0.875	5951	1231(87)	5886	1244(88)
309.50	5212(92)	695(35)	0.954	5915	1233(87)	5781	1261(89)
313.47	4725(76)	845(42)	1.196	5778	1223(86)	5390	1311(93)
317.52	4473(69)	933(47)	1.363	5656	1211(86)	5059	1354(96)
317.54	4659(65)	822(37)	1.237	5656	1175(79)	5058	1314(88)
319.46	4379(66)	970(49)	1.435	5603	1207(85)	4920	1374(97)
321.46	4321(64)	990(50)	1.482	5552	1203(85)	4787	1395(99)
322.50	4489(69)	865(43)	1.352	5527	1157(82)	4721	1355(96)
327.46	4005(56)	1189(60)	1.783	5414	1232(87)	4441	1502(107)
329.46	3915(53)	1270(64)	1.884	5373	1254(89)	4340	1552(110)
331.46	3857(52)	1321(67)	1.955	5334	1267(90)	4246	1591(113)
335.45	3794(50)	1356(69)	2.036	5260	1267(90)	4074	1635(116)
340.46	3690(48)	1416(72)	2.180	5176	1255(89)	3883	1673(119)
345.46	3548(45)	1596(81)	2.402	5100	1303(93)	3715	1788(128)
351.47	3441(90)	1696(172)	2.590	5018	1305(148)	3539	1851(209)
355.46	3411(41)	1662(85)	2.645	4967	1265(91)	3434	1829(131)

Table 3.38: Expansion Velocities of SN 1999cr

JD- 2451000	Date(UT)	$v(CC)$ (km s $^{-1}$)	$v(Fe\bar{5}169)$ (km s $^{-1}$)
257.80	1999 Mar 20	6063(927)	5456
267.77	1999 Mar 30	4465(389)	4701
291.79	1999 Apr 23	3693(465)	3250
301.68	1999 May 03	3519(418)	3192
305.65	1999 May 07	3275(500)	3598

Table 3.39: EPM Quantities Derived for SN 1999cr

JD- 2451000	$T_{V,I}$ K	$10^{11} \text{cm Mpc}^{-1}$	$\theta\zeta_{V,I}$	$\zeta_{V,I}$	$v(F_r)$ km s^{-1}	$\theta/v(F_r)$ 100s Mpc^{-1}	$v(CC)$ km s^{-1}	$\theta/v(CC)$ 100s Mpc^{-1}
256.78	8266(188)	92(3)	0.423	5494	396(24)	5894	369(22)	
257.82	7954(167)	99(3)	0.428	5404	428(25)	5784	400(24)	
257.85	8317(184)	91(3)	0.422	5402	398(24)	5781	372(22)	
259.82	7994(174)	96(3)	0.427	5241	429(26)	5585	403(24)	
261.82	7639(157)	102(3)	0.438	5088	460(28)	5401	433(26)	
263.77	7540(153)	103(3)	0.443	4949	471(28)	5234	445(27)	
266.73	7272(141)	107(3)	0.460	4753	488(29)	5002	463(28)	
266.78	7221(158)	109(4)	0.464	4750	497(30)	4998	472(29)	
266.81	7164(168)	111(4)	0.469	4748	500(32)	4996	475(30)	
267.82	7646(180)	100(4)	0.438	4686	489(30)	4922	466(29)	
267.84	7078(157)	111(4)	0.477	4684	498(31)	4921	474(29)	
274.83	6772(132)	115(4)	0.517	4297	519(31)	4472	499(30)	
275.82	6895(121)	111(3)	0.499	4248	524(31)	4415	504(30)	
277.78	6890(125)	110(4)	0.500	4155	530(31)	4309	511(30)	
277.80	6653(116)	116(4)	0.537	4154	519(31)	4308	501(30)	
285.68	6468(133)	118(4)	0.575	3820	537(33)	3932	521(32)	
291.82	6429(111)	116(4)	0.585	3600	552(33)	3686	539(32)	
291.86	6197(213)	124(8)	0.650	3598	531(43)	3685	518(42)	
294.74	6280(99)	122(4)	0.625	3504	559(33)	3581	547(32)	
296.70	6229(97)	124(4)	0.640	3444	563(33)	3515	551(32)	
296.71	6380(164)	115(6)	0.597	3443	558(39)	3514	547(38)	
298.53	5987(234)	131(11)	0.728	3389	533(50)	3455	523(49)	
299.51	6761(327)	103(9)	0.519	3361	589(59)	3424	578(58)	
301.55	6404(162)	115(5)	0.591	3303	587(40)	3361	577(39)	
302.79	6170(187)	124(6)	0.659	3269	577(42)	3324	567(41)	

Table 3.39: EPM Quantities for SN 1999cr – continued

JD- 2451000	T_{VI} K	$\theta\zeta_{VI}$ $10^{11} \text{cm Mpc}^{-1}$	ζ_{VI}	$v(Fe)$ km s^{-1}	$\theta/v(Fe)$ 100s Mpc^{-1}	$v(CC)$ km s^{-1}	$\theta/v(CC)$ 100s Mpc^{-1}
304.74	6220(97)	121(4)	0.643	3217	583(34)	3268	574(33)
305.60	6117(97)	124(4)	0.678	3195	571(34)	3244	563(33)
305.79	6220(97)	122(4)	0.643	3190	597(35)	3239	588(34)
308.76	5962(100)	131(4)	0.739	3116	568(34)	3159	561(34)
308.78	6188(115)	120(4)	0.653	3116	592(36)	3158	584(36)
320.57	6099(112)	120(4)	0.684	2857	614(38)	2881	609(38)
347.47	5527(121)	107(5)	0.986	2415	450(31)	2415	450(31)
353.47	5097(339)	92(13)	1.396	2337	283(43)	2333	283(43)

Table 3.40: EPM Solutions for SN 1999cr

Filter Subset	$t_0(Fe)$ JD	$D(Fe)$ (Mpc)	$t_0(CC)$ JD	$D(CC)$ (Mpc)	interpolation
{BVI}	2451227.0(4)	72.0(7)	2451229.3(4)	71.5(7)	velocity
{VI}	2451207.5(21)	101.0(32)	2451214.1(11)	95.1(18)	velocity
{BVI}	2451224.4(3)	74.7(4)	2451226.9(2)	74.0(4)	velocity

Table 3.41: Expansion Velocities of SN 1999eg

JD- 2451000	Date(UT)	$v(CC)$ (km s $^{-1}$)	$v(Fe\bar{5}169)$ (km s $^{-1}$)
467.77	1999 Oct 16	7140(963)	6790
501.69	1999 Nov 19	3971(584)	3192

Table 3.42: EPM Quantities Derived for SN 1999eg

JD- 2451000	T_{BV} K	$\theta\zeta_{BV}$ $10^{11} \text{ cm Mpc}^{-1}$	ζ_{BV}	$v(Fe)$ km s^{-1}	$\theta/v(Fe)$ 100 s Mpc^{-1}	$v(CC)$ km s^{-1}	$\theta/v(CC)$ 100 s Mpc^{-1}
464.76	11838(536)	53(3)	0.400	7557	174(14)	7698	170(14)
467.75	9880(462)	67(5)	0.401	6795	246(23)	7143	234(22)
471.76	7428(219)	104(6)	0.500	5988	347(27)	6517	319(25)
472.72	7089(259)	111(9)	0.534	5823	358(33)	6384	326(30)
479.73	5736(245)	163(17)	0.786	4849	428(50)	5557	373(44)
481.73	5342(170)	191(16)	0.918	4629	448(45)	5360	387(38)
486.75	4794(263)	245(41)	1.181	4156	500(86)	4924	422(73)
487.80	4704(121)	250(20)	1.236	4070	498(47)	4842	418(39)
489.80	4787(106)	236(16)	1.185	3914	509(42)	4693	424(35)
490.71	4849(121)	225(17)	1.150	3847	509(46)	4628	423(38)
493.72	4599(130)	259(23)	1.305	3642	544(55)	4426	448(45)
498.71	4409(122)	285(25)	1.446	3347	588(60)	4130	477(49)
508.68	3949(332)	380(109)	1.901	2881	693(203)	3644	548(160)
509.72	4179(328)	322(83)	1.651	2840	688(180)	3600	542(142)

Table 3.43: EPM Solutions for SN 1999eg

Filter Subset	$t_0(Fe)$ JD	$D(Fe)$ (Mpc)	$t_0(CC)$ JD	$D(CC)$ (Mpc)	interpolation
{BV}	2451438.9(4)	83.6(9)	2451428.6(8)	120.8(20)	velocity
{VI}	2451443.3(4)	74.3(9)	2451430.4(9)	117.2(22)	velocity
{BVI}	2451444.8(3)	68.4(6)	2451436.9(4)	96.5(9)	velocity
{BV}	2451444.9(4)	77.8(8)	2451436.7(6)	110.8(15)	photometry
{VI}	2451436.9(6)	83.8(12)	2451423.6(11)	126.0(24)	photometry
{BVI}	2451442.5(3)	80.0(8)	2451433.0(6)	115.6(14)	photometry

Table 3.44: Expansion Velocities of SN 1999em

JD- 2451000	Date(UT)	$v(CC)$ (km s $^{-1}$)	$v(Fe5169)$ (km s $^{-1}$)	Source
481.79	1999 Oct 30	11328(611)	...	here
484.64	1999 Nov 02	10776(721)	...	here
485.67	1999 Nov 03	10023(859)	...	here
487.9	1999 Nov 05	...	7947	Leonard et al. (2001)
488.9	1999 Nov 06	...	7997	Leonard et al. (2001)
489.9	1999 Nov 07	...	7607	Leonard et al. (2001)
490.9	1999 Nov 08	...	7177	Leonard et al. (2001)
491.67	1999 Nov 09	7817(1238)	7080	here
491.9	1999 Nov 09	...	7167	Leonard et al. (2001)
496.67	1999 Nov 14	6652(811)	6035	here
500.64	1999 Nov 18	4975(442)	...	here
501.66	1999 Nov 19	4976(402)	5107	here
501.9	1999 Nov 19	...	5457	Leonard et al. (2001)
504.9	1999 Nov 22	...	5117	Leonard et al. (2001)
506.9	1999 Nov 24	...	4967	Leonard et al. (2001)
510.63	1999 Nov 28	4307(415)	...	here
510.9	1999 Nov 28	...	4577	Leonard et al. (2001)
514.9	1999 Dec 02	...	4327	Leonard et al. (2001)
517.9	1999 Dec 05	...	3827	Leonard et al. (2001)
520.9	1999 Dec 08	...	3807	Leonard et al. (2001)
524.9	1999 Dec 12	...	3877	Leonard et al. (2001)
527.9	1999 Dec 15	...	3787	Leonard et al. (2001)
528.76	1999 Dec 16	2916(496)	3250	here
529.9	1999 Dec 17	...	3577	Leonard et al. (2001)
543.76	1999 Dec 31	2149(452)	3018	here
556.9	2000 Jan 13	...	2817	Leonard et al. (2001)
575.9	2000 Feb 01	...	2577	Leonard et al. (2001)
576.9	2000 Feb 02	...	2577	Leonard et al. (2001)
604.9	2000 Mar 01	...	1877	Leonard et al. (2001)

Table 3.45: EPM Quantities Derived for SN 1999em

JD- 2451000	T_{VH} K	$\theta\zeta_{VH}$ $10^{11}\text{cm Mpc}^{-1}$	ζ_{VH}	$v(Fe)$ km s^{-1}	$\theta/v(Fe)$ 100 s Mpc^{-1}	$v(CC)$ km s^{-1}	$\theta/v(CC)$ 100 s Mpc^{-1}
481.80	11318(192)	400(7)	0.590	11923	569(30)	12518	542(29)
482.69	10338(179)	456(9)	0.583	11096	704(38)	11543	677(37)
483.76	10542(163)	452(8)	0.585	10283	751(40)	10604	729(38)
483.78	9923(207)	498(13)	0.581	10269	835(47)	10588	810(46)
484.76	10706(169)	449(8)	0.586	9654	794(42)	9890	775(41)
485.73	10279(284)	466(17)	0.583	9134	875(54)	9308	859(53)
486.77	9909(142)	489(8)	0.580	8654	974(51)	8776	961(51)
487.75	9836(140)	490(8)	0.580	8259	1023(54)	8343	1012(53)
488.76	9525(130)	511(8)	0.577	7899	1121(59)	7952	1114(59)
489.81	9304(155)	527(9)	0.576	7567	1211(64)	7594	1207(64)
495.74	9206(120)	548(9)	0.575	6215	1535(80)	6159	1549(81)
498.68	9252(245)	535(21)	0.575	5752	1618(102)	5676	1639(103)
501.71	8324(96)	624(9)	0.566	5362	2056(107)	5272	2091(109)
504.74	7983(87)	657(10)	0.562	5035	2318(121)	4936	2365(123)
505.72	7646(79)	707(10)	0.558	4941	2562(133)	4839	2616(136)
507.80	7834(129)	673(18)	0.561	4755	2522(142)	4650	2580(146)
510.75	7653(79)	699(10)	0.558	4522	2770(144)	4412	2839(148)
513.72	7475(119)	727(19)	0.556	4316	3027(171)	4203	3108(176)
516.71	6953(64)	828(12)	0.549	4133	3651(189)	4017	3756(195)
519.72	7067(71)	804(13)	0.550	3968	3681(193)	3851	3793(199)
522.59	6885(63)	848(12)	0.548	3826	4045(210)	3708	4174(217)
527.63	6809(82)	860(13)	0.547	3608	4360(228)	3489	4509(236)
528.59	6740(60)	874(12)	0.545	3570	4488(233)	3451	4643(241)
538.60	6557(68)	914(13)	0.542	3230	5219(272)	3112	5418(282)
546.61	6352(52)	959(13)	0.539	3014	5908(306)	2897	6147(318)

Table 3.45: EPM Quantities for SN 1999em – continued

JD- 2451000	T_{VH} K	$\theta\zeta_{VH}$ $10^{11} \text{ cm Mpc}^{-1}$	ζ_{VH}	$v(Fe)$ km s^{-1}	$\theta/v(Fe)$ 100 s Mpc^{-1}	$v(CC)$ km s^{-1}	$\theta/v(CC)$ 100 s Mpc^{-1}
547.60	6399(53)	945(13)	0.540	2990	5856(303)	2873	6095(316)
551.66	6463(55)	924(12)	0.541	2896	5899(306)	2780	6146(318)
558.55	6357(53)	932(13)	0.539	2754	6280(325)	2639	6553(339)
565.57	6224(50)	954(13)	0.536	2627	6773(350)	2514	7077(366)
572.54	6305(52)	892(12)	0.538	2516	6590(341)	2405	6895(357)
578.55	6502(55)	796(11)	0.541	2430	6050(313)	2320	6336(328)
592.53	6124(87)	717(21)	0.534	2256	5943(343)	2150	6238(360)
599.52	5393(72)	721(22)	0.518	2181	6378(375)	2076	6701(394)
606.54	4948(67)	608(20)	0.506	2113	5687(342)	2009	5981(360)
613.53	4883(77)	577(24)	0.504	2050	5589(361)	1948	5882(380)
620.52	4950(71)	545(20)	0.506	1992	5412(335)	1891	5701(353)
627.50	4953(68)	525(18)	0.506	1938	5357(327)	1838	5647(344)
634.49	5022(79)	493(20)	0.508	1888	5141(328)	1790	5423(346)
641.50	5018(56)	480(13)	0.508	1841	5137(293)	1744	5422(309)
653.48	5267(52)	411(9)	0.515	1768	4511(247)	1673	4767(261)
655.48	5341(49)	395(7)	0.517	1756	4357(233)	1662	4605(246)
656.48	5415(45)	380(7)	0.519	1751	4184(221)	1656	4422(234)

Table 3.46: EPM Solutions for SN 1999em

Filter Subset	$t_0(Fe)$ JD	$D(Fe)$ (Mpc)	$t_0(CC)$ JD	$D(CC)$ (Mpc)	interpolation
{BV}	2451472.3(0.6)	9.5(0.2)	2451474.1(0.6)	8.7(0.3)	velocity
{VI}	2451473.8(0.4)	10.1(0.2)	2451475.0(0.6)	9.4(0.4)	velocity
{BVI}	2451471.8(0.6)	10.1(0.2)	2451473.9(0.6)	9.1(0.3)	velocity
{VZ}	2451472.4(0.6)	10.9(0.3)	2451474.1(0.6)	9.9(0.3)	velocity
{VJ}	2451475.2(0.5)	10.9(0.2)	2451475.8(0.5)	10.5(0.4)	velocity
{VH}	2451475.0(0.6)	10.7(0.2)	2451475.7(0.6)	10.2(0.4)	velocity
{VK}	2451474.1(0.6)	11.2(0.2)	2451475.2(0.5)	10.5(0.4)	velocity
{JHK}	2451471.3(1.2)	11.8(0.5)	2451473.9(0.9)	10.5(0.4)	velocity
{BV}	2451473.2(0.9)	9.2(0.3)	2451479.0(0.7)	6.6(0.3)	photometry
{VI}	2451473.8(1.2)	9.8(0.4)	2451480.0(0.6)	6.9(0.3)	photometry
{BVI}	2451473.1(1.0)	9.5(0.3)	2451479.2(0.6)	6.8(0.3)	photometry
{VZ}	2451472.3(1.0)	10.4(0.4)	2451478.7(0.8)	7.3(0.3)	photometry
{VJ}	2451475.6(0.9)	10.5(0.4)	2451480.6(0.7)	7.5(0.3)	photometry
{VH}	2451476.7(0.8)	10.0(0.3)	2451481.1(0.6)	7.2(0.3)	photometry
{VK}	2451476.4(0.9)	10.3(0.3)	2451480.8(0.6)	7.5(0.3)	photometry
{JHK}	2451479.8(1.3)	9.5(0.6)	2451481.8(0.9)	7.5(0.6)	photometry

Table 3.47: Expansion Velocities of SN 2000cb

JD- 2451000	Date(UT)	$v(CC)$ (km s $^{-1}$)	$v(Fe\bar{5}169)$ (km s $^{-1}$)
663.87	2000 Apr 29	12126(539)	9460
666.62	2000 May 02	9825(290)	7197
672.65	2000 May 08	7179(788)	6558
689.64	2000 May 25	6182(206)	5223
693.91	2000 May 29	5960(612)	5165
694.91	2000 May 30	5913(634)	5572
695.59	2000 May 31	5575(597)	5165
728.76	2000 Jul 03	4733(731)	4121

Table 3.48: EPM Quantities Derived for SN 2000cb

JD- 2451000	T_{BVI} K	$\theta\zeta_{BVI}$ $10^{11}\text{cm Mpc}^{-1}$	ζ_{BVI}	$v(Fe)$ km s^{-1}	$\theta/v(Fe)$ 100 s Mpc^{-1}	$v(CC)$ km s^{-1}	$\theta/v(CC)$ 100 s Mpc^{-1}
663.81	6975(83)	121(3)	0.508	8660	276(15)	11397	210(12)
675.70	6159(53)	233(4)	0.593	6565	599(32)	7778	505(27)
676.76	6158(53)	241(5)	0.593	6449	629(34)	7600	534(29)
677.77	6104(52)	251(5)	0.600	6344	660(35)	7441	563(30)
681.74	5999(50)	283(5)	0.616	5981	768(41)	6904	666(36)
682.81	6006(52)	289(6)	0.615	5895	798(43)	6778	694(37)
683.78	5990(50)	295(6)	0.617	5820	821(44)	6669	717(38)
683.75	5965(50)	298(6)	0.621	5822	823(44)	6673	719(38)
684.75	6713(112)	247(7)	0.530	5748	811(47)	6566	710(41)
695.57	5296(40)	422(8)	0.756	5103	1094(59)	5669	985(53)
699.72	5002(35)	487(9)	0.840	4912	1181(63)	5412	1072(57)
705.70	4708(31)	567(10)	0.945	4674	1282(68)	5096	1176(63)
730.67	4282(25)	730(13)	1.150	3977	1596(85)	4203	1510(80)
738.64	4265(27)	725(14)	1.160	3817	1639(88)	4004	1562(84)
745.66	4182(25)	735(14)	1.210	3692	1645(88)	3851	1577(84)
757.64	3978(22)	714(13)	1.349	3508	1509(80)	3626	1459(78)
795.49	4259(42)	429(11)	1.163	3077	1200(68)	3113	1186(67)

Table 3.49: EPM Solutions for SN 2000cb

Filter Subset	$t_0(Fe)$ JD	$D(Fe)$ (Mpc)	$t_0(CC)$ JD	$D(CC)$ (Mpc)	interpolation
{BV}	2451652.3(0.8)	34.0(1.2)	2451655.0(0.7)	35.4(1.2)	velocity
{VI}	2451654.8(0.6)	30.7(1.0)	2451656.4(0.3)	33.2(1.0)	velocity
{BVI}	2451650.6(1.1)	35.7(1.5)	2451653.7(0.8)	36.9(1.5)	velocity
{BV}	2451651.2(0.9)	36.4(1.7)	2451653.7(0.9)	38.0(1.7)	photometry
{VI}	2451651.5(1.2)	38.2(2.1)	2451653.9(1.0)	40.1(2.0)	photometry
{BVI}	2451651.5(1.2)	35.8(2.2)	2451653.9(0.9)	37.4(2.2)	photometry

CHAPTER 4 THE PERFORMANCE OF THE EXPANDING PHOTOSPHERE METHOD

4.1 Introduction

In the previous chapter I obtained EPM distances for 12 SNe from the original sample of 17 objects. In this chapter I assess the performance of EPM. First I discuss the internal precision of EPM and the sensitivity of the method to dust. I find that the typical uncertainty in an EPM distance is 20%. Then I evaluate the accuracy of the method from comparison with distances derived using other techniques. A comparison between EPM and Tully-Fisher shows that EPM produces somewhat shorter distances. The analysis of the Hubble diagram yields a Hubble constant between 63 and $68 \text{ km s}^{-1} \text{ Mpc}^{-1}$.

4.2 Internal precision

EPM predicts that the distance to the SN at epoch i is given by

$$D_i = \frac{v_i (t_i - t_0) \zeta(T_{S,i})}{(\theta\zeta)_{S,i}}. \quad (4.1)$$

This equation shows that the method has the great advantage that observations at different epochs are essentially independent distance measurements, thus offering a valuable *internal* consistency check as the properties of the photosphere change over time. Equation 4.1 shows that the uncertainty in a single-epoch distance is due to errors in $(\theta\zeta)_{S,i}$ and $T_{S,i}$ (which depend on the photometric errors and the uncertainty in dust extinction), errors

in the photospheric velocity v_i (which come from the CC technique and the interpolation scheme), and errors in the dilution factor $\zeta(T_{S,i})$. The analysis of Chapter 3 shows that the distance residuals for a given SN are generally within 15% from the average, but in some cases they reach 50% as the SN approaches the end of the plateau. SNe 1987A and 2000cb are examples of a remarkable performance of the method, especially considering that these objects are not prototypes of plateau SNe. SNe 1986L and 1999cr, on the other hand, provide examples of large distance residuals that vary systematically with time (see Figures 3.12 and 3.37). Next I examine the different sources of error that could explain such spread.

The photometric error in an individual magnitude is given by Poisson statistics. In general (see Table 2.4) they range between 0.02-0.05 mag during the plateau, and the resulting statistical errors in $(\theta\zeta)_{S,i}$ and $T_{S,i}$ are roughly constant, of the order of 5% (see Table 3.23, for example). Besides the nominal uncertainties due to photon statistics, the transformation of instrumental magnitudes to the standard system can be affected by systematic errors owing to the non-stellar nature of the SN spectrum. Although these can be significant as the SN spectrum approaches the nebular phase (Hamuy et al., 1990), comparison of photometry obtained with different instruments shows that they remain at the level of 0.05 mag or lower during the plateau phase, which is comparable to the Poisson uncertainties. The value adopted for dust extinction in the host galaxy also affects the determination of $(\theta\zeta)_{S,i}$ and $T_{S,i}$. Its effect, however, is to affect the global value of the distance and not the individual point-to-point fluctuations. Hence, I defer the study of its consequences to the next section. It is clear for now that the large distance fluctuations displayed by some SNe cannot be explained by the photometric errors.

The next possibility to consider are errors in the dilution factor. In the examples mentioned above (SNe 1986L and 1999cr) it proves interesting to note that 1) these objects have well-sampled velocity curves, so that interpolation errors in the velocities cannot

explain these residuals; and 2) the photospheric temperatures of these objects always remained within the range of temperatures encompassed by the models of E96 so that no extrapolations are required. The most likely interpretation to the observed spread is, therefore, that the systematic errors in the average dilution factors can exceed the 5-10% range predicted by E96. It is useful to mention that such problems occur at later times when the temperature drops near the value of H recombination. At earlier epochs the dilution factors perform much better and yield consistent distances, although for some SNe this period is quite short. Next I proceed to estimate the error in distance due to the dilution factors.

To disentangle errors due to velocity and dilution factor I proceed now to compare distances from different filter subsets derived from the *same* velocity curve. For this purpose I employ the distances obtained from the CC velocity curve for 10 SNe with data from more than one filter subset. This analysis yields an average dispersion of 11% (with a minimum of 4% for SN 1999br and a maximum of 19% for SN 1993A). The observed dispersion can be compared to the formal errors computed for the individual distances. From the 39 distances (12 SNe) derived from the CC curve, the average error is 8% (with a minimum of 2% for SN 1986L and a maximum of 22% for SN 1990E). The formal error only accounts for statistical errors in the photometry and 5% in the individual velocity measurements. It does not include errors in the dilution factors. Hence, I interpret the larger empirical spread as a symptom of systematic errors in the dilution factors, which typically amount to 11%.

The formal errors in the individual distances include a 5% error in the individual velocity points, but no uncertainty associated to velocity interpolations. SN 1999em is a very good example that illustrates the sensitivity of EPM to different procedures of velocity interpolations. With a power-law fit to the $v(CC)$ points I get a distance that proves 37% greater than the method of interpolating magnitudes. Since the SN luminosity varies

slowly during the plateau, this method is almost exact (provided the light curves are properly sampled) and should be preferred. In practice, however, only six of my SNe possess well-sampled velocity curves to which I can apply such procedure, so it proves necessary to use the distances derived from the power-law interpolation and estimate the noise introduced by this method. From the eight SNe for which I could apply both methods I get $D(\text{inter})/D(\text{no} - \text{inter})=1.02\pm0.12$. Below I adopt the 12% rms difference between $D(\text{inter})$ and $D(\text{no} - \text{inter})$ as a global estimate to the uncertainties of using the power-law fits.

More insight about the sensitivity of EPM to the adopted velocity can be obtained by comparing distances yielded by the Fe and CC curves. Figure 4.1 shows that there are three cases (SNe 1988A, 1999br, and 1999eg) where the two solutions differ by more than 20%. For the ensemble of 38 distances I get $D(\text{CC})/D(\text{Fe})=1.01\pm0.17$ (rms) which reveals no significant overall bias between the two methods. This is somewhat surprising since the minimum of the Fe I $\lambda 5169$ line is expected to form near the thermalization surface which should expand slower than the photosphere in a homologous expansion (as discussed in section 3.4). According to equation 4.1 smaller velocities should lead to shorter distances, which is not the case. It is possible that scattering of photons by free electrons in the expanding atmospheres of SNe II could shift the line minimum to higher velocities. In any case, the 8% rms scatter of $D(\text{Fe})$ and $D(\text{CC})$ about the mean gives an estimate to the uncertainties of adopting different velocity curves. This compares to the 12% rms difference between $D(\text{inter})$ and $D(\text{no} - \text{inter})$ given above.

4.3 The sensitivity to dust

The sensitivity of EPM distances to the adopted value for $A_{\text{host}}(V)$ changes from object to object, depending on the sampling of the light curves and the filters used. I estimate the effect of dust for each case by varying $A_{\text{host}}(V)$ and computing the derivative

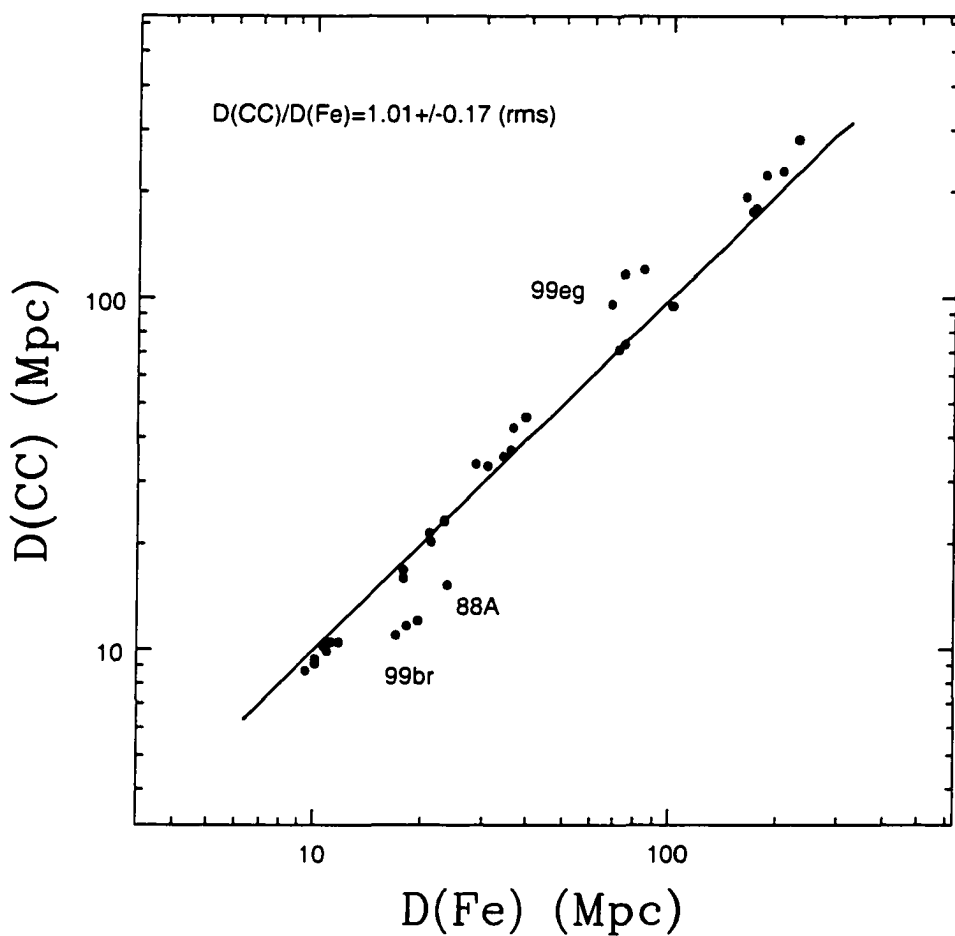


Figure 4.1: Comparison between EPM distances derived from CC and Fe velocities. The ridge line has a slope of one and is not a fit to the data. The three objects with significant differences are labeled.

$d\ln(D)/dA_{host}(V)$ which gives the fractional change in D from a change in $A_{host}(V)$. Figure 4.2 presents the resulting distributions for filter subsets $\{BV, VI, BVI\}$. In all cases the derivative is negative, i.e., the EPM distance decreases with increasing $A_{host}(V)$. The average derivative is -0.54, -0.43, and -0.51 for $\{BV, VI, BVI\}$, respectively, which compares with the -0.46 value for the standard candle technique in the V band. This implies that the EPM distances are as sensitive to dust as the standard candle technique, which contrasts with the predictions of S94 and E96. Their argument was that, while dust makes the SN to appear fainter, it also makes it appear cooler and therefore with a lower intrinsic luminosity. They argued that to first order, the two effects tend to cancel out. Their analysis, however, did not include the effects of dust in the dilution factors which are mainly determined by temperature and thus, by the adopted $A_{host}(V)$. This analysis demonstrates that the sensitivity of EPM to dust is larger than previously suspected.

The great wavelength coverage obtained for SN 1999em allows me to ask whether IR observations can help at decreasing the uncertainties due to dust. For filter subsets $\{VJ, VH, VK\}$ $d\ln(D)/dA_{host}(V)$ proves to be +0.25, +0.28, +0.21, respectively. By contrast to subsets including optical filters alone, the distance increases with increasing $A_{host}(V)$. Despite the change in sign, the magnitude of the derivative is not less than that obtained for this same SN from $\{BV, VI, BVI\}$. The value from $\{JHK\}$ is even larger, namely, +0.47. A similar value of +0.50 is derived for SN 1987A from the same subset. This analysis reveals that, even though IR photometry is less affected by dust, the EPM distances derived from filter subsets including one or more IR filters are not less sensitive to dust than those determined from optical filters alone. This result challenges the suggestion of Schmidt et al. (1992), namely, that one of the advantages of using IR for EPM is that “the uncertainty in a distance due to extinction is less than half that incurred when optical photometry is used”. My analysis shows that the $\{VI\}$ subset has the least sensitivity to the effects of dust and that the majority of the objects have

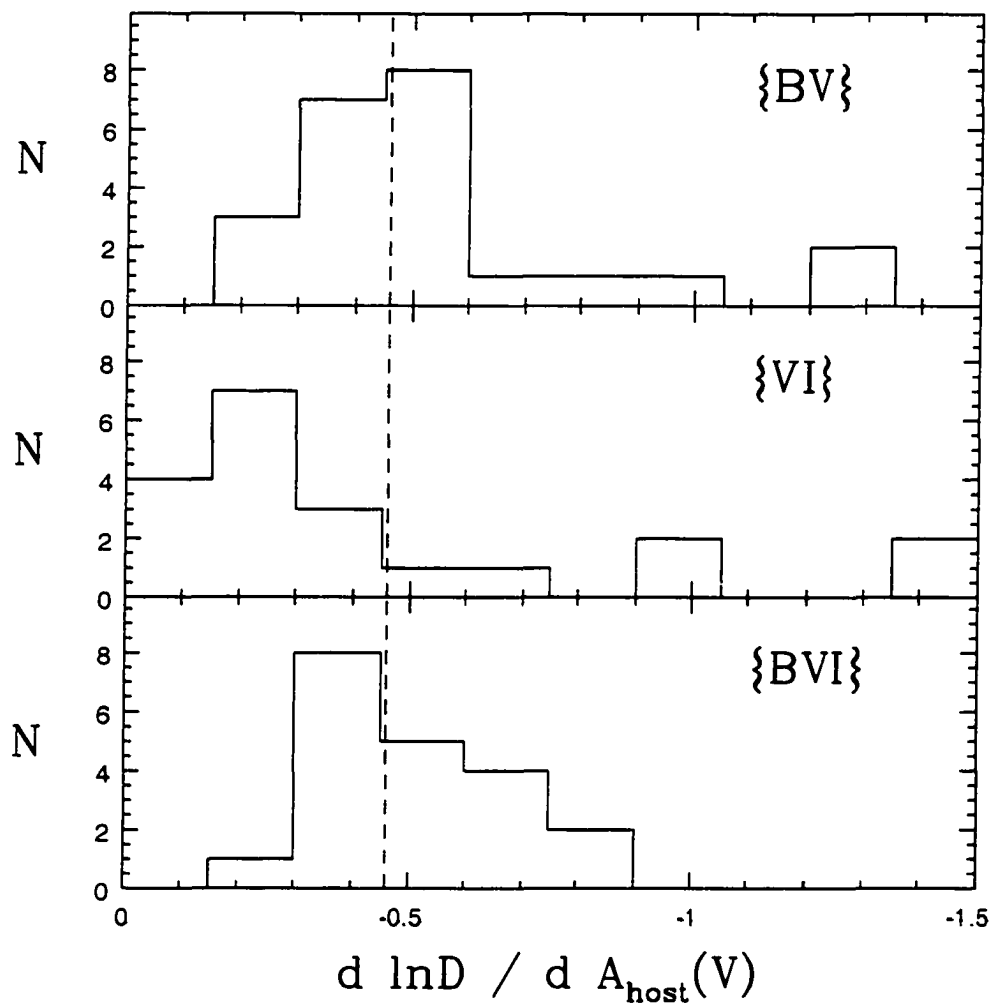


Figure 4.2: Distributions of $d \ln(D)/d A_{\text{host}}(V)$ for filter subsets $\{BV, VI, BVI\}$. For comparison, the vertical dashed line shows the corresponding value for the standard candle technique in the V filter.

$d\ln(D)/dA_{host}(V)$ values smaller than the reference value for the standard candle method (see Figure 4.2).

4.4 Error estimates for EPM distances

As discussed above the precision of an EPM distance is determined by observational uncertainties, systematic errors in dilution factors, interpolation of velocities to the time of the photometric observations, and errors incurred in the estimate of dust absorption.

To estimate the total error for an individual distance I sum in quadrature the statistical error associated to the photometry and the velocity measurements, the uncertainty due to dilution factors (estimated from the distance spread obtained for each SN from the different filter subsets), 12% uncertainty that accounts for velocity interpolations, and the error due to dust absorption in the host galaxy [obtained from the computed $d\ln(D)/dA_{host}(V)$ value for each SN and an adopted ± 0.3 mag error for $A_{host}(V)$]. Table 4.1 summarizes all these uncertainties. On average the four components amount to 8% (statistical), 11% (dilution factors), 12% (velocity interpolations), and 14% (extinction). Evidently, all error sources can be important. The total error in the individual EPM distances is as large as 50% (SN 1990E) and as low as 13% (SN 2000cb), with an average of 24%. Next I carry out external comparisons in order to check the reality of these assumptions and estimates.

4.5 External comparisons

In order to compare my results with other published distances I summarize in Table 4.2 distances computed by S94, Tully-Fisher (TF) and Cepheid values, as well as recession velocities for the SN host galaxies in the CMB frame.

4.5.1 Comparison with other EPM distances

SKE92 carried out an EPM analysis of 10 SNe II. In their 1994 paper they updated their results for these objects using an unpublished version of the dilution factors of E96. They

included a number of new SNe, bringing the total of EPM distances to 16. There are seven SNe in common with my sample.

For consistency, I use the distances derived from the Fe curve as done by S94. In three cases (SNe 1986L, 1990K and 1992af) my analysis shows that no EPM solution is possible. The comparison for the remaining four SNe is presented in Figure 4.3. For SNe 1988A and 1990E I take the results from the $\{BVI\}$ filters, whereas for SNe 1992am and 1992ba I employ the $\{BVI\}$ subset, in the same manner as done by S94.

The comparison shows that, within the error bars, the agreement is reasonable. The most discrepant point corresponds to SN 1992ba. For this object they reported 14 Mpc, which contrasts with the 23.3 Mpc result found here (2σ larger). Most of the difference is due to the 0.3 mag greater visual extinction adopted by them and velocities somewhat lower than the Fe curve (see Figure 3.26). This plot reveals that my error estimates are larger (and probably more realistic) than those reported by S94. SN 1992ba is a good example that supports this claim.

4.5.2 Comparison with the cosmic distance ladder

The determination of extragalactic distances is the result of a concatenation of different methods, all of which require an external calibration. This “cosmic distance ladder” is ultimately defined by the distance to the LMC, which is used as the zero point for the Cepheid scale. The establishment of this scale has been the purpose of the *HST* Key Project, which has recently provided Cepheid distances to 18 nearby spiral galaxies (Freedman et al., 2001). This Cepheid calibration provides then the zero point for various secondary distance indicators like Type Ia SNe, Tully-Fisher, surface brightness fluctuations, and the fundamental plane of elliptical galaxies, which allows us to extend the reach of the distance scale to greater distances and solve for the Hubble constant. Since EPM does not require an external calibration it affords a valuable independent check to the “cosmic distance ladder”, which is the topic of the next sections.

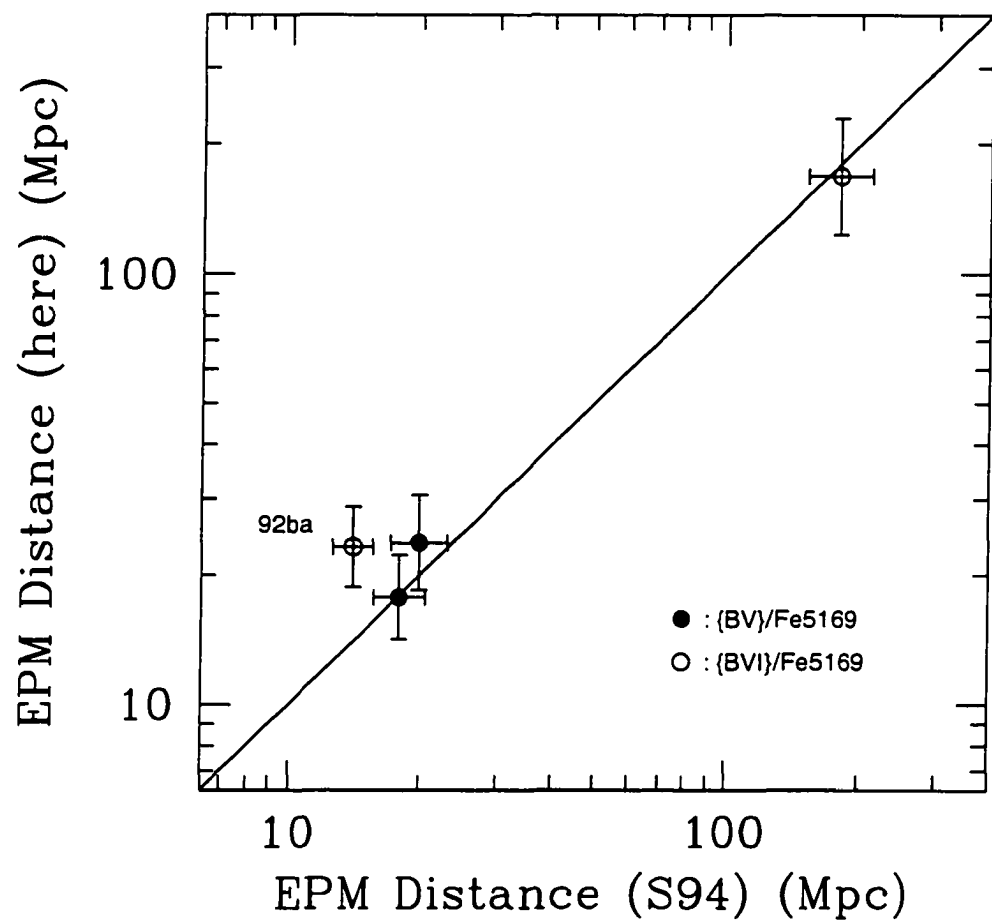


Figure 4.3: Comparison of EPM distances derived here and by S94. The ridge line corresponds to $D_{here} = D_{S94}$.

4.5.2.1 The EPM distance to the LMC

The EPM distance to the LMC derived from SN 1987A permits me to check the zero point of 50 ± 3 kpc adopted by Freedman et al. (2001) for the Cepheid scale, although it must be kept in mind that this object was not a genuine SN II-P.

The EPM values derived for SN 1987A from CC velocities range between $D(CC) = 34\text{--}46$ kpc, depending on the filter subset employed. These values all prove significantly lower than zero point of the Cepheid scale. This implies that either the Cepheid scale should be shortened, the application of EPM to SN 1987A underestimates the LMC distance, or both. A direct geometric distance to the LMC has been obtained from the ring of SN 1987A. Using this method Panagia et al. (1997) and Gould & Uza (1998) derived LMC distances of 50.9 ± 1.8 and 48.8 ± 1.1 kpc, respectively. Indirect distances calibrated with Hipparcos parallaxes have been obtained using Cepheids, RR Lyraes, and Mira variables. The full range of LMC distances from these methods after the Hipparcos mission is 49–55 kpc (Walker, 1999). From *HST* photometry of the globular cluster NGC 1866 Walker et al. (2001) performed a ZAMS fitting relative to the Hipparcos calibration of the Hyades and derived 47 ± 1 kpc for the LMC.

Despite the $\sim 5\%$ uncertainty in the LMC distance yielded by the different methods, the EPM distance falls in the low side of the plausible range. I mentioned earlier that SN 1987A was not a typical plateau SN. Owing to its compact blue supergiant progenitor, the light curve was promptly powered by radioactivity. The dilution factors computed by E96 are recommended for use on genuine SNe II-P events, i.e., objects with red supergiants progenitors whose light curves are powered by shock deposited energy. It is possible that the radioactive heating could have significant effects in the dilution factors and the derived distances. The internal consistency among the EPM distances derived from different epochs over the entire plateau phase is remarkably good (see Figure 3.14), and suggests that either the dilution factors and/or the photospheric velocities are under-

estimated by a constant offset.

Eastman & Kirshner (1989) did an EPM analysis of SN 1987A and found a distance of 49 ± 6 kpc using V / I photometry for the first 10 days since explosion and specific atmosphere models for SN 1987A, in much better agreement to estimates from other methods. Their distance compares to my estimate of $D(CC)=43$ kpc from the same filters. Most of the difference is due to higher dilution factors and not to the velocity curve adopted. This suggests that the dilution factors of E96 employed here are too low for SN 1987A, and that this underestimate is even larger for other filter subsets, particularly in JHK which produces the shortest distance [$D(CC)=34$ kpc]. It remains to see whether such underestimate also applies to the other SNe of this sample. D. Leonard and collaborators will soon provide a Cepheid distance to the host galaxy of SN 1999em which will help us to clarify this issue, both in the optical and IR. Another independent check of the dilution factors can be obtained from the study of the Hubble diagram, which I proceed to examine.

4.5.2.2 The Hubble diagram

In a uniform and isotropic expanding Universe, the recession velocities of the galaxies increase linearly with their distances. Hence, if the galaxies are expanding with the Hubble flow the redshifts provide a precise estimate of their relative distances and afford a great opportunity to check the precision and accuracy of EPM. For the test to work the observed heliocentric redshifts must be corrected for the motion of the observer relative to the CMB. For this purpose I add the vectors $(-30,297,-27)$ and $(7,-542,302)$ km s $^{-1}$ (in Galactic Cartesian Coordinates) to the observed redshifts. The former is the motion of the sun with respect to the Local Group (Lynden-Bell & Lahav, 1988) while the latter is the motion of the Local Group with respect to the CMB as measured with COBE (Smoot et al., 1992). I assign an uncertainty of ± 300 km s $^{-1}$ to the corrected redshifts for a possible component of peculiar velocity of each galaxy. The resulting redshifts are listed in Table

4.2.

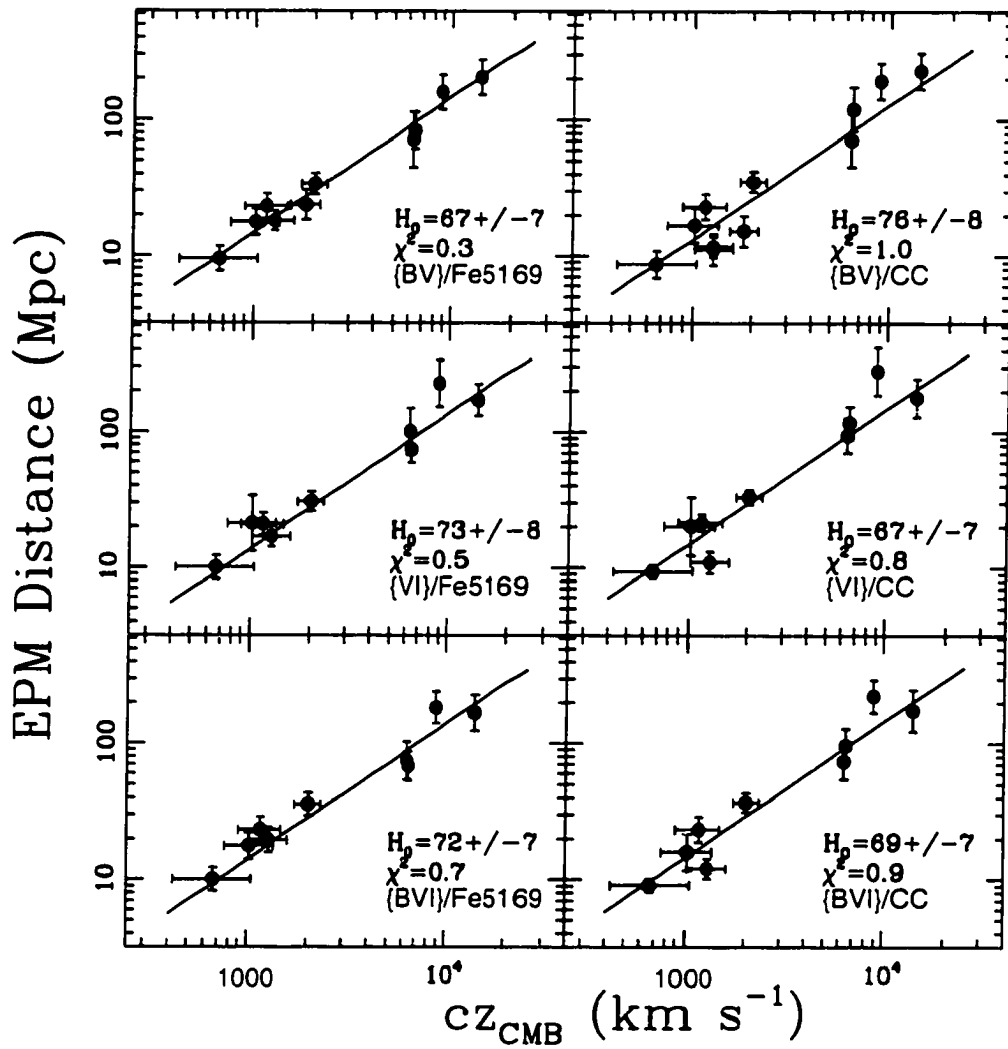


Figure 4.4: EPM distance versus CMB redshift for six filter/velocity combinations.

Figure 4.4 presents the distance-redshift relations (Hubble diagrams) for the six filter/velocity EPM combinations, revealing that the EPM distances increase linearly with redshift. The ridge lines correspond to Hubble laws characterized by reduced χ^2 ranging between 0.3-1. On average the EPM errors prove 20% higher than the scatter around the

ridge lines. In other words, I do not find evidence for significant error sources other than those considered earlier, namely, statistical errors in photometry and velocities, dilution factors, velocity interpolations, extinction, and peculiar motion of the host galaxies. If I force the value of reduced χ^2 to unity, I would have to reduce the EPM errors by 17%. i.e., the typical error for an individual EPM distance becomes 20%. This leads me to conclude that the EPM assumption that SNe II are spherically symmetric explosions is a reasonable approximation. This is consistent with the conclusion by Leonard & Filippenko (2001) from the low level of polarization measured from SNe II-P. The 20% uncertainty that I find here contrasts with the 10% error derived from the Hubble diagram of S94. The analysis of the various errors sources presented above demonstrate that 20% is a more realistic estimate of the uncertainty in an EPM distance.

The values for H_0 from the Fe velocities range between 67 ± 7 and $73 \pm 6 \text{ km s}^{-1} \text{ Mpc}^{-1}$, which prove statistically consistent with the result by S94, namely, $H_0 = 73 \pm 7$. The CC method yields similar solutions, namely, $H_0 = 76 \pm 8$, 67 ± 7 , 69 ± 7 , from $\{BV\}$, $\{VI\}$, and $\{BVI\}$, respectively. These are indistinguishable from the Fe values, which is not unexpected of course given the good overall agreement between the Fe and CC distances (see Figure 4.1). Since the nearest SNe are potentially more affected by the peculiar motion of their host galaxies, it proves interesting to consider the five SNe with recession velocities greater than $2,000 \text{ km s}^{-1}$. This yields somewhat lower values for H_0 , namely, 60 ± 8 from $\{BV\}$, 63 ± 8 from $\{VI\}$, and 66 ± 8 from $\{BVI\}$.

This EPM analysis provides an independent check of the cosmic distance ladder. Despite all of the efforts over recent years to measure the Hubble constant, its value still remains controversial. For example, the calibration of SNe Ia peak luminosities (the best secondary distance indicator) based on Cepheid distances measured by the *HST* Key Project yields $H_0 = 71 \pm 6$ (Freedman et al., 2001), for an adopted LMC distance of 50 ± 2 kpc. Sandage and collaborators have also addressed the calibration of SNe Ia from

Cepheid distances measured with *HST*. In their last paper (Sandage et al., 2001) they reported $H_0=58\pm2$ from an adopted LMC distance of 52 kpc. If I convert this value to the same zero point of 50 kpc used by Freedman et al., I obtain $H_0=60$. The 15% difference in the Hubble constant derived by the two groups is due to many subtleties in the analysis of the Cepheid and SN data [see Freedman et al. (2001), Sandage et al. (2001), Gibson et al. (2000) for further details about the controversy]. Our study of the Calán/Tololo SN Ia Hubble diagram – calibrated with the *HST* Cepheid distances published by Sandage et al. from an LMC distance of 50 kpc – gives an intermediate value of $H_0=63\pm3$ (Hamuy et al., 1996; Phillips et al., 1999).

The discussion above suggests that the interval 65 ± 5 represents reasonably well the currently accepted range of H_0 measurements from Cepheid/SNe Ia distances. This interval compares with the EPM range of 67-76 (±7) derived from the CC method and the full sample of SNe. From the sample of the five most distant objects the range of H_0 between 60-66 (±8) agrees remarkably well with the Cepheid scale. This is an encouraging result, although it proves hard to draw strong conclusions from five objects and clearly more observations of SNe II in the Hubble flow ($2,000 < cz < 20,000$) will be required to keep testing the EPM and Cepheid distance scales.

It is worth mentioning that, since line blanketing is relatively stronger in the *B* band (E96), the $\{V\}$ combination is less sensitive to metallicity variations from SN to SN than the other two filter subsets. This implies that the idea of using average dilution factors for all SNe must work better in $\{V\}$. It is interesting to remark that among all filter subsets the $\{V\}$ combination appears to yield the best agreement with the Hubble constant of the Cepheid scale. Also, these filters give a distance to the LMC of 43 ± 8 kpc that compares reasonably well with the 50 kpc zero point of the Cepheid scale (especially considering that SN 1987A is not a typical SN II-P). It appears that, before the grid of dilution factors is expanded, the $\{V\}$ subset should be preferred for the EPM analysis.

4.5.2.3 Tully-Fisher versus EPM

R. Giovanelli kindly provided me unpublished Tully-Fisher distances for the hosts of SNe 1990K, 1999ca, 1999em, and 2000cb, derived from his line-width measurements and luminosity-line-width template calibrated with *HST* Cepheid distances (Giovanelli et al., 1997). In this scale the value of the Hubble constant is $H_0=69 \text{ km s}^{-1} \text{ Mpc}^{-1}$, which is very close to the more recent TF estimate of $H_0=71 \text{ km s}^{-1} \text{ Mpc}^{-1}$ obtained by the *HST* Key Project from the full set of Cepheid distances (Freedman et al., 2001). The resulting TF distances are listed in Table 4.2.

TF distances for SNe 1986L, 1988A, 1990E, and 1990K were published by Pierce (1994) based on the template calibrated by Pierce & Tully (1992) which yielded a Hubble constant of $86 \text{ km s}^{-1} \text{ Mpc}^{-1}$. For consistency, I need to transform his distances to the most modern *HST* Cepheid scale. For this purpose I use his line-widths and I band apparent magnitudes for the host galaxies of these four SNe, and the I band TF template of Giovanelli et al. (1997). For the specific case of the host of SN 1986L which does not have an I magnitude, I employ the integrated H magnitude given by Pierce (1994) and an adopted $I - H$ color of 1. The results are given in Table 4.2 with errors corresponding to the 0.35 mag scatter of the TF template. Note that these distances prove significantly larger (~ 1 mag) than those given by Pierce.

Figure 4.5 compares $D(CC)$ and $D(TF)$, independently for the $\{BV, VI, BVI\}$ subsets. The six $\{VI\}$ and $\{BVI\}$ EPM distances agree well with TF. The five SNe with $\{BV\}$ distances (top panel), on the other hand, yield $D(EPM)/D(TF) = 0.70 \pm 0.09$ which suggests that the EPM distances are actually smaller than the TF values. It must be mentioned, however, that the number of SNe is small and that χ^2 is dominated by one object: SN 1986L. Also the EPM analysis of this object revealed a poor performance of the dilution factors so that the distance had to be computed from the very early observations. Leaving aside SN 1986L the remaining four objects yield $D(EPM)/D(TF) = 0.82 \pm 0.12$

which is only 1.5σ different than unity.

S94 performed a similar comparison and found $D(TF)/D(EPM) = 0.89 \pm 0.07$, which is the opposite that I find here. Part of the problem is that S94 used the TF distances computed by Pierce that were derived using a luminosity-line-width template corresponding to a Hubble constant of $86 \text{ km s}^{-1} \text{ Mpc}^{-1}$ (Pierce, 1994).

4.6 Future applications of the expanding photosphere method

The previous chapters show that EPM is very labor-intensive and that great care must be exercised to avoid biases. For this specific purpose I implement various methods and techniques in order to obtain objective and less-of-an-art results. These methods involve 1) the subtraction of the host galaxy from the SN images in order to avoid biases in the SN magnitudes, 2) the computation of synthetic magnitudes in a well-defined photometric system to minimize biases in the derived angular radii, 3) the measurement of true photospheric velocities from cross-correlating SN spectra and atmosphere models, 4) the use of a model to interpolate observed velocities to the time of the photometric observations that avoids fitting artifacts and incorrect results, 5) the estimate of extinction by dust in the host galaxies using the SN color curves, and 6) a model to estimate uncertainties in the resulting EPM distances.

Despite this effort to lend credence to the method, EPM shows other weaknesses owing to the limited time over which the dilution factors work properly, particularly as the photosphere approaches the temperature of H recombination. In my experience the EPM lifetime of the SNe of my sample is partly shortened by the need to extrapolate dilution factors to temperatures lower than those encompassed by the models of E96. I show examples, however, where the method breaks down without extrapolations. To get around these difficulties a careful inspection of the results is needed and a personal judgment is required. To improve this situation it will be necessary in the future to expand the

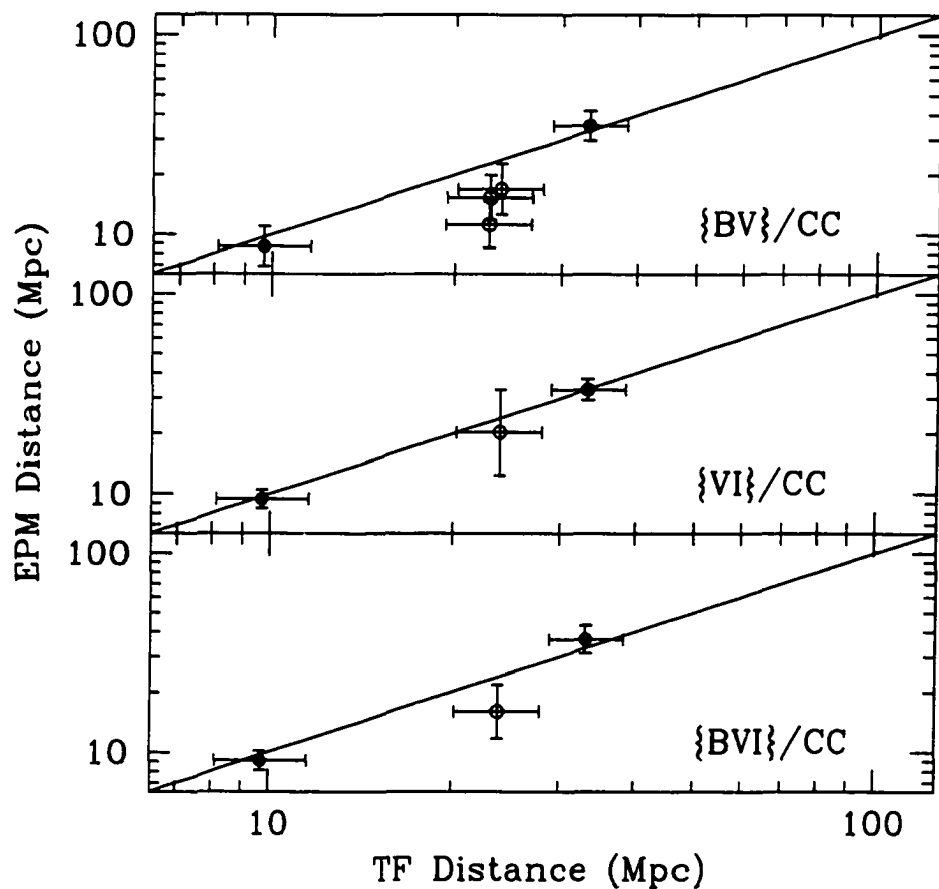


Figure 4.5: Comparison between EPM and Tully-Fisher distances measured by Pierce (1994) (open circles) and Giovanelli (2001) (filled circles). The ridge lines show $D_{EPM}=D_{TF}$.

grid of atmosphere models and dilution factors to lower temperatures, and examine their sensitivity to parameters representative of SN 1987A-like events in order to determine the range of applicability of the method.

The EPM analysis of the 17 SNe leaves us with some lessons that should be considered in the future to optimize the observations and the results. First, the observations must begin early (~ 1 week) after explosion in order to better constrain the EPM solution and avoid extrapolating dilution factors in temperature or poor performance of such factors at low temperatures. Given the very successful ongoing SN surveys, the prompt discovery of SNe happens routinely nowadays, thus offering a great advantage to EPM. Second, a baseline of 60 days is needed to properly constrain the EPM solution. Otherwise the solution can be seriously biased. A minimum of two spectra are required to obtain a solution, but the optimum sampling is one spectrum every five nights. Photometric observations do not have to be obtained each night but it is very important to obtain simultaneous photometry and spectroscopy in order to avoid velocity interpolations. Even poorly sampled light curves do not seem to be a problem. I can check this by randomly drawing three data points from the $\{V\}$ dataset for SN 1999em. From 100 realizations the computed distances is within 10% of the distance derived from the entire dataset (on average). For five data points the distribution of distances has an rms of 6% around the mean, while for ten points the rms drops to only 4%. This implies that poorly-sampled light curves can yield precise distances, as long as the spacing in time is reasonable. The $\{V\}$ subset offers the best advantages for EPM because: it is less sensitive to metallicity effects; it yields the best agreement with the Cepheid scale; and it has the least sensitivity to the effects of dust. Future studies should give priority to observations through V and I .

The analysis of the Hubble diagram of SNe II shows that the typical error in the distance from an individual filter subset is 20%, which proves larger than the 16% of the Tully-Fisher method (Giovanelli et al., 1997) and certainly far greater than the 7% of

SNe Ia (Hamuy et al., 1996; Phillips et al., 1999). Compared to the precision yielded by SNe Ia, it will be necessary to obtain $10 \times$ more SN II distances to reach the same level of precision in distance. For the particular purpose of checking the cosmological results yielded by SNe Ia, it will be necessary to discover and observe SNe II at the maximum possible redshift (Wagoner, 1977). For a typical SN II on the plateau with $M_V = -17.5$ (see chapter 5) the apparent magnitude at $z=0.3$ should be ~ 23 , which nowadays is clearly possible with 8-m class telescopes. The limiting factor, indeed, is the need to obtain spectroscopic data. The CC technique offers the possibility to estimate photospheric velocities from lower S/N spectra, thus extending the potential of EPM to high redshifts where high-quality spectra are difficult to obtain. If such velocities could be obtained at $z=0.3$ it will be necessary to measure 20 SNe II to be able to measure the distance moduli of such objects to a level of precision of 5%. This should provide a robust check on the results of SNe Ia.

4.7 Summary

I presented a detailed discussion about the performance of EPM. I carried out an analysis of the internal errors, including sources of random and systematic uncertainties. Then I performed an assessment of the accuracy of the method from a comparison to other methods. I summarized the pros and cons of EPM and discussed the strategies to optimize the results from future observations and the prospects to apply the method to high- z SNe.

Table 4.1: Summary of EPM distances

SN	Filter	Vel.	D	Stat.	ζ	Vel.	$\frac{d\ln D}{dA_{host}(V)}$	$A_{host}(V)$	Total
	Subset	Curve	(Mpc)	Error	Error	Error		Error	Error (Mpc)
1986L	{BV}	CC	11.2	2%	14%	12%	-0.55	17%	3 (25%)
1987A	{BV}	Fe	0.032	1%	14%	12%	-0.22	7%	0.006 (20%)
1987A	{BV}	CC	0.037	2%	14%	12%	-0.22	7%	0.007 (20%)
1987A	{VI}	Fe	0.036	1%	14%	12%	-0.18	5%	0.007 (19%)
1987A	{VI}	CC	0.043	1%	14%	12%	-0.19	6%	0.008 (19%)
1987A	{BVI}	Fe	0.039	2%	14%	12%	-0.30	9%	0.008 (21%)
1987A	{BVI}	CC	0.046	2%	14%	12%	-0.30	9%	0.009 (21%)
1987A	{JHK}	Fe	0.028	2%	14%	12%	+0.50	15%	0.007 (24%)
1987A	{JHK}	CC	0.034	3%	14%	12%	+0.50	15%	0.008 (24%)
1988A	{BV}	Fe	23.8	9%	14%	12%	-0.41	12%	6 (24%)
1988A	{BV}	CC	15.3	16%	14%	12%	-0.45	14%	4 (28%)
1990E	{BV}	Fe	17.8	8%	11%	12%	-0.58	17%	4 (25%)
1990E	{BV}	CC	16.9	15%	13%	12%	-0.58	17%	5 (29%)
1990E	{VI}	Fe	21.3	14%	11%	12%	-1.42	43%	10 (48%)
1990E	{VI}	CC	20.3	22%	13%	12%	-1.36	41%	10 (50%)
1990E	{BVI}	Fe	17.8	9%	11%	12%	-0.45	14%	4 (23%)
1990E	{BVI}	CC	16.0	19%	13%	12%	-0.48	14%	5 (29%)
1992am	{BV}	Fe	206.0	17%	11%	12%	-0.61	18%	61 (30%)
1992am	{BV}	CC	230.1	16%	16%	12%	-0.53	16%	69 (30%)
1992am	{VI}	Fe	171.6	15%	11%	12%	-0.50	15%	46 (27%)
1992am	{VI}	CC	179.7	17%	16%	12%	-0.62	19%	58 (32%)
1992am	{BVI}	Fe	168.4	10%	11%	12%	-0.80	24%	52 (31%)
1992am	{BVI}	CC	175.5	11%	16%	12%	-0.89	27%	62 (35%)
1992ba	{BV}	Fe	23.3	7%	6%	12%	-0.52	16%	5 (22%)
1992ba	{BV}	CC	23.2	5%	5%	12%	-0.46	14%	5 (20%)

Table 4.1: EPM distances – continued

SN	Filter	Vel.	D	Stat.	ζ	Vel.	$\frac{d\ln D}{dA_{host}(V)}$	$A_{host}(V)$	Total
	Subset	Curve	(Mpc)	Error	Error	Error	Error	Error	Error (Mpc)
1992ba	{VI}	Fe	21.0	6%	6%	12%	-0.27	8%	4 (17%)
1992ba	{VI}	CC	21.5	5%	5%	12%	-0.20	6%	3 (15%)
1992ba	{BVI}	Fe	23.3	6%	6%	12%	-0.59	18%	5 (23%)
1992ba	{BVI}	CC	23.4	4%	5%	12%	-0.50	15%	5 (20%)
1993A	{BV}	Fe	160.5	12%	18%	12%	-0.52	16%	47 (29%)
1993A	{BV}	CC	194.5	12%	19%	12%	-0.53	16%	59 (30%)
1993A	{VI}	Fe	227.5	14%	18%	12%	-0.99	30%	90 (40%)
1993A	{VI}	CC	282.9	16%	19%	12%	-1.01	30%	115 (41%)
1993A	{BVI}	Fe	184.3	8%	18%	12%	-0.46	14%	50 (27%)
1993A	{BVI}	CC	224.5	9%	19%	12%	-0.48	14%	63 (28%)
1999br	{BV}	Fe	18.2	7%	7%	12%	-0.33	10%	3 (18%)
1999br	{BV}	CC	11.7	5%	4%	12%	-0.32	10%	2 (17%)
1999br	{VI}	Fe	17.0	5%	7%	12%	-0.23	7%	3 (16%)
1999br	{VI}	CC	11.0	5%	4%	12%	-0.14	4%	2 (14%)
1999br	{BVI}	Fe	19.6	6%	7%	12%	-0.42	13%	4 (20%)
1999br	{BVI}	CC	12.1	6%	4%	12%	-0.33	10%	2 (17%)
1999br	{VZ}	Fe	19.5	6%	7%	12%	-0.33	10%	4 (18%)
1999br	{VZ}	CC	12.1	6%	4%	12%	-0.21	6%	2 (15%)
1999cr	{BV}	Fe	72.0	10%	19%	12%	-1.32	40%	34 (47%)
1999cr	{BV}	CC	71.5	10%	16%	12%	-1.28	38%	32 (44%)
1999cr	{VI}	Fe	101.0	31%	19%	12%	-0.37	11%	40 (40%)
1999cr	{VI}	CC	95.1	19%	16%	12%	-0.32	10%	28 (29%)
1999cr	{BVI}	Fe	74.7	6%	19%	12%	-0.73	22%	24 (32%)
1999cr	{BVI}	CC	74.0	6%	16%	12%	-0.70	21%	22 (30%)
1999eg	{BV}	Fe	83.6	11%	10%	12%	-0.84	25%	26 (31%)

Table 4.1: EPM distances – continued

SN	Filter	Vel.	D	Stat.	ζ	Vel.	$\frac{d\ln D}{dA_{host}(V')}$	$A_{host}(V')$	Total
Subset	Curve	(Mpc)	Error	Error	Error	Error	Error	Error (Mpc)	
1999eg	{BV}	CC	120.8	16%	12%	12%	-0.95	29%	45 (37%)
1999eg	{VI}	Fe	74.3	12%	10%	12%	-0.28	8%	16 (21%)
1999eg	{VI}	CC	117.2	19%	12%	12%	-0.36	11%	33 (28%)
1999eg	{BVI}	Fe	68.4	8%	10%	12%	-0.61	18%	17 (25%)
1999eg	{BVI}	CC	96.5	10%	12%	12%	-0.71	21%	28 (29%)
1999em	{BV}	Fe	9.5	2%	7%	12%	-0.43	13%	2 (19%)
1999em	{BV}	CC	8.7	3%	7%	12%	-0.33	10%	2 (17%)
1999em	{VI}	Fe	10.1	2%	7%	12%	-0.17	5%	2 (15%)
1999em	{VI}	CC	9.4	4%	7%	12%	-0.02	1%	1 (14%)
1999em	{BVI}	Fe	10.1	2%	7%	12%	-0.44	13%	2 (19%)
1999em	{BVI}	CC	9.1	3%	7%	12%	-0.26	8%	1 (16%)
1999em	{VZ}	Fe	10.9	3%	7%	12%	-0.24	7%	2 (16%)
1999em	{VZ}	CC	9.9	3%	7%	12%	-0.05	2%	1 (14%)
1999em	{VJ}	Fe	10.9	2%	7%	12%	+0.23	7%	2 (16%)
1999em	{VJ}	CC	10.5	4%	7%	12%	+0.27	8%	2 (17%)
1999em	{VH}	Fe	10.6	2%	7%	12%	+0.27	8%	2 (16%)
1999em	{VH}	CC	10.2	4%	7%	12%	+0.28	8%	2 (17%)
1999em	{VK}	Fe	11.2	2%	7%	12%	+0.16	5%	2 (15%)
1999em	{VK}	CC	10.5	4%	7%	12%	+0.25	8%	2 (17%)
1999em	{JHK}	Fe	11.8	4%	7%	12%	+0.47	14%	2 (20%)
1999em	{JHK}	CC	10.5	4%	7%	12%	+0.47	14%	2 (20%)
2000cb	{BV}	Fe	34.0	4%	8%	12%	-0.24	7%	6 (17%)
2000cb	{BV}	CC	35.4	3%	5%	12%	-0.31	9%	6 (16%)
2000cb	{VI}	Fe	30.7	3%	8%	12%	-0.03	1%	5 (15%)
2000cb	{VI}	CC	33.2	3%	5%	12%	-0.02	1%	4 (13%)

Table 4.1: EPM distances – continued

SN	Filter	Vel.	D	Stat.	ζ	Vel.	$\frac{d\ln D}{dA_{host}(V)}$	$A_{host}(V)$	Total
	Subset	Curve	(Mpc)	Error	Error	Error	Error	Error	Error (Mpc)
2000cb	{BVI}	Fe	35.7	4%	8%	12%	-0.36	11%	7 (19%)
2000cb	{BVI}	CC	36.9	4%	5%	12%	-0.34	10%	6 (17%)
2000cb	{BVI}								

Table 4.2: Distances from Other Sources

SN	cz_{CMB} $\pm 300 \text{ km s}^{-1}$	$D(\text{S94})$ (Mpc)	$D(\text{Cepheids})$ (Mpc)	$D(\text{Tully-Fisher})$ (Mpc)
1986L	1293	16.0(2.0)	...	22.7(3.7) ^a
1987A	0.050(0.003)	...
1988A	1842	20.0(3.0)	...	22.8(3.7) ^a
1990E	1023	18.0(2.5)	...	23.8(3.8) ^a
1990K	1303	20.0(5.0)	...	27.5(4.4) ^a -30.5(4.3) ^b
1991al	4484
1992af	5438	55.0(22.5)
1992am	14009	180.0(30.0)
1992ba	1165	14.0(1.5)
1993A	8933
1993S	9649
1999br	1292
1999ca	3105	29.1(7.3) ^b
1999cr	6376
1999eg	6494
1999em	669	9.7(1.7) ^b
2000cb	2038	33.4(4.8) ^b

^ataken from Pierce (1994), and transformed to TF scale of Giovanelli et al. (1997)^bGiovanelli (2001)

CHAPTER 5 ON THE INTRINSIC PROPERTIES OF TYPE II SUPERNOVAE

5.1 Introduction

In this chapter I use the photometric/spectroscopic database for the 17 SNe with the purpose to compare intrinsic properties of these objects. I begin with a comparison of the absolute V magnitudes. Then I proceed to derive calibrations for bolometric corrections and effective temperatures from BVI magnitudes and colors, which permit me to convert the observed optical light curves of SNe II-P into bolometric luminosities and effective temperatures. Despite the widely different light curve morphologies displayed by SNe II-P, some regularities emerge. This analysis suggests that, even though SNe II-P encompass a range of ~ 4 magnitudes in plateau luminosities, these objects can be used as standard candles, provided their apparent magnitudes are corrected for expansion velocities.

5.2 Absolute magnitudes

In order to compare the SNe against each other it first proves necessary to place them at the same distance. Even though EPM provides distance estimates to these objects, below I adopt the more precise values derived from the CMB redshifts (listed in Table 4.2) and the currently best estimate of $65 \text{ km s}^{-1} \text{ Mpc}^{-1}$ for the Hubble constant from Cepheids/SNe Ia. For SN 1987A, whose redshift is too close to be in the Hubble flow, I use the standard 50 kpc distance, which is consistent with the previous value of H_0 .

Extinction corrections for dust in the Galaxy and the SN host galaxy are also required. I perform such corrections using the visual absorption values given in Tables 2.1 and 3.3,

respectively.

In order to place all SNe in the same time scale, I adopt the time of explosion of each SN, as previously discussed in Chapter 3. In general these times come from the EPM analysis and considerations about the epoch of discovery. Then I divide the resulting SN age by the $(1+z)$ to transform it to the SN rest-frame.

Since SNe II have temperatures close to the H recombination value between 5000-6000 K, the peak of the emission is close to the V band, so that the V light curves represent better the bolometric luminosity. Hence, I begin to examine the absolute V light curves, which are shown in Figures 5.1 and 5.2. This comparison reveals a high degree of individuality among these SNe II and a rich variety of light curve morphologies, a remark often cited in the literature (Barbon et al., 1979; Young & Branch, 1989). The plateau phases show increasing, constant or decreasing luminosities. Often, astronomers quote the maximum luminosity for SNe II. Except for SNe 1986L, 1987A, and 2000cb the luminosity evolution of these objects is quite flat so it proves hard to talk about maximum light. A characteristic brightness for the plateau seems more adequate. Among the 17 SNe, there is a wide range between $M_V = -18$ (SN 1992am) and -14 (SN 1999br). It is interesting to note that, among the eight objects with sufficient data, the end of the plateau seemed to happen at about the same age near 110 days. Perhaps SN 1992am showed a somewhat longer plateau.

The exponential tails were all consistent with the same decline rate near 0.01 mag day $^{-1}$, which can be interpreted as due to the radioactive decay of ^{56}Co . The luminosity of the tails were not consistent with a single value for all objects, thus challenging the idea that these objects all synthesize the same amount of ^{56}Co (Patat et al., 1994).

For the comparison of observations and theoretical models it is necessary to convert the observed fluxes and colors into bolometric luminosities and effective temperatures, respectively. The bolometric luminosity can be used to obtain the energy release in the

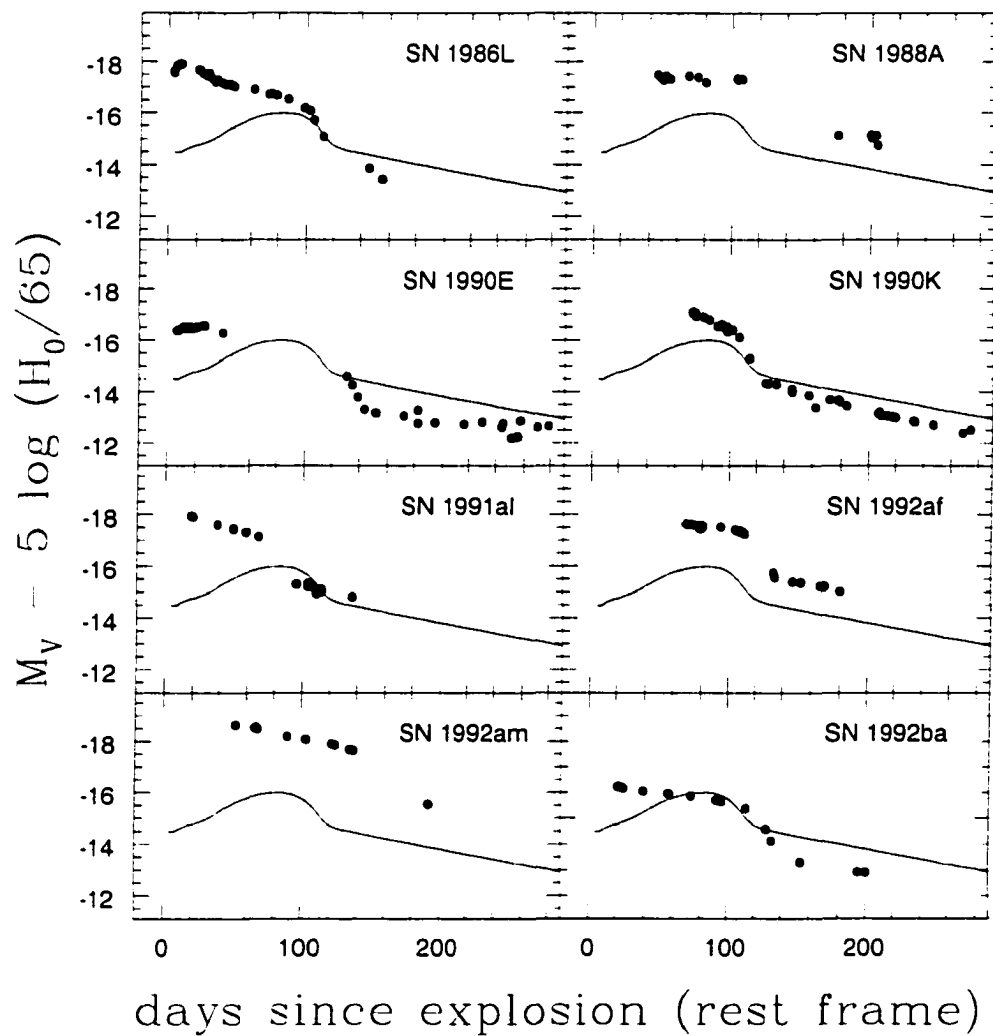


Figure 5.1: Absolute V light curves of SNe II (part 1). For comparison, the light curve of SN 1987A is included as the solid line in all panels.

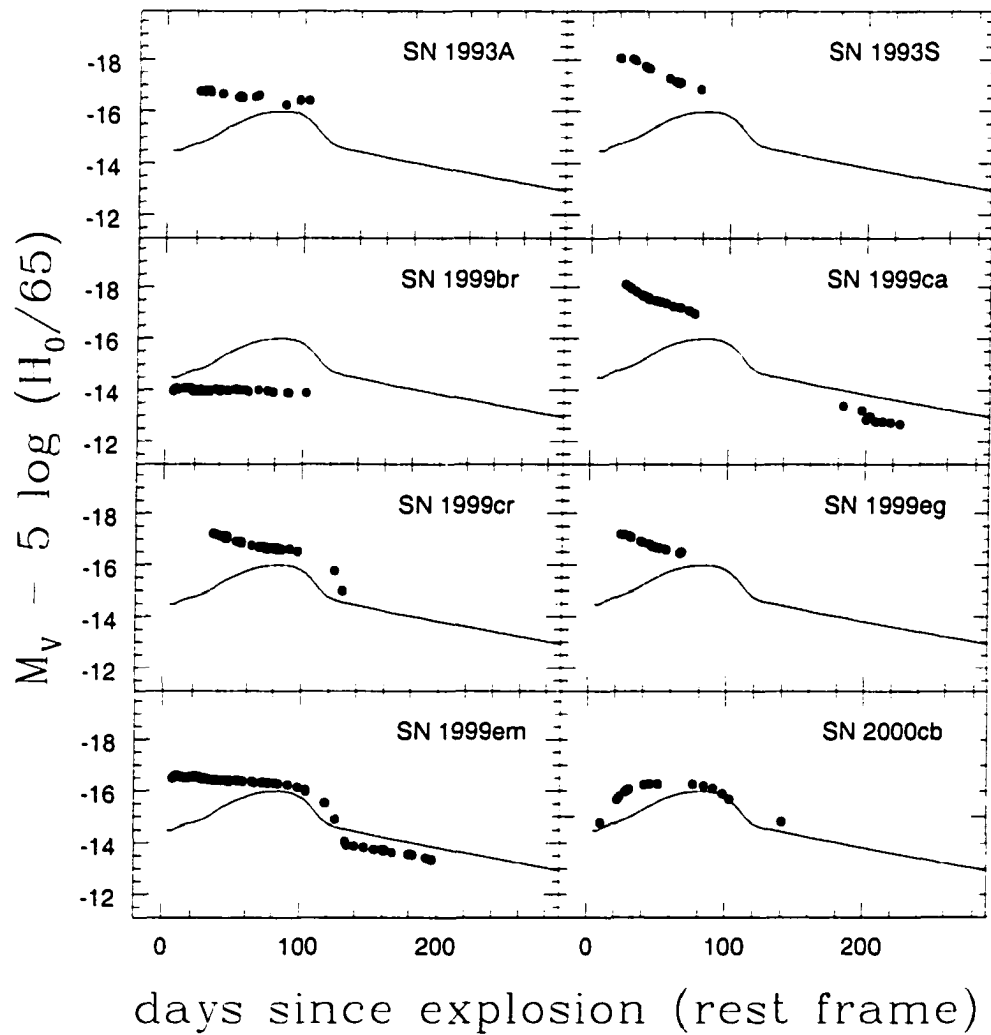


Figure 5.2: Absolute V light curves of SNe II (part 2). For comparison, the light curve of SN 1987A is included as the solid line in all panels.

form of radiation which is determined by the explosion energy and the properties of the progenitor's envelope. The temperature is also related to these parameters and tells us how the spectrum changes over time. Next I discuss methods to derive such quantities from optical data.

5.3 Bolometric corrections

By definition, the bolometric luminosity is the integration of the flux over all frequencies. In practice this is very hard to get because the observations are limited to a few filters. There are only two SNe II with good wavelength and time coverage of the light curves: SNe 1987A and 1999em. This pair of objects afford a great opportunity to examine if a bolometric correction for the V^* filter can be derived from the optical colors, so that we can apply it to other SNe with optical observations alone.

For this pair of SNe I begin by computing their apparent bolometric magnitudes by fitting at each epoch Planck functions to the reddening-corrected BV^*IJHK^* magnitudes. If T_{BK} and θ_{BK} are the color temperature and angular radius of the SN yielded from the best blackbody fit, the bolometric magnitude in the Vega system is,

$$m_{bol} = -2.5 \log_{10} [4 \pi \sigma T_{BK}^4 \theta_{BK}^2] - 8.14. \quad (5.1)$$

Here σ is the Stefan-Boltzmann constant (in cgs units) and -8.14 is the zero point chosen so that the bolometric magnitude of Vega is identically zero. From the bolometric magnitude it is straightforward to compute the bolometric correction, defined as the difference between the bolometric magnitude and the observed V^* magnitude.

$$BC = m_{bol} - [V^* - A_{total}(V^*)]. \quad (5.2)$$

Figure 5.3 shows the corrections derived from the plateau phases of SN 1987A (open circles) and SN 1999em (filled circles), as a function of the $B - V^*$ and $V^* - I$ colors. Also

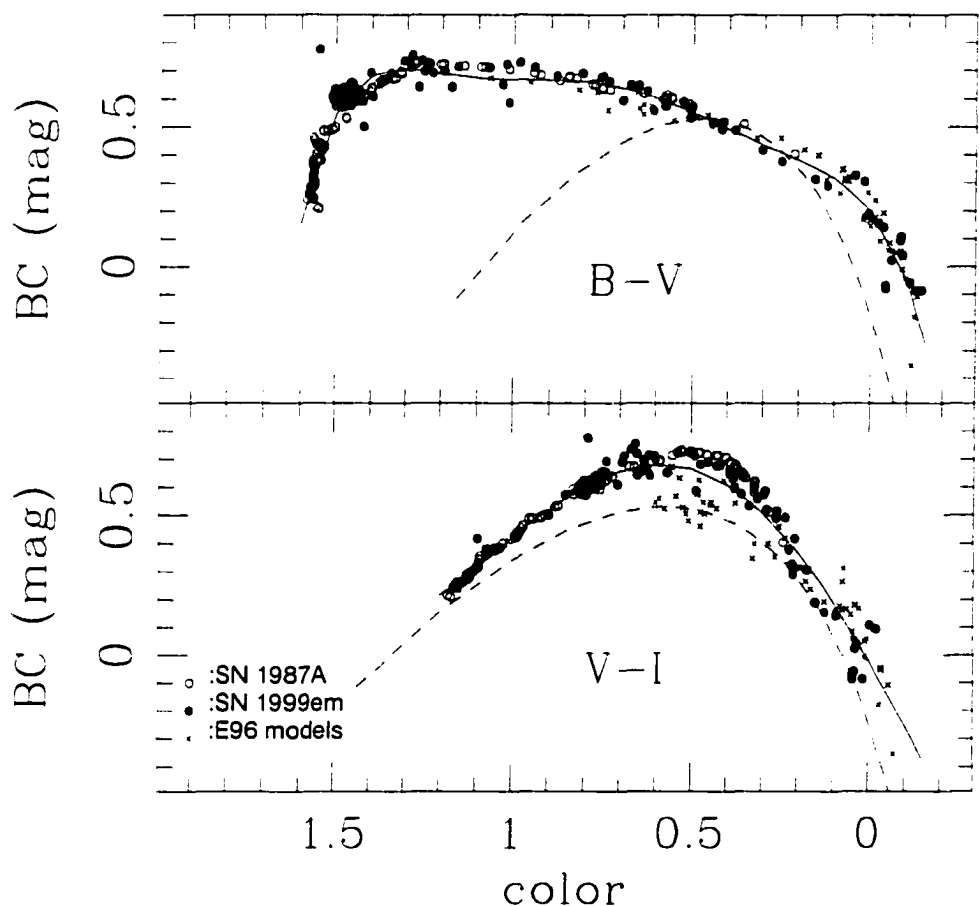


Figure 5.3: Bolometric corrections versus intrinsic color, from the plateau phases of SNe 1987A (open circles), 1999em (filled circles), and the models of E96 (crosses). With solid lines are shown polynomial fits to the points. The dashed curves correspond to bolometric corrections for blackbody spectra.

included in these plots are the corrections measured from the models of E96. These plots reveal a remarkable correlation between BC and intrinsic color, both for the two objects and the models over the entire plateau era. A fair representation of this correlation can be obtained from a polynomial fit of the form,

$$BC(color) = \sum_{i=0}^6 c_i (color)^i. \quad (5.3)$$

The fits, shown with solid lines, are characterized by residuals of only 0.06 mag. In the past it has been customary to transform observed SN magnitudes into bolometric luminosities assuming that SNe have blackbody spectra. Such bolometric corrections are shown as dashed lines in Figure 5.3. Clearly this method works fine when the $V - I$ color is employed, but significant errors can be made if the effective temperature is derived from $B - V$, especially at low temperatures. Most likely, this difference is due to line blanketing in the B band which becomes more pronounced as the photosphere cools down. The coefficients corresponding to the solid lines are given in Table 5.1. and can be applied to any other SN with observations through only two optical filters. With an estimate of the extinction, it is straightforward to deredden the color, get the bolometric magnitude with equation 5.3, and then solve for the bolometric luminosity in erg s^{-1} using the formula,

$$\log_{10} L = \frac{-[V - A_{total}(V) + BC(color)] + 5 \log_{10} D - 8.14}{2.5}. \quad (5.4)$$

where D is the distance to the SN. Combining these equations it is easy to show that L is independent of the arbitrary zero point chosen for the Vega magnitude scale, and that it depends solely on the observed flux density, color, extinction and distance.

The calibration shown in Figure 5.3 is only valid for the optically thick phase and not for the radioactive tail. During the nebular phase I do not find a clear correlation between BC and color. Nevertheless, it is reasonable to use the average of $BC=0.26$ yielded by the two SNe which is characterized by a scatter of 0.06 mag (comparable to that obtained

from earlier epochs).

Figure 5.4 presents the bolometric luminosity of SN 1987A computed with this method for an adopted distance to the LMC of 50 kpc and total visual extinction of 0.465. For comparison is shown with a solid line the uvoir bolometric luminosity obtained by Suntzeff & Bouchet (1990) from the direct integration of the flux between U and M (with the same distance and extinction employed here). The blackbody fits provide a good match to the uvoir values during the plateau phase. On the radioactive tail the differences are the largest and amount to ~ 0.06 dex (15% in energy), which is not unexpected given that the SN spectrum was nebular and the blackbody fit becomes a poor approximation to the SN spectrum. Nonetheless, the match is quite good and the blackbody fit yields a reasonable result.

A similar test can be done with SN 1999em. Figure 5.5 shows the blackbody luminosity of SN 1999em obtained with an adopted distance of 10.3 Mpc and total visual extinction of 0.31. The solid curve corresponds to the direct flux integration between U and K . At early epochs the difference is large owing to the high photospheric temperature and the large fraction of flux emitted shortward of the U band. As the temperature decreases the disagreement drops and by the end of the plateau the methods coincide very closely. Even during the nebular phase when the blackbody is not a good representation of the spectrum, the agreement is remarkably good. Clearly the blackbody method gives an accurate and useful measurement of the bolometric flux for these SNe and has the potential to be applied to SNe with small wavelength coverage.

5.4 Effective temperature-color relation

To examine the possibility to convert observed broadband colors into effective temperatures I use the model spectra of E96. For this purpose I compute synthetic BVI magnitudes and colors from the models. Figure 5.6 shows the synthetic $B - V$ and $V - I$ color

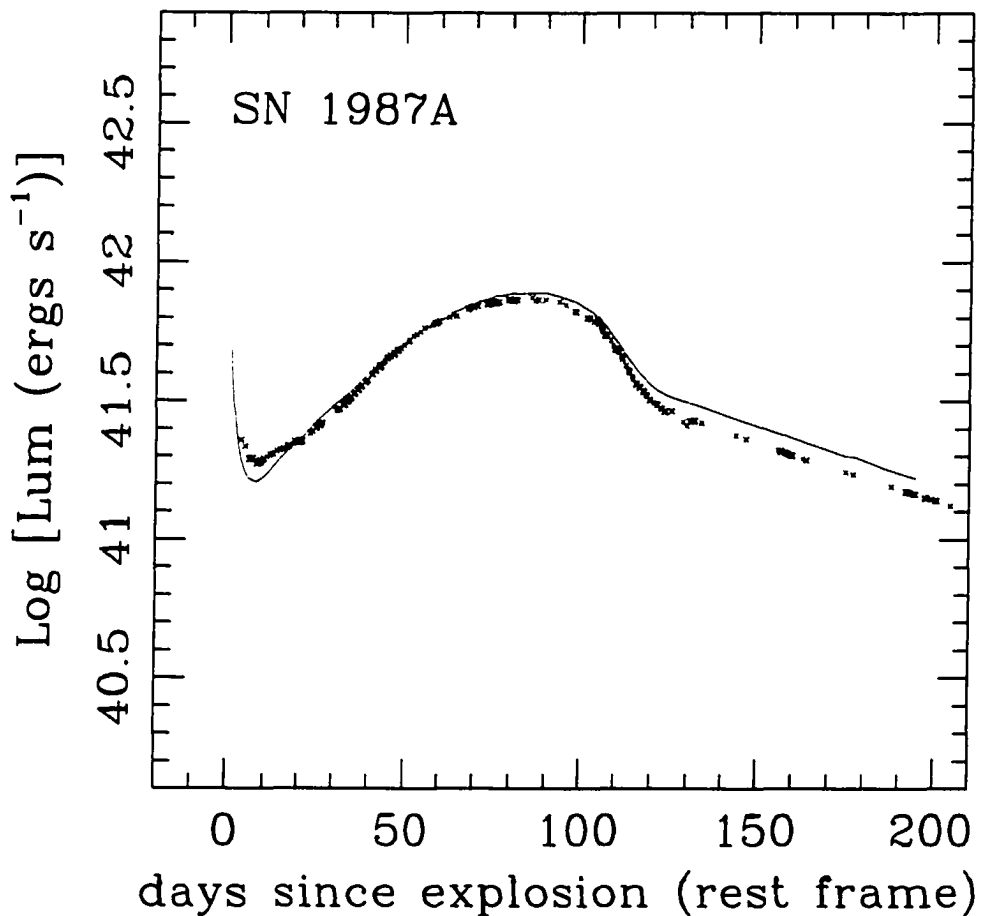


Figure 5.4: The bolometric luminosity of SN 1987A computed from blackbody fits to the $BVIJHK$ photometry (crosses), compared to the direct integration of the flux between U and M obtained by Suntzeff & Bouchet (1990) (solid line).

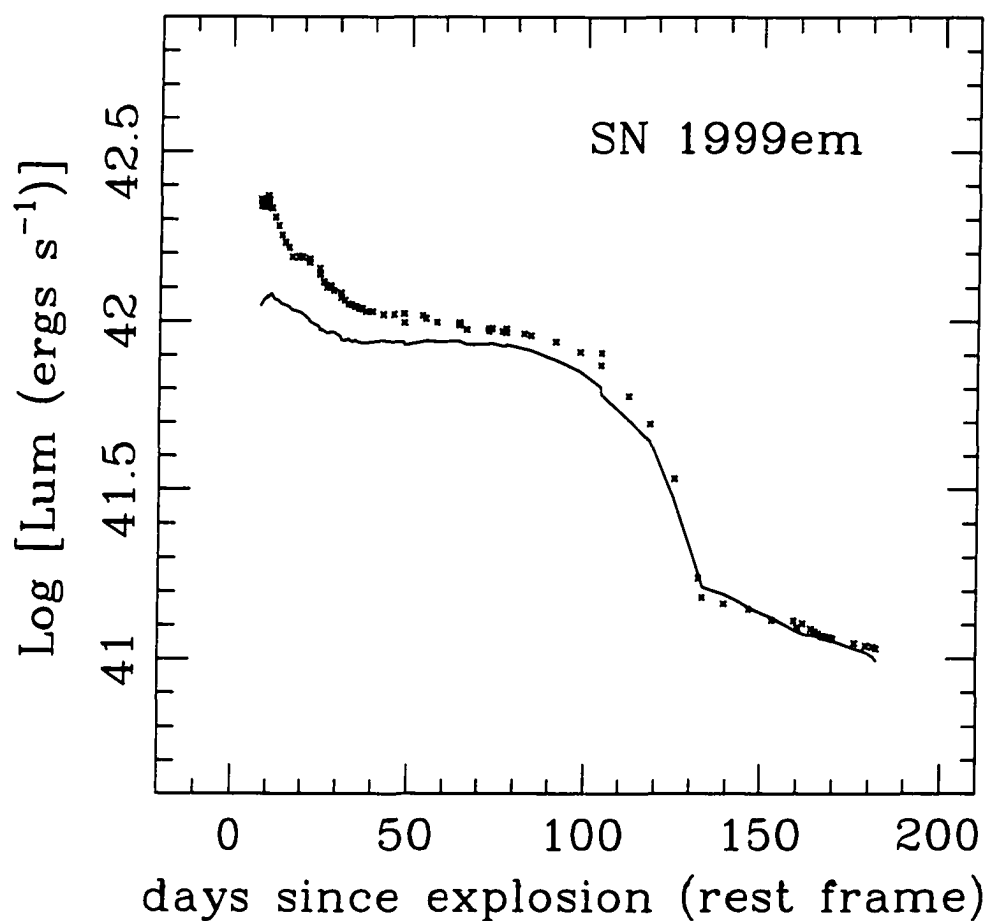


Figure 5.5: The bolometric luminosity of SN 1999em computed from blackbody fits to the BV^*IJHK^* photometry (crosses), compared to the direct integration of the flux between U^* and K^* (solid line).

versus effective temperature. Not surprisingly, there is a reasonable correlation between these quantities which permits me to fit a polynomial of the form,

$$T_{eff}(\text{color}) = \sum_{i=0}^4 c_i (\text{color})^i. \quad (5.5)$$

The fits (shown with solid lines) have a typical scatter of 600 K in T_{eff} and the c_i coefficients are summarized in Table 5.2. Since the models of E96 are only valid for the plateau phase where the spectrum is thermal, these calibrations are not valid for the nebular era.

Kirshner & Kwan (1974) derived a calibration between $B - V$ and photospheric temperature based on a spectrum and color of SN 1969L, which was later used by Arnett & Falk (1976) as a measure of effective temperature for the interpretation of their theoretical light curves. Such calibration is shown as a dotted line in Figure 5.6. Clearly, the use of the blackbody temperature is only a first step toward obtaining the effective temperature and the solid line should be preferred.

5.5 Physical analysis of the plateau phase

Figures 5.7-5.10 present the bolometric light curves and effective temperatures obtained for the 17 SNe. As anticipated from the comparison of the absolute V magnitudes, the radiative output of these SNe is quite different. In the case of SNe 1987A and 2000cb the bolometric flux reached a well-defined maximum several weeks after explosion. For the other cases I observe a plateau where the luminosity remained constant or decreased slowly during several weeks. Apparently, maximum light occurred promptly after shock breakout in these cases, which is the expected behavior in theoretical models that predict a sharp spike in temperature and luminosity. There are ten SNe for which the transition between the plateau and the nebular phase was well observed. It proves interesting to note that the duration of the plateau was nearly the same for all these objects, with a maximum range between 90 and 170 days and strongly peaked about day 110 (although the explo-

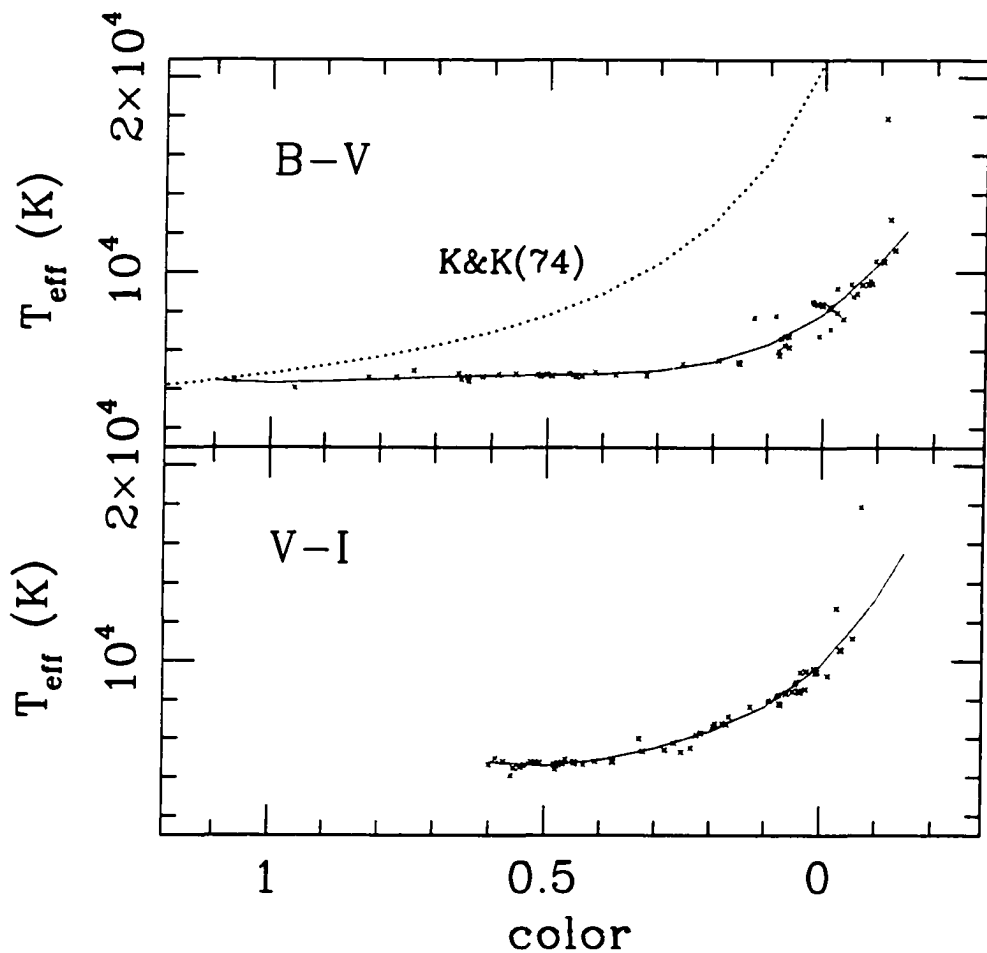


Figure 5.6: T_{eff} versus color from the models of E96 (crosses). With solid lines are shown polynomial fits to the points. The calibration of Kirshner & Kwan (1974) is included as a dotted line.

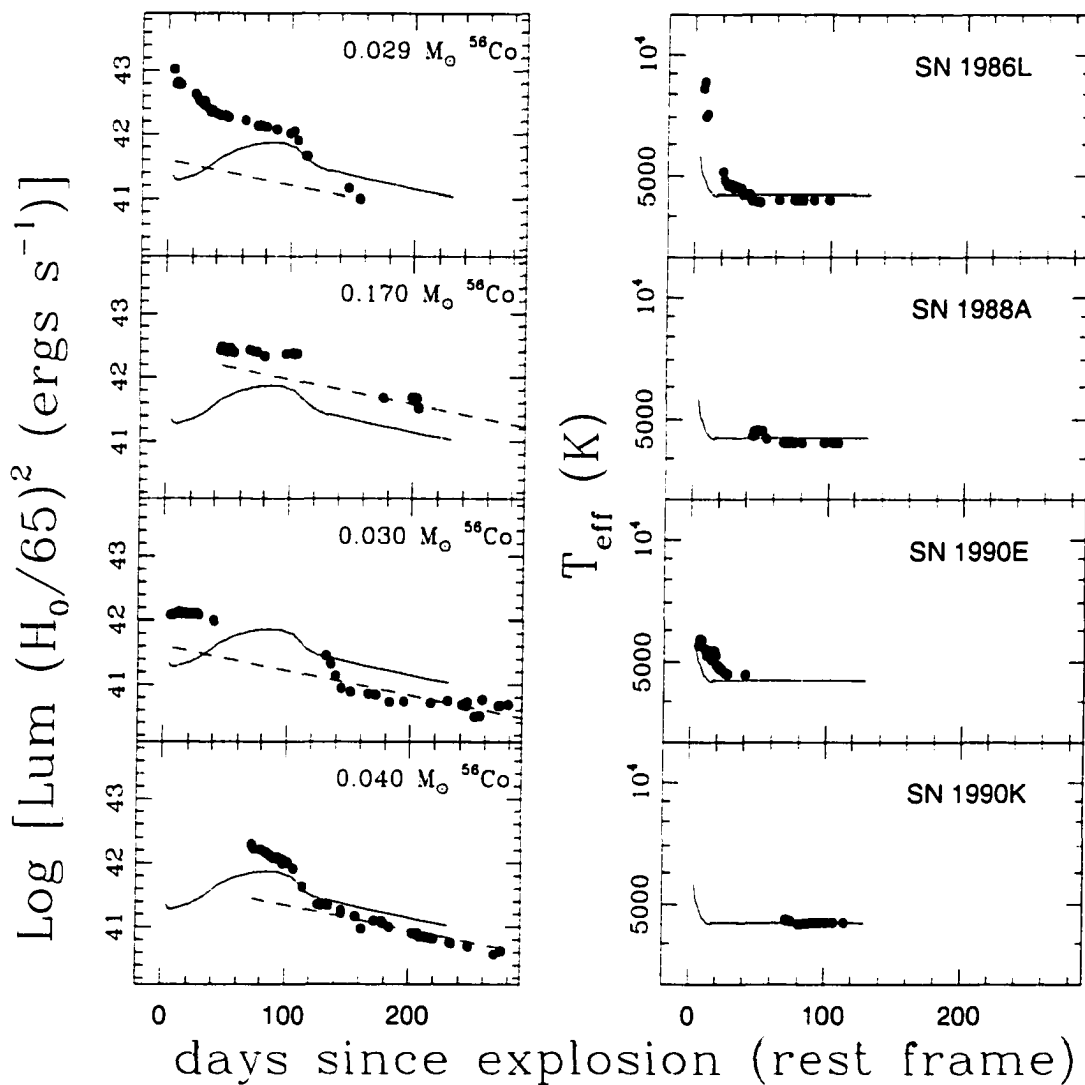


Figure 5.7: Bolometric luminosities (left) and effective temperatures (right) for SNe II, versus time since explosion (part 1). For comparison the luminosities and temperatures for SN 1987A are shown as solid lines. The dashed line corresponds to the luminosity due to radioactive decay of ^{56}Co . The mass required to match the luminosity of the tail is indicated in each case.

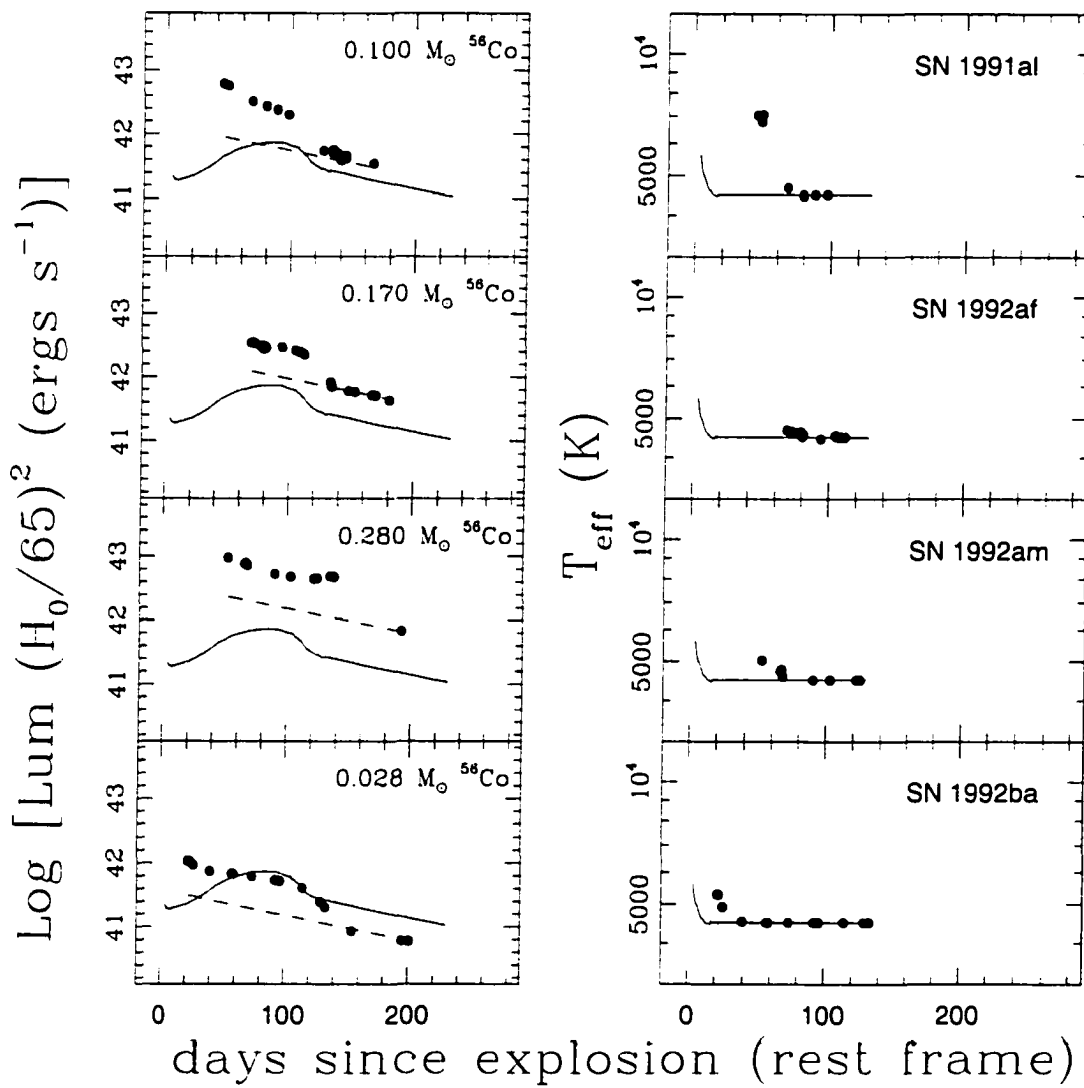


Figure 5.8: Bolometric luminosities (left) and effective temperatures (right) for SNe II, versus time since explosion (part 2). For comparison the luminosities and temperatures for SN 1987A are shown as solid lines. The dashed line corresponds to the luminosity due to radioactive decay of ${}^{56}\text{Co}$. The mass required to match the luminosity of the tail is indicated in each case.

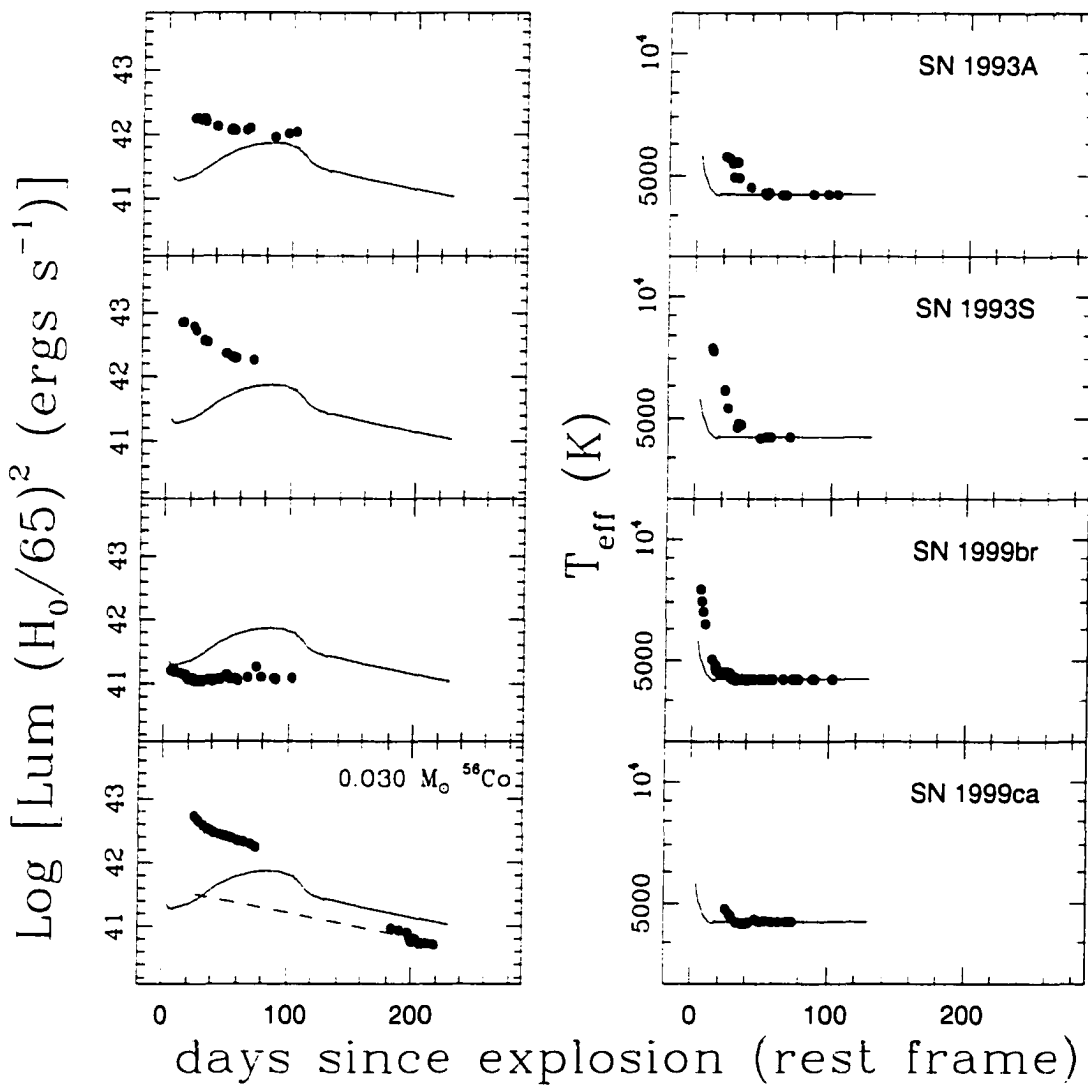


Figure 5.9: Bolometric luminosities (left) and effective temperatures (right) for SNe II, versus time since explosion (part 3). For comparison the luminosities and temperatures for SN 1987A are shown as solid lines. The dashed line corresponds to the luminosity due to radioactive decay of ^{56}Co . The mass required to match the luminosity of the tail is indicated in each case.

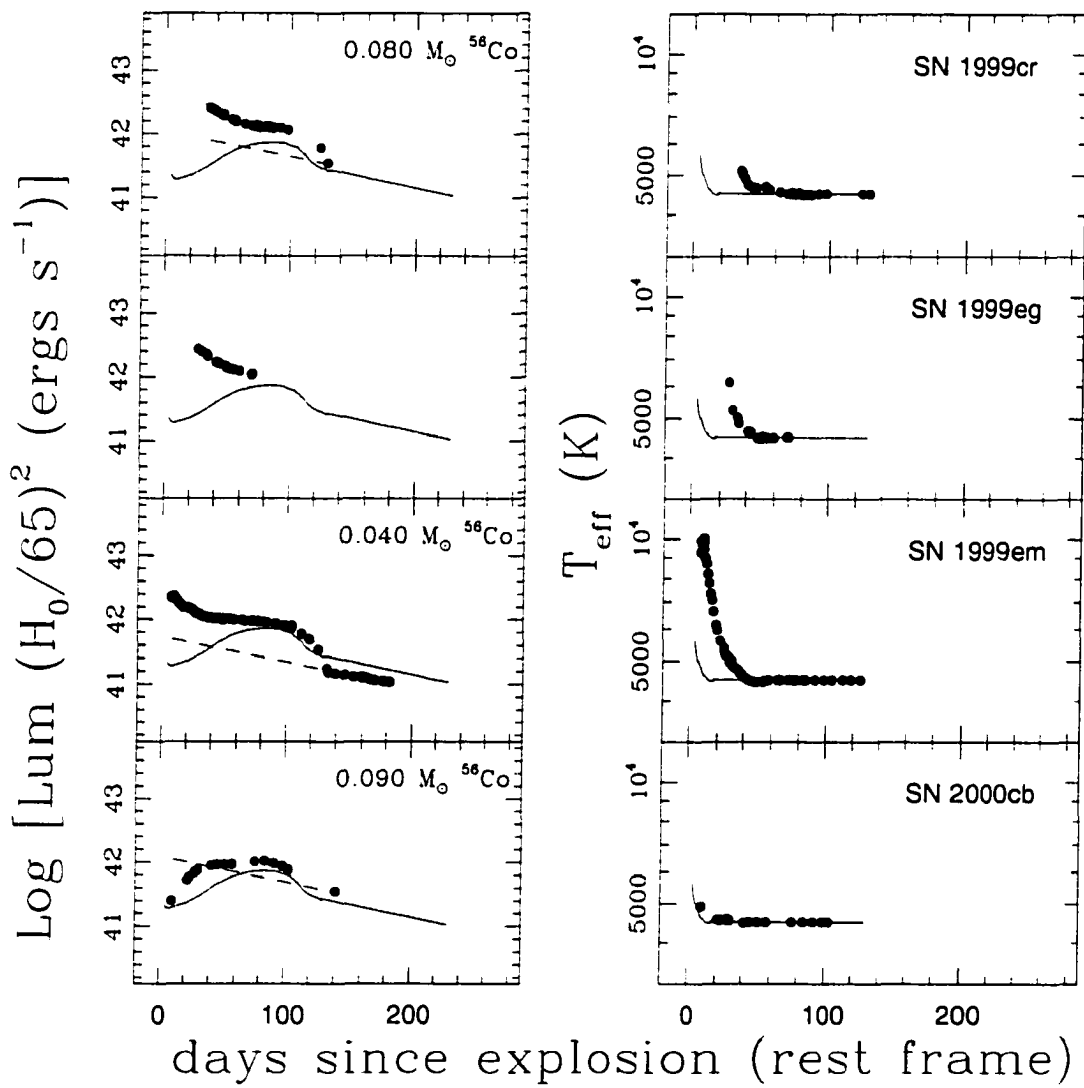


Figure 5.10: Bolometric luminosities (left) and effective temperatures (right) for SNe II, versus time since explosion (part 4). For comparison the luminosities and temperatures for SN 1987A are shown as solid lines. The dashed line corresponds to the luminosity due to radioactive decay of ⁵⁶Co. The mass required to match the luminosity of the tail is indicated in each case.

sion times for SNe 1990K, 1991al, and 1992af are chosen to match the plateau/nebular transition at this age).

The analytical models of Popov (1993) predict that the duration of the plateau phase is given by

$$t_p \propto M^{1/2} R_0^{1/6} E^{-1/6}, \quad (5.6)$$

where E is the explosion energy, R_0 is the initial radius, and M is the envelope mass. The dependence of t_p on E and R_0 is quite weak so that the observation that t_p is approximately constant leads to the conclusion that the envelope mass in this sample of SNe II does not vary much. For an envelope mass of $10 M_{\odot}$ the models predict $t_p=99$ days, in remarkable good agreement with our observed value around 110 days.

The models of Popov (1993) also make predictions for two more observable parameters: the plateau expansion photospheric velocity given by,

$$v_p \propto M^{-1/2} E^{1/2}. \quad (5.7)$$

and the plateau bolometric luminosity,

$$L_p \propto M^{-1/2} R_0^{2/3} E^{5/6}. \quad (5.8)$$

This parameter refers to the maximum bolometric luminosity that occurs promptly after explosion which, as shown in Figures 5.7-5.10, proves hard to measure from this SN sample due to missing data at early epochs. It is more practical, instead, to estimate L_p from the middle of the plateau. Table 5.3 summarizes such luminosities measured at a fiducial epoch (day 50) for the 17 SNe.

Figures 5.11 and 5.12 present comparative mosaics for all SNe that illustrate how the velocity changed with time, as measured from the absorption minimum of Fe II $\lambda 5169$. To facilitate the comparison, I include SN 1987A in each panel as a solid line. Evidently

there was a significant range of expansion rates. To get an estimate of the expansion velocities for these objects, I simply pick the fiducial time used above and I interpolate velocities at day 50. I assign a typical error of 300 km s^{-1} , except for SNe 1990K, 1991al, 1992af, and 1999ca for which I need to perform extrapolations to earlier epochs. In these three cases I assign a larger uncertainty of 2000 km s^{-1} . The results for the 17 SNe are presented in Table 5.3. Note that the v_p parameter defined by Popov refers to the early part of the plateau so it is not directly comparable to the parameters used here.

Figure 5.13 compares the characteristic luminosity and velocity for the plateau phase. A remarkable correlation emerges, in the sense that objects with brighter plateaus expand faster. SN 1992am and SN 1999br appear as extreme objects with high and low velocities, respectively. A weighted least-squares fit yields $v_p \propto L_p^{0.33(\pm 0.04)}$, with a reduced χ^2 of 0.7. Combining equations 5.7 and 5.8, the theoretical models give $v_p \propto L_p^{0.6} R_0^{-0.4}$ for the specific case of constant M (as suggested above), which gives a luminosity dependence $\sim 2 \times$ greater than the observed relation. The dependence of v_p on R_0 can be examined from the two objects with compact progenitors: SNe 1987A and 2000cb. In theory both objects should have higher velocities than SNe with extended progenitors with the same luminosities. Figure 5.13 shows that these SNe lie on opposite sides of the best-fit line, which suggests no obvious dependence of v_p on R_0 . For a fair comparison between theory and observations it will be necessary to derive observable parameters in the middle of the plateau and include radioactive heating in the models, both of which are beyond the scope of this study.

5.6 Physical analysis of the radioactive phase

If all of the γ rays resulting from $^{56}\text{Co} \rightarrow ^{56}\text{Fe}$ are thermalized in the SN interior, the exponential tail provides an estimate of the freshly synthesized ^{56}Co mass and, hence the mass of its parent ^{56}Ni . Here I assume that ^{56}Co decays to ^{56}Fe with a half-life of 77.12

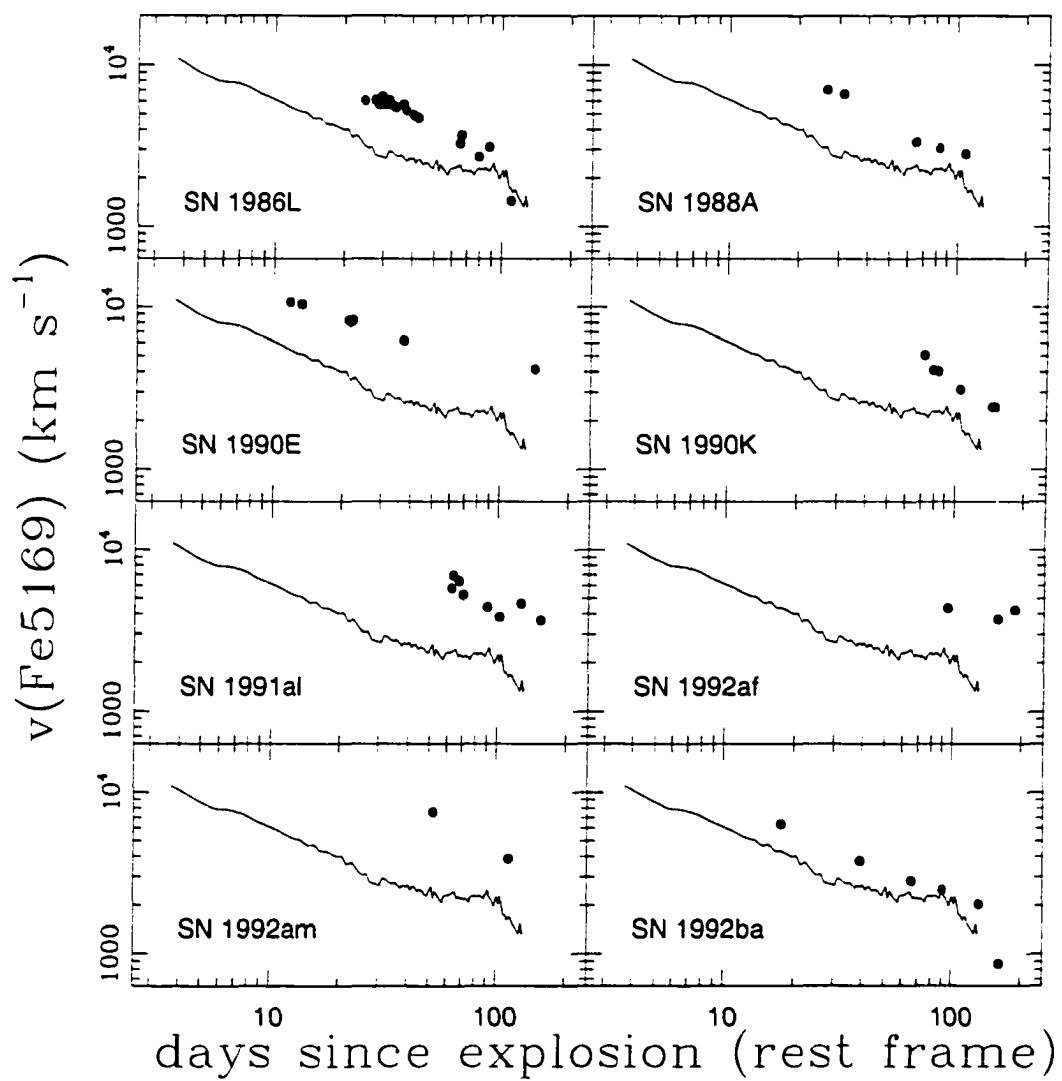


Figure 5.11: Expansion velocities for SNe II derived from the absorption minimum of Fe II $\lambda 5169$, as a function of time (part 1). For comparison, the velocity curve of SN 1987A is shown in each panel with a solid line.

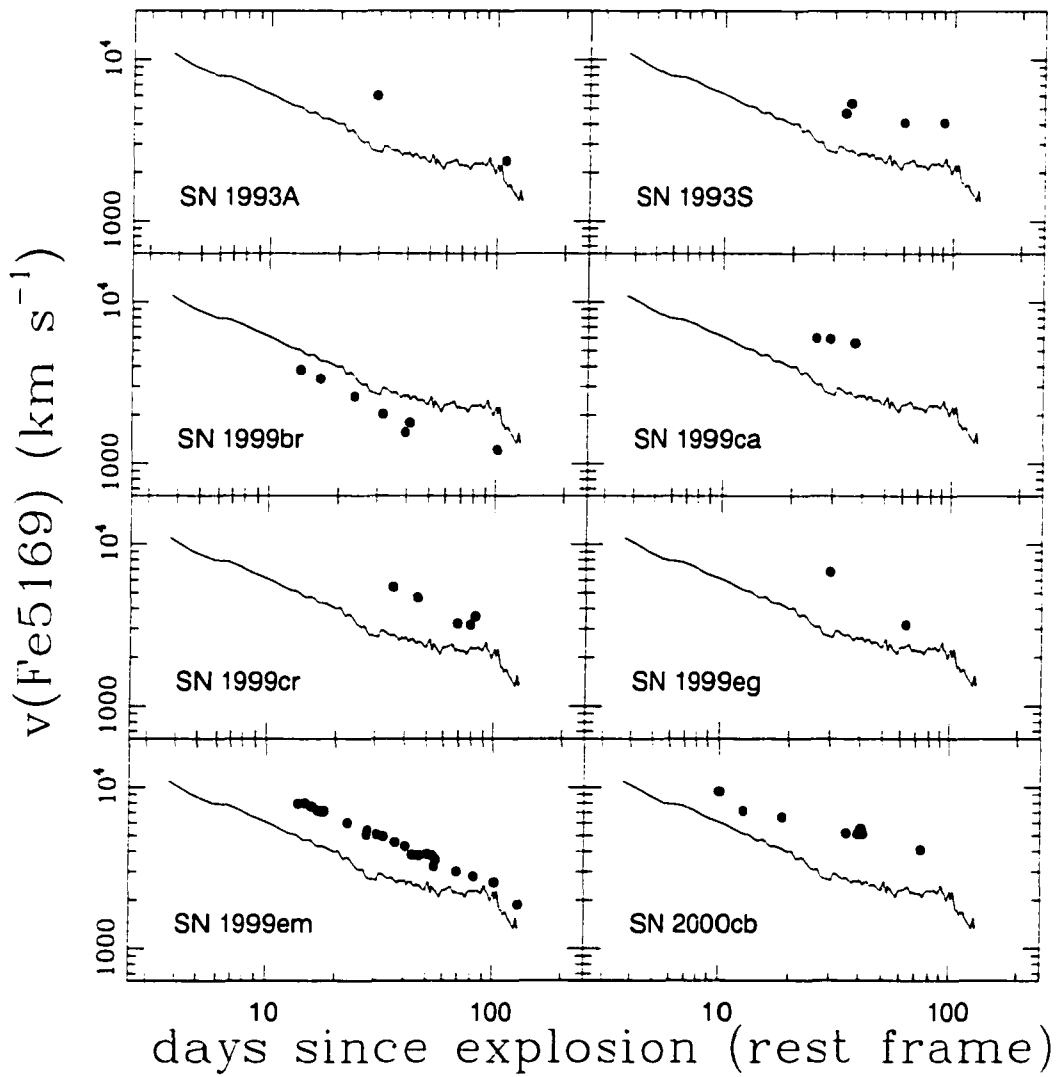


Figure 5.12: Expansion velocities for SNe II derived from the absorption minimum of Fe II $\lambda 5169$, as a function of time (part 2). For comparison, the velocity curve of SN 1987A is shown in each panel with a solid line.

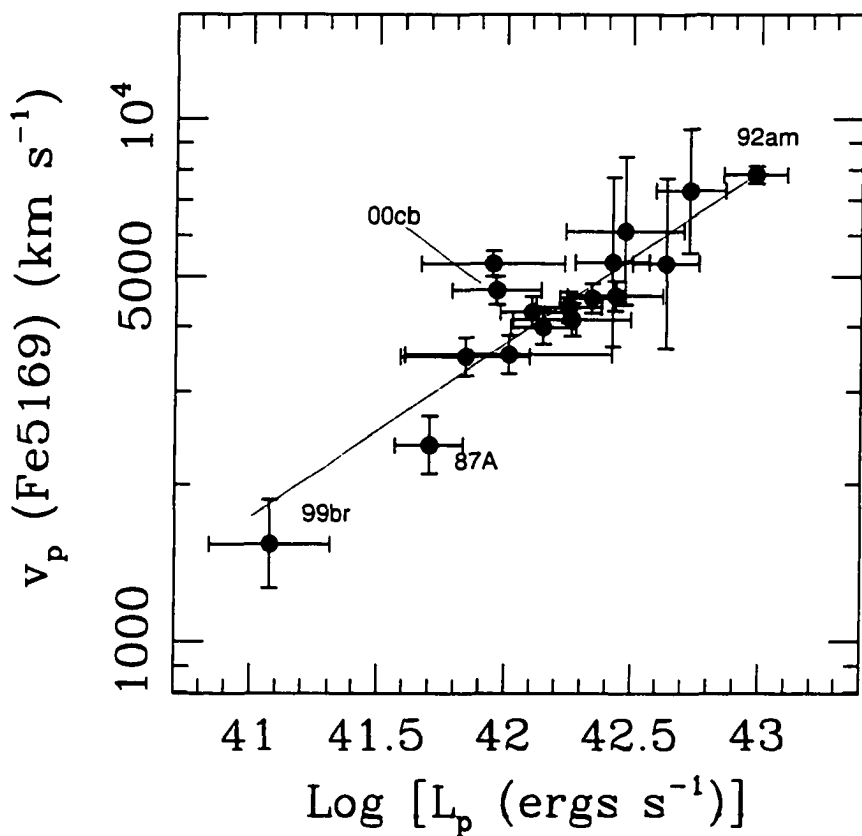


Figure 5.13: Expansion velocities from Fe II $\lambda 5169$ versus bolometric luminosity, both measured in the middle of the plateau (day 50). The ridge line is a weighted fit to the points and corresponds to $v_p \propto L_p^{0.33(\pm 0.04)}$ (with reduced χ^2 of 0.7).

days, and that each decay releases 3.57 MeV in the form of γ -rays (Woosley et al., 1989). It is possible that some of the γ -rays escape without being thermalized, in which case the estimated ^{56}Co must be taken as a lower limit. The dashed lines in Figures 5.7-5.10 give the luminosity due to radioactive heating corresponding to the ^{56}Co mass that yields the best match to the luminosity of the tail. Clearly the late-time decline rates displayed by these SNe are all consistent with the complete thermalization of the γ rays from $^{56}\text{Co} \rightarrow ^{56}\text{Fe}$, at least in the initial phases of the nebular era. For SN 1987A I get $M_{Co}=0.065 M_{\odot}$ if I use the bolometric light curve derived above. If instead, I use the light curve of Suntzeff & Bouchet (1990) I obtain $M_{Co}=0.07 M_{\odot}$, which is identical to their result and an encouraging sanity check. Although the difference is small, for consistency in the comparison with the other SNe, below I use my estimate of M_{Co} .

Table 5.3 summarizes the ^{56}Co masses derived, and Figure 5.14 presents the distribution for the 13 SNe with late-time photometry. This histogram reveals that SNe II produce a wide range of ^{56}Co masses, which challenges previous claims that they all form similar amounts (Benetti et al., 1991). Here I find that most SNe produce less than $0.1 M_{\odot}$ of Co, but there are several examples with $0.15\text{-}0.3 M_{\odot}$.

Among the objects of the sample, SN 1992am was the one with the greatest Co mass. It also had the brightest plateau. On the other end, SN 1999br was characterized by a dim plateau. Although the tail was not observed for this object, it is possible to get an upper limit of $0.02 M_{\odot}$ of Co. This pair of objects suggests that the luminosity of the plateau is correlated with the Co mass. To examine this issue, in Figure 5.15 I compare the plateau luminosity with M_{Co} . Since the Hubble constant and the visual extinction affect both parameters in the same proportion, the comparison should not include uncertainties in these parameters, but just those due to uncertainty in the photometry. Error bars for a typical photometric error of 10% are shown in this figure. There is some evidence that SNe with brighter plateaus produce more Co, although the scatter is larger than the errors,

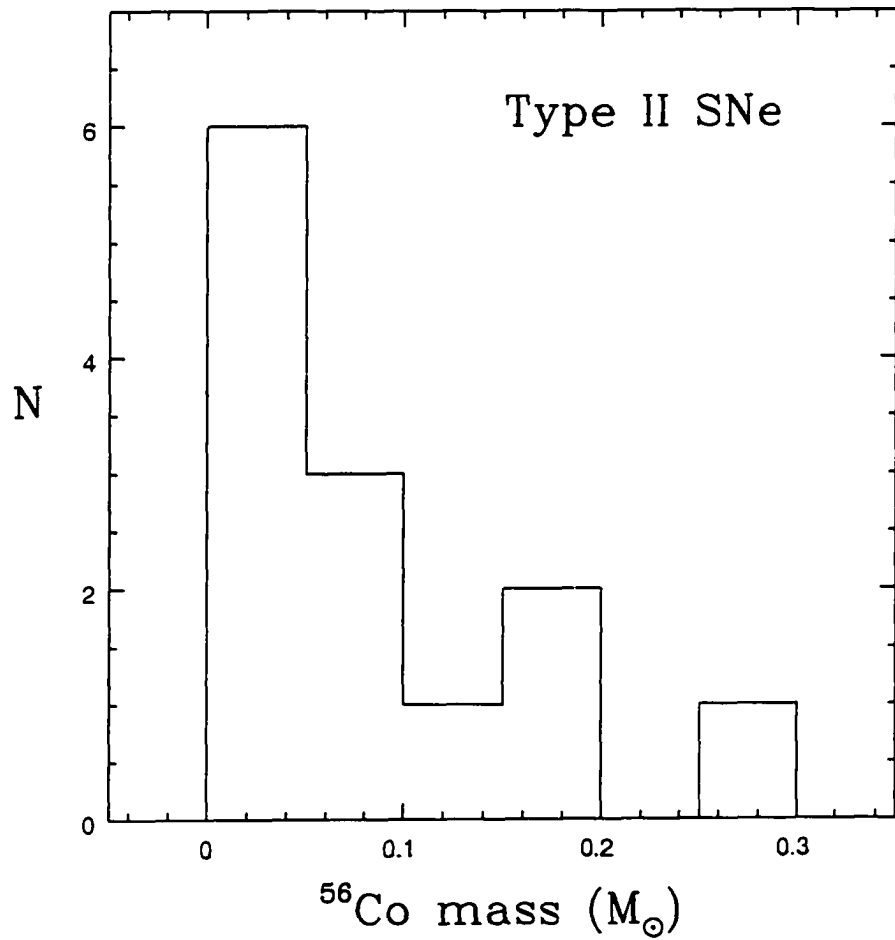


Figure 5.14: The distribution of ^{56}Co masses measured from the brightness of the radioactive tail of the Type II SNe.

thus suggesting that this is not a one parameter family. It is interesting to note that the two SNe with compact progenitors (SNe 1987A and 2000cb) both produced more Co than other SNe with the same luminosities. Figure 5.16 compares the plateau velocity to the Co mass. Again, SNe 1992am and 1999br suggest a trend where faster SNe produce larger amounts of Co, although the scatter is substantial.

In numerical simulations the shock wave generated by the collapse of the core propagates through the star's envelope heating the material and triggering nuclear processing. The production of Ni is confined to the layers just above the core where the temperatures are sufficiently high. Since

$$T \approx \left[\frac{3E}{4\pi R^3 a} \right]^{1/4}. \quad (5.9)$$

the amount of nucleosynthesis is expected to be relatively greater for SNe with smaller progenitors and greater luminosities (Weaver & Woosley, 1980). It is remarkable that this is qualitatively consistent with the behavior shown in Figure 5.15, considering that the amount of observed Ni (the parent of Co) depends on how much of the material located at the bottom of the envelope falls back to the neutron star. Current models do not currently provide physical constraints to this process and the amount of infalling material is freely adjusted via a mass cut parameter, so there is no real theoretical constraint between the explosion energy, initial radius, and Co mass. The observations suggest some connection between these quantities.

5.7 Type II supernovae as standard candles

The tight correlation between plateau luminosities and expansion velocities shown in Figure 5.13 has interesting implications for the use of SNe II-P as standard candles. This correlation implies that the apparent magnitude of a SN must be a function of its expansion velocity and distance. To test this hypothesis I measure plateau V/I magnitudes on day 50

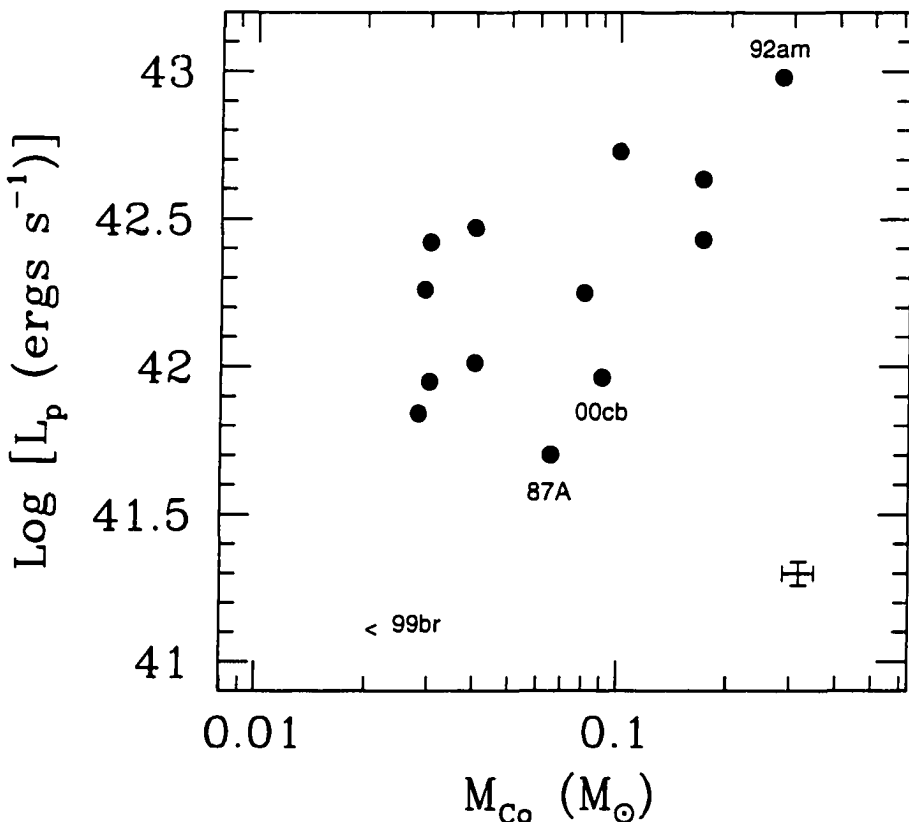


Figure 5.15: The plateau luminosity measured 50 days after explosion, versus the mass of freshly synthesized Co. The upper limit of M_{Co} for SN 1999br is included. Also shown are representative error bars in each quantity, corresponding to 10% uncertainty in the photometry.

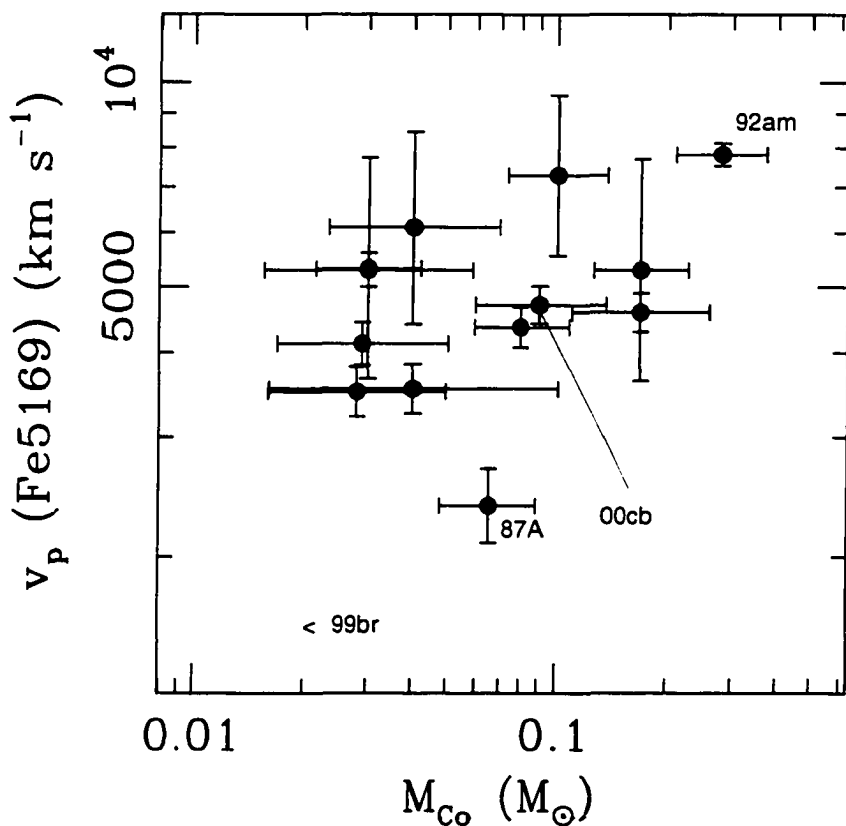


Figure 5.16: Expansion velocities measured from Fe II $\lambda 5169$ in the middle of the plateau (day 50), versus the mass of freshly synthesized Co. The upper limit of M_{Co} for SN 1999br is included.

(listed in Table 5.4) and use them in combination with the Fe 5169 expansion velocities measured above and listed in Table 5.3. In the bottom panel of Figure 5.17 I present the Hubble diagram in the V filter for all SNe of my sample but SN 1987A (which is not in the Hubble flow), and in the top panel I show the same magnitudes after correction for expansion velocities. A least-squares fit yields the following solution,

$$V = A_V + 6.504(\pm 0.995) \log(v_p/5000) = 5 \log(cz) - 1.29(\pm 0.13). \quad (5.10)$$

The scatter drops from 0.99 mag to 0.39 mag, thus demonstrating that the correction for expansion velocities standardizes the luminosities of SNe II significantly. It is interesting to note that most of the spread comes from the nearby SNe which are potentially more affected by peculiar motions of their host galaxies. When I restrict the sample to the eight objects with $z > 2,000 \text{ km s}^{-1}$, the scatter drops to only 0.20 mag. This implies that the standard candle method can produce relative distances with a precision of 9%, which can be compared to the 7% precision yielded by SNe Ia.

Figure 5.18 shows the same analysis but in the I band. In this case the scatter in the raw Hubble diagram is 0.80 mag, which drops to only 0.29 mag after correction for expansion velocities. This is even smaller than the 0.39 spread in the V band, possibly due to the fact that the effects of dust extinction are smaller at these wavelengths. When the eight most distant objects are employed the spread is 0.21 mag, very similar to that obtained from the V magnitudes.

Overall, the standard candle method is characterized by a scatter between 0.39-0.20 mag. Evidently more objects in the Hubble flow are required to pin down the actual precision of this technique. In any case, in its present form the method appears very promising for the determination of cosmological distances. Note also that this precision is better than that yielded by EPM (20% in distance, or 0.43 mag) and the standard candle technique is far less complicated. It only requires a few spectra and photometry around

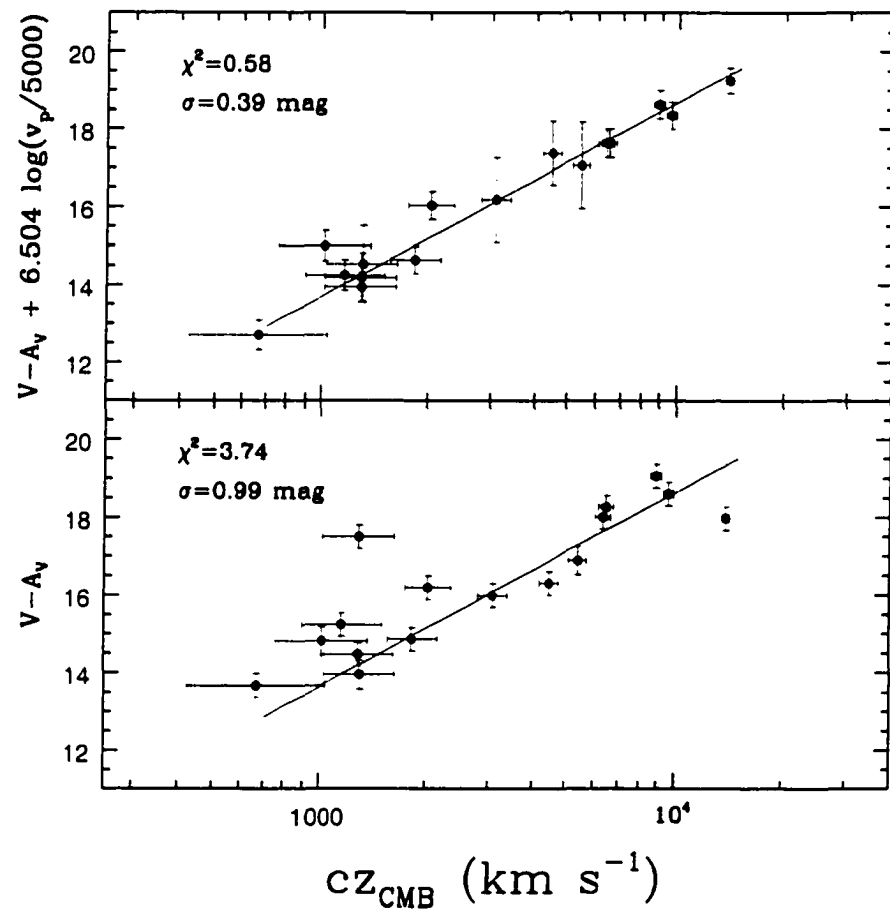


Figure 5.17: (bottom) Raw Hubble diagram from SNe II plateau V magnitudes. (top) Hubble diagram from V magnitudes corrected for expansion velocities.

day 50. A few extra photometric and spectroscopic observations are required during the plateau in order to solve for dust extinction in the host galaxy. The time of explosion is also required. Since the duration of the plateau does not vary much among the different SNe II, it would suffice to get some photometric observations during the plateau/nebular phase transition. Alternatively, an EPM analysis can help at determining t_0 , but this requires early-time observations.

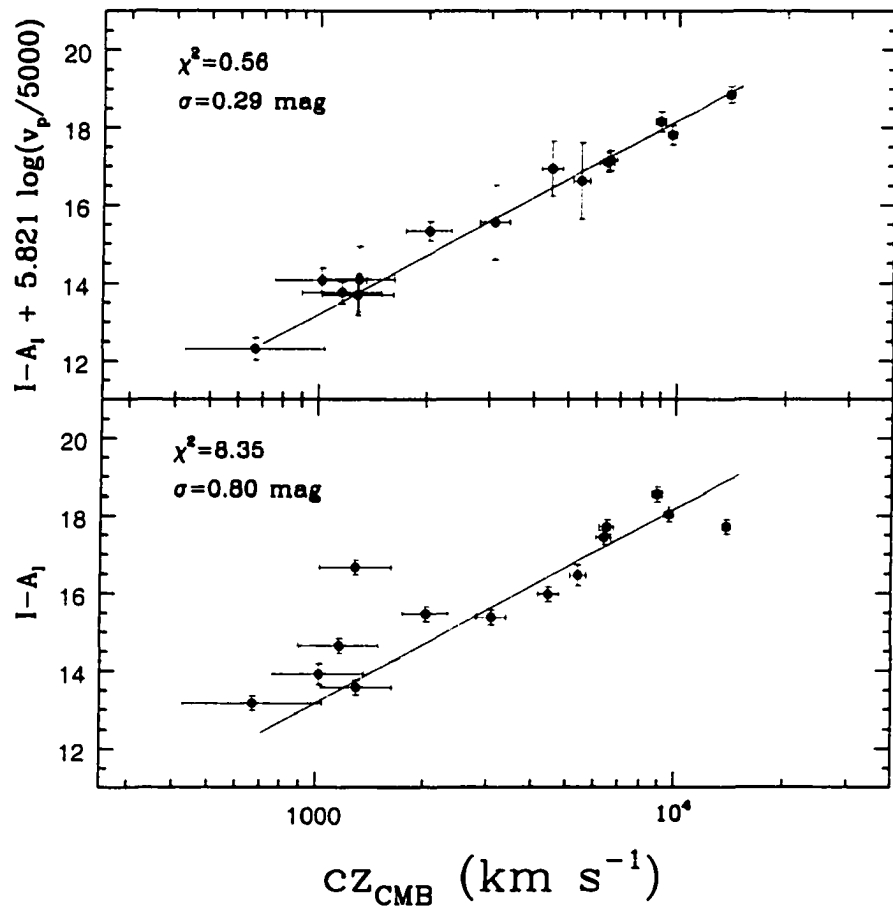


Figure 5.18: (bottom) Raw Hubble diagram from SNe II plateau I magnitudes. (top) Hubble diagram from I magnitudes corrected for expansion velocities.

The standard candle method can be used to solve for the Hubble constant, provided a distance calibrator is available. Among the objects of my sample, only SN 1987A has a precise distance in the Cepheid scale. Assuming an LMC distance of 50 kpc I get $H_0=54\pm12$ from the entire sample of V magnitudes. When I restrict the sample to the eight most distant objects I get $H_0=55\pm12$. The I magnitudes yield $H_0=53\pm9$ and $H_0=56\pm9$, respectively. These values agree comfortably well with the 65 ± 5 value from Cepheids/SNe Ia. Clearly, more calibrators are required to improve this estimate. It will be interesting to see the results from SN 1999em which will soon have a Cepheid distance measured with *HST*. It will be interesting also to derive a Hubble diagram in the JHK bands where the effects of dust are much less than at optical wavelengths.

5.8 Summary

I found a reliable bolometric correction and a calibration for effective temperature from BVI photometry for Type II SNe. Based on these calibrations I derived bolometric and effective temperature curves for the 17 SNe of this sample, which prove a useful resource to extract physical information about these objects. Despite the widely different photometric and spectroscopic properties of SNe II, some regularities emerge. In particular, there is a tight correlation between envelope expansion velocity and bolometric luminosity for the plateau phase. Using this correlation I discussed the use of SNe II-P as standard candles in the determination of cosmological distances.

Table 5.1: Fits to BC(color)^a

<i>i</i>	c _{<i>i</i>}	c _{<i>i</i>}
	B - V	V - I
0	+0.199215	-0.017371
1	+1.654947	+2.232705
2	-6.576745	-1.246158
3	+18.46060	-1.412987
4	-25.27718	+0.862287
5	+15.98919	0.000
6	-3.783559	0.000

$$^a \text{BC(color)} = \sum_{i=0}^6 c_i (\text{color})^i$$

Table 5.2: Fits to $T_{eff}(\text{color})^a$

i	c_i	c_i
	$B - V$	$V - I$
0	+7,920.7	+9,760.1
1	-20,017.7	-26,272.4
2	+47,200.8	+64,367.5
3	-48,657.1	-10,291.3
4	+17,905.6	+75,898.3

$$^a T_{eff}(\text{color}) = \sum_{i=0}^4 c_i (\text{color})^i$$

Table 5.3: Physical Parameters for Type II SNe

SN	$M_{Co} \times (H_0/65)^2$ (M_\odot)	v_p (km s $^{-1}$)	$\log L_p \times (H_0/65)^2$ (ergs s $^{-1}$)
1986L	0.029(0.016)	4150(300)	42.261(0.235)
1987A	0.065(0.020)	2391(300)	41.702(0.133)
1988A	0.170(0.074)	4613(300)	42.431(0.189)
1990E	0.030(0.019)	5324(300)	41.950(0.283)
1990K	0.040(0.022)	6142(2000)	42.471(0.234)
1991al	0.100(0.031)	7330(2000)	42.728(0.136)
1992af	0.170(0.051)	5322(2000)	42.634(0.131)
1992am	0.280(0.080)	7868(300)	42.980(0.124)
1992ba	0.028(0.016)	3523(300)	41.842(0.254)
1993A	...	4290(300)	42.103(0.126)
1993S	...	4569(300)	42.339(0.125)
1999br	...	1545(300)	41.073(0.235)
1999ca	0.030(0.010)	5353(2000)	42.422(0.148)
1999cr	0.080(0.024)	4389(300)	42.249(0.129)
1999eg	...	4012(300)	42.148(0.129)
1999em	0.040(0.037)	3757(300)	42.013(0.407)
2000cb	0.090(0.037)	4732(300)	41.963(0.177)

Table 5.4: Plateau V/I magnitudes for Type II SNe

SN	V	I
1986L	14.57(05)	...
1987A	3.42(05)	2.45(05)
1988A	15.00(05)	...
1990E	15.90(20)	14.56(20)
1990K	14.50(20)	13.90(05)
1991al	16.62(05)	16.16(05)
1992af	17.06(20)	16.56(20)
1992am	18.44(05)	17.99(05)
1992ba	15.43(05)	14.76(05)
1993A	19.64(05)	18.89(05)
1993S	18.96(05)	18.25(05)
1999br	17.58(05)	16.71(05)
1999ca	16.65(05)	15.77(05)
1999cr	18.33(05)	17.63(05)
1999eg	18.65(05)	17.94(05)
1999em	13.98(05)	13.35(05)
2000cb	16.56(05)	15.69(05)

CHAPTER 6 CONCLUSIONS

In the first part of this dissertation I used the photometric/spectroscopic database of 17 Type II SNe, in order to perform a detailed assessment about the performance of EPM. The main conclusions of this study are the following.

- EPM is very labor-intensive. The method is very sensitive to the many steps involved in the analysis which can make it an art rather than an objective measurement tool. To avoid some of the problems I implemented objective procedures to: 1) subtract the host galaxy from the SN images in order to avoid biases in the SN magnitudes, 2) compute synthetic magnitudes and derive consistent angular radii and color temperature from the SN photometry, 3) derive true photospheric velocities from cross-correlating observed and synthetic spectra, 4) interpolate velocities to the time of the photometric observations based on a two-parameter power-law fit, 5) estimate dust extinction in the SN host galaxy, and 6) obtain realistic error estimates in the derived distances.
- I used a Monte Carlo technique to estimate statistical errors in the EPM distances owing to observational uncertainties in the photometry and the velocities. On average these errors amounted to 8%.
- I found that the distance residuals at different epochs of SN evolution were generally within 15%, but sometimes reached 50% toward the end of the plateau. Although in some cases these residuals were due to extrapolations in temperature, there were other cases (e.g. SN 1986L) where the residuals were due to systematic errors in the dilution factors. Despite all the effort to lend credence to the method, it proved necessary to exercise great

care to avoid biases in the results. A comparison of the distances derived from different filters suggested that the systematic errors in distance due to dilution factors were 11% on average.

- The comparison between distances obtained from the cross-correlation technique implemented here and the traditional method of measuring expansion velocities from the Fe II $\lambda 5169$ line yielded a mean difference of only 1%, but a scatter of 17%. The cross-correlation method should be preferred as, in principle, it provides a measurement of the true photospheric velocity.
- The approach of interpolating velocities to the time of the epoch of the photometric observations can have significant impact on the derived distances. From eight SNe with well-sampled velocity and light curves I obtained distances by interpolating magnitudes to the time of the spectroscopic observations. Since the SN luminosity varies slowly during the plateau, this method is almost exact and is nearly equivalent to no interpolation. A comparison of the distances derived with this method and those obtained from interpolated velocities using power-law fits showed that the noise introduced by interpolation is 12% on average. The advantage of the power-law method is that it yields a reasonable fit to the observations, it only has two degrees of freedom so it can be applied to SNe with only two spectra, and avoids introducing artifacts in the results.
- I examined empirically the sensitivity of EPM to the effects of dust by computing $d\ln(D)/dA_{host}(V)$. My analysis showed that, among optical filters, the V - I combination had the least sensitivity to dust. For these filters I got an average of $d\ln(D)/dA_{host}(V) = -0.43$, which was very close to the -0.46 value for the standard candle technique in the V band. This demonstrates that the effect of dust on EPM is larger than previously suspected. I also found that, even though IR photometry was less affected by dust, the EPM distances derived from observations through these wavelengths were more sensitive to dust than those yielded from optical filters. For an adopted ± 0.3 mag error in $A_{host}(V)$,

the corresponding uncertainty was 14% in the EPM distances.

- Summing in quadrature the four error components mentioned above (statistical, dilution factors, velocity interpolations, and extinction) I obtained an average uncertainty of 24% in distance from all of the objects analyzed. The study of the EPM Hubble diagram showed that my error estimates were 15% higher than the observed scatter, so that the actual error in an individual EPM distance was probably 20%. This implied also that there was no evidence for significant error sources (like asymmetries in the explosion) other than those mentioned above. The 20% uncertainty found here contrasts with the 10% error derived from the Hubble diagram of S94. If nearly simultaneous photometry and spectroscopy can be obtained the 12% interpolation error would disappear, bringing the total error down to 16%.
- I derived a value between 63 ± 8 and $67 \pm 7 \text{ km s}^{-1} \text{ Mpc}^{-1}$ for the Hubble constant from the CC method and the $\{V\text{ }I\}$ filters, depending on the redshift sample chosen for the analysis. Both of these estimates prove in good agreement with the 65 ± 5 value yielded by Cepheid/SNe Ia distances.
- The comparison of four EPM and Tully-Fisher distances in the Cepheid scale of Giovanelli et al. (1997) ($H_0=69$) yielded $D(\text{EPM})/D(\text{TF})=0.82 \pm 0.12$. Clearly more objects will be required to check or rule out systematic differences between EPM and TF. In any case, this result contrasts with the result by S94 that TF distances average $11(\pm 7)\%$ smaller than EPM. The discrepancy is due to the fact that S94 used TF distances derived from a luminosity-line-width corresponding to $H_0=86$.

In the second part of this dissertation I studied the intrinsic properties of the 17 Type II SNe, which yielded the following conclusions.

- Using the optical/IR data for SNe 1987A and 1999em I found a reliable bolometric correction for the plateau and nebular phases of SNe II, which permitted me to derive bolometric luminosities from BV or $V\text{ }I$ photometry with a precision of 0.06 mag and

accuracy of 0.15 mag. This calibration proved in excellent agreement with that obtained from atmosphere models.

- The model spectra of E96 allowed me to derive a photometric calibration for effective temperature during the plateau phase. I presented calibrations for $B - V$ and $V - I$ characterized by scatters of 600 K in temperature.
- I derived bolometric and temperature curves for the 17 SNe. For comparable epochs these objects showed a range of $\times 80$ in luminosity, and a rich variety of light curve morphologies. Despite this great diversity, the duration of the plateau was approximately the same for seven SNe with sufficient photometric data. The analytical models of Popov (1993) suggests that the envelope masses of SNe II-P do not vary much.
- I measured characteristic luminosities and expansion velocities from the plateau phase of the 17 SNe and found that these parameters were tightly correlated, in the sense that objects with brighter plateaus expanded faster.
- The exponential tails showed a wide range of luminosities, yet they were all consistent with the decline rate expected from radioactive decay of ^{56}Co . I estimated the Co masses produced in the explosions of the 13 SNe with sufficient late-time photometry. I obtained a wide range between 0.02 and $0.28 M_{\odot}$ of Co, and some evidence that SNe with brighter plateaus produced more Co. However, the scatter in this correlation was significant and suggested that at least a second parameter was required to explain the production of Ni (and its daughter Co).
- The correlation between expansion velocity and luminosity in the plateau phase, permitted me to normalize the apparent magnitudes to a common expansion velocity. The resulting Hubble diagram shows a scatter of 0.39-0.20 mag in the V band, and between 0.29-0.21 mag in the I band, depending on the redshift range considered in the analysis. This implies that SNe II-P have potential as standard candles. More observations are required to pin down the actual spread, but it seems clear that this technique can produce

relative distances with better precision than EPM (20% in distance, or 0.43 mag) and is far less complicated. Using SN 1987A to calibrate the Hubble diagram and assuming a distance to the LMC of 50 kpc, I got $H_0=55\pm12$ and $H_0=56\pm9$ from the V and I filters, respectively. These values agree comfortably well with the $H_0=65\pm5$ derived from Cepheids/SN Ia.

APPENDIX A THE COMPUTATION OF SYNTHETIC MAGNITUDES

The implementation of EPM requires fitting the observed SN magnitudes to those of a blackbody, from which the color temperature and the angular radius of the SN can be obtained. This process involves synthesizing broadband magnitudes from blackbody spectra. It is crucial, therefore, to place the synthetic magnitudes on the same photometric system employed in the observations of the SN.

Since the SN magnitudes are measured with photon detectors, a synthetic magnitude is the convolution of the observed photon number distribution, N_λ , with the filter transmission function [$S(\lambda)$], i.e.,

$$mag = -2.5 \log_{10} \int N_\lambda S(\lambda) d\lambda + ZP. \quad (\text{A.1})$$

where ZP is the zero point for the magnitude scale and λ is the wavelength in the observer's frame.

For an adequate use of equation A.1, $S(\lambda)$ must include the transparency of the Earth's atmosphere, the filter transmission, and the detector quantum efficiency (QE). For *BVRI* I adopt the filter functions B_{90} , V_{90} , R_{90} , I_{90} published by Bessell (1990). However, since these curves are meant for use with energy and not photon distributions [see Appendix in Bessell (1983)], I must divide them by λ before employing them in equation A.1. Also, since these filters do not include the atmospheric telluric lines, I add these features to the *R* and *I* filters (in *B* and *V* there are no telluric features) using my own atmospheric transmission spectrum. Figure A.1 shows the resulting curves.

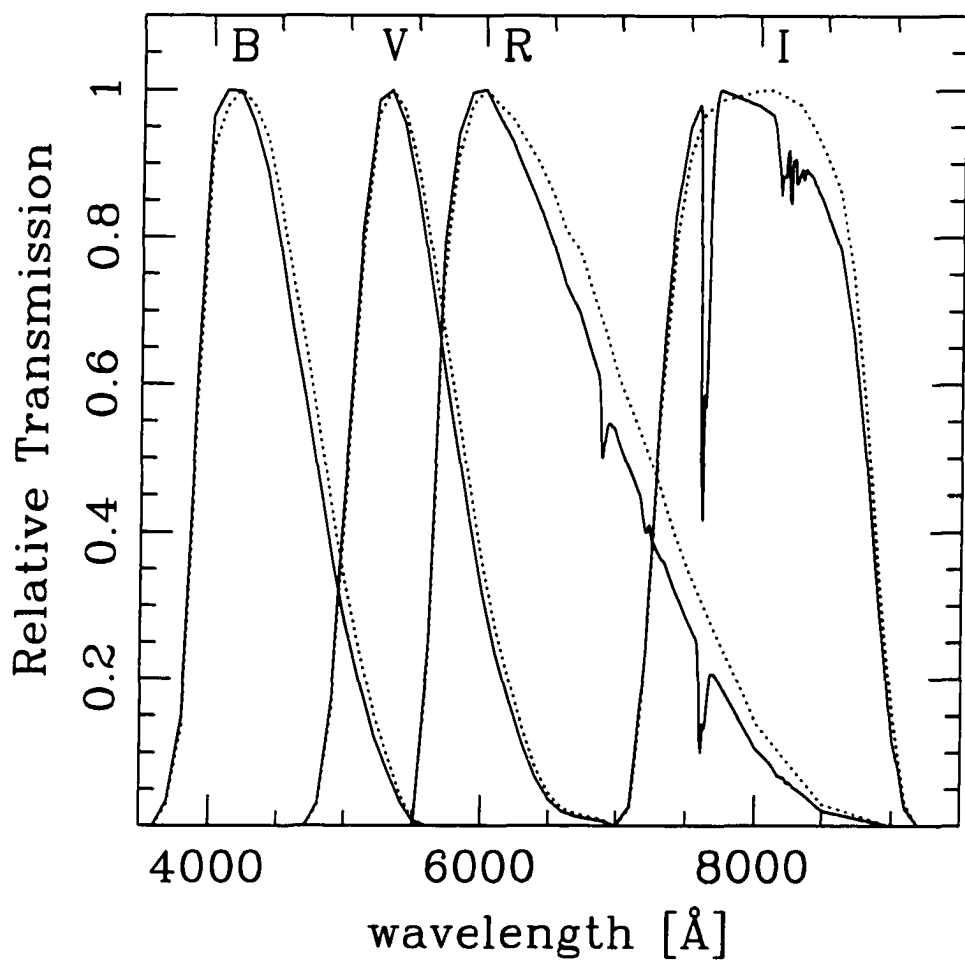


Figure A.1: $BVRI$ filters functions of Bessell (1990) meant for use with energy distributions (dotted curves). With solid lines are shown the curves modified for use with photon distributions, to which I added the telluric lines.

For the Z filter I use the transmission curve of filter 611 and the QE of CCD TEK36 of the NTT/EMMI instrument. I include the telluric lines, but I ignore continuum atmospheric opacity which is very small at these wavelengths. For JHK I use the J_S , H , and K_S filter transmissions tabulated by Persson et al. (1998), a nominal NICMOS2 QE, and the IR atmospheric transmission spectrum (kindly provided to me by J.G. Cuby). Figure A.2 shows the resulting $ZJHK$ filter functions, along with the corresponding detector QEs.

The ZP in equation A.1 must be determined by forcing the synthetic magnitude of a star to match its observed magnitude. I use the spectrophotometric calibration of Vega published by Hayes (1985) in the range 3300-10405 Å and the V magnitude of 0.03 mag measured by Johnson et al. (1966), from which I solve for the ZP in the V band. In principle, I can use the same procedure for BRI , but Vega's photometry in these bands is not very reliable as it was obtained in the old Johnson standard system. To avoid these problems I employ ten stars with excellent spectrophotometry Hamuy et al. (1994a) and photometry in the modern Kron-Cousins system (Cousins, 1971, 1980, 1984). Before using these standards I remove the telluric lines from the spectra since the filter functions already include these features. With this approach I obtain an average and more reliable zero point for the synthetic magnitude scale with rms uncertainty of ~ 0.01 mag. With these ZPs I find that the synthetic magnitudes of Vega are brighter than the observed magnitudes (Johnson et al., 1966) by 0.016 mag in B , 0.025 in R , and 0.023 in I (see Table A.1), which is not so disappointing considering that this comparison requires transforming the Johnson RI magnitudes to the Kron-Cousins system (Taylor, 1986).

In my Z photometric system Vega has a magnitude of 0.03. Note that this value is not the result of a measurement but, instead, of my own definition of the zero point for the Z photometric system (Appendix B).

At longer wavelengths, where no continuous spectrophotometric calibration is avail-

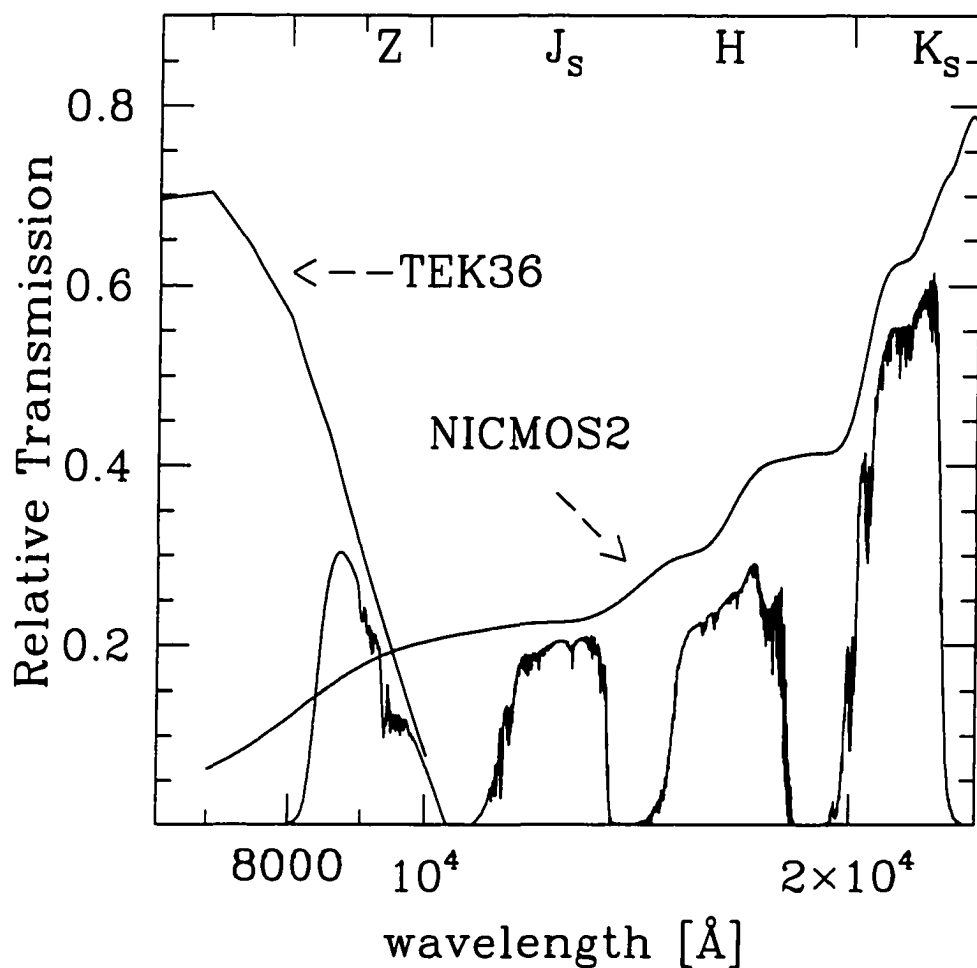


Figure A.2: Z , J_s , H , K_s filters functions. Also shown are the QE of TEK36 and NICMOS2 that I employed to construct these functions.

able for Vega (or any other star), I adopt the solar model of Kurucz with the following parameters: $T_{eff}=9,400$ K, $\log g=3.9$, [Fe/H]=-0.5, $V_{microturb}=0$ [see Cohen et al. (1992) for a detailed description of the model and Gray & Corbally (1994) for the calibration of the MK spectral system]. After flux scaling this model and bringing it into agreement with the $V=0.03$ magnitude of Vega, the model matches the Hayes calibration at the level of 1% or better over the $BVRI$ range, lending credence to the calibration assumed for longer wavelengths. Figure A.3 shows the adopted spectrophotometric calibration for Vega in the optical and IR. To calculate the zero points in JHK , I adopt the magnitude of Vega in the CIT photometric system (Elias et al., 1982), namely, 0.00 mag at all wavelengths. The original CIT system comprises stars of 4-7th magnitude. It was recently extended by Persson et al. (1998) to fainter standards which are the stars employed for the calibration of the JHK light curves of the SNe.

Table A.1 summarizes the zero points computed with equation A.1, and the corresponding magnitudes for Vega in such system. For the proper use of these ZPs it is necessary to express N_λ in ($\text{sec}^{-1} \text{cm}^{-2} \text{cm}^{-1}$) and λ in Å. From the ten secondary standards I estimate that the uncertainty in the zero points is ~ 0.01 mag in $BVRI$. At longer wavelengths the zero points are more uncertain since they come from the adopted model energy distribution of Vega, which is probably accurate to better than 5%.

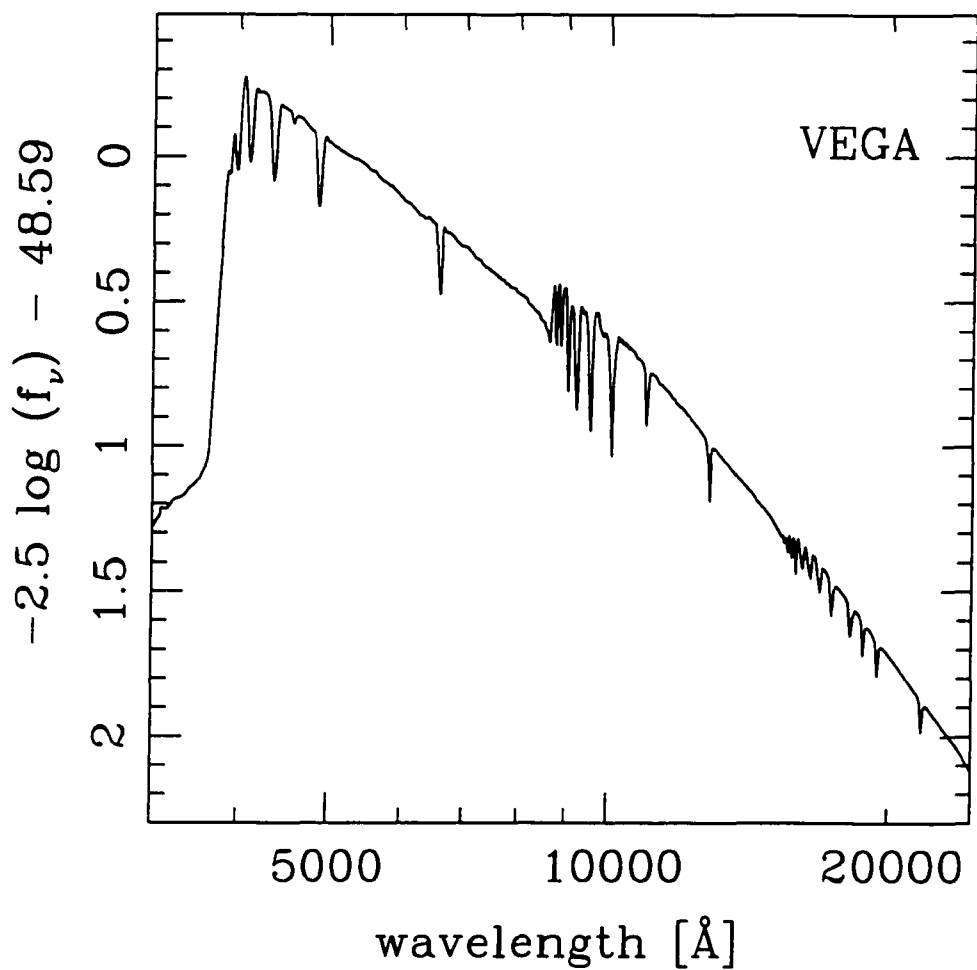


Figure A.3: Adopted spectrophotometric calibration for Vega. In the optical ($\lambda \leq 10,500$ Å) the calibration is from Hayes (1985), and at longer wavelengths I adopted the Kurucz spectrum with parameters $T_{eff}=9,400$ K, $\log g=3.9$, $[Fe/H]=-0.5$, $V_{microturb}=0$.

Table A.1: Photometric Zero points and Synthetic Magnitudes for Vega

	<i>B</i>	<i>V</i>	<i>R</i>	<i>I</i>	<i>Z</i>	<i>J_S</i>	<i>H</i>	<i>K_S</i>
Zero point	35.287	34.855	35.060	34.563	32.724	32.230	32.098	32.175
Vega	0.014	0.030	0.042	0.052	0.030	0.00	0.00	0.00

APPENDIX B THE Z BAND PHOTOMETRIC SYSTEM

I define the Z band as the product of the transmission of the Z filter (number 611) and the QE of CCD TEK36 of the NTT/EMMI instrument. The resulting bandpass also includes telluric lines (see Figure A.2). I employ this filter function to compute synthetic magnitudes from the tertiary spectrophotometric standards published by Hamuy et al. (1994a). However, since these spectra contain telluric lines it is necessary first to remove these features. Then I use equation A.1 and an *adopted* ZP of 32.724 that yields a magnitude of 0.03 for Vega. I choose this ZP so that $(V - Z) = 0$ for Vega. The resulting synthetic magnitudes for the tertiary standards are listed in Table B.1 and this is the system relative to which I calibrate the photometric sequences around the SNe. In Hamuy et al. (1994a) we showed that synthetic magnitudes in the I band had typical uncertainties of 0.018 mag. Therefore, I believe that the Z magnitudes in Table B.1 have errors of 0.02 mag.

Table B.1: Standard Stars for the Z band

<i>Star</i>	<i>Z</i>
	± 0.020
LTT 377	10.523
LTT 1020	10.648
EG 21	11.619
LTT 1788	12.369
LTT 2415	11.526
Hiltner 600	10.132
L745-46A	12.670
LTT 3218	11.652
LTT 3864	11.374
LTT 4364	11.181
Feige 56	11.154
LTT 4816	13.792
CD -32	10.041
LTT 6248	10.966
EG 274	11.359
LTT 7379	9.376
LTT 7987	12.437
LTT 9239	11.144
Feige 110	12.249
LTT 9491	14.071

REFERENCES

- Arnett, W. D., & Falk, S. W. 1976, ApJ, 210, 733
- Arnett, W. D. 1980, ApJ, 237, 541
- Arnett, D. 1996, *Supernovae and Nucleosynthesis*, (New Jersey: Princeton Univ. Press)
- Baade, W. 1926, Astr. Nachr., 228, 359
- Baade, W., & Zwicky, F. 1934, Phys. Rev., 45, 138
- Baade, W. 1938, ApJ, 88, 285
- Barbon, R., Ciatti, F., & Rosino, L. 1979, A&A, 72, 287
- Barbon, R., Benetti, S., Rosino, L., Capellaro, & Turatto, M. 1990, A&A, 237, 79
- Baron, E., et al. 2000, ApJ, 545, 444
- Benetti, S., Capellaro, E., & Turatto, M. 1991, A&A, 247, 410
- Benetti, S., Capellaro, E., Turatto, M., Della Valle, M., Mazzalli, P. A., & Gouiffes, C. 1991, A&A, 285, 147
- Bessell, M. S. 1983, PASP, 95, 480
- Bessell, M. S. 1990, PASP, 102, 1181
- Blinnikov, S. I., & Bartunov, O. S. 1993, A&A, 273, 106
- Blinnikov, S., Lundqvist, P., Bartunov, O., Nomoto, K., & Iwamoto, K. 2000, ApJ, 532, 1132
- Bouchet, P., Monetti, A., Slezak, E., Le Bertre, T., & Manfroid, J. 1989, A&AS, 80, 379
- Branch, D. 1990, in *Supernovae*, ed. A. G. Petschek (New York:Springer), 30
- Burrows, A. 2000, Nature, 403, 727

- Capellaro, E., Danziger, I. J., Della Valle, M., Gouiffes, C., & Turatto, M. 1995, A&A, 293, 723
- Cardelli, J. A., Clayton, G. C., & Mathis, J. S. 1989, ApJ, 345, 245
- Cohen, M., Walker, R. G., Barlow, M. J., & Deacon, J. R. 1992, AJ, 104, 1650
- Cousins, A. W. J. 1971, R. Obs. Ann. No 7
- Cousins, A. W. J. 1980, SAAO Circ. 1, 234
- Cousins, A. W. J. 1984, SAAO Circ. 8, 69
- Dwek, E. et al. 1983, ApJ, 274, 168
- Eastman, R. G., & Kirshner, R. P. 1989, ApJ, 347, 771
- Eastman, R. G., Schmidt, B. P., & Kirshner, R. 1996, ApJ, 466, 911 (E96)
- Elias, J. H., Frogel, J. A., Matthews, K., & Neugebauer, G. 1982, AJ, 87, 1029
- Evans, R. 1986, IAU Circ. 4260
- Evans, R. 1988, IAU Circ. 4533
- Evans, R. 1990, IAU Circ. 5022
- Evans, R. 1992, IAU Circ. 5625
- Falk, S. W., & Arnett, W. D. 1977, ApJS, 33, 515
- Freedman, W. L. et al. 2001, ApJ, 553, 47
- Garnavich, P., Jha, S., Challis, P., & Kirshner, R. 1999, IAU Circ. 7143
- Gibson, B. K. et al. 2000, ApJ, 529, 723
- Giovanelli, R., Haynes, M. P., da Costa, L. N., Freudling, W., Salzer, J. J., & Wegner, G. 1997, ApJ, 477, L1
- Giovanelli, R. 2001, private communication
- Gould, A., & Uza, O. 1998, ApJ, 494, 118
- Gray, R. O., & Corbally, C. J. 1994, AJ, 107, 742
- Hamuy, M., Suntzeff, N. B., Bravo, J., & Phillips, M. M. 1990, PASP, 102, 888
- Hamuy, M., & Suntzeff, N. B. 1990, AJ, 99, 1146

- Hamuy, M., et al. 1993, AJ, 106, 2392
- Hamuy, M., Suntzeff, N. B., Heathcote, S. R., Walker, A. R., Gigoux, P., & Phillips, M. M. 1994, PASP, 106, 566
- Hamuy, M., et al. 1994, AJ, 108, 2226
- Hamuy, M., Phillips, M. M., Maza, J., Suntzeff, N. B., Schommer, R. A., & Avilés, R. 1995, AJ, 109, 1
- Hamuy, M., Phillips, M. M., Suntzeff, N. B., Schommer, R. A., Maza, J., & Avilés, R. 1996, AJ, 112, 2398
- Hamuy, M., et al. 2001, ApJ, 558, 615
- Harkness, R. P., & Wheeler, J. C. 1990, in *Supernovae*, ed. A. G. Petschek (New York:Springer), 1
- Hayes, D. S. 1985, in *Calibration of Fundamental Stellar Quantities*, ed. D. S. Hayes, L. E. Pasinetti, & A. G. Philip (Dordrecht: Reidel), 225
- Hurst, G. M. 1999, IAU Circ. 7275
- Jeffery, D. J., & Branch, D. 1990, in *Jerusalem Winter School for Theoretical Physics: Supernovae*, Vol. 6, ed. J. C. Wheeler, T. Piran, & S. Weinberg (Singapore: World Scientific), 149
- Johnson, H. L., Iriarte, B., Mitchell, R. I., & Wisniewski, W. Z. 1966, Commun. Lunar Plan. Lab., 4, 99
- King, J. Y. 1999, IAU Circ. 7141
- Kirshner, R. P., & Kwan, J. 1974, ApJ, 193, 27
- Kowal, C. T. 1968, AJ, 73, 1021
- Kosai, H. 1988, IAU Circ. 4533
- Kunkel, W., & Madore, B. 1987, IAU Circ. 4316
- Landolt, A. U. 1992, AJ, 104, 340
- Leibundgut, B. 1990, in *Supernovae*, ed. S.E. Woosley (Berlin:Springer), 751
- Leonard, D. C., & Filippenko, A. V. 2001, PASP, 113, 920
- Leonard, D. C., et al. 2001, PASP, in press (astro-ph/0109535)

- Li, W. 1999a, IAU Circ. 7143
- Li, W. D. 1999b, IAU Circ. 7294
- Litvinova, I. I., & Nadezhin, D. K. 1983, *Ap&SS*, 89, 89
- Lynden-Bell, D., & Lahav, O. 1988, in *Large-Scale Motions in the Universe*, ed. V.C. Rubin & G.V. Coyne (Princeton: Princeton Univ. Press), 199
- Mattila, S., & Meikle, W. P. S. 2000, *MNRAS*, 324, 325
- Maza, J., Wischnjewsky, M., Torres, C., González, I., Costa, E., & Wroblewski, H. 1981, *PASP*, 93, 239
- Maza, J., & Hamuy, M. 1993a, IAU Circ., 5693
- Maza, J., & Hamuy, M. 1993b, IAU Circ., 5812
- Maza, J., & Hamuy, M. 1999, IAU Circ., 7210
- McNaught, R. H. 1992, IAU Circ. 5632
- Minkowski, R. 1941, *PASP*, 53, 224
- Oke, J. B., & Sandage, A. 1968, *ApJ*, 154, 21
- Panagia, N., Gilmozzi, R., Kirshner, R. P., Pun, C. S. J., & Sonneborn, G. 1997, *BAAS*, 191, #19.09
- Papenkova, M., & Li, W. D. 2000, IAU Circ. 7410
- Pastorello, A., et al. 2001, in preparation
- Patat, F., Barbon, R., Capellaro, E., & Turatto, M. 1994, *A&A*, 282, 731
- Pennypacker, C., & Perlmutter, S. 1990, IAU Circ. 4965
- Perlmutter, S., et al. 1999, *ApJ*, 517, 565
- Persson, S. E., Murphy, D. C., Krzeminski, W., Roth, M., & Rieke, M. J. 1998, *AJ*, 116, 2475
- Phillips, M. M., et al. 1987, *PASP*, 99, 592
- Phillips, M. M., Heathcote, S. R., Hamuy, M., & Navarrete, M. 1988, 95, 1087
- Phillips, M., & Maza, J. 1992, IAU Circ. 5570
- Phillips, M. M. 1993, *ApJ*, 413, L105

- Phillips, M. M., Lira, P., Suntzeff, N. B., Schommer, R. A., Hamuy, M., & Maza, J. 1999, AJ, 118, 1766
- Pierce, M. J., & Tully, R. B. 1992, ApJ, 387, 47
- Pierce, M. J. 1994, ApJ, 430, 53
- Pooley, D., et al. 2001, astro-ph/0103196
- Popov, D. V. 1993, ApJ, 414, 712
- Riess, A. G., et al. 1998, AJ, 116, 1009
- Ruiz-Lapuente, P., Kidger, M., López, R., & Canal, R. 1990, AJ, 100, 782
- Saha, A., Sandage, A., Tammann, G. A., Labhardt, L., Macchetto, F. D., & Panagia, N. 1999, ApJ, 522, 802
- Sandage, A., & Tammann, G. A. 1993, ApJ, 415, 1
- Sandage, A., Tammann, G. A., & Saha, A. 2001, Conference report for the May 1999 Space Telescope Science Institute's workshop on "Supernovae and Gamma Ray Bursts"
- Schlegel, E. M. 1996, AJ, 111, 1660
- Schlegel, D. J., Finkbeiner, D. P., & Davis, M. 1998, ApJ, 500, 525
- Schmidt, B. P., Kirshner, R. P., & Eastman, R. G. 1992, ApJ, 395, 366 (SKE92)
- Schmidt, B. P., et al. 1993, AJ, 105, 2236
- Schmidt, B. P., et al. 1994a, AJ, 107, 1444
- Schmidt, B. P., et al. 1994b, ApJ, 432, 42 (S94)
- Smoot, G.F., et al. 1992, ApJ, 396, L1
- Strolger, L. G., et al. 1999, AAS, 195, 3801
- Suntzeff, N. B., & Bouchet, P. 1990, AJ, 99, 650
- Suntzeff, N. B., et al. 2001, in preparation
- Svoboda, R. 1987, IAU Circ. 4340
- Swartz, D., Wheeler, J. C., & Harkness, R. P. 1991, ApJ, 374, 266
- Taylor, B. J. 1986, ApJS, 60, 577

- Turatto, M., Capellaro, E., Benetti, S., & Danziger, I. J. 1993, MNRAS, 265, 471
- van Belle, G.T., et al. 1999, AJ, 117, 521
- van den Bergh, S., & Pazder, J. 1992, ApJ, 390, 34
- Wagoner, R. V. 1977, ApJ, 214, L5
- Walker, A. R. 1999, in Post-Hipparcos Cosmic Candles, ed. A. Heck and F. Caputo (Dordrecht:Kluwer), 125
- Walker, A. R., Raimondo, G., Di Carlo, E., Brocato, E., Castellani, V., & Hill, V. 2001, ApJL, in press (astro-ph/0109147)
- Weaver, T. A., & Woosley, S. E. 1980, in Proceedings of the Texas Symposium on Relativistic Astrophysics, 9th, (New York: New York Acad. Sci.), 335
- Weiler, K. W., van der Hulst, J. M., Sramek, R. A., & Panagia, N. 1981, ApJ, 243, L151
- Weiler, K. W., Van Dyk, S. D., Montes, M. J., Panagia, N., & Sramek, R. A. 1998, ApJ, 500, 51
- Wells, L., & Maza, J. 1991, IAU Circ. 5310
- Wells, L., & Maza, J. 1992, IAU Circ. 5554
- Woodings, S., Martin, R., & Williams, A. 1999, IAU Circ. 7158
- Woosley, S. E., Pinto, P. A., Martin, P. G., & Weaver, T. A. 1987, ApJ, 318, 664
- Woosley, S. E., Pinto, P. A., & Hartmann, D. 1989, ApJ, 346, 395
- Young, T. R., & Branch, D. 1989, ApJ, 342, L79
- Zwicky, F. 1935, Sci. Mon., 40, 461
- Zwicky, F. 1938, PASP, 50, 215